DEVELOPMENT OF VALIDATED MODELS FOR BRAKE SQUEAL PREDICTIONS

A thesis submitted to the University of London

for the degree of Doctor of Philosophy

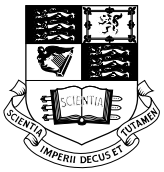

By

ANANTAWIT TUCHINDA

Department of Mechanical Engineering

Imperial College London

September 2003

Abstract

Disc brake squeal is an irritating high-pitched sound which still remains a major problem facing the automotive industry. The main concern over the squeal problem is that it can cause discomfort to passengers and pedestrians and, hence, reduce the overall acceptability of the vehicle. The overall aim of this project is to gain some new and better insight into the problem of disc brake squeal.

In this thesis, general squeal characteristics are studied via the use of a pin-on-disc system which is used as a representative model to include the essential features of the actual brake assembly. By assuming that the friction coefficient is constant, a linear pin-on-disc model can be derived. The onset of instability of the linear pin-on-disc system can be obtained via a complex eigenvalue analysis. A possible mechanism in which instability is generated is also discussed. The linear pin-on-disc model is extended into a more realistic model by incorporating a new friction model in which the friction coefficient is a continuous function of the relative velocity between the two contact surfaces. The responses of this new pin-on-disc model are calculated using a time-integration method. A particular interest has been concentrated on the limit-cycle characteristics of the system, especially when mistuning has been added to the disc. To make certain that the theoretical models can represent the dynamic behaviour of the real structure, the simulated results are verified against test data.

Apart from the squeal modelling, the current research also investigate free vibration characteristics of three-dimensional "tophat-like" structures widely used in disc brake design. A systematic method for unambiguous mode identification of these structures has been developed. Furthermore, the current study also demonstrates a systematic method for classifying vibration modes of "tophat-like" structures into appropriate families according to their similarity both in the $r - \theta$ and $r - z$ planes.

Acknowledgements

I would like to express my gratitude to my supervisor Professor David Ewins for his valuable advice, interest, encouragement and guidance throughout this project. Also, the valued input of Mr David Robb is much appreciated.

I would also like to thank Robert Bosch GmbH for funding the research with particular recognition of Dr. Michael Fischer and Dr. Norbert Hoffmann for their guidance and valuable discussions. I gratefully acknowledge receiving a number of very useful advice from Professor J. Woodhouse and Professor S.G. Hutton.

Special thanks are extended to my colleagues from the Dynamics Section, especially Enrique Gutierrez-Wing, Götz von Groll, Antony Stanbridge, Paul Woodward and six of my Italian co-workers for the useful conversations and for so willingly offering all the technical assistance.

The funding from the Thai Government throughout the course of my study is gratefully acknowledge.

Last but not least, thanks to my family and friends for their love and supports. Without their help this thesis would not have been completed.

To my beloved brother

Sarawut Tuchinda

1973-1993

Contents

Nomenclature

Basic Terms and Dimensions

E	Young's modulus
N	Static load
V_0	Velocity of the disc at the point of contact
a	Outer radius of the disc
b	Inner radius of the disc
c	Contact damping
$\hat{c}$	Contact damping per unit length
k	Contact stiffness
$\hat{k}$	Contact stiffness per unit length
m	Number of nodal circle
m_0	Mistuning mass
n	Number of nodal diameter
t	Time
v	In-plane displacement
w	Out-of-plane displacement
r, θ, z	Cylindrical polar coordinates for the disc
x, y, z	Cartesian coordinates for the pin

Subscripts and Superscripts

b	Backward
c	Combined system
d	Disc
f	Forward
h	h^{th} contact node
i	Numbers of the original disc modes
j	Numbers of the original pin modes
n	Normal direction
p	Pin
t	Tangential direction

Matrices and vectors

$[\ \ ]$	Matrix
$[\ddots]$	Diagonal matrix
$[\ \ ]^T$	Transpose of a matrix
$[\ \ ]^{-1}$	Inverse of a matrix
$\{\}$	Column vector
$[\Phi]$	Mass-normalised mode shape matrix
$\{F\}$	Vector of applied forces
$[I]$	Identity matrix
$[K]$	Stiffness matrix
$[M]$	Mass matrix
$\{q\}$	Vector of generalised coordinates
$\{x\}$	Vector of physical coordinates

Greek Symbols

Ω	Rotational speed of the disc, rad/s
α	Angle of inclination
δ	Dirac delta function
λ	Eigenvalue
μ_d	Dynamic coefficient of friction
μ_s	Static coefficient of friction
ν	Poisson's ratio
ρ	Density
ω	Natural frequency

Standard Abbreviations

DOF(s)	Degree(s) of freedom
FE	Finite Element
FRF	Frequency Response Function
IC	Imperial College
LDV	Laser Doppler Vibrometer
nND	n nodal diameter (diametral) pattern, n can be any integer
ODS	Operating deflection shape

List of Figures

List of Tables

Chapter 1

Introduction

1.1 Overview

Disc brake squeal still remains a major problem facing the automotive industry, despite substantial time and effort devoted to solving the problem during the past few decades. The main concern over the squeal problem is that it can cause discomfort to passengers and pedestrians and, hence, reduce the overall acceptability of the vehicle. The automotive industry also loses substantial revenue from warranty costs but, more importantly, customer dissatisfaction may result in a loss of future business. Thus, eliminating squeal becomes one of the top priorities in current brake development.

Squeal has been a problem from as early as 1938, and since then there have been many attempts to solve this problem by both theoretical and experimental approaches. However, research over many years has failed to provide a reliable means of preventing brake squeal. One of the main reasons for these unsuccessful attempts is a lack of fundamental understanding of the phenomenon. Thus, the overall aim of this project is to gain some new and better insight into the problem of disc brake squeal and to find the basic mechanism in which instability (squeal) is generated.

1.1.1 Definition of disc brake squeal

There are several types of noise or vibration associated with disc brake systems. These are usually classified into two major categories, according to the frequency range in which they occur: (i) low-frequency rigid-body vibration, called "judder" or "groan", and (ii) medium and high frequency noise, called "squeal". Although there is no rigorous definition for the threshold frequency which separates these two classes of brake noise, it is generally accepted that squeal is an intermittent and high-pitched sound with the frequency within the range of 1 to 20 kHz. Squeal is also known to have a fugitive nature that is it can sometimes be non-repeatable. From many experimental observations, it is known that squeal usually occurs at slow rotational speeds (around 0.1-1 Hz or 6-60 rev/min) towards the end of a stop.

From a theoretical perspective, disc brake squeal can be classified as a friction-induced type of vibration problem. The phenomenon is also known to be associated with geometrically-induced instability where a small perturbation can grow exponentially into audible noise. However, there is still no generally accepted explanation of the mechanism which produces the squeal noise.

1.1.2 Disc brake components

A disc brake assembly, such as the one shown in Figure 1.1, generally consists of four main components: (i) a brake disc (also called the rotor), (ii) a calliper, (iii) two brake pads, and (iv) mounting components. Although brake discs may come in many different designs (e.g. solid or vented), most of them have the same basic structure which is in the form of "top-hat" configuration, as illustrated in Figure 1.2. The main purpose of the "top-hat" shape is to provide the geometric offset necessary for mounting the brake disc onto the vehicle. The calliper, which contains a cylinder with a piston (multiple-pistons may be used in some types of heavy-duty brakes), holds the two brake pads on either side of the rotor, as shown in Figure 1.3. The movement of the piston is controlled by a hydraulic system. When hydraulic pressure is applied, the piston is

pushed forward to press the inner pad against the rotor while the housing is pushed in the opposite direction to press the outer pad against the rotor, hence, generating a braking torque. Brake pads are normally made of complex resin-based, short fibre-reinforced composites containing various friction modifiers (some types of brake pad also contain metallic material).

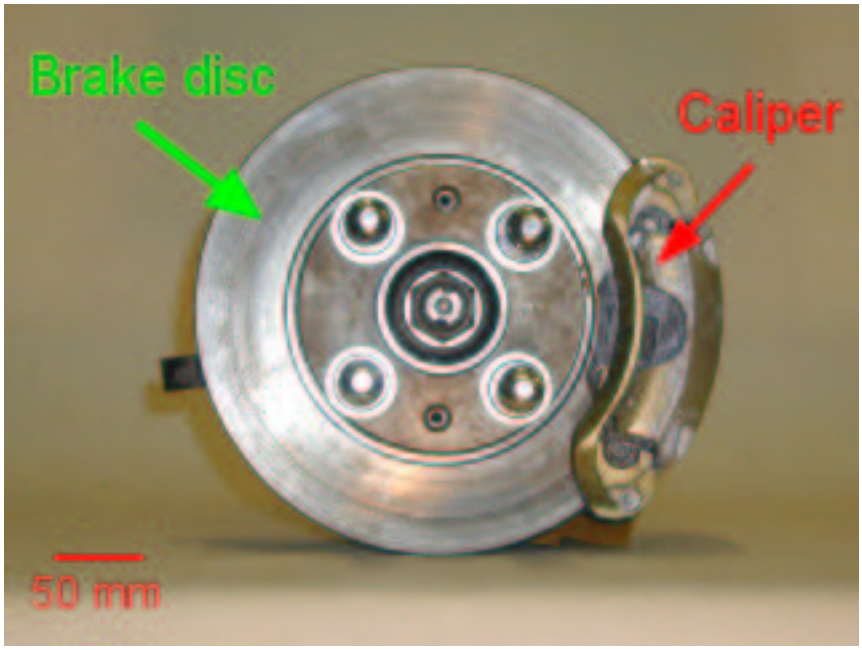

Figure 1.1: *Disc brake assembly.*

(a) (b) (c)

Figure 1.2: *Typical brake disc with a "top-hat" shape: (a) cross-section sketch, (b) side-view, and (c) top-view.*

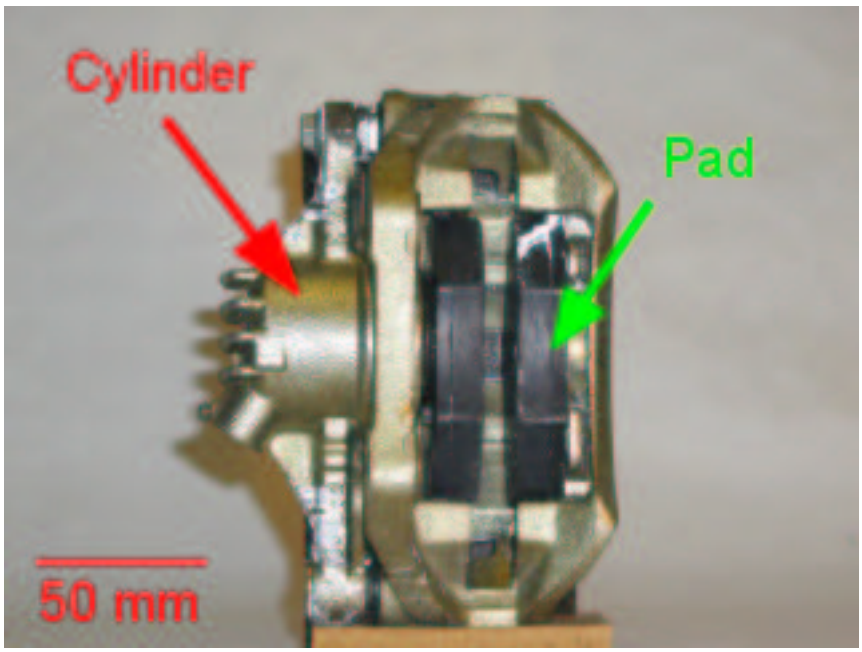

Figure 1.3: *Brake calliper holding two brake pads.*

1.2 Literature review

1.2.1 Overview

Disc brake squeal can be classified as a vibration problem which involves two major areas of vibration study: (i) rotor/stator interaction, and (ii) friction-induced vibration. In the past, there have been a vast number of studies related to these two topics and, thus, it is not possible to cover every aspect of these two areas of research. The aim of this literature review is, therefore, to concentrate on the historical background and the most recent developments in disc brake squeal studies and also to review some other relevant applications, such as circular saws, computer disc drives, and turbine bladed discs, in search of new techniques which could be used to solve the problem of disc brake squeal. Further information on disc brake squeal research can also be found in the literature reviews conducted by Papinniemi *et al.* [1] in 2002 and Kinkaid *et al.* [2] in 2003. As for the subject of friction, a thorough review was given by Gaul and Nitsche [3] in 2001.

1.2.2 Historical background

Prior to 1960, it was commonly believed that brake squeal was caused by a rapid increase in the friction coefficient with decreasing speed in braking (also known as the negative slope of the friction-speed curve). According to North [4], the effect of the negative slope of the friction-speed curve on the instability of brake systems can easily be demonstrated and is described below.

First, consider a simple elastic rubbing system shown in Figure 1.4 (a). If the coefficient of friction is assumed to be of the form

$$\mu = \mu_s[1 - \lambda(V_0 - \dot{x})], \tag{1.1}$$

where μ_s is the static friction coefficient, and λ is the magnitude of the slope of the friction-speed curve (a positive value), as illustrated in Figure 1.4 (b). Then, the

equation of motion of the rubbing block can be written as

$$m\ddot{x} + kx = \mu_s N[1 - \lambda(V_0 - \dot{x})]. \tag{1.2}$$

This equation can be re-arranged as

$$m\ddot{x} - \lambda\mu_s N\dot{x} + kx = \mu_s N(1 - \lambda V_0). \tag{1.3}$$

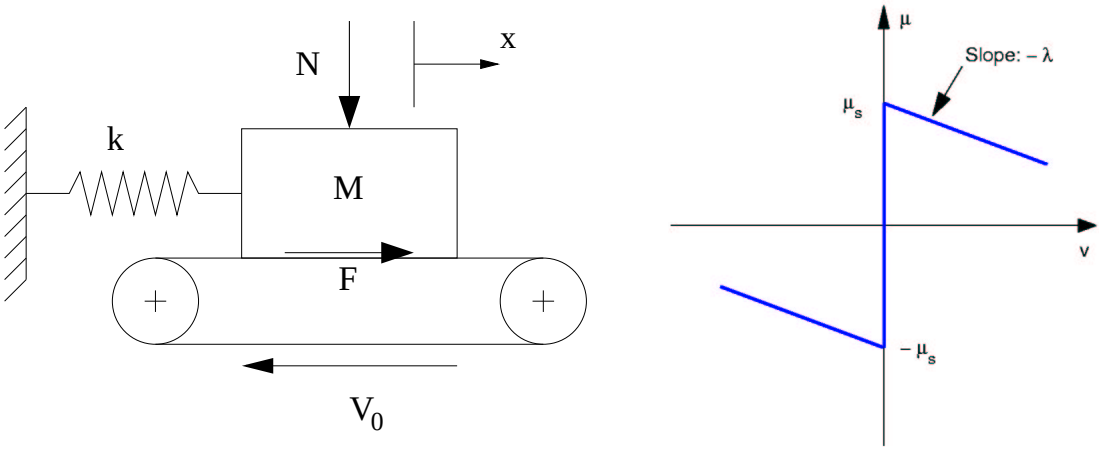

Figure 1.4: *A simple elastic rubbing system*

Since the value of λ is always positive, equation (1.3) has a negative damping term and, thus, the system becomes unstable. As a result, the negative slope of the friction-speed curve gives a plausible mechanism for instability generation. However, many experimental observations show that squeal can occur even when the coefficient of friction is constant. Hence, it becomes obvious that the negative slope of the friction-speed curve alone could not explain all the phenomena of brake squeal.

A major breakthrough in brake squeal research came between 1961-1962 when Spurr [5] first proposed a "sprag-slip" model. The essence of this model was that the squeal mechanism involved a geometrically-induced instability arising with a constant friction coefficient. The implication of this idea has opened up a new area of research

in which, later, many researchers have followed. Thus, it is worth considering the "sprag-slip" model in more detail.

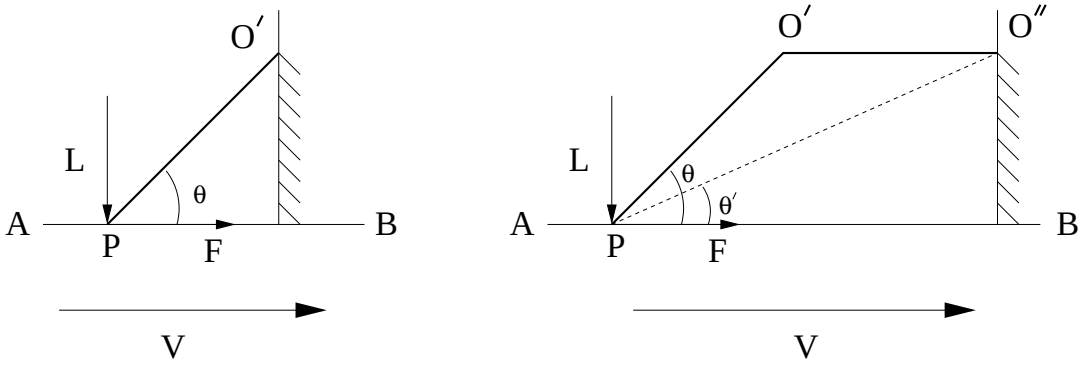

(a) (b)

Figure 1.5: *"Sprag-slip" models proposed by Spurr in 1961-1962.*

First, consider a rigid strut $O'P$ pivoted at O' loaded against a moving surface AB at an angle θ, as shown in Figure 1.5 (a). By taking moments about O', it can be shown that

$$F = \frac{\mu L}{1 - \mu \tan\theta}\,, \tag{1.4}$$

where F is the friction force and L is the applied normal load. If the pivot O' is rigidly fixed, the friction force, F, will approach infinity as $\cot\theta$ approaches μ and at $\cot\theta = \mu$ the strut $O'P$ becomes "spragged" or locked and further motion is impossible. However, if the pivot O' is mounted on a flexible support $O'O''$ with O'' as the new pivot point, as shown in Figure 1.5 (b), a "stick-slip" motion could occur instead of the "spragging" as described by the following argument. When $O'P$ is at the spragging angle, there is no slip between the strut $O'P$ and the moving surface AB. As AB continues to move, the strut $O'P$ will displace elastically and an elastic moment at O' opposing further deflection of $O'P$ is generated. Eventually, the moment at O' will be so large that $PO'O''$ becomes equivalent to a rigid strut with a new pivot at O''. Thus,

the effective angle reduces from θ to θ' which leads to a fall in the friction force, F (according to equation (1.4)). The moment stored in O' is then released and tends to swing P off the surface AB and slip occurs. Due to the geometry of the system, the normal contact force between P and the surface AB will vary as the value of F alters and this will excite transverse modes of the surface AB. It must be emphasised that the "sprag-slip" mechanism does not require the negative slope of the friction curve and, furthermore, it also explains the way in which the out-of-plane modes are excited by the in-plane friction force. However, the system used in the "sprag-slip" model is still quite far away from a real brake assembly.

Since the proposal of the "sprag-slip" model, the idea of geometrically-induced instability was widely accepted and led to many studies during the past few decades. The first to apply Spurr's idea to a more realistic structure were Jarvis and Mills [6] in 1963. They formulated the cantilever-disc system using Lagrange's method and confirmed that the variation of the coefficient of friction alone is insufficient to have caused the instability. To validate their theoretical model, Jarvis and Mills have constructed a pin-on-disc rig which, later, becomes a widely used tool to experimentally study basic squeal characteristics.

During the 1970s, Earles and his co-workers [7, 8, 9, 10] developed a series of lumped-mass-parameter models, as illustrated in Figure 1.6. The key result from their studies was that the pin-on-disc system will be unstable if either of the pins has a negative (digging-in) angle of orientation to the disc surface within the range $0 < \theta < \arctan \mu$. This result was considered to be a necessary, but not sufficient, condition. However, as will be seen in Chapter 4, this condition is true only for simple lumped-mass-parameter models but would not hold in general.

A series of experimental measurements on drum brakes was conducted by Lang *et al.* [11, 12] in 1989. According to their experiments, the mode shapes of the shoes and the drum exhibit the existence of travelling waves. This characteristic was not observed previously on the pin-on-disc rigs. The most thorough experimental study on drum brake squeal was documented in Lang [13].

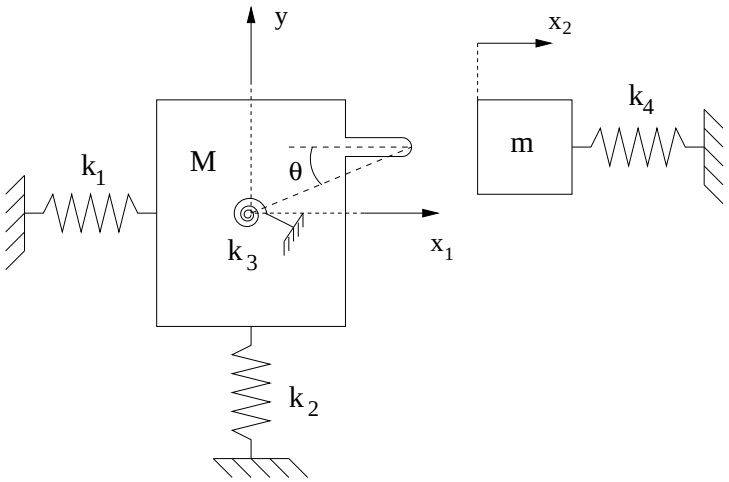

Figure 1.6: *Four-degree-of-freedom model for a pin-on-disc system.*

In the same period as Earles *et al.*, North [14] created an 8-degree-of-freedom model which represents the whole brake assembly, as shown in Figure 1.7. His model consisted of four components: two brake pads, the disc and the calliper. Each of them was allowed to rotate and to move in the transverse direction. From this model, North was the first to suggest that the instability generated by brake assemblies might be similar to aircraft wing flutter.

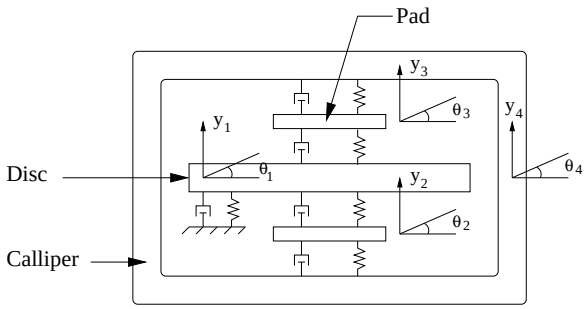

Figure 1.7: *Eight-degree-of-freedom model of a brake assembly.*

In all the lumped-mass-parameter models described so far, the instability of the system has been obtained via a complex eigenvalue analysis. If at least one of the eigenvalues has a positive real part, then the system is said to be unstable. It should be emphasised that this technique can only give the likelihood of squeal but does not

ensure that squeal will always occur (i.e. a necessary, but not sufficient, condition). Nevertheless, the complex eigenvalue analysis could be a useful tool for brake manufacturers to avoid designing brake components within the unstable region in the first place.

As a final comment, one major drawback of the lumped-mass-parameter models is the difficulty in determining realistic system parameters, for example - the spring stiffnesses and masses. Furthermore, most lumped-mass-parameter models consider only the rigid body modes which means that the multi-natural frequency feature due to the flexibility of the components has been neglected.

1.2.3 Friction models

Friction phenomena have been studied in many fields of research (e.g tribology, material science and mechanical engineering). Very often, researchers from different fields independently use different approaches to solve the same (or similar) problems. As a result, there have been many friction models created over the years. They range from very simple ones (e.g. Coulomb friction model) to very complicated models which take into account "stiction" and presliding displacement. However, most friction models commonly used in the modelling of disc brake squeal describe the friction coefficient as a function of the relative velocity, v, of the two contact surfaces. This class of friction models is often called "static friction models".

In this section, four different types of static friction models are reviewed. The first, and simplest, is the Coulomb friction model developed in the 18th century. In this model, the magnitude of the friction force is proportional to the normal load and its direction depends on the direction of the relative velocity of the two contact surfaces. The constant of proportionality, also known as the friction coefficient, is traditionally plotted against the relative velocity as in Figure 1.8 (a). The negative sign of the friction coefficient indicates the reversal in the direction of the friction force.

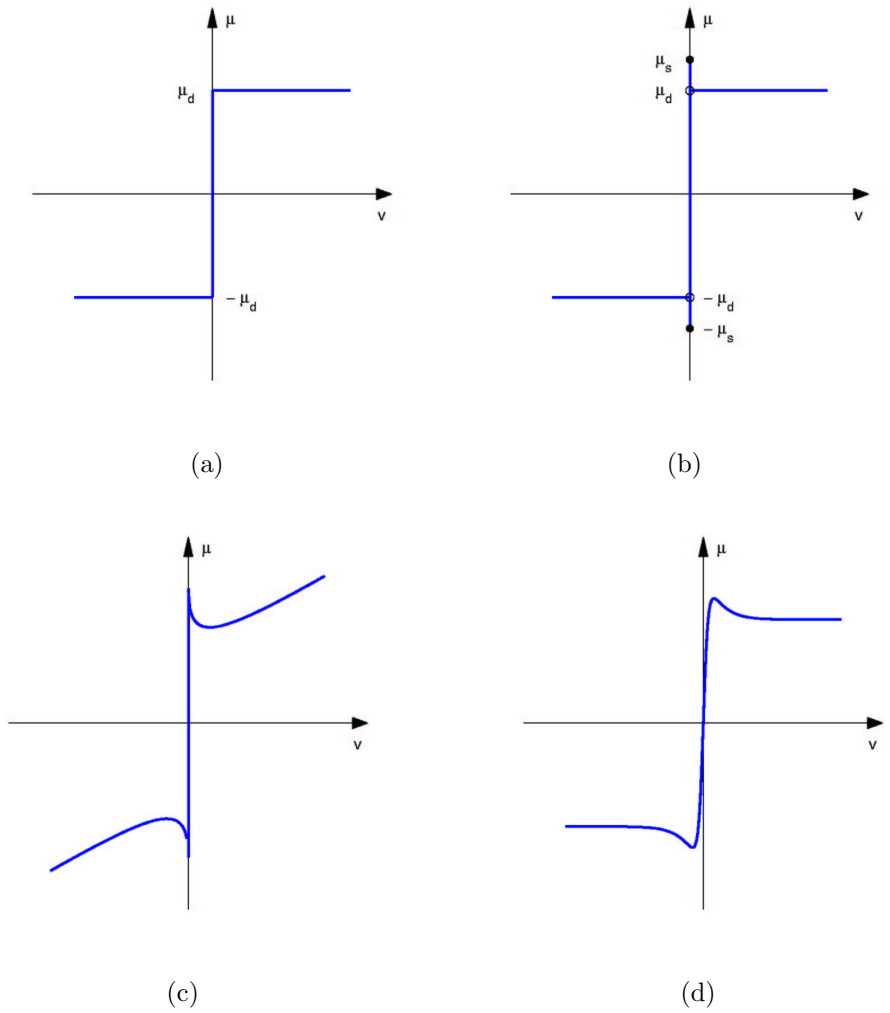

Figure 1.8: *Static friction models: (a) Coulomb model, (b) Stiction plus Coulomb friction model, (c) Stribeck's friction model, and (d) Continuous friction model.*

The second friction model, which is an extension of the Coulomb friction model, is known as "stiction friction model". The stiction friction model is very similar to the Coulomb friction model - except that the maximum friction force during the sticking phase can be higher than during the sliding phase (i.e. $\mu_s > \mu_d$), as shown in Figure 1.8 (b). The inequality $\mu_s > \mu_d$ in the stiction friction model is meant to account for the fact that it is easier to keep a sliding body moving than to set it into motion from rest. For vanishing relative velocity (i.e. "sticking phase" with $v = 0$), the magnitude of the friction force depends on the reactive force governed by the equations of

motion and its direction depends on the tendency of the motion. To calculate responses of systems with a stiction friction model, it is necessary to separate the motion into 2 phases: (i) sliding and (ii) sticking. The description of the "stick-slip" oscillations with some examples will be given in the next section.

The third friction model is known as "Stribeck's friction model". In 1902, Stribeck [15] observed that for low relative velocities the friction force decreased continuously with increasing relative velocities. However, in the high velocity region, the friction force increased with increasing relative velocities, as illustrated in Figure 1.8 (c). A common formulation for the Stribeck's friction coefficient, $\mu(v)$, can be written as

$$\mu(v) = \left[\mu_d + (\mu_s - \mu_d)e^{-(\frac{v}{v_s})^{\delta_s}}\right] sgn(v) + \mu_v v, \tag{1.5}$$

where v is the relative velocity between the two contact surfaces, μ_d is the dynamic friction coefficient, μ_s is the static friction coefficient, v_s is called the Stribeck velocity (helping to define the velocity dependence of friction), δ_s is an application dependent exponent. The last term in equation (1.5) represents the viscous friction and μ_v is the constant of proportionality.

The three static friction models described so far share one common characteristic in which the friction coefficient has a discontinuity at zero relative velocity. This characteristic of the friction curve usually leads to a set of highly nonlinear equations of motion which can be very difficult and time-consuming to solve, refer to Leine *et al.* [16]. To avoid the discontinuity, many friction models, where the friction coefficient has been smoothed around the zero relative velocity region, have been developed. One of the most recent continuous friction models has been proposed by Pilipchuk and Ibrahim [17] in 2002. The expression for their new friction model is

$$\mu(v) = \left[\mu_d + \frac{\mu_s - \mu_d}{\cosh(\alpha v)}\right] \times \tanh(\beta v), \tag{1.6}$$

where α and β are constant coefficients. An example of this function is shown in Figure 1.8 (d). However, the relative velocity in which the maximum friction coefficient

occurs cannot easily be found from this expression and has to be obtained using a numerical method. Thus, an alternative continuous friction model which consists of a simpler expression will be created in the current project, refer to Chapter 5.

1.2.4 Stick-slip oscillations

In the past, many theoretical studies often used the stiction friction curve to model the dynamics of brake systems because it requires only two friction parameters, the dynamic and static coefficients of friction. One implication of the stiction friction model is the existence of so-called "stick-slip" oscillations which are worth considering in more detail as they could bound the response of an unstable system into a limit-cycle oscillation.

In this section, a simple system (Figure 1.4 (a)) which is commonly used to give an account of the "stick-slip" oscillations, is described. This system was first studied by Den Hartog in 1931 [18]. A more recent comprehensive study of such systems has been conducted by Chambrette [19] in 1991 where the equations of motion of the system were derived using the non-dimensional analysis.

To find responses of a system undergoing stick-slip oscillations, it is necessary to treat the equations of motion into two phases: (i) the slipping (sliding) phase, and (ii) the sticking phase. During each phase, the equations of motion can be written as

$$\text{Slipping phase:} \qquad m\ddot{x} + kx = \mu_d N, \tag{1.7}$$

$$\text{Sticking phase:} \qquad \dot{x} = V_0, \tag{1.8}$$

where N is the normal applied load and V_0 the velocity of the belt. Note: during the slipping phase, the motion of the of the system is unknown whereas the friction force is known. On the other hand, during the sticking phase, the friction force is unknown but the motion of the system is known. Furthermore, during the sticking phase, the magnitude of the friction force, F, must also obey the inequality constraint:

$$F \leq \mu_s N. \tag{1.9}$$

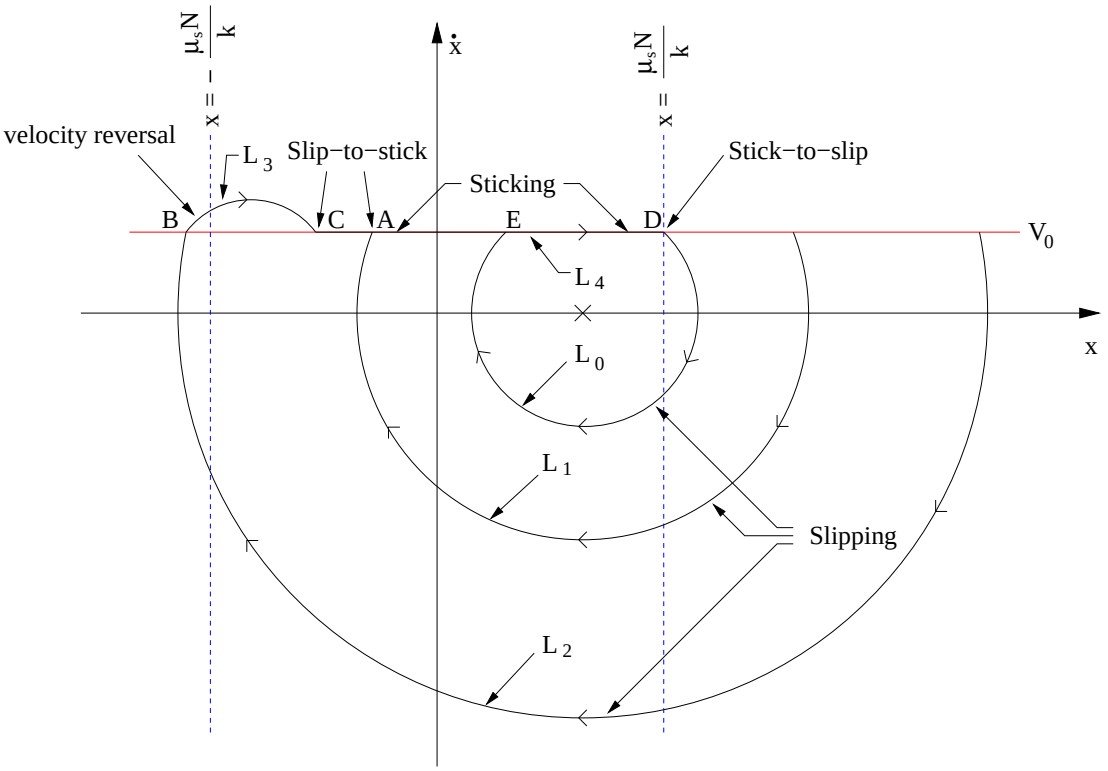

Figure 1.9: *Phase-plane diagram (Poincare map) of the system in Figure 1.4 (a) when it undergoes stick-slip oscillations.*

The most difficult part in solving the stick-slip oscillations is the determination of the transition from the slipping phase to the sticking phase, and vice-versa. The criteria for the slip-to-stick transition are: (i) $\dot{x} = V_0$, and (ii) $F < \mu_s N$. If both criteria are satisfied, the mass will stick to the belt, as shown by the transition from L_1 to L_4 at point A in Figure 1.9. However, if only the first criterion is satisfied, the mass will not stick to the belt but will accelerate beyond the speed of the belt, as illustrated by $L_2 \rightarrow L_3$ at point B in Figure 1.9. This phenomenon is known as the "velocity reversal". When velocity reversal takes place, the friction force will reverse its direction so as to oppose further motion of the mass and, eventually, the velocity of the mass will be reduced to the belt velocity and the slip-to-stick transition will occur,

as shown by $L_3 \rightarrow L_4$ at point C in Figure 1.9. The stick-to-slip transition will occur when the friction force reaches its maximum allowable value, $\mu_s N$. The mass then slips backwards relative to the belt, as shown by the transition from L_4 to L_0 at point D. Finally, the mass oscillates repeatedly between L_0 and L_4 and the system enters the limit-cycle vibration.

1.2.5 Rotating discs

Early work on rotating discs was conducted by Lamb and Southwell [20] in 1921. They considered a circular disc of a uniform thickness rotating about its axis with a constant angular velocity. Their work was concerned mostly with the determination of the natural frequencies of rotating discs when both the centrifugal force and flexural rigidity are both operative. By applying Rayleigh's theorem, they provided approximate natural frequencies which are the lower limit to the true values. Later in the same year, Southwell [21] extended the analysis and showed that the natural frequencies of a spinning disc are of the form:

$$p^2 = p_0^2 + \lambda\Omega^2, \tag{1.10}$$

where p is the natural frequency of the rotating disc, p_0 the natural frequency of the disc in the stationary configuration, Ω the rotational speed of the disc, and λ the constant coefficient.

In 1957, Tobias and Arnold [22] investigated the vibration of turbine discs. In particular, they were interested in using mistuning as a possible means of reducing the maximum vibration. It had been previously observed that the failure of turbine discs was, in most cases, involved with the presence of a stationary wave. By introducing imperfections, Tobias and Arnold discovered that it was possible to convert part of stationary wave into two vibration modes fixed to the disc. These fixed vibrations become subjected to high damping as a result of rotation and consequently reduce the maximum amplitude in the disc.

A comprehensive study on the forced vibration of rotating discs was conducted by Mehdigholi [23] in 1991. This work was concerned with vibration responses of a disc rotating past a non-rotating harmonic force. It has been shown that the response frequencies measured with a stationary sensor are ω and $\omega \pm 2n\Omega$ where ω is the excitation frequency in the stationary frame of reference.

1.2.6 rotor/stator systems

The foundation of rotor/stator interaction research is based upon the studies of rotating discs described previously. Early investigations of rotor/stator interaction itself were conducted in the 1970s by Iwan and co-workers. First, Iwan and Stahl [24] in 1973 considered the interaction between a stationary elastic disc and a moving mass-spring-dashpot system (also called a "subsystem"), as illustrated in Figure 1.10, to simulate the dynamics of computer disc drives. It has been shown that there were many regions of instability not directly related to the classical critical speeds of the disc. The most relevant type of instability to the problem brake squeal is referred to as the modal interaction instability which might occur when the natural frequencies of any two modes make an intersection. However, they did not explain why instability was generated.

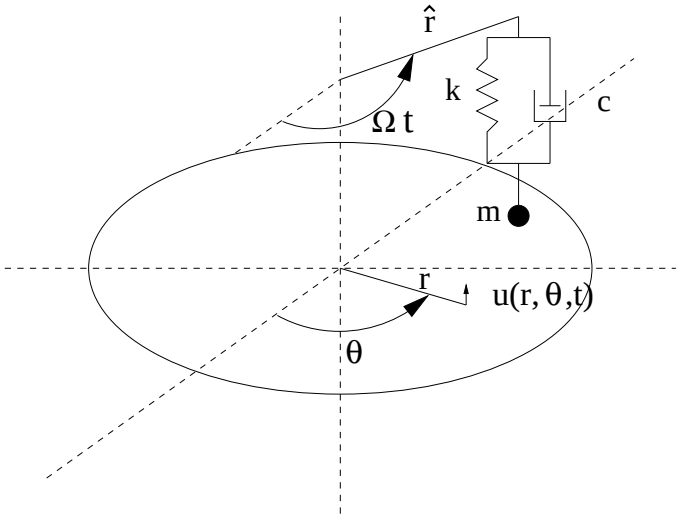

Figure 1.10: *Circular disc with a moving load system.*

Later in 1976, Iwan and Moeller [25] improved the earlier model by considering the disc to be spinning and the stiffening effect due to the rotation was included. They found that the primary effect of disc rotation is to stiffen the disc and thereby to increase its natural frequencies. In their examples, the stiffening effect was of such a magnitude that the one nodal diameter mode no longer exhibited a critical speed. Furthermore, they showed that the additional viscous damping generally caused the disc system to become unstable for all speeds greater than the lowest critical speed. However, no explanation was given as to why this behaviour occurred.

Ono *et al.* [26] were the first to study the effect of pitch moment on the stability of computer disc drives. They found that a large pitch moment of inertia and a large pitch stiffness have destabilising effects. Moreover, they have also included a constant friction force in their model and found that the friction force generally causes the forward (or increasing frequency) modes to become unstable while keeps the backward modes stable. It must be emphasised here that the static friction force has an effect on the stability of the system because it has been modelled as a follower force.

Between 1987 and 1988, Hutton *et al.* [27, 28] used a similar model to study vibration characteristics of guided circular saws. In sawblade applications, the lowest critical speed is usually the cutting speed limit because the saw blade is likely to be subjected to high levels of vibration around this speed region which may result in poor cutting accuracy. In their studies, guides were used as a possible means to raise the critical speed in order to permit higher operating speeds. They have found that the critical speeds of the blade can be increased significantly by using a suitable guide configuration. In a publication with Yang [29] in 1995, a friction interface between the disc and the stationary subsystem was included. In this work, Hutton and Yang also explained the effect of the friction force on the stability of the system, which had originally been discovered by Ono *et al.*, in terms of the relative phase between the friction force and the displacement of the forward and backward travelling waves.

As a final remark, although most of the instability characteristics found in the previous work on rotor/stator interaction may not occur in the case of brake appli-

cation, since the regions of instability were considered at very high rotational speeds (i.e. above the critical speed), the derivation of equations of motion for such systems is essential and can be applied to the brake application.

1.2.7 Experimental investigations

The measurement techniques which are suitable for measuring squeal during operating conditions, must possess two important features. The first feature is the ability to measure responses of rotating components (e.g. brake rotors). This requirement discards the use of many conventional measurement methods (e.g piezoelectric transducers) and turns our attention to non-contacting measurement techniques. The second feature is the ability to measure responses in a relatively short duration (typically less than 1 second) because squeal cannot easily be maintained for a long period of time even in the controlling environment.

From the above considerations, there are two possible techniques commonly used to measure brake squeal, which are (i) the laser Doppler vibrometer (LDV) and (ii) the holographic and speckle interferometry. Both techniques are non-contacting measurements and are capable of determining the operating deflection shape (ODS) from a relatively short measurement duration.

1.2.7.1 Laser Doppler vibrometer (LDV)

The LDV has already been used as a non-contacting response transducer for many years. The operating principles of LDVs, which are based upon the Doppler effect and the interferometric technique, will be described briefly here. A monochromatic, coherent, laser beam is split into two beams of approximately equal intensity. The first beam is directed at the target surface while the second beam, the reference beam, is combined with the return light of the first beam. Fluctuations in the velocity of the target along the direction of beam can be determined from the phase difference of the two laser beams.

In 1995, Stanbridge and Ewins [30] used a scanning LDV to perform modal testing on rotating discs. The key result was that the ODS of rotating discs can be determined by using an LDV beam scanned around the disc at an independent angular speed. In a paper [31] published in 1999, they extended the use of scanning LDV to cover some other applications, such as straight-line scans and two-dimensional area scans. A comprehensive study of the continuous scanning LDV was conducted by Martarelli [32] in 2001. Stanbridge *et al.* [33] also developed a circular-arc LDV scan which can be used when a part of the disc is blocked from view by an obstruction (e.g. a calliper). This technique can easily be employed to determine the ODS of the brake disc during squeal.

1.2.7.2 Holographic and Speckle Interferometry

Holographic interferometry is a non-contacting and full-field measurement technique which is commonly used to study disc brake vibration during squeal. Holographic images are recorded through the use of a double pulsed laser with a pulse duration typically around 20-30 ns. When the two images are brought together, they will interfere with each other and produce a set of bright and dark fringes. With a degree of expertise and experience, these fringes can be interpreted to yield the ODS.

Early experimental studies on disc brake squeal using dual pulsed holographic interferometry were conducted by Felske *et al.* [34] in 1979. The technique was employed mainly to examine the operating deflection shape of the disc and the calliper during squeal. Later, Fieldhouse and his co-workers [35, 36] extended the technique so that the ODS can be directly extracted from holographic images and presented the ODS as an animation. This development makes the technique much more accessible.

Due to the difficulty in applying and interpreting holographic techniques, researchers in recent years have developed another optical technique, known as "speckle interferometry". In speckle interferometry, a laser beam is expanded by a lens and illuminates the surface to be measured. The reflected light is combined with a so-called reference beam which is directly coupled from the laser to the camera. The camera then records

a series of speckle images. The process of obtaining the actual responses is similar to that used by LDVs but this technique operates on an area rather than on a single light beam. The latest development on this technique was carried out by Krupka and Ettemeyer [37] in 2001. This new improvement was capable of measuring responses in three principal directions by using three image acquisition sensors.

1.2.8 State-of-the-art research

During the past decade, Mottershead and co-workers have developed a series of loaded disc with moving mass models. Chan *et al.* [38] in 1994 studied instability of a stationary disc excited by a rotating mass-spring-damper system and a frictional follower load at subcritical speeds. Both the state-space eigenvalue analysis and the multiple scales method [39] were used to obtain the instability regions. They showed that the effect of the frictional follower load rotating at a constant angular speed, remotely below the parametric resonances, around a stationary disc, is to destabilise the backward waves of all modes with nodal diameters.

Ouyang *et al.* [40] in 1998 followed the same line of modelling as that of Chan but made two modifications. First, an in-plane spring-dashpot element has been added to the rotating mass-spring-damper system. Second, the friction coefficient was allowed to vary with the relative velocity with a negative slope. The effect of these two modifications is to reduce the regions of instability of the existing resonances but could also introduce some additional instability regions elsewhere. In 1999, Ouyang *et al.* [41] extended their previous model to include the stiction friction model. The responses of the system were calculated using a time integration method and the limit-cycle oscillations have been observed. Recently, Ouyang and Mottershead [42, 43] have studied a situation where a number of mass-spring-dashpot systems were in contact with the disc. When there are two mass-spring-dashpot systems (one on either side of the disc), they discovered that a frictional follower force is the most destabilising factor among other system parameters. It should be emphasised here that although a number of vi-

bration modes of the disc have been included in the models developed by Mottershead and co-workers, the pad (represented by the mass-spring-dashpot system) was treated as a single degree-of-freedom model.

Disc brake squeal research has recently been advanced by the use of the Finite Element (FE) method which enables us to model brake components more accurately. A summary of comparison between different tools used in conjunction with the FE method for analysing brake squeal has been given by Mahajan *et al.* [44]. Nack [45] in 1999 constructed large-scale FE models under steady sliding conditions with constant friction coefficient. It should be noted that the coalescence of complex roots (also called the "lock-in" point) described in his work does not occur for initially-damped systems (as demonstrated by Kung *et al.* [46] and some simulations in this thesis).

A complete model of a front disc brake assembly was constructed by Kung *et al.* [46] in 2000. To find potentially unstable modes, the complex eigenvalue analysis, which had previously been applied to the problem of drum brake by Hamabe *et al.* [47] in 1999, was employed. Their results suggested that by changing the rotor material (e.g. altering the amount of graphite in the cast iron), the low frequency squeal can be prevented. Blaschke *et al.* [48] applied a similar technique and also showed the way to incorporate the negative slope of the $\mu - v$ curve into FE models. A good correlation between the predicted squeal frequencies and test data has been obtained.

The latest development in brake squeal research has been focused on employing multi-physics capability available in many commercial FE packages. For example, Hu *et al.* [49] attempted to model the friction coefficient as functions of the relative velocity, contact pressure, temperature and humidity. However, the use of multi-physics in brake squeal research is still in its early stage and more work needs to be done before the technique becoming standard practice.

1.3 Scope and approach of the project

The main concern of this project is to find the basic mechanisms involved in instability generation resulting in brake squeal via the use of theoretical models. From the literature review conducted in the previous section, it can clearly be seen that structural dynamics and friction interfaces play critical roles in the modelling of brake squeal. Thus, the scope of the current project will cover these two areas of research. However, it should also be emphasised here that it is not the aim of this project to attempt to predict squeal produced from the actual brake assembly. The approach for the current brake noise project can be summarised graphically as shown in Figure 1.11.

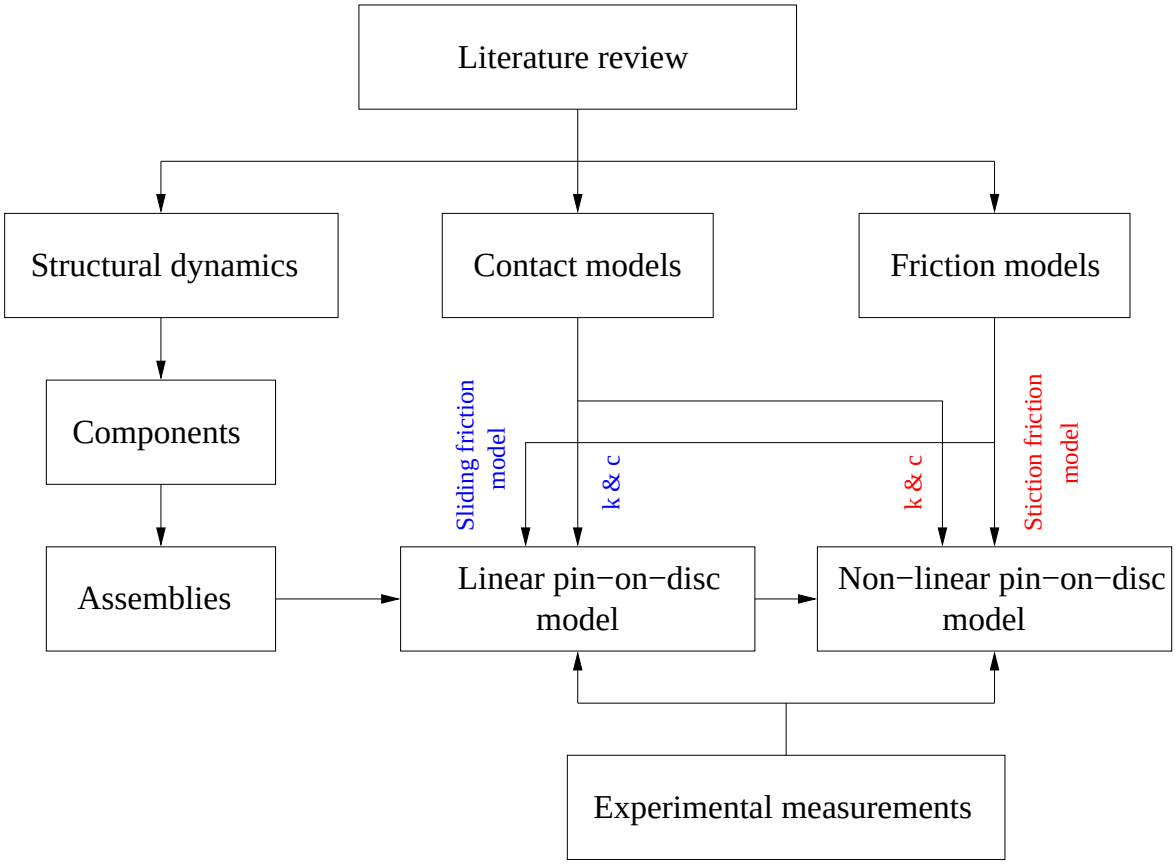

Figure 1.11: *The roadmap of the brake noise project.*

In the area of structural dynamics, the previous theoretical models found in literature are either too small to be realistic or too large to be used for parameter studies. Thus, it seems necessary to create an intermediate model which can represent squeal produced from an actual brake assembly but has a relatively simple geometry. As a result, a pin-on-disc model is created. Each individual component of the pin-on-disc model will be modelled using the FE method but the combined model will be constructed using the modal model technique in order to reduce the size of the problem.

Furthermore, it has also been found from the literature review that the effect of the rotation was usually neglected in the previous theoretical studies. However, to simulate the limit-cycle oscillations, the rotation of the disc is an important parameter and, thus, it will be incorporated into the present pin-on-disc model. The effect of the rotation on squeal characteristics can then be investigated, especially when mistuning has been applied to the disc.

In addition to structural dynamics, the modelling of the friction interface is also equally important. In this project, two friction models will be used. The first model assumes that the friction coefficient is constant and the friction force does not change its direction. With this friction model, a linear pin-on-disc model can be created and the onset of instability can be obtained by using the complex eigenvalue analysis. In the second friction model, the coefficient of friction is assumed to be a continuous function of the relative velocity. By applying this continuous friction model, the equations of motion of the pin-on-disc model become non-linear and the time integration method is used to find the responses. From this non-linear pin-on-disc model, the limit-cycle characteristics can be studied.

Apart from the pin-on-disc modelling, this project will also investigate free vibration characteristics of three-dimensional "tophat-like" structures. A representative model of the actual brake discs will be constructed using the FE technique. The modal properties - namely the natural frequencies and mode shapes - will be extracted for modes within the frequency range of 0 to 20 kHz. A number of nodal variables will be defined in order to distinguish the vibration modes uniquely. Furthermore, an AutoMAC diagram will

be used to classify the vibration modes into appropriate families according to their similarity.

1.4 Objectives of the current study

As stated, the overall aim of this project is to gain some insight into the problem of disc brake squeal which would provide the basic understanding of the contributing mechanisms which cause the instability. The specific objectives of this project can be described as follows:

- to study free vibration characteristics of simple rotor/stator systems;
- to find a way to distinguish vibration modes of three-dimensional "tophat-like" structures and to find a systematic method for classifying them into appropriate families according to their similarity;
- to create a simple theoretical model which can predict the onset of instability and to use this model to explain the mechanism for instability generation;
- to extend the simple model to a more realistic one which can then be used to study the limit-cycle characteristics;
- to design and build a relatively simple test rig which can produce similar squeal behaviour as the real disc brake assembly;
- to conduct experimental measurements which can be used to (i) provide the numerical values for some of the system parameters used in the theoretical models and (ii) validate the theoretical models.

1.5 Outline of the thesis

Chapter 1 : Introduction.

The problem of disc brake squeal is addressed and the definition of brake squeal

is given. Descriptions of disc brake components are presented. The literature review, which covers the historical background, the recent development on the brake noise research and other related applications, is conducted. The specific objectives of the project are stated.

Chapter 2 : Free vibration of rotor/stator systems.

A simple model of a rotor/stator system is created and its free vibration characteristics are studied. The use of different frames of reference in determining the pattern of the responses is demonstrated. Furthermore, the work developed in this chapter provides a foundation for a more advanced model in Chapter 5.

Chapter 3 : General disc vibration.

In this chapter, free vibration characteristics of "tophat-like" structures are studied. The main objectives are: (i) to find a way to distinguish vibration modes of three-dimensional "tophat-like" structures and (ii) to find a systematic method for classifying them into appropriate families according to their similarity.

Chapter 4 : Dynamics of linear pin-on-disc systems.

A pin-on-disc model, which is used as a representative model to the actual brake disc, is constructed using the FE method. The complex eigenvalue analysis is employed to obtain the onset of instability. The mechanism in which the instability is generated is discussed. A number of systematic parameter studies are also conducted to find a set of controlling parameters which will be used in a more realistic model in Chapter 5.

Chapter 5 : Non-linear dynamics of pin-on-disc systems.

The pin-on-disc model created in Chapter 4 is extended into a more realistic model by incorporating a new friction model in which the friction coefficient is a continuous function of the relative velocity between the two contact surfaces and can take into account the change in the friction direction. The solutions

are calculated using the time-integration method based on an explicit Runge-Kutta formula. A particular interest has been concentrated on the limit-cycle characteristics of the system, especially when mistuning has been added to the disc.

Chapter 6 : Design and development of the test rig.

In this chapter, the design and development of the test rig, IC (Imperial College) pin-on-disc rig, are presented. Specific requirements, which are essential for the validation of the theoretical models, are described. A brief description of the data acquisition system is also given.

Chapter 7 : Experimental studies.

Experimental measurements conducted on the IC pin-on-disc rig are presented. The normal and tangential contact stiffnesses between the pin and the disc are estimated using a combination of test data and the theoretical models. The operating deflection shape of the disc during squeal is obtained using a circular scanning laser Doppler vibrometer.

Chapter 8 : Conclusions.

This chapter begins with a summary of the work conducted during the course of this project. Then, the main conclusions and contributions gained from the current study to the brake squeal research are summarised. Finally, the thesis is concluded with suggestions for future work.

Chapter 2

Free vibration of rotor/stator systems

2.1 Overview

Vibration problems due to rotor/stator interaction are common and can be found in several fields of engineering, such as circular saws, computer disc drives and turbine bladed discs. The generation of disc brake squeal can also be classified as one type of rotor/stator interaction applications. Although most studies on the rotor/stator interaction are usually concerned with instability at high rotational speeds, i.e. close to the critical speed, several techniques for deriving and solving the governing equations of motion can be applied to the brake noise application. Thus, it is worth studying the dynamics of a simple rotor/stator interaction system before considering more complex problems (e.g. real disc brake systems).

In this chapter, a simple rotor/stator model, which consists of a rotating flexible disc in contact with a stationary dynamic system, is created. For simplicity, no friction will be included in the model at this stage. The primary objective of this work is to show that the dynamics of rotor/stator systems could be complex even with a relatively simple configuration and, thus, that care must be taken when analysing such systems. Furthermore, this work will illustrate the use of different frames of reference

in determining the variation of the mode shapes along the circumferential direction. Finally, the theoretical model of the rotating disc developed in this section will lay a foundation for a more advanced model in Chapter 5.

In the following section, three different types of frame of reference will be referred to regularly and, for clarity, it is appropriate to define them here. First, the "stationary frame of reference" is a set of coordinates which are fixed in space. Second, the "rotating frame of reference" is a set of coordinates which are fixed in the disc and, hence, rotate at the same angular speed as the disc from the perspective of a stationary observer. Note: in some other presentations, the "rotating frame of reference" may be referred to as the "disc coordinates". Third, the "observer frame of reference" is a set of coordinates which are fixed with an observer and rotate at an independent speed, depending on the angular speed of the observer.

2.2 Modelling

The system studied in the present work consists of a circular disc and a mass-spring-dashpot system which will be called the "subsystem", as illustrated in Figure 2.1. The disc is assumed to be fully clamped at the inner bore and free at the outer rim and to spin with speed, Ω, in the anti-clockwise direction viewed in the stationary frame of reference. The location of the mass-spring-dashpot subsystem is fixed in space at $\theta_S = 0$.

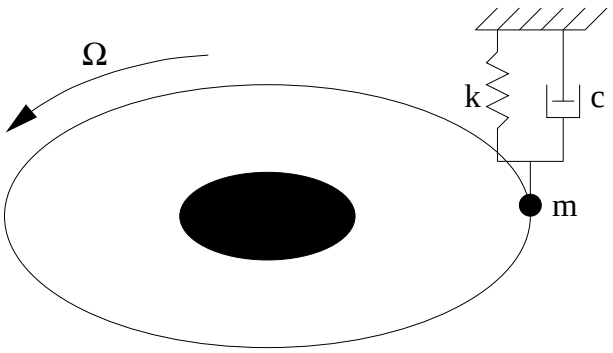

Figure 2.1: *A rotating disc in contact with a stationary mass-spring-dashpot system.*

2.2.1 Assumptions

Although friction is critical in the study of disc brake squeal, the aim of the current study is to investigate the free vibration characteristics of systems with simple rotor/stator interaction and, hence, no friction will be included in the model at this stage. The consideration of a friction interface will be conducted in Chapter 5. Furthermore, with brake squeal as a possible application, and to avoid unnecessary complex calculations, the theoretical study in this chapter will cover only slowly rotating discs. As a result of these simplifications, a number of assumptions can be made in the theoretical model, as follows:

1. the disc is made of a thin circular plate and the assumptions associated with thin plate theory can be found in Section 3.2;
2. the rotational speed is slow enough that gyroscopic and centrifugal stiffening effects can be neglected;
3. at this stage, no friction occurs at the interface between the subsystem and the disc; and
4. the subsystem and the disc stay in contact at all times.

2.2.2 Equations of motion

First, when considering the system in a frame of reference fixed on the disc (the "rotating frame of reference"), the disc appears to be stationary but the subsystem would appear to move around the disc in a clockwise direction. Hence, in the rotating coordinates, (r, θ_R), the equation of motion of the combined system can be written as:

$$D\nabla^4 w(r,\theta_R,t) + \rho h \frac{\partial^2 w(r,\theta_R,t)}{\partial t^2} = -\frac{1}{r}\delta(r-r_0)\delta(\theta_R+\Omega t-\theta_0)[m\ddot{w}+c\dot{w}+kw], \quad (2.1)$$

where

- w is the out-of-plane displacement,
- D is the flexural rigidity of the disc, and
- ρ its density,
- h is the disc thickness;
- δ is the Dirac delta function,
- m, c and k are the mass, the damping and the stiffness of the subsystem, respectively,
- Ω is the rotational speed of the disc, and
- r_0 and θ_0 define the initial location of the subsystem at $t = 0$ in the radial and circumferential directions, respectively.

The reason for deriving the governing equation of motion of the combined system in the rotating frame of reference first is that the familiar differential equation of motion for the transverse displacement of a circular plate can then be taken directly from the literature, as shown on the left-hand-side of equation (2.1). However, equation (2.1) cannot easily be solved because its right-hand-side contains time-dependent terms. According to Ewins [50], it is possible to construct mass, damping and stiffness matrices with constant coefficients by transforming the problem into the stationary frame of reference. In this way, the problem can be reduced considerably. The relationship between the set of rotating coordinates, θ_R, and the set of stationary coordinates, θ_S, is

$$\theta_S = \theta_R + \Omega t. \tag{2.2}$$

Substituting equation (2.2) into equation (2.1), the equation of motion in the stationary frame of reference can be written as:

$$D\nabla^4 w(r,\theta_S,t) + \rho h\left[\frac{\partial^2 w(r,\theta_S,t)}{\partial t^2} + 2\Omega\frac{\partial^2 w(r,\theta_S,t)}{\partial\theta_S\partial t} + \Omega^2\frac{\partial^2 w(r,\theta_S,t)}{\partial\theta_S^2}\right]$$
$$= -\frac{1}{r}\delta(r-r_0)\delta(\theta_S-\theta_0)[m\ddot{w} + c\dot{w} + kw]. \tag{2.3}$$

It is appropriate to seek a solution of equation (2.3) in terms of a free disc solution of the form

$$w(r,\theta,t) = \sum_{n=0}^{\infty}\sum_{m=0}^{\infty} {}_c\phi_{nm}(r,\theta)\ {}_cq_{nm}(t) + \sum_{n=1}^{\infty}\sum_{m=0}^{\infty} {}_s\phi_{nm}(r,\theta)\ {}_sq_{nm}(t), \tag{2.4}$$

where $q_{nm}(t)$ is the generalised coordinate for a mode which has n nodal diameters and m nodal circles; ϕ_{nm} is the corresponding mass-normalised mode shape function whose explicit formula is given by equation (3.3). Subscripts c and s denote cosine and sine modes, respectively.

To separate equation (2.3) into a set of linear ordinary differential equations with constant coefficients, first substitute equation (2.4) into equation (2.3) and apply standard modal analysis procedures; second, multiply equation (2.3) by ${}_cr\phi_{nm}$ or ${}_sr\phi_{nm}$, integrate from 0 to 2π in θ and from b to a in r, and make use of the orthogonality of the eigenfunctions of the free disc problem, to derive an equation of motion which can be expressed as:

$$[I]\ddot{q} + [E]\dot{q} + \big[[F] + [J]\big]q = -[\psi]\{m\ddot{q} + c\dot{q} + kq\}, \tag{2.5}$$

where $[I]$ is an identity matrix. $[E]$ is a skew-symmetric matrix which is defined as:

$$[E] = \begin{bmatrix} 0 & & & & & & & \\ & \ddots & & & & & & \\ & & 0 & & & & & \\ & & & 2n\Omega & & & & \\ & & -2n\Omega & & & & & \\ & & & & \ddots & & & \\ & & & & & & 2n\Omega & \\ & & & & & -2n\Omega & & \end{bmatrix}. \tag{2.6}$$

$[F]$ and $[J]$ are diagonal matrices and are defined as:

$$[F] = \begin{bmatrix} {}_c\omega_{00}^2 & & & & & & & \\ & \ddots & & & & & & \\ & & {}_c\omega_{0m}^2 & & & & & \\ & & & {}_c\omega_{10}^2 & & & & \\ & & & & {}_s\omega_{10}^2 & & & \\ & & & & & \ddots & & \\ & & & & & & {}_s\omega_{nm}^2 & \\ & & & & & & & {}_c\omega_{nm}^2 \end{bmatrix}, \tag{2.7}$$

$$[J] = \begin{bmatrix} 0 & & & & & & & \\ & \ddots & & & & & & \\ & & 0 & & & & & \\ & & & -n^2\Omega^2 & & & & \\ & & & & -n^2\Omega^2 & & & \\ & & & & & \ddots & & \\ & & & & & & -n^2\Omega^2 & \\ & & & & & & & -n^2\Omega^2 \end{bmatrix}. \tag{2.8}$$

It should also be noted that the displacement-dependent matrix on the left-hand-side of equation (2.5) is deliberately written as a summation of two matrices, $[F]$ and $[J]$, because the origins of these two matrices are not the same. Matrix $[F]$ corresponds to the natural frequencies of the disc in the stationary configuration. On the other hand, matrix $[J]$ arises from the rotation of the disc and, thus, is a function of the rotational speed, Ω. Matrix $[\psi]$ on the right-hand-side of equation (2.5) is defined as:

$$[\psi] = [\Phi][\Phi]^T, \tag{2.9}$$

where

$$[\Phi] = \begin{bmatrix} {}_c\phi_{00}(r_0, \theta_0) \\ \vdots \\ {}_c\phi_{0m}(r_0, \theta_0) \\ {}_c\phi_{10}(r_0, \theta_0) \\ {}_s\phi_{10}(r_0, \theta_0) \\ \vdots \\ {}_c\phi_{nm}(r_0, \theta_0) \\ {}_s\phi_{nm}(r_0, \theta_0) \end{bmatrix}. \tag{2.10}$$

Finally, equation (2.5) can be re-arranged into a standard second-order differential equation, as follows:

$$[A]\ddot{q} + [B]\dot{q} + [C]q = 0, \tag{2.11}$$

where

$$[A] = [I] + m[\psi], \tag{2.12}$$

$$[B] = [E] + c[\psi], \tag{2.13}$$

$$[C] = [F] + [J] + k[\psi]. \tag{2.14}$$

Since matrices $[A]$, $[B]$ and $[C]$ contain only constant coefficients, the standard state-space technique can be used to obtain the natural frequencies and mode shapes

of the combined system. Once the modal properties of the combined system in the stationary frame of reference are known, it is then possible to visualise them in a different frame of reference. As mentioned earlier, when considering rotating structures, there are three different types of frame of reference commonly used: (i) the "stationary", (ii) the "rotating", and (iii) the "observer" frames of reference. In practice, responses in the rotating frame of reference can be measured by strain gauges fixed to the disc and responses in the observer frame of reference can be measured by a circular scanning Laser Doppler Vibrometer (LDV). The relationships between these three sets of coordinates can be expressed as follows:

$$\theta_S = \theta_R + \Omega t, \tag{2.15}$$

$$\theta_S = \theta_b + \Omega_b t, \tag{2.16}$$

where θ_S, θ_R and θ_b, define the circumferential position in the "S"tationary, "R"otating, and O"b"server frames of reference, respectively; Ω and Ω_b are the angular speeds of the disc and the observer with respect to the stationary coordinates, respectively. The directions of Ω and Ω_b are chosen according to the right-hand set of coordinates, i.e. anti-clockwise direction.

2.3 Numerical simulations and discussion

The numerical simulations presented in this section are calculated for the specific case of an aluminium disc which is assumed to have the following material properties: Young's modulus of 70 GPa, the density of 2720 kg/m^3 and the Poisson's ratio of 0.33 and physical dimensions at: disc thickness, h, of 22.7 mm, the outer radius, a, of 179 mm and the inner radius, b, of 8 mm, as shown in Figure 2.2. The stationary subsystem, when present, is located at $r_0 = a$ and $\theta_S = 0$ and has the following properties: $m = 1\,kg$, $c = 0\,kg/s$ and k varying between 0 and 8 GN/m.

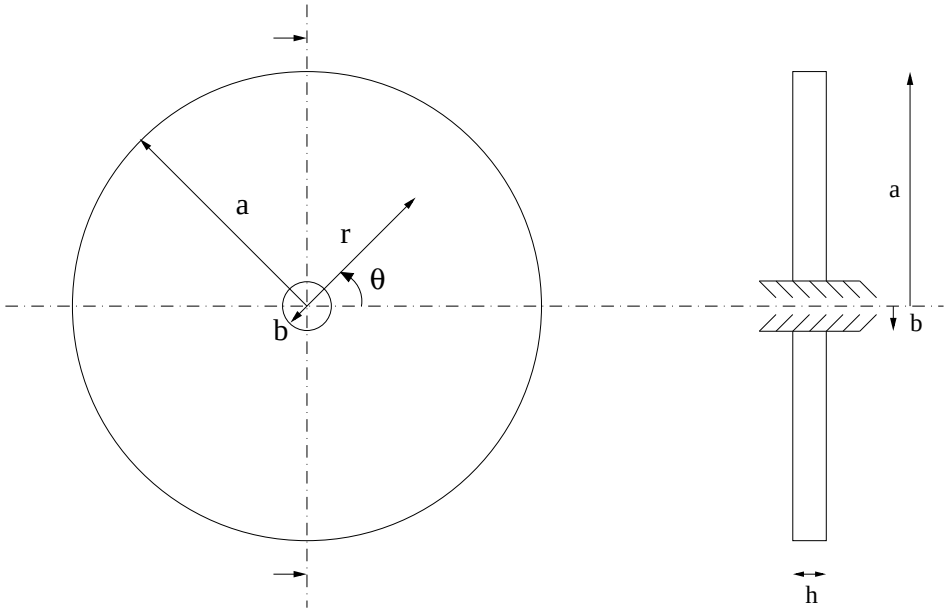

Figure 2.2: *Sketch of the disc indicating the rigidly clamped boundary condition at the inner bore.*

2.3.1 Case A: Rotating discs without the subsystem

First, calculations of the modal properties are performed without the presence of the subsystem to establish the free vibration characteristics of the rotating disc both in the stationary and rotating (disc) frames of reference. This can be done by setting m, c and k to zero i.e. by considering only the left-hand side of equation (2.5). Thus, the governing equation of motion in the stationary frame of reference is reduced to

$$[I]\ddot{q} + [E]\dot{q} + \big[[F] + [J]\big]q = [0]. \tag{2.17}$$

2.3.1.1 Natural frequencies of rotating discs in the stationary and rotating frames of reference

Equation (2.17) can be solved to find the natural frequencies of the rotating disc as a function of the disc rotational speed. In the rotating (disc) frame of reference, the disc would appear to be stationary and, hence, the natural frequencies of the double mode pair described in the rotating frame of reference would be identical to each other and would remain constant regardless of the change in the disc rotational speed, as shown in Figure 2.3. On the other hand, the double mode pair will split into 2 distinct modes with different "apparent" natural frequencies if they are measured in the stationary frame of reference. The first mode of the pair corresponds to a forward travelling wave (a wave that travels in the same direction as the rotation of the disc) as viewed in the stationary frame of reference whereas the second mode corresponds to a backward travelling wave (a wave that travels in the opposite direction to the rotation of the disc). In general, the apparent natural frequencies of the "forward" and "backward" modes, ω^f_{nm} and ω^b_{nm} respectively, can be described as a function of the rotational speed by the following relationships:

$$\begin{aligned} \omega^f_{nm} &= \omega_{nm} + n\Omega, \\ \omega^b_{nm} &= \omega_{nm} - n\Omega, \end{aligned} \tag{2.18}$$

where ω_{nm} is the natural frequency of the disc in the rotating frame of reference. Note: the relationships in equation (2.18) still hold true even if stress stiffening effects are included: refer to Mehdigholi [23]. The forward travelling waves would appear to travel faster when viewed in the stationary frame of reference than in the rotating frame of reference because of the additional speed of the disc. Hence, the forward travelling waves would appear to increase their frequencies when the speed of the disc increases, as illustrated in Figure 2.3. Conversely, the frequencies of the backward travelling waves decrease as the speed of the disc increases.

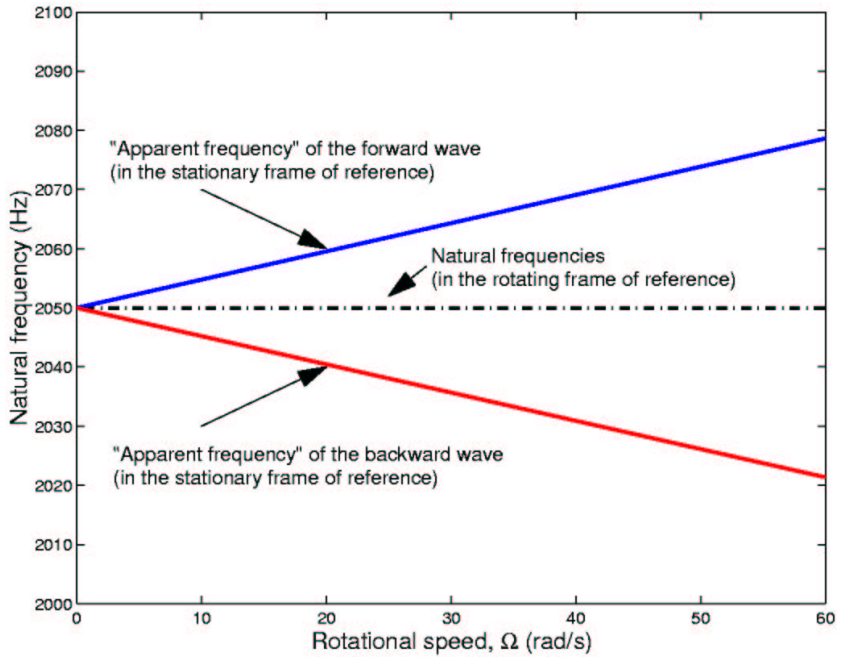

Figure 2.3: *Natural frequencies of a rotating disc (n = 3) as seen from: (i) the rotating frame of reference (the black dashed lines), and (ii) the stationary frame of reference (the blue and red lines).*

2.3.1.2 Mode shapes of slowly rotating discs in the stationary and rotating frames of reference

Structures which possess a degree of symmetry, especially the axisymmetry found in discs, would generally have a number of repeated eigenvalues. Furthermore, if the system is not defective, i.e. if a set of linearly independent eigenvectors can be found for

all the repeated eigenvalues, any linear combination of the corresponding eigenvectors will also be a possible solution to the equations of motion: refer to Ewins [50]. Hence, the mode shapes of such systems may exist in many forms and will not be unique. It is worth mentioning that although there are an infinite number of possible eigenvectors, there always be a set of eigenvectors which are orthogonal.

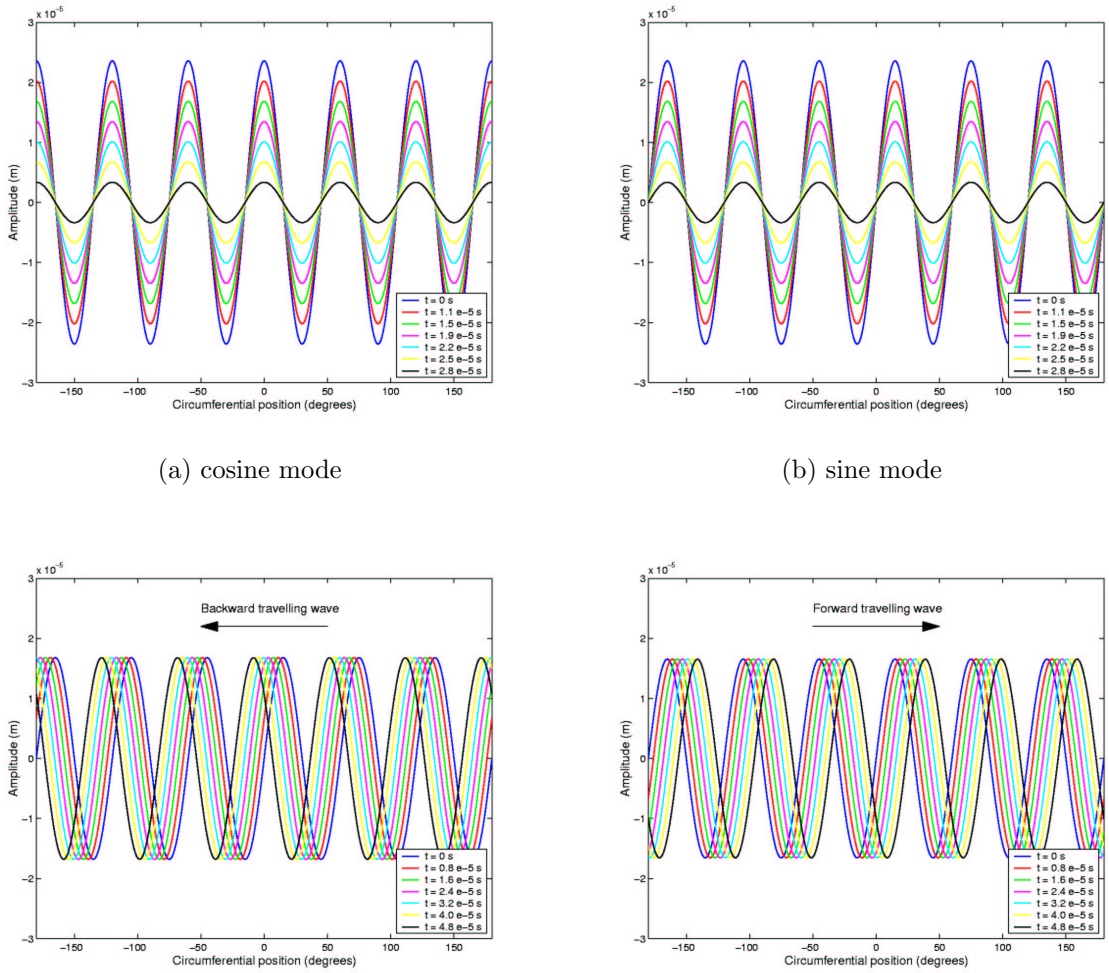

(a) cosine mode

(b) sine mode

(c) backward travelling wave

(d) forward travelling wave

Figure 2.4: *Examples of mode shapes of a rotating disc as viewed in the rotating frame of reference ((a) and (b)) and in the stationary frame of reference ((c) and (d)).*

For slowly rotating discs, if gyroscopic effects are neglected completely, the systems will have a number of repeated eigenvalues when analysed in the rotating frame of reference. In this case, the mode shapes of the double mode pair are not unique, as

discussed above. Figures 2.4 (a) and (b) show, as examples, a pair of possible mode shapes. In these examples, the two modes shapes are chosen to be orthogonal and both of them are in the form of stationary waves. However, certain linear combinations of the two mode shapes, which are also possible mode shapes, could result in a pure travelling wave.

When rotating discs are analysed in the stationary frame of reference, the natural frequencies of the double mode pairs are seen to split into two distinct frequencies, as shown in Figure 2.3. As a result, the mass-normalised mode shapes of rotating discs in the stationary frame of reference become unique. Figures 2.4 (c) and (d) show the mode shapes of the rotating disc as viewed in the stationary frame of reference. The backward travelling wave shown in Figure 2.4 (c) corresponds to the lower "apparent natural frequency" in Figure 2.3 and the forward travelling wave shown in Figure 2.4 (d) corresponds to the higher "apparent natural frequency".

2.3.1.3 Discussion of the derivation of the equations of motion

From many experimental studies and observations, it is evident that disc brake squeal occurs at very low rotational speeds (around 0.1-1 Hz or 6-60 rev/min). As a result, gyroscopic effects due to the rotational speed and stiffening effects due to centrifugal stresses have been neglected completely in the derivation of the equations of motion. Because of these simplifications, it should be noted that the results of the current study can only be applied directly to slowly rotating discs such as the brake noise application.

In the present study, the equation of motion is first derived in the rotating frame of reference. By using an appropriate coordinate transformation, the equation of motion in the stationary frame of reference can be obtained, as shown in equation (2.17). As a result of the coordinate transformation, two extra matrices, $[E]$ and $[J]$, have been introduced. The velocity-dependent matrix $[E]$ is a function of the number of nodal diameters, n, and rotational speed, Ω, and is a skew-symmetric matrix, as shown in equation (2.6). Because the form of the matrix $[E]$ is similar to that of the "gyroscopic" matrix, some confusion could arise. To clarify this, the velocity-dependent matrix in

equation (2.118) of Ewins [50], which shows a similar structure to the matrix $[E]$, is quoted here for comparison:

$$\begin{bmatrix} \frac{I_0}{L^2} & 0 \\ 0 & \frac{I_0}{L^2} \end{bmatrix} \begin{Bmatrix} \ddot{x}_R \\ \ddot{y}_R \end{Bmatrix} + \begin{bmatrix} 0 & -\frac{2\Omega I_0}{L^2} + \frac{J\Omega}{L^2} \\ \frac{2\Omega I_0}{L^2} - \frac{J\Omega}{L^2} & 0 \end{bmatrix} \begin{Bmatrix} \dot{x}_R \\ \dot{y}_R \end{Bmatrix} + \begin{bmatrix} -\frac{I_0\Omega^2}{L^2} + \frac{J\Omega^2}{L^2} + k & 0 \\ 0 & -\frac{I_0\Omega^2}{L^2} + \frac{J\Omega^2}{L^2} + k \end{bmatrix} \begin{Bmatrix} x_R \\ y_R \end{Bmatrix} = \{0\}, \tag{2.19}$$

refer to Appendix A for the sketch of the system and the definition of each symbol.

It can be seen from equation (2.19) that the off-diagonal elements of the velocity-dependent matrix contain two terms. The first of these terms corresponds to the "coordinate transformation" and it should also be noted that they originate from the inertia term because they contain the quantity, I_0. The second term, on the other hand, comes directly from gyroscopic effects as it contains a factor of "J". Now, considering our matrix $[E]$ from equation (2.6), each of the off-diagonal element contains only a single term and this comes from the inertia effect: refer to equation (2.3). It can thus be concluded that the matrix $[E]$ arises solely because of the coordinate transformation and has nothing to do with gyroscopic effects.

2.3.2 Case B: Non-rotating disc with the subsystem

In the case of a non-rotating disc with an attached subsystem, it is clear from Figure 2.5 that the natural frequencies of the sine modes are not affected by the presence of the subsystem. This is only to be expected since the subsystem is always located at a nodal line of each sine mode. On the other hand, the subsystem would be at the antinode of each cosine mode and, hence, would generally affect the natural frequencies of the cosine modes of the combined system. Thus, the natural frequencies of the double mode pairs would generally split into two distinct frequencies due to the presence of the subsystem, as shown in Figure 2.5.

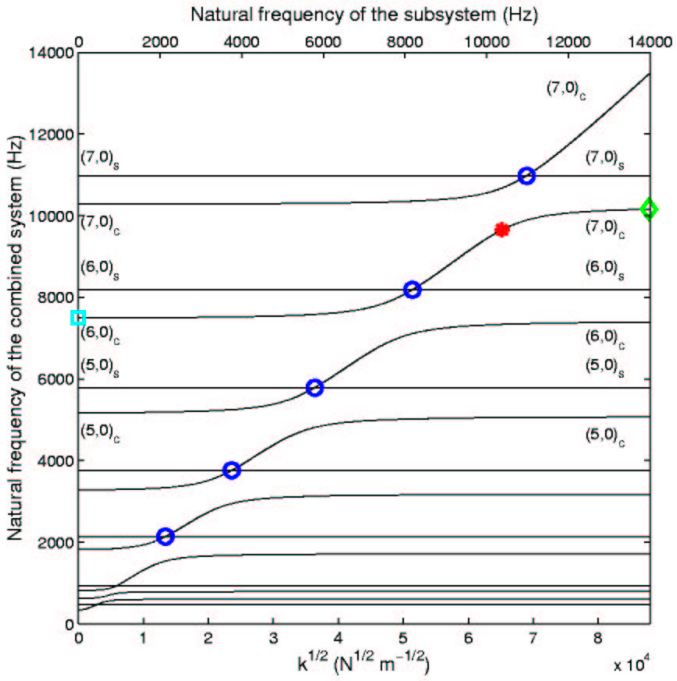

Figure 2.5: *The natural frequencies of the combined system as a function of the subsystem stiffness when $\Omega = 0$ rev/min (since the mass of the subsystem is always constant in this set of calculations, the corresponding natural frequency of the subsystem can be superimposed on the top axis).*

Note: The notation $(n, m)_c$ or $(n, m)_s$ used in Figures 2.5 and 2.7 indicates the dominant component for that particular mode shape. The first and second indices represent the numbers of nodal diameters and nodal circles, respectively, while the subscript c or s identifies the cosine or sine mode, respectively. For example, when the spring stiffness of the subsystem is equal to zero, the mode shape of the combined system at 7.5 kHz (marked by a cyan square on Figure 2.5) is dominated by the 6 nodal diameter cosine component.

Another important remark on Figure 2.5 is that there are a number of repeated natural frequencies, as marked by the blue circles. Repeated natural frequencies usually indicate the occurrence of the double modes. Hence, the mode shapes of the combined system at these points are not unique: refer to Ewins [50] for further explanation. The reason that the combined system still exhibits double mode characteristics even when the subsystem is present, is because the natural frequencies of the subsystem coincide with the natural frequencies of the disc at these points. At its natural frequency, the effective stiffness of the subsystem reduces to zero and, as a result, the disc and the subsystem are completely decoupled from one another, i.e. the disc does not feel the

presence of the subsystem. Thus, the double mode characteristics of the disc reappear.

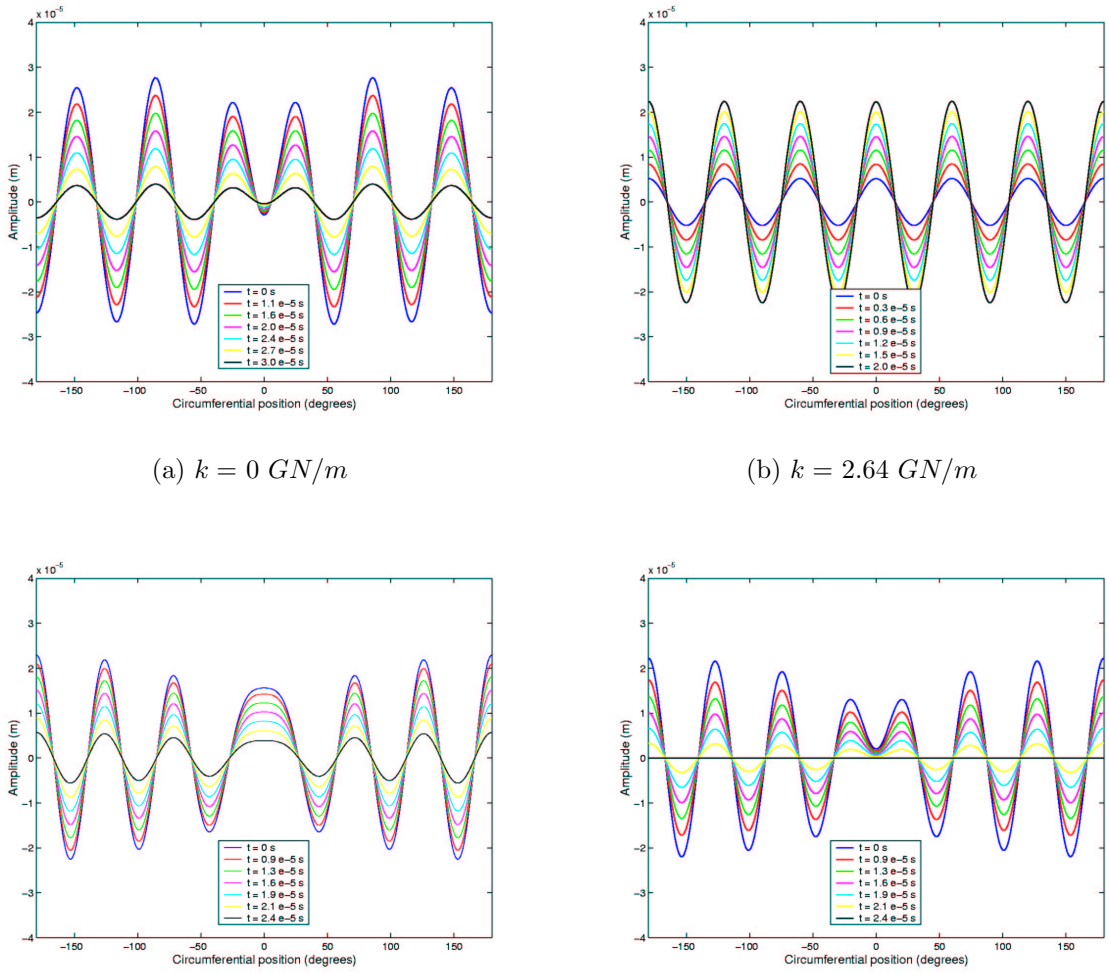

(a) $k = 0\ GN/m$ (b) $k = 2.64\ GN/m$

(c) $k = 4.25\ GN/m$ (d) $k = 7.71\ GN/m$

Figure 2.6: *Mode shapes of a non-rotating disc in contact with a stationary subsystem, as viewed in the stationary frame of reference.*

Figure 2.6 shows, as an example, the progressive change of the six nodal diameter cosine mode as the stiffness of the subsystem is increased. In general, if the disc does not rotate, mode shapes of the cosine modes of the combined system may consist of components of many of the original cosine disc modes. For example, the mode shape at 7.5 kHz (marked by a cyan square on Figure 2.5) consists of all the cosine components of the original disc modes but the $(6, 0)_c$ component is the dominant one, as shown in Figure 2.6 (a). As the spring stiffness increases until the natural frequency of the

subsystem is equal to one of the natural frequencies of the original disc modes (marked by blue circles on Figure 2.5), the disc is completely decoupled from the subsystem and the double mode characteristics of the disc reappear, as discussed previously. It should be noted that, at these points, the mode shapes would consist of only one single nodal diameter component, such as the one shown on Figure 2.6 (b), which consists only of the 6 nodal diameter component.

If the spring stiffness is increased further, the $(7,0)_c$ component will become more and more pronounced until the natural frequency of the subsystem reaches the critical point at 10.4 kHz (marked by the red cross on Figure 2.5), when the $(6,0)_c$ and $(7,0)_c$ components will have the same amplitude, as depicted in Figure 2.6 (c). If the spring stiffness is increased beyond this critical point, the $(7,0)_c$ component will become the dominant component, as illustrated in Figure 2.6 (d).

2.3.3 Case C: Rotating discs with a stationary subsystem

When the disc has a non-zero rotational speed, the natural frequencies of the combined system modes, which have the sine components of the original disc modes as the dominant components, are now affected by the presence of the subsystem. This is because the subsystem does not always locate at nodal lines of the sine components as in the case of non-rotating discs. It should also be noted from Figures 2.7 and 2.8 that the frequency curves avoid crossing each other. This phenomenon is called "curve veering" and has been studied previously by Yang *et al.* [29]. Since there is no crossing of the frequency curves, the double mode characteristics of the combined system do not occur in this case. As a result of the curve veering phenomenon, the progressive change in the mode shapes of rotating discs, as the stiffness of the subsystem increases, is different to that of non-rotating discs. In the case of non-rotating discs, the $(6,0)_c$ mode would evolve to the $(7,0)_c$ mode as the stiffness of the subsystem increases, as illustrated in Figure 2.5. In contrast, the $(6,0)_c$ mode of the rotating disc would evolve to the $(6,0)_s$ mode as the stiffness of the subsystem increases, as shown in Figure 2.7.

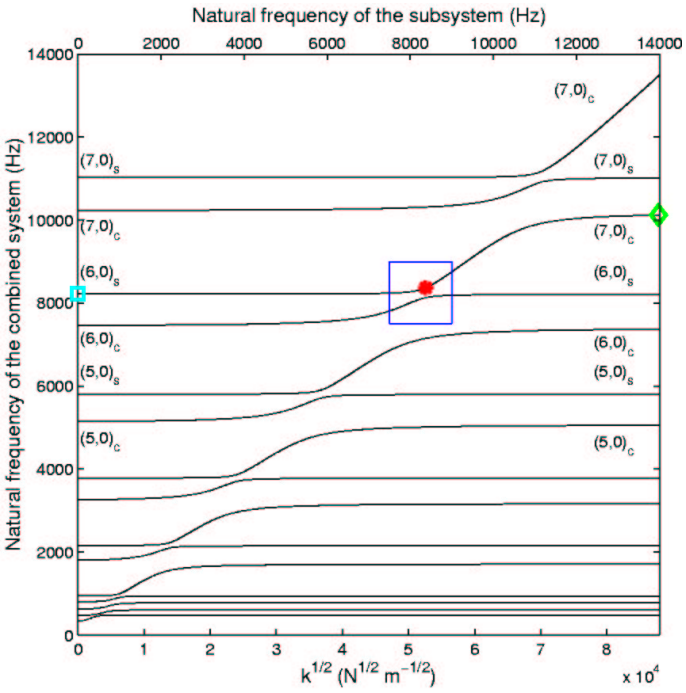

Figure 2.7: *The natural frequencies of the combined system as a function of the subsystem stiffness when Ω = 1800 rev/min (since the mass of the subsystem is always constant in this set of calculations, the corresponding natural frequency of the subsystem can be superimposed on the top axis).*

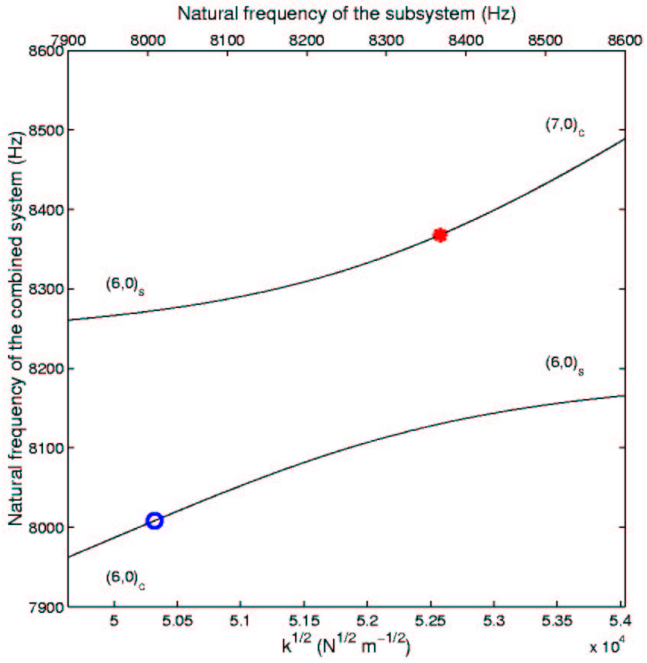

Figure 2.8: *Close-up of the region bound by the blue box in Figure 2.7.*

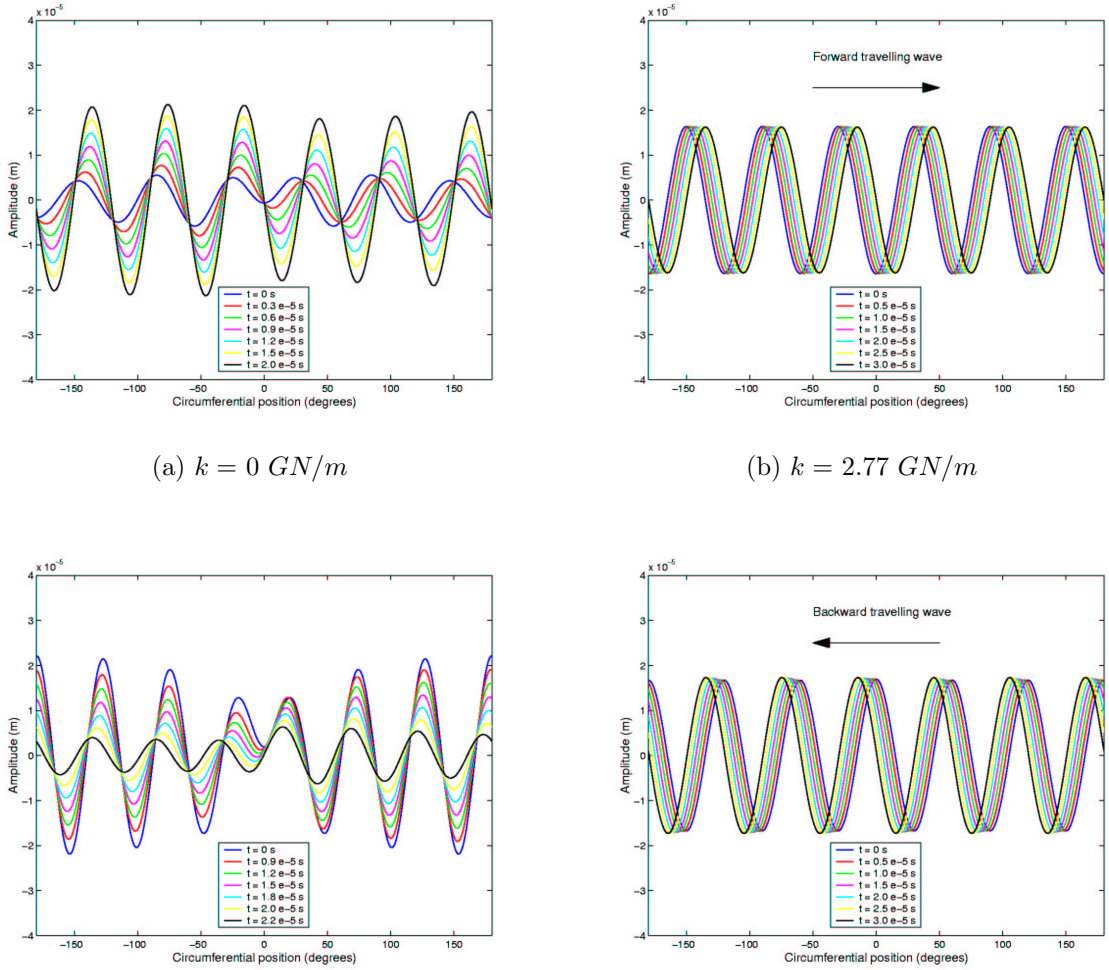

(a) $k = 0\ GN/m$

(b) $k = 2.77\ GN/m$

(c) $k = 7.71\ GN/m$

(d) $k = 2.53\ GN/m$

Figure 2.9: *Mode shapes of a rotating disc in contact with a stationary subsystem;* Ω *= 1800 rev/min, as viewed in the stationary frame of reference.*

In general, mode shapes of the rotating disc in contact with a stationary subsystem consist of both sine and cosine components of the original disc modes, which can lead to complex mode shapes. Figures 2.9 (a) and (c) demonstrate the complexity of mode shapes of the rotating disc in contact with a stationary subsystem. However, there are a number of cases where the mode shapes of the combined system are simply pure travelling waves. First consider the case when the stiffness of the subsystem reaches 2.77 GN/m, as marked by the red cross in Figure 2.8. The natural frequency of the subsystem at this point would coincide with the "apparent natural frequency"

of the 6 nodal diameter forward travelling wave. Again, the effective stiffness of the subsystem would virtually reduce to zero and, hence, the mode shape of the combined system remains the same as the mode shape of the rotating disc without a subsystem - which is a pure forward travelling wave, as shown in Figure 2.9 (b). Similarly, when the stiffness of the subsystem reaches 2.53 GN/m, as marked by the blue circle in Figure 2.8, the natural frequency of the subsystem would coincide with the "apparent natural frequency" of the 6 nodal diameter backward travelling wave. Hence, at this point, the shape of the combined system mode remains as a pure backward travelling wave as illustrated in Figure 2.9 (d).

2.3.4 Case D: Responses of the rotating discs with a stationary subsystem in the observer frame of reference

So far, the mode shapes of the combined system are viewed in either the stationary or the rotating frames of reference. It is also possible, theoretically and experimentally, to describe or examine mode shapes (or responses) in another frame of reference which rotates at an arbitrary but constant speed which is different to that of the spinning disc. This frame of reference is called the "observer" frame of reference and the relationship between it and the stationary frame of reference is given by equation (2.16).

To demonstrate a practical use of the observer frame of reference, a set of calculations are performed for the case of a rotating disc without the subsystem, excited by a single impulse. This situation represents an experimental measurement of a rotating disc in which the excitation is provided by a hammer and the responses are measured by a circular scanning LDV. Figure 2.10 shows the impulse response spectra as viewed by observers rotating at different speeds. If the observer has the same angular velocity as the disc, only one peak in the spectrum line corresponding to each nodal diameter mode will be observed, as shown by the central line on Figure 2.10. This is to be expected since the natural frequencies of the double mode pair do not split in the rotating frame of reference, as discussed in Case A. However, if the same response is

measured in the observer frame of reference rotating at the speed other than the disc rotational speed, the central peak would split into two sidebands equally spaced on either side of the central peak and the frequency separation between the two sidebands is $2n(\Omega - \Omega_b)$. If the rotational speed of the observer is less than that of the disc, the magnitude of the higher frequency sideband will correspond to the amplitude of the forward travelling wave as viewed by the observer. Conversely, the lower frequency sideband will correspond to amplitude of the backward travelling wave as viewed by the observer. In practice, the nodal diametral components of the operating deflection shapes (ODS) of the disc are determined by measuring the frequency gaps between the forward and backward peaks.

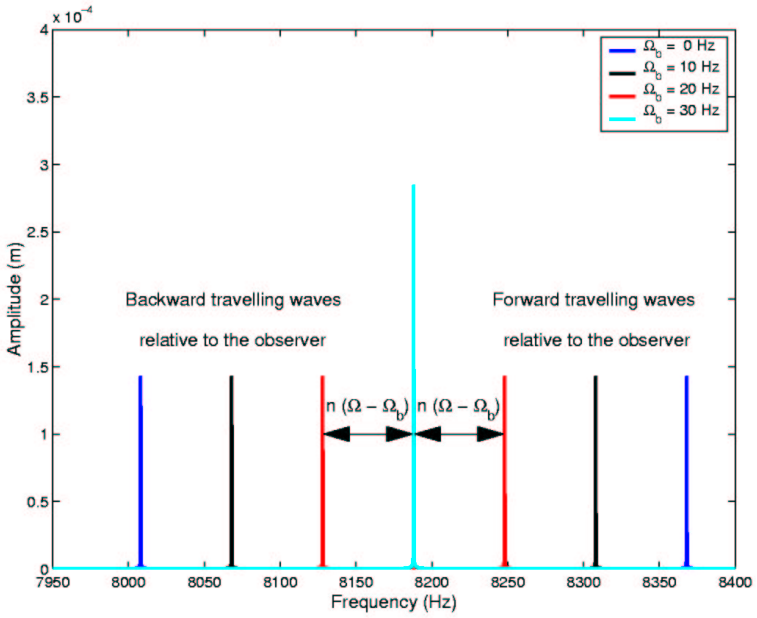

Figure 2.10: *Impulse-response of the rotating disc without the presence of the subsystem as viewed from the observer frame.*

Next, consider the case where the rotating disc is in contact with the subsystem ($m = 1$ kg, $c = 0$ Ns/m, and $k = 0$ N/m). The disc is rotating at 30 Hz in the anti-clockwise direction and is excited by an impulse at $r = a$ and $\theta_S = 7.5°$. Figure 2.11 shows the response spectra as viewed from: (i) the stationary, and (ii) the observer (Ω_b = 10 Hz) frames of reference. In the stationary frame of reference, each mode produces

one single peak in the spectrum, as shown by the red line in Figure 2.11. The origin of this behaviour arises from the fact that constant coefficient matrices can be obtained for all of the system matrices (i.e. mass, damping and stiffness matrices) only in the stationary frame of reference. As a result, "conventional" eigenvalues and eigenvectors can only be found in the stationary frame of reference. For example, mode 13 of the combined system may consist of all the components of the original disc modes but all of these components vibrate at the same frequency when measured in the stationary frame of reference. Hence, when mode 13 is excited by an impulse, and the response is measured in the stationary frame of reference, only one peak is produced in the spectrum.

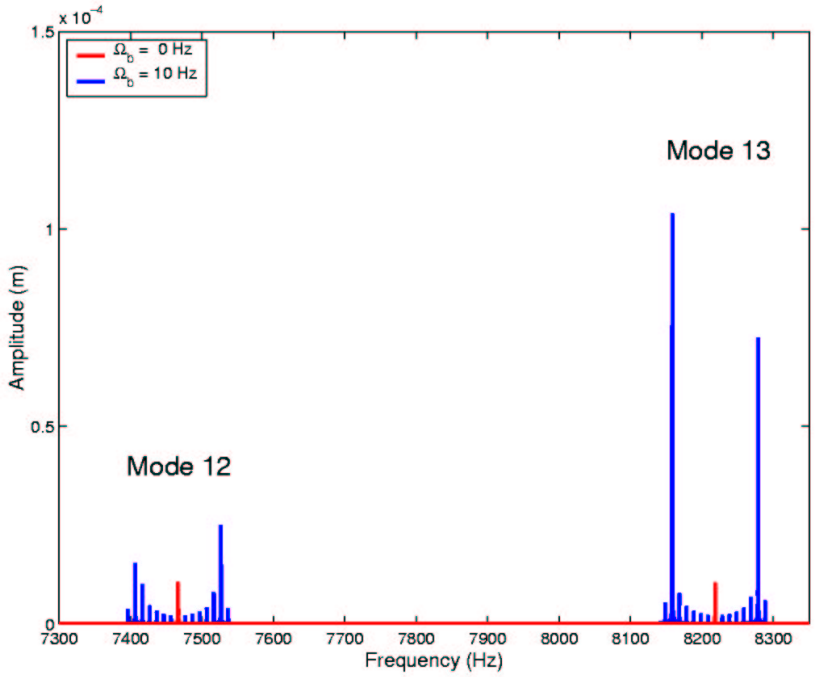

Figure 2.11: *Impulse response of the combined system as viewed from: (i) the stationary frame of reference, and (ii) the observer frame of reference rotating at 10 Hz in the anti-clockwise direction. Disc rotation is at 30 Hz.*

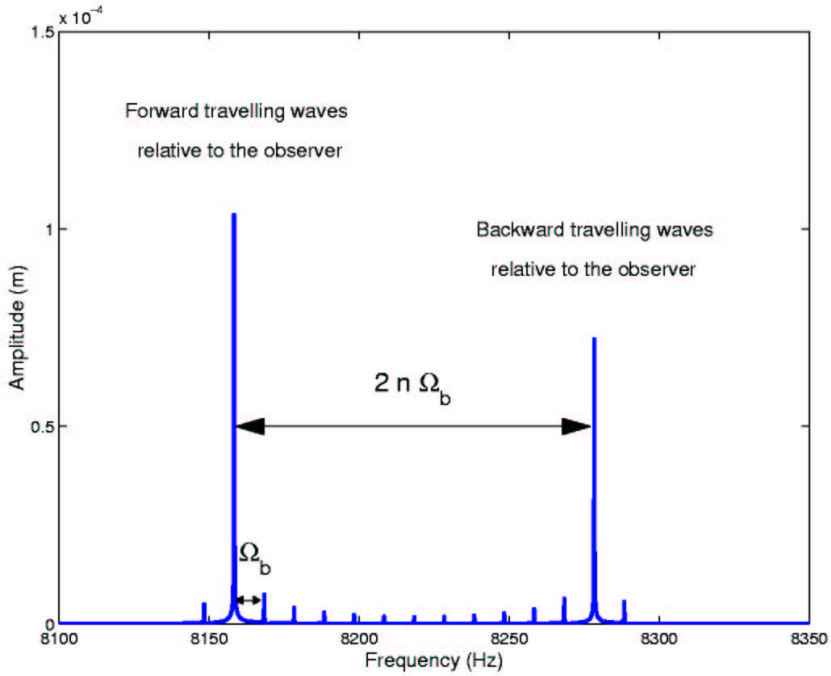

Figure 2.12: *Close-up of the response spectrum of mode 13 in Figure 2.11.*

However, if the response is measured in the observer frame of reference, a number of sidebands will be produced, as shown by the blue spectrum in Figure 2.11. These sidebands are created because the observer will observe different frequencies for different nodal diameter components as it scans around the disc. For each nodal diameter component, a pair of sidebands are produced in the spectrum and it is also possible to determine which sidebands correspond to the forward and backward travelling waves. For example, considering mode 13, which has a natural frequency at 8218 Hz in the stationary frame of reference, we see that its 6 nodal diameter component produces two sidebands at 8158 Hz and 8278 Hz, as shown in Figure 2.12, when viewed in the observer frame of reference rotating at 10 Hz in the same direction as the disc rotation. For the wave travelling forward, the observer would see the wave at a lower frequency than when the wave is viewed in the stationary frame of reference. This is because the observer moves in the same direction as the wave. Conversely, the observer would see the wave travelling backward at a higher frequency than when the wave is viewed in the stationary frame of reference. Thus, the sideband at 8158 in Figure 2.12 will correspond

to the forward travelling wave with 6 nodal diameters and the sideband at 8278 will correspond to the wave travelling backward. As can be seen from this example, there are two advantages of using the observer frame of reference: (i) the amount of each of the original disc modes which is present in the mode shapes of the combined system can be obtained instantly, and (ii) the patterns of the mode shapes of the combined system, i.e. forward or backward travelling patterns, can also be established.

2.4 Conclusions

A number of conclusions can be drawn from the current study, as follows:

- in the case of rotating discs without a connected stationary subsystem, if gyroscopic and stress stiffening effects are completely neglected, the natural frequencies of the double modes split into two distinct values when viewed in the stationary frame of reference. The mode shapes of the higher "apparent natural frequencies" correspond to pure forward travelling waves and the mode shapes of the lower "apparent natural frequencies" correspond to pure backward travelling waves, as viewed in the stationary frame of reference;

- in the case of rotating discs with the connected subsystem, the mode shapes of the combined system may appear in any of three different patterns: (i) a pure forward travelling wave, (ii) a pure backward travelling wave, and (iii) a combination of the first two. Exactly which pattern the mode shape of the combined system adopts depends on the relationship between the natural frequency of the subsystem and the "apparent natural frequency" of the rotating disc; and

- an observer frame of reference can be used to determine: (i) the amount of each of the original disc modes which is present in the mode shapes of the combined system, and (ii) the patterns of the mode shapes of the combined system, i.e. forward or backward travelling waves.

Chapter 3

General disc vibration

3.1 Overview

Typical brake discs usually come in the form of a "tophat-like" structure, as shown by a sketch in Figure 3.1 (a). Although their actual shapes and sizes may vary depending on the operation requirements, the basic structure of most brake discs consists of an assembly of 2 simple components: (i) an annular disc and (ii) a cylinder. In general, brake discs are designed to have 2 flat annular discs - one on each end of the connecting cylinder, as shown in Figure 3.1. The first annular disc, which is attached around the inside of the cylinder, provides a mounting surface between the brake disc and the vehicle axle. The second annular disc, which is attached around the outside of the cylinder, provides braking surfaces. The main purpose of the connecting cylinder is to provide the geometric offset necessary for mounting the brake disc onto the vehicle.

Although the generation of squeal noise may involve the whole of the disc brake assembly, it is the brake disc that can radiate squeal noise most effectively because of its relatively large surface area. Hence, to gain a better understanding of the brake squeal phenomenon, the vibration characteristics of brake discs must be thoroughly studied. One of the fundamental problems facing the study of three-dimensional (3D) "tophat-like" structures is the lack of a systematic method for identifying and classifying their vibration modes. Thus, the main objectives of the current study are: (i) to find a way

to distinguish vibration modes of three-dimensional "tophat-like" structures and (ii) to find a systematic method for classifying them into appropriate families according to their similarity.

(a) (b) (c)

Figure 3.1: *Typical brake disc with a "top-hat" shape: (a) cross-section sketch, (b) side-view, and (c) top-view.*

Before embarking on the vibration analysis of "tophat-like" structures, it is worth considering the conventional method for mode identification and classification of some axisymmetric structures, such as two-dimensional (classical) and three-dimensional circular discs. This chapter is, therefore, divided into three main sections: (i) free vibration of classical discs, (ii) free vibration of three-dimensional plain discs, and (iii) free vibration of "tophat-like" structures. In the first section, the conventional methods for mode identification and classification of simple two-dimensional discs are introduced. The second section looks at vibration characteristics of three-dimensional plain discs, where the in-plane and out-of-plane motions are both active. A set of nodal variables, which are used in the identification process, are introduced. In the third section, the idea of nodal variables is extended to cope with three-dimensional "tophat-like" structures. The use of the AutoMAC diagram for the purpose of mode classification is also presented. Of particular interest in this chapter as a whole will be the way vibration modes of different types of discs are identified and classified.

3.2 Free vibration of classical discs

The vibration theory of thin circular plates was first developed by Kirchhoff [51] in 1850. Over the years, the theory has been revisited and revised by many researchers, such as Rayleigh [52]. However, the most comprehensive study on the free vibration of classical discs, which covered many different kinds of boundary conditions, was conducted by Leissa [53]. The free vibration of classical discs can also be found in many standard vibration text books, such as Prescott [54], Soedel [55] and Timoshenko [56].

Based upon the following assumptions:

1. plane sections remain plane and deflections due to shear may be neglected;
2. the stresses normal to the mid-plane of the plate are negligible in comparison with the stresses in the plane of the plate; and
3. the slope of the deflected plate is small so that its square may be ignored in comparison with unity,

the classical differential equation of motion for the transverse displacement $w(r, \theta, t)$ of a circular disc can then be written as:

$$D\nabla^4 w + \rho h \frac{\partial^2 w}{\partial t^2} = 0, \tag{3.1}$$

and the flexural rigidity, D, is defined by:

$$D = \frac{Eh^3}{12(1-\nu^2)}, \tag{3.2}$$

where ρ is density, E Young's modulus, ν Poisson's ratio, h the plate thickness, and t time. The general solution to equation (3.1) in polar coordinates is

$$\begin{aligned} W(r,\theta) = & \sum_{n=0}^{\infty} \{A_n J_n(kr) + B_n Y_n(kr) + C_n I_n(kr) + D_n K_n(kr)\} \cos n\theta \\ & + \sum_{n=0}^{\infty} \{A'_n J_n(kr) + B'_n Y_n(kr) + C'_n I_n(kr) + D'_n K_n(kr)\} \sin n\theta \,, \end{aligned} \tag{3.3}$$

where J_n and Y_n are the Bessel functions of the first and second kinds, respectively, and I_n and K_n are the modified Bessel functions of the first and second kinds, respectively. The coefficients A_n,...,D'_n can be solved from the boundary conditions in each specific case and the explicit formula for k is given by:

$$k^4 = \frac{\rho h \omega^2}{D}, \tag{3.4}$$

where ω is the natural frequency.

According to the form of the solution in equation (3.3), the transverse displacement of a circular disc depends on 2 spatial variables, r and θ. Furthermore, the solution can be expressed into a separable form in r and θ. As a result, vibration modes of two-dimensional circular plates are conventionally classified into a two-dimensional family, according to: (i) the number of nodal diameters, n, and (ii) the number of nodal circles, m, as shown in Figure 3.2. It should be emphasised that classical plate theory takes into account only the out-of-plane displacements and does not consider any motion in the in-plane directions.

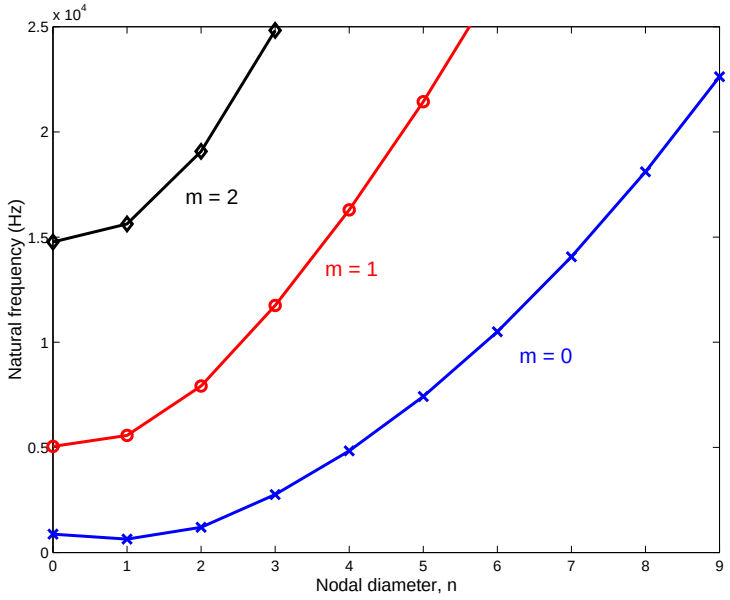

Figure 3.2: *The natural frequencies of a circular disc fully clamped at the inner bore as functions of the number of nodal diameters, n and nodal circles, m.*

3.3 Free vibration of three-dimensional plain discs

3.3.1 Background

The three-dimensional plain discs considered in this section are assumed to be perfectly flat, as shown in Figure 3.3, and are treated as three-dimensional structures. In contrast to classical theory, the motions of the three-dimensional plain discs may take place in all three principal directions. In the past, most of the research done on free vibration of plain discs was aimed at obtaining very accurate natural frequencies and the validity of the solutions. For example, Mindlin and his co-workers [57, 58] included the effect of rotary inertia and shear deformation to improve the predicted natural frequencies. Hutchinson [59] in 1984, on the other hand, compared the exact solutions with the approximate solutions and showed the validity of the approximate solutions. However, the majority of the past research usually considered the in-plane and out-of-plane vibrations separately, such as Tzou *et al.* [60] in 1998.

One of the most recent works on free vibration of three-dimensional plain discs, which considered both the in-plane and out-of-plane vibrations at the same time, was conducted by So *et al.* [61] in 1998. Their primary objective was again to obtain truly accurate values of the free-vibration natural frequencies of thick three-dimensional annular plates. Although their method is capable of calculating in-plane modes, only the natural frequency of the first in-plane mode (pure torsional mode) was presented.

In this section, vibration modes of three-dimensional plain discs are studied using the Finite Element (FE) method. The main objective is to develop a general method for identifying vibration modes when both the in-plane and out-of-plane displacements are of equal interest. Moreover, the method developed in this section will form the basis for mode identification method of “tophat-like” structures in the next section.

3.3.2 Modelling

To study the in-plane and out-of-plane modes at the same time, an FE model of a three-dimensional plain disc is necessary. The model is assumed to be fully clamped around the inner bore and completely free at the outer edge. Twenty-node brick elements are used - 10 elements along the radial direction, 120 elements around the circumferential direction and 4 elements through the thickness, as shown in Figure 3.3.

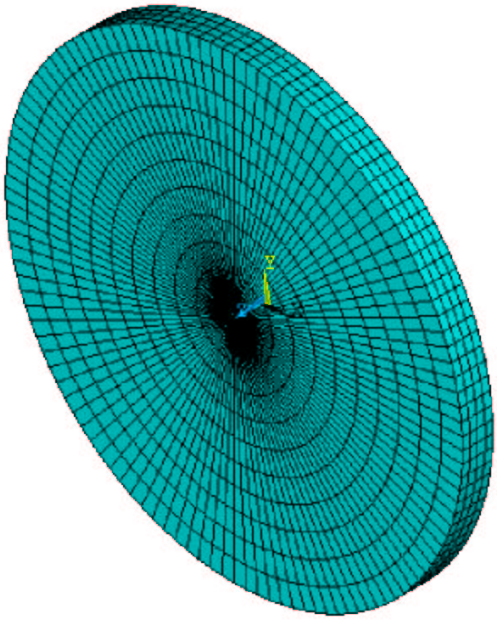

Figure 3.3: *An FE model of a three-dimensional plain disc.*

3.3.3 Identification of vibration modes of three-dimensional plain discs

As described previously in Section 3.2, when only the out-of-plane motion was of primary concern, classical plate theory indicates that the family of modes of a circular disc can be described uniquely by 2 parameters: (i) the number of nodal diameters, n, and (ii) the number of nodal circles, m. However, when the in-plane motion is to be considered together with the out-of-plane motion, the families of modes can no

longer be described uniquely by only 2 parameters. To distinguish vibration modes of three-dimensional plain discs, many studies use the fact that the coupling between the in-plane and out-of-plane motions is usually small and, hence, the out-of-plane modes can easily be separated from the in-plane modes and vice-versa. As a result, vibration modes of three-dimensional discs are conventionally classified into either "in-plane" or "out-of-plane" classes.

If vibration modes belong to the out-of-plane class, they are further sorted by the numbers of nodal diameters and nodal circles, as discussed in Section 3.2. However, for the in-plane vibration, modes could also appear in two different classes depending on the direction of the dominant motion and these two classes are usually called: (i) "radial modes" where the dominant motion takes place mainly in the r-direction and (ii) "tangential modes" where the dominant motion takes place mainly in the θ-direction. Each of these two in-plane classes is further categorised according to the number of nodal diameters and nodal circles along the directions of the dominant motion.

The classification of modes into in-plane or out-of-plane classes is only possible if the coupling between the two directions is small. However, if the coupling between the in-plane and out-of-plane motions is strong as, for example, in the case of "tophat-like" structures, it is sometimes impossible to classify vibration modes into the in-plane or out-of-plane classes because the vibration amplitudes in both planes are comparable. To eliminate the need of specifying vibration modes into the in-plane or out-of-plane, a set of nodal variables, which are based upon the idea of nodal diameters and nodal circles, are introduced. Although the identification method using nodal variables may seem at first more complicated than the conventional method, it later provides the possibility of extending the technique to be used on more complex structures, e.g. "tophat-like" structures.

For three-dimensional plain discs, there are 6 nodal variables required to describe their vibration modes uniquely and they are defined as follows (Note: all of the nodal variables are defined at the mid-plane of the disc):

1. Nodal variables in the (axial) z-direction, ND_z and NC_z :

   1.1 Nodal diameters in the z-direction. ND_z is defined as the number of nodal diameters at which the translations in the z-direction are all equal to zero for all points along the diametral lines.

   1.2 Nodal circles in the z-direction. NC_z is defined as the number of nodal circles at which the translations in the z-direction are all equal to zero for all points along the circumferential lines.

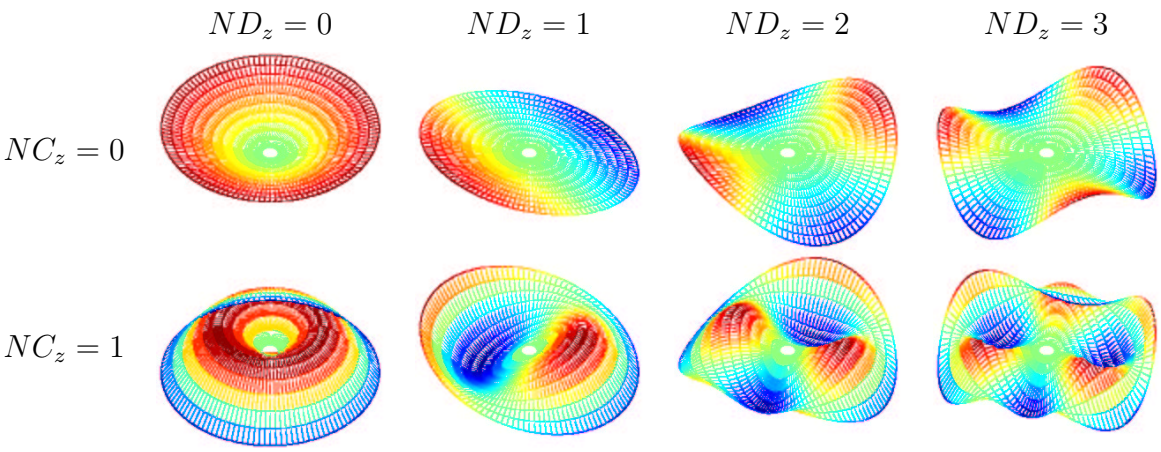

Figure 3.4: *Graphical interpretations of the nodal variables in the z-direction, ND_z and NC_z.*

2. Nodal variables in the (circumferential) θ-direction, ND_θ and NC_θ :

   2.1 Nodal diameters in the θ-direction. ND_θ is defined as the number of nodal diameters at which the translations in θ-direction are all equal to zero for all points along the diametral lines.

   2.2 Nodal circles in the θ-direction. NC_θ is defined as the number of nodal circles at which the translations in θ-direction are all equal to zero for all points along the circumferential lines.

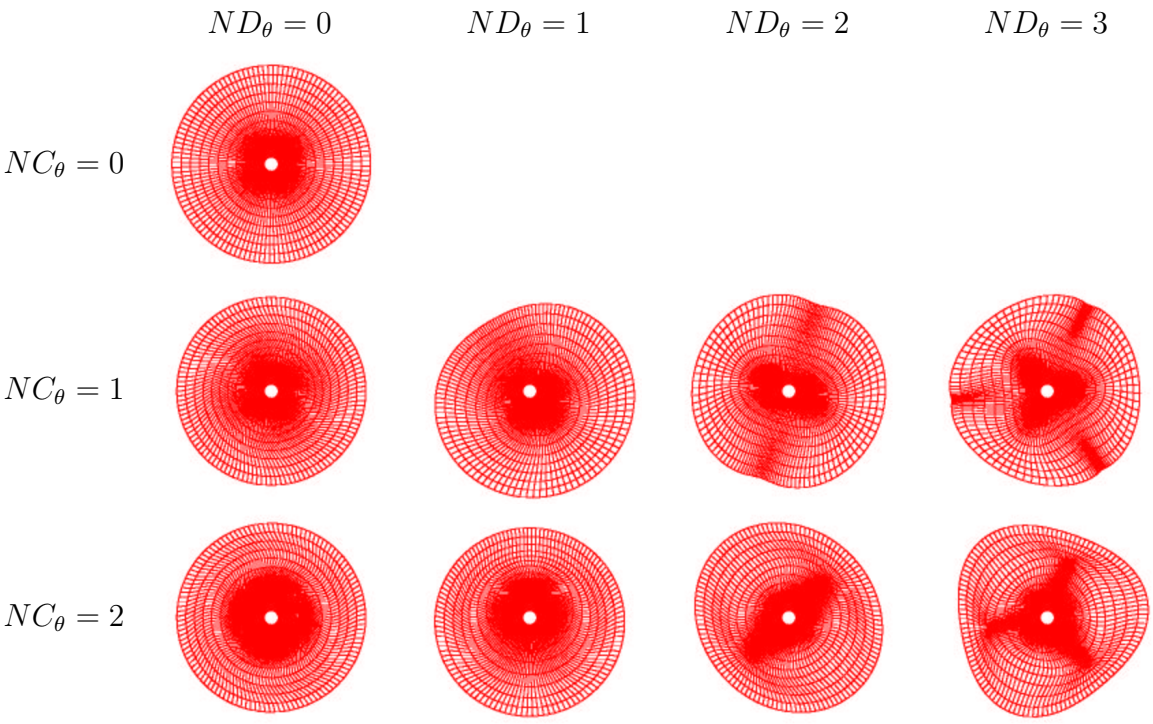

Figure 3.5: *Graphical interpretations of the nodal variables in the θ-direction, ND_θ and NC_θ.*

3. Nodal variables in the (radial) r-direction, ND_r and NC_r :

   3.1 Nodal diameters in the r-direction. ND_r is defined as the number of nodal diameters at which the translations in the r-direction are all equal to zero for all points along the diametral lines.

   3.2 Nodal circles in the r-direction. NC_r is defined as the number of nodal circles at which the translations in the r-direction are all equal to zero for all points along the circumferential lines.

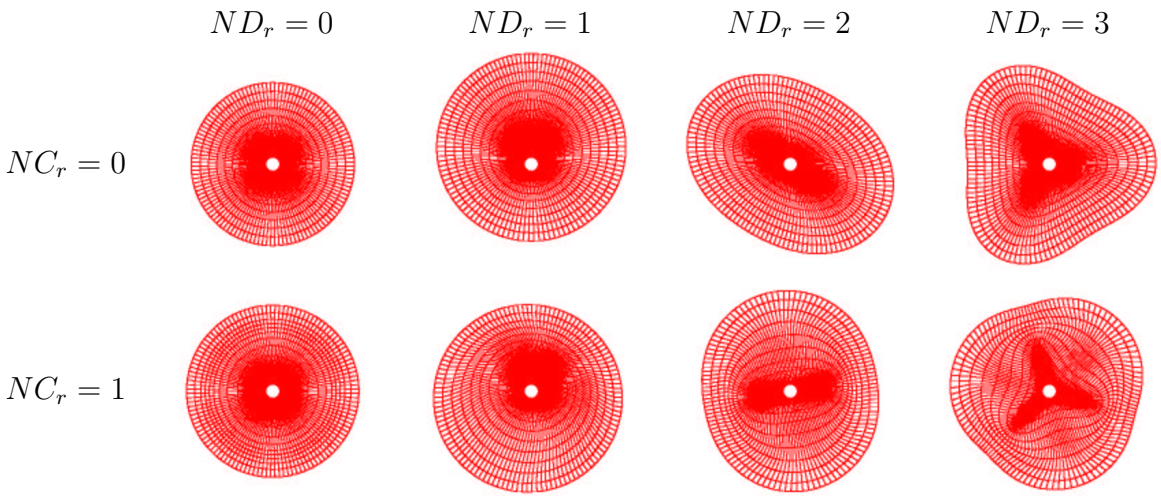

Figure 3.6: *Graphical interpretations of the nodal variables in the r-direction, ND_r and NC_r.*

3.3.4 Results for test case

In this section, results are shown for a three-dimensional disc which has the following physical dimensions: outer diameter of 0.15 m, inner diameter of 0.0114 m and thickness of 0.02 m. The disc is made of steel with Young's modulus of 210 GPa, density of 7840 kg/m^3 and Poisson's ratio of 0.3. Table 3.1 shows all the nodal variables of the first 40 modes of the disc. Note: the values of nodal variables are determined at the mid-plane of the disc and the notation "-" refers to "no motion in the specified direction" (see detailed discussion in the next section).

Mode number	Frequency (Hz)	In-plane (r-direction)		In-plane (θ-direction)		Out-of-plane (z-direction)	
		ND_r	NC_r	ND_θ	NC_θ	ND_z	NC_z
1	00620	-	-	-	-	1	0
2	00739	-	-	0	0	-	-
3	00875	-	-	-	-	0	0
4	01176	-	-	-	-	2	0
5	02628	-	-	-	-	3	0
6	04060	1	0	1	0	-	-
7	04486	-	-	-	-	4	0
8	04632	-	-	-	-	0	1
9	05098	-	-	-	-	1	1
10	06671	-	-	-	-	5	0
11	07134	-	-	-	-	2	1
12	08127	2	0	2	0	-	-
13	09125	-	-	-	-	6	0
14	10147	-	-	-	-	3	1
15	10832	1	0	1	1	-	-
16	11798	-	-	-	-	7	0
17	11931	0	0	-	-	-	-
18	12238	-	-	-	-	0	2
19	12267	3	0	3	1	-	-
20	12953	-	-	-	-	1	2
21	13465	-	-	-	-	4	1
22	14540	2	0	2	1	-	-
23	14649	-	-	-	-	8	0
24	15519	-	-	-	-	2	2
25	15968	4	0	4	1	-	-
26	16948	-	-	-	-	5	1
27	17644	-	-	-	-	9	0
28	17890	-	-	0	1	-	-
29	19281	-	-	-	-	3	2
30	19439	5	0	5	1	-	-
31	19861	3	1	3	1	-	-
32	20548	-	-	-	-	6	1
33	20753	-	-	-	-	10	0
34	21674	-	-	-	-	0	3
35	22562	1	1	1	1	-	-
36	22563	-	-	-	-	1	3
37	22798	6	0	6	1	-	-
38	23332	-	-	-	-	4	2
39	23953	-	-	-	-	11	0
40	24232	-	-	-	-	7	1

Table 3.1: *Mode identification of the three-dimensional plain disc using nodal variables.*

Figure 3.7 shows the first 40 natural frequencies of the three-dimensional disc plotted as a function of Fourier order. The concept of Fourier order, which is a generalisation of "nodal diameter", is discussed in the next section. The lines linking modes with different Fourier orders are drawn according to their classification, i.e. out-of-plane or in-plane radial or in-plane tangential classes.

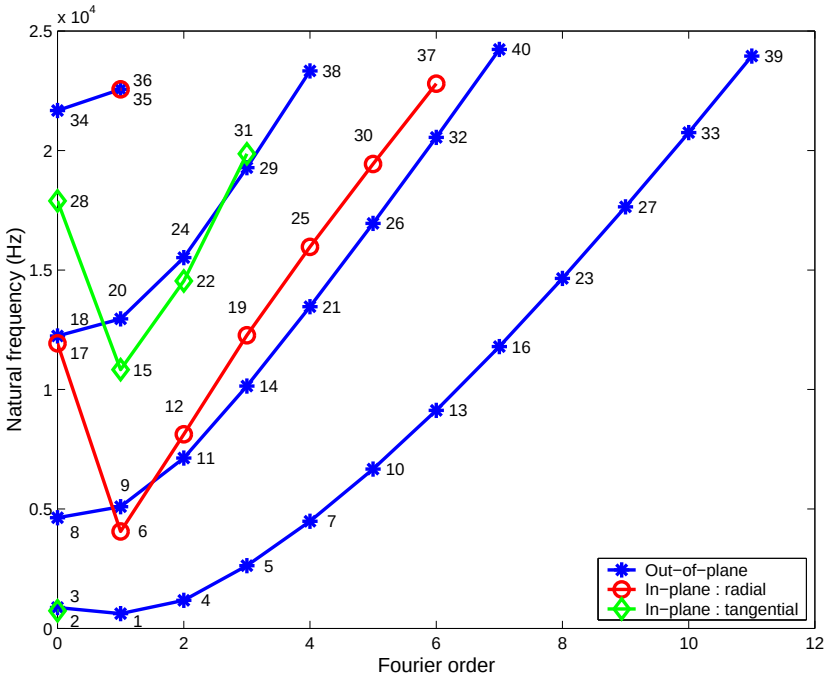

Figure 3.7: *The natural frequencies of a 3D circular disc fully clamped at the inner bore as a function of Fourier order.*

3.3.5 Discussion

3.3.5.1 The concept of "Fourier order" in mode classification

When dealing with axisymmetric structures, it is a common practice to classify vibration modes according to the number of nodal diameters. Although there are three types of nodal diameters for three-dimensional plain discs, i.e. ND_r, ND_θ and ND_z, as defined in Section 3.3.3, So *et al.* [61] have shown that they generally have the same value - except when one of them is equal to zero. Hence, for the purpose of mode classification only, these three types of nodal diameters can be reduced to one single

parameter, which will be called "Fourier order". It should be noted that Fourier order does not indicate in which plane is the dominant motion taking place. For example, both modes shown in Figure 3.8 have the same Fourier order of 4.

(a) Out-of-plane mode at 4486 Hz

(b) In-plane radial mode at 15968 Hz

Figure 3.8: *Modes with the same Fourier order of 4 : (a) Out-of-plane mode with* $ND_z = 4$ *and (b) In-plane radial mode with* $ND_r = 4$.

3.3.5.2 The uncoupling characteristics for modes with zero Fourier order

When one of the nodal variables of the "nodal diameter" type is equal to zero, the motion in the θ-direction will be uncoupled from the motion in the r and z-directions: refer to So *et al.* [61]. In such cases, the nodal variables, ND_r, ND_θ and ND_z, must be specified individually. For example: considering the first out-of-plane mode with zero nodal diameters (the "umbrella" mode), all the displacements of this mode are symmetric about the z-axis and, hence, there cannot be any displacement in the θ-direction. In this mode, the values of ND_z and ND_r are clearly equal to zero. However, the value of ND_θ cannot be zero because $ND_\theta = 0$ would imply pure torsional mode. As a result, a new notation must be given to ND_θ. One possible notation would be "-", which refers to "no motion in the specified direction", as utilised in Table 3.1. For classification purpose only, vibration modes, which have, at least, one of the nodal variables of the "nodal diameter" type equal to zero, are classified as zero Fourier order.

3.3.5.3 The coupling between in-plane and the out-of-plane motions

There is still one remaining difficulty in using the nodal variables to distinguish vibration modes of three-dimensional plain discs. The difficulty arises due to the coupling of the in-plane and out-of-plane motions. The best way to address this issue is by way of example. First, consider the out-of-plane mode with 2 nodal diameters in the z-direction and the in-plane radial mode with 2 nodal diameters in the r-direction, as shown in Figure 3.9. If the nodal variables are obtained from any $r-\theta$ plane, except the mid-plane, both modes will have exactly the same set of nodal variables, i.e. $ND_r = ND_\theta = ND_z = 2$ and $NC_r = NC_\theta = NC_z = 0$, due to the coupling between the in-plane and out-of-plane motions. This would lead to repeated sets of nodal variables in the identification method. However, if the nodal variables are obtained from the mid-plane of the disc where the coupling between the in-plane and out-of-plane motions disappears, the out-of-plane mode will clearly exhibit 2 nodal diameters in the z-direction with no motion in the r-direction whereas the in-plane mode will clearly exhibit 2 nodal diameters in the r-direction with no motion in the z-direction. Making use of the "-" notation, these two modes can be distinguished from one another, as listed in Table 3.1.

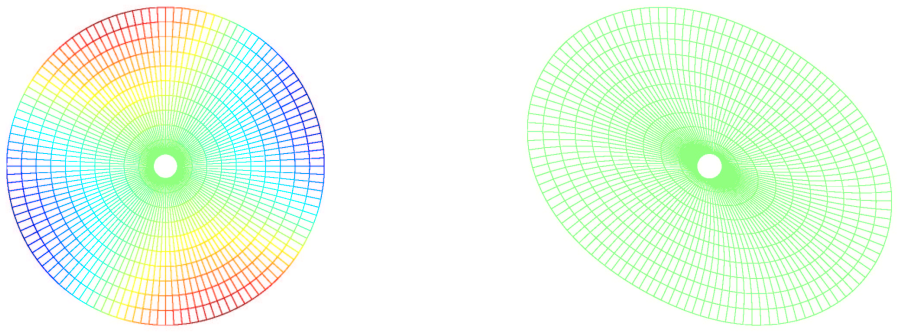

(a) Out-of-plane mode at 1176 Hz (b) In-plane radial mode at 8127 Hz

Figure 3.9: *Comparison between the out-of-plane mode with $ND_z = 2$ and the in-plane mode with $ND_r = 2$.*

3.4 Free vibration of three-dimensional "tophat-like" structures

3.4.1 Background

Over the years, there have been many related references which studied the vibration characteristics of discs and cylinders individually. For example, Gladwell *et al.* [62] used the finite element technique to obtain natural frequencies of hollow cylinders for modes up to 2 nodal diameters (in the radial direction). Tzou *et al.* [60] studied the manner in which the in-plane and out-of-plane modes of thick discs evolve with increasing disc's thickness. However, the studies of coupled disc-cylinder ("tophat-like") structures were rare. The most recent study on the free vibration of three-dimensional "tophat-like" structures was conducted by Bae *et al.* [63]. The purpose of their study was to investigate the effect of the disc's thickness and the hat's depth on the natural frequency of the structure.

One of the fundamental problems facing the study of three-dimensional "tophat-like" structures is the lack of a systematic method for identifying and classifying their vibration modes. Hence, the main objectives of the current study are: (i) to find a set of variables which can be used to identify each vibration mode uniquely and (ii) to develop a systematic method for classifying vibration modes of the top-hat type structures widely used in disc brake design.

3.4.2 Modelling

To demonstrate the method of identifying and classifying vibration modes of brake disc type structures, a "tophat-like" model is studied. Although the real brake disc consists of two flat annular discs (i.e. mounting and braking discs), the mounting disc is usually fixed firmly onto the brake knuckle. Hence, the vibration of the actual brake disc occurs mainly in the braking disc and the connecting cylinder. As a result, the representative model used in the current study is designed as a single annular disc mounted onto one end of a cylinder which is fully clamped at the other end, as shown in Figure 3.10.

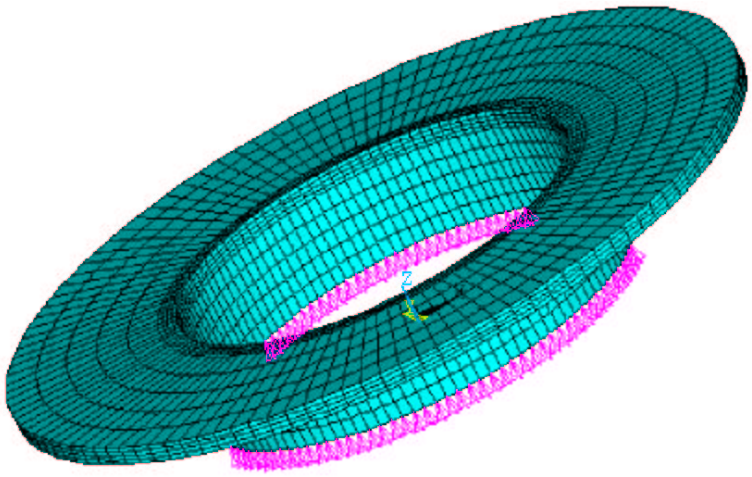

Figure 3.10: *A three-dimensional FE model of a "tophat-like" structure.*

In the present study, three different lengths of the connecting cylinder - 0.03, 0.06 and 0.09 m - are used whereas the inner and outer diameters of the annular disc and the common disc and cylinder wall thickness are kept constant at 0.132, 0.246 and 0.006 m, respectively. Twenty-node brick elements are used and the numbers of elements are set as follows: 120 along the circumferential direction, 5 along the radial direction of the annular disc and 4 through the thickness, as shown in Figures 3.10 and 3.11. Along the length of the connecting cylinder, the length of element is fixed at 0.006 m for all of the three models.

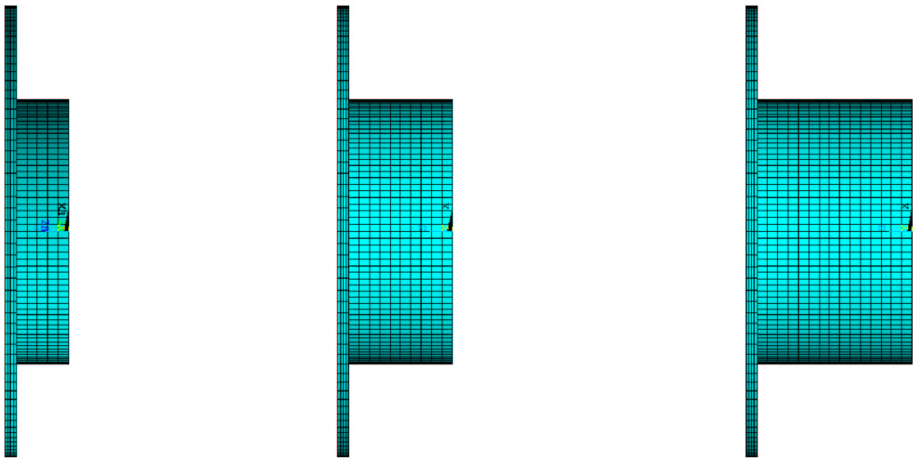

(a) Step 1 (b) Step 2 (c) Step 3

Figure 3.11: *Three models of the tophat discs with different connecting cylinder length: (a) 0.03, (b) 0.06 and (c) 0.09 m.*

3.4.3 Identification method for vibration modes of "tophat-like" structures

Since the "tophat-like" models consist only of a disc and a cylinder, it is appropriate to describe the mode shapes of the disc part using the set of nodal variables (i.e. ND_r, ND_θ, ND_z, NC_r, NC_θ and NC_z) adopted for the three-dimensional plain discs in Section 3.3.3. However, a number of extra nodal variables which are required to describe the mode shapes of the cylinder must be added to the full set of nodal variables. The extra nodal variables associated with the mode shapes of the cylinder part, which are called the "nodal ring" class, are defined below.

1. Nodal ring class, NR_r, NR_θ and NR_z :

   1.1 Nodal rings in the r-direction. NR_r is defined as the number of nodal rings at which the translations in the r-direction are all equal to zero for all points along the rings.

   1.2 Nodal rings in the θ-direction. NR_θ is defined as the number of nodal rings

at which the translations in the θ-direction are all equal to zero for all points along the rings.

1.3 Nodal rings in the z-direction. NR_z is defined as the number of nodal rings at which the translations in the z-direction are all equal to zero for all points along the rings.

As an example, Figure 3.12 demonstrates graphical interpretations of the nodal variables of the disc and the cylinder parts. The top row shows the nodal variables of the "nodal diameter" type for the disc part, ND_r, ND_θ and ND_z. The middle row shows the nodal variables of the "nodal circle" type for the disc part, NC_r, NC_θ and NC_z. The bottom row shows the nodal variables of the "nodal ring" type for the cylinder part, NR_r, NR_θ and NR_z.

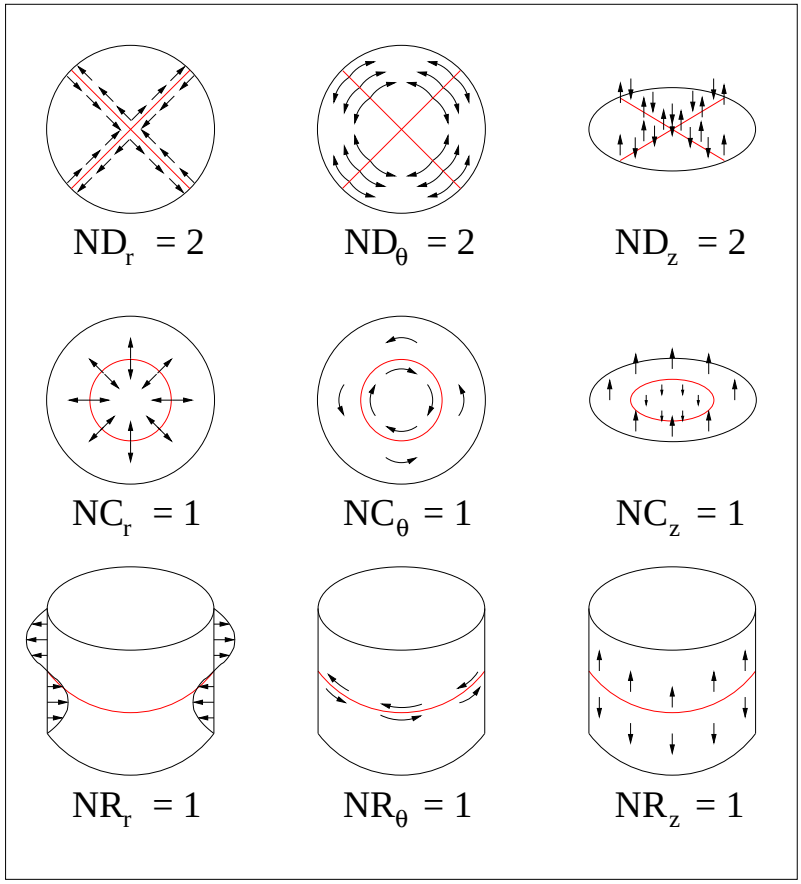

Figure 3.12: *Graphical interpretations of the nodal variables of the disc and the cylinder parts.*

All the nodal variables discussed and defined up until now are associated with zero translation. There are, however, another set of nodal variables which are associated with zero rotation (or zero slope). For "tophat-like" structures, there are 2 important rotation-type nodal variables, NCR_θ and NRR_θ, and they are defined below.

2 Rotation-type nodal variables, NCR_θ and NRR_θ:

2.1 Rotation-type nodal circles about the θ-axis. NCR_θ is defined as the number of nodal circles at which the rotations about the θ-axis are all equal to zero for all points around the circumferential lines.

2.2 Rotation-type nodal rings about the θ-axis. NRR_θ is defined as the number of nodal rings at which the rotations about the θ-axis are all equal to zero for all points along the rings.

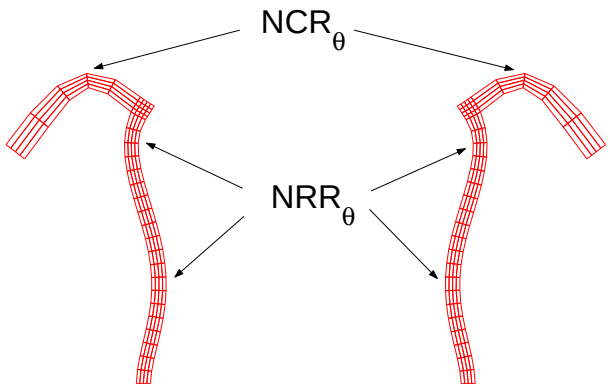

Figure 3.13: *A graphical interpretation of nodal variables of the rotation type, NCR_θ and NRR_θ (Note: in this example $NCR_\theta = 1$ and $NRR_\theta = 2$).*

In total, there are 11 nodal variables which are required in order to identify uniquely a mode of "tophat-like" structures. The first 9 nodal variables are associated with the translation whereas the last 2 nodal variables are associated with the rotation.

3.4.4 Classification of vibration modes of brake disc type structures

As for the three-dimensional plain discs discussed earlier, Fourier order (which represents the variation of mode shapes in the θ-direction) can be used to classify vibration modes of "tophat-like" structures. However, it is also possible to classify vibration modes according to the variation of mode shapes in the $r-z$ plane. To classify vibration modes of "tophat-like" structures according to the variation of mode shapes in the $r-z$ plane, the AutoMAC, in which a set of mode shape vectors are correlated with themselves, is adopted.

Although the full set of degrees-of-freedom for each mode shape vector are available, it is not possible to use them all when comparing two mode shapes with different Fourier orders. The reason is that the eigenvectors with different Fourier orders will certainly be orthogonal to one another and the AutoMAC would indicate low correlation, even if the variation of the two mode shapes in the r- and z-directions is perfectly matched. To avoid such problems, only the DOFs of the cross-section of the tophat model, as shown in Figure 3.14, are used in the AutoMAC calculations. Since modes with different Fourier orders have different variations in the θ-direction, the cross-sections used in the AutoMAC calculations are selected along an antinode of the disc's transverse displacement. The formula for AutoMAC, given in Ewins [50], can be written as

$$AutoMAC(i,j) = \frac{|\{\psi_j\}^T\{\psi_i\}|^2}{(\{\psi_j\}^T\{\psi_j\})(\{\psi_i\}^T\{\psi_i\})}, \tag{3.5}$$

where ψ is a mode shape vector which consists only of the DOFs on the selected cross-section and subscripts i and j represent the mode numbers.

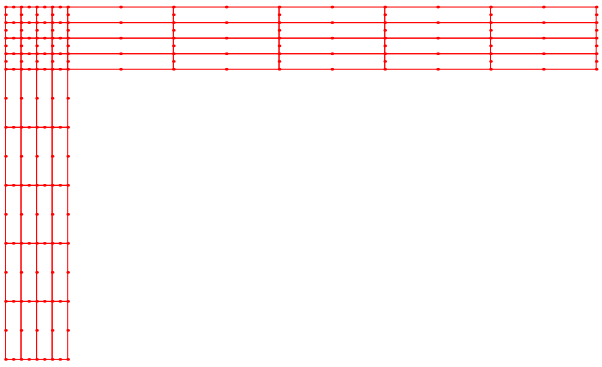

Figure 3.14: *Cross-sectional view of the "tophat" model: there are 3 DOFs at each node.*

3.4.5 Results for test cases

In this section, the three tophat models are made of steel with the following material properties: Young's modulus of 210 GPa, a density of 7840 kg/m^3 and a Poisson's ratio of 0.3. Vibration modes which have their natural frequencies within the frequency range of 0 to 20 kHz, are shown below. All of the 11 nodal variables used in the identification process are listed in Tables 3.2, 3.3 and 3.4. Figures 3.15 (a), 3.16 (a) and 3.17 (a) show the natural frequencies as a function of Fourier order for the tophat models in Steps 1, 2 and 3, respectively. The classification of vibration modes according to their similarity in the $r - z$ plane, i.e. lines linking modes with different Fourier order, is conducted with the aid of the corresponding AutoMAC diagrams, as illustrated in Figures 3.15 (b), 3.16 (b) and 3.17 (b). The cross-sectional view of all the mode shapes obtained from the three tophat models can be found in Appendix B.

Mode number	Frequency (Hz)	ND_r	ND_θ	ND_z	NC_r	NC_θ	NC_z	NR_r	NR_θ	NR_z	NCR_θ	NRR_θ
1	01389	0	-	0	0	-	1	1	-	0	0	1
2	01413	1	1	1	0	0	1	1	0	0	0	1
3	01580	2	2	2	0	1	1	1	0	0	0	1
4	01968	3	3	3	0	1	1	1	1	0	0	1
5	02631	4	4	4	0	1	1	1	1	0	0	1
6	03577	5	5	5	0	1	1	1	1	0	0	1
7	04779	6	6	6	0	1	1	1	1	0	0	1
8	06082	-	0	0	-	0	-	-	0	-	-	-
9	06211	7	7	7	0	1	1	1	1	0	0	1
10	06241	1	1	1	0	0	2	0	0	0	1	0
11	07341	2	2	2	0	0	2	0	0	0	1	0
12	07850	8	8	8	0	1	1	1	1	0	0	1
13	08553	0	-	0	0	-	2	1	-	0	1	1
14	09336	1	1	1	1	0	2	1	0	0	1	1
15	09680	9	9	9	0	1	1	1	1	0	0	1
16	09873	2	2	2	0	0	2	1	0	0	1	1
17	10172	3	3	3	0	1	2	0	0	0	1	0
18	10336	0	0	0	0	0	2	0	0	0	2	1
19	11042	3	3	3	0	1	2	0	0	1	1	1
20	11510	4	4	4	0	1	2	1	1	0	1	1
21	11686	10	10	10	0	0	1	1	1	0	0	1
22	12095	1	1	1	0	0	2	0	0	1	2	0
23	12887	5	5	5	0	1	2	1	1	0	1	1
24	13855	11	11	11	0	1	1	1	1	0	0	1
25	14541	6	6	6	0	1	2	1	1	0	1	1
26	15132	4	4	4	0	1	2	0	0	0	1	1
27	16176	12	12	12	0	1	1	1	1	0	0	1
28	16464	7	7	7	0	1	2	1	1	0	1	1
29	17579	2	2	2	0	0	2	0	0	1	2	0
30	18637	8	8	8	0	1	2	1	1	0	1	1
31	18640	13	13	13	0	1	1	1	1	0	0	1
32	19841	5	5	5	0	1	2	0	0	0	1	1

Table 3.2: *Nodal variables of the tophat model in Step 1.*

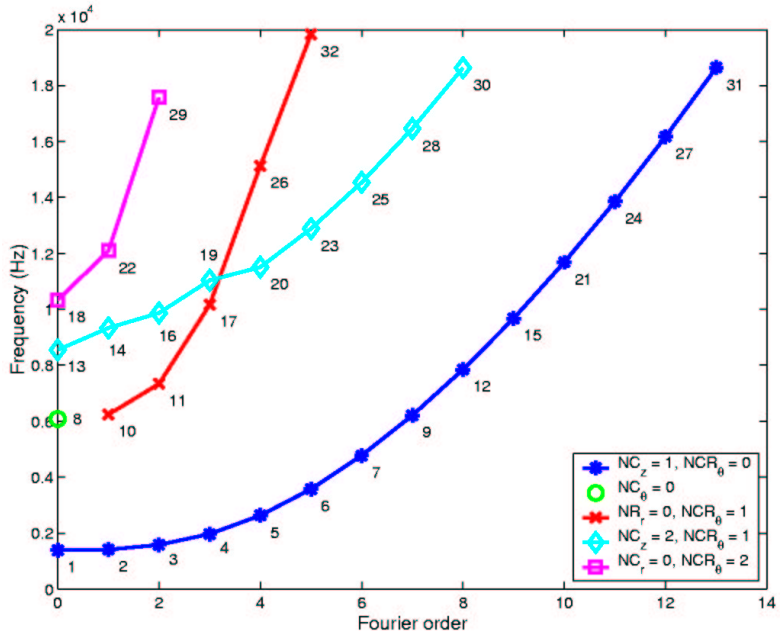

(a) Natural frequency as a function of Fourier order for Step 1

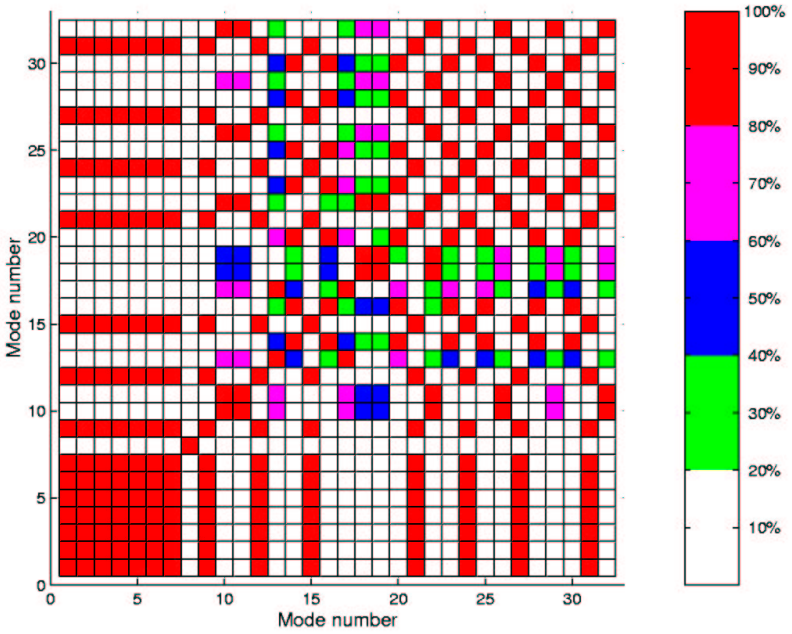

(b) AutoMAC of the cross-section of the tophat model for Step 1

Figure 3.15: *Mode classification for the tophat model with the cylinder length of 0.03 m (Step 1).*

Mode number	Frequency (Hz)	ND_r	ND_θ	ND_z	NC_r	NC_θ	NC_z	NR_r	NR_θ	NR_z	NCR_θ	NRR_θ
1	01360	0	-	0	0	-	1	1	-	0	0	1
2	01388	1	1	1	0	0	1	1	0	0	0	1
3	01543	2	2	2	0	1	1	1	1	0	0	1
4	01918	3	3	3	0	0	1	1	1	0	0	1
5	02594	4	4	4	0	1	1	1	1	0	0	1
6	03557	5	5	5	0	1	1	1	1	0	0	1
7	04412	1	1	1	0	0	1	0	0	0	1	1
8	04630	-	0	0	-	0	-	-	0	-	-	-
9	04770	6	6	6	0	1	1	1	1	0	0	1
10	05158	2	2	2	0	0	1	0	0	0	1	1
11	06207	7	7	7	0	1	1	1	1	0	0	1
12	07849	8	8	8	0	1	1	1	1	0	0	1
13	08164	3	3	3	0	1	2	0	0	0	1	1
14	08425	0	-	0	0	-	2	1	-	0	1	1
15	08849	1	1	1	0	0	2	1	0	0	1	1
16	09128	2	2	2	0	1	2	1	1	0	1	1
17	09680	9	9	9	0	1	1	1	1	0	0	1
18	09894	3	3	3	0	1	2	1	1	0	1	1
19	09972	0	-	0	0	-	2	0	-	0	2	1
20	10355	4	4	4	0	1	2	0	0	1	1	1
21	11686	10	10	10	0	1	1	1	1	0	0	1
22	11948	1	1	1	0	0	2	0	0	1	2	0
23	12038	4	4	4	0	1	1	0	0	0	1	1
24	12101	5	5	5	0	1	2	1	0	1	1	1
25	13559	2	2	2	0	0	3	1	1	0	2	1
26	13807	1	1	1	0	1	1	1	0	0	2	1
27	13855	11	11	11	0	1	1	1	1	0	0	1
28	13984	3	3	3	0	1	2	1	1	0	2	1
29	14047	0	-	0	0	-	1	1	-	0	1	1
30	14118	6	6	6	1	1	2	1	1	1	1	1
31	14193	5	5	5	0	1	1	0	0	0	1	1
32	16041	4	4	4	0	1	2	1	1	1	2	1
33	16176	12	12	12	0	1	1	1	1	0	0	1
34	16276	7	7	7	0	1	2	1	1	1	1	1
35	16525	6	6	6	0	1	3	0	0	0	2	1
36	17544	2	2	2	0	0	2	1	0	0	2	1
37	18559	8	8	8	0	1	2	1	1	0	1	1
38	18640	13	13	13	0	1	1	1	1	0	0	1
39	19493	7	7	7	0	1	3	0	0	2	2	1

Table 3.3: *Nodal variables of the tophat model in Step 2.*

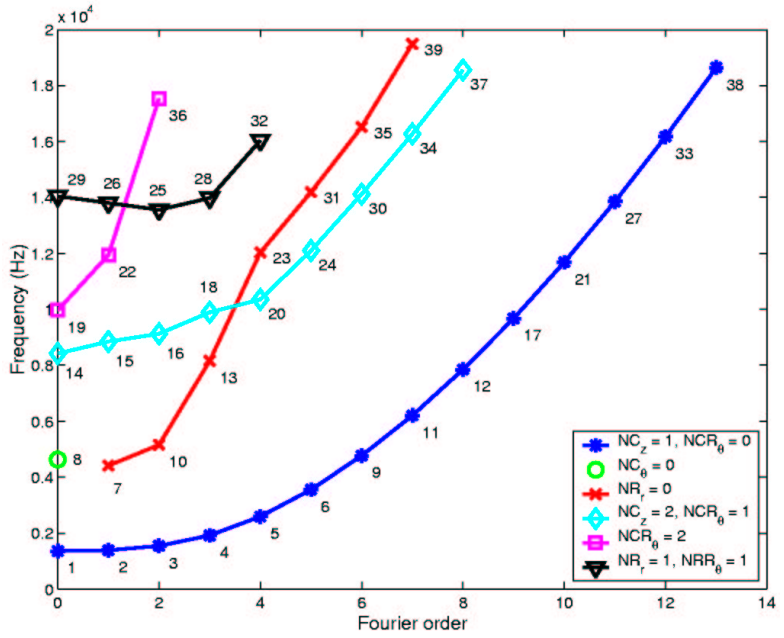

(a) Natural frequency as a function of Fourier order for Step 2

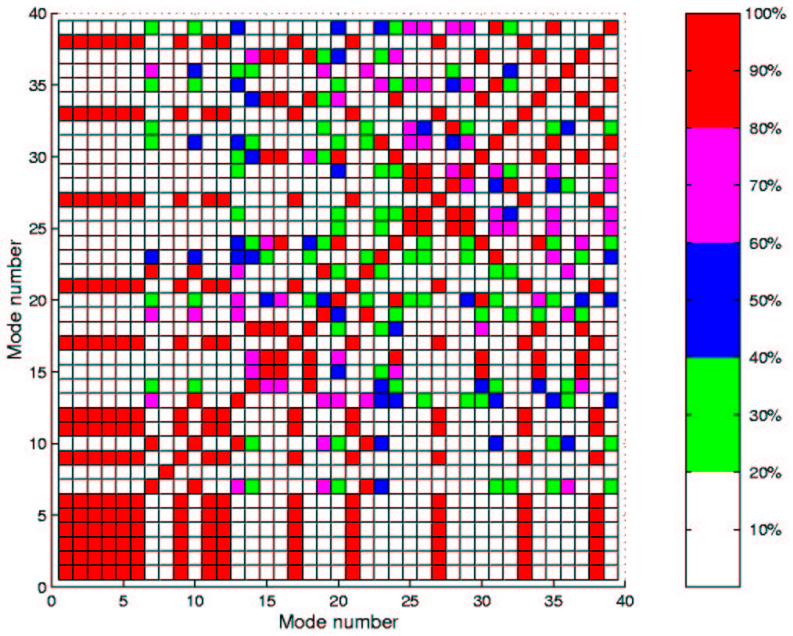

(b) AutoMAC of the cross-section of the tophat model for Step 2

Figure 3.16: *Mode classification for the tophat model with the cylinder length of 0.06 m (Step 2).*

Mode number	Frequency (Hz)	ND_r	ND_θ	ND_z	NC_r	NC_θ	NC_z	NR_r	NR_θ	NR_z	NCR_θ	NRR_θ
1	01357	0	-	0	0	-	1	1	-	0	0	1
2	01379	1	1	1	0	0	1	1	0	0	0	1
3	01529	2	2	2	0	0	1	1	1	0	0	1
4	01897	3	3	3	0	0	1	1	1	0	0	1
5	02583	4	4	4	0	0	1	1	1	0	0	1
6	03390	1	1	1	0	0	1	0	0	0	1	0
7	03554	5	5	5	0	1	1	1	1	0	0	1
8	03822	-	0	-	-	0	-	-	0	-	-	-
9	04027	2	2	2	0	0	0	0	0	0	1	1
10	04769	6	6	6	0	1	1	1	1	0	0	1
11	06207	7	7	7	0	1	1	1	1	0	0	1
12	06302	3	3	3	0	1	2	0	0	1	1	1
13	07783	4	4	4	0	1	2	0	0	1	1	1
14	07849	8	8	8	0	1	1	1	1	0	0	1
15	08213	0	-	0	0	-	1	2	-	0	1	2
16	08288	2	2	2	0	0	1	1	1	0	1	1
17	08520	1	1	1	0	0	1	1	0	0	1	1
18	09407	3	3	3	0	1	1	1	1	0	1	1
19	09680	9	9	9	0	1	1	1	1	0	0	1
20	09838	0	-	0	0	-	1	1	-	0	2	2
21	09873	5	5	5	0	1	2	0	0	1	1	1
22	10193	2	2	2	0	0	2	1	1	0	1	2
23	10690	3	3	3	0	1	2	1	1	0	1	2
24	10874	1	1	1	0	0	1	1	1	0	2	2
25	11439	4	4	4	0	1	2	2	2	0	1	2
26	11686	10	10	10	0	1	1	1	1	0	0	1
27	11765	0	-	0	0	-	2	0	-	0	1	1
28	11914	1	1	1	0	0	1	1	1	0	2	0
29	12680	6	6	6	0	1	2	0	1	1	1	1
30	12881	5	5	5	0	1	2	2	2	0	1	2
31	13241	4	4	4	0	1	1	1	1	0	1	2
32	13855	11	11	11	0	1	1	1	1	0	0	1
33	14631	6	6	6	0	1	2	2	2	1	1	2
34	15027	1	1	1	0	1	2	2	1	0	1	2
35	15586	2	2	2	0	0	3	2	2	0	2	2
36	15739	0	-	0	0	-	2	2	-	0	1	3
37	15881	7	7	7	0	1	2	0	1	1	1	1
38	15991	1	1	1	0	0	2	2	2	0	2	2
39	15998	3	3	3	0	1	3	2	2	1	2	2
40	16109	0	-	0	0	-	3	2	-	0	2	2

Continued on next page

Mode number	Frequency (Hz)	ND_r	ND_θ	ND_z	NC_r	NC_θ	NC_z	NR_r	NR_θ	NR_z	NCR_θ	NRR_θ
41	16176	12	12	12	0	1	1	1	1	0	0	1
42	16438	5	5	5	0	1	1	1	1	0	1	2
43	16650	-	0	-	-	1	-	-	0	-	-	-
44	16852	7	7	7	0	1	2	1	0	2	1	2
45	17396	2	2	2	0	0	2	2	1	0	1	2
46	17410	4	4	4	0	1	2	2	2	0	2	2
47	18122	2	2	2	1	1	2	2	1	0	1	3
48	18640	13	13	13	0	1	1	1	1	0	0	1
49	19248	6	6	6	0	1	1	1	1	0	1	2

Table 3.4: *Nodal variables of the tophat model in Step 3.*

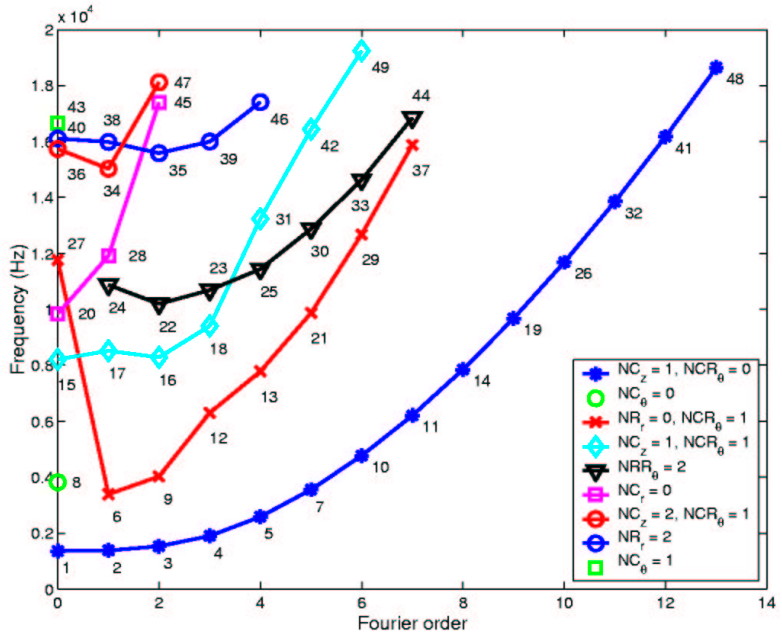

(a) Natural frequency as a function of Fourier order for Step 3

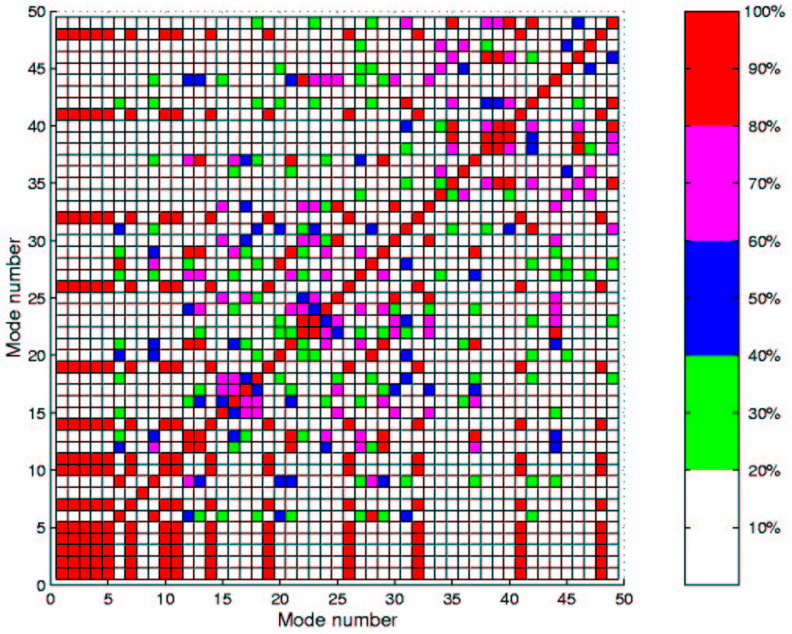

(b) AutoMAC of the cross-section of the tophat model for Step 3

Figure 3.17: *Mode classification for the tophat model with the cylinder length of 0.09 m (Step 3).*

3.4.6 Discussion

3.4.6.1 The need for the rotation-type nodal variables for mode identification

In some cases, it might not be possible to distinguish vibration modes of "tophat-like" structures uniquely by specifying only the translation-type nodal variables. For example, considering modes 25 and 46 of the tophat model in Step 3, it can be seen from Table 3.4 that both modes share the same set of the translation-type nodal variables and, thus, they cannot be distinguished from one another using only the translation-type nodal variables. However, careful examination on the two mode shapes suggests that the cylinder part of mode 25 vibrates in an opposite phase to that of mode 46, as shown in Figure 3.18. This phase difference arises because mode 46 has an extra rotation-type nodal circle, NCR_θ, near the connection between the disc and the cylinder, as marked by the blue circle in Figure 3.18 (b). In this case, modes 25 and 46 can be separated from one another if the rotation-type nodal variables are specified. In general, it is necessary to identify the rotation-type nodal variables as well as the translation-type in order to distinguish vibration modes of "tophat-like" structures uniquely.

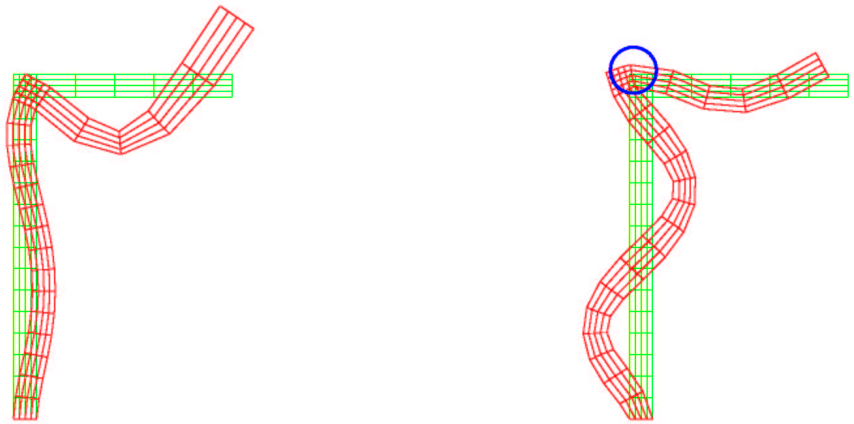

(a) Mode 25 (b) Mode 46

Figure 3.18: *Cross-sectional view of (a) mode 25 and (b) mode 46 of the tophat model in Step 3*

Bae *et al.* [63] have also noticed the existence of mode pairs similar to modes 25 and 46. According to their definition, mode pairs of this type have similar transverse displacements over the disc part but different phase relationships between the disc and the cylinder parts. The first mode of the mode pair, which has the disc and the cylinder parts moving in the same direction, is called the "in-phase" mode, and the second mode of the pair, which has the disc and the cylinder parts moving in the opposite directions is called the "out-of-phase" mode. This type of identification is plausible only for low-frequency modes, such as those given in their examples. For high-frequency modes, where mode shapes become very complex, as illustrated by modes 25 and 46 in Figure 3.18, it becomes less clear as to which points should be taken as the reference for phase determination and, hence, the separation of this type of mode pair according to phase relationships is not rigorous. Thus, the use of nodal variables proposed here provides a better and more rigorous way of uniquely distinguishing vibration modes of three-dimensional "tophat-like" structures.

3.4.6.2 The use of AutoMAC diagrams in mode classification

The classification of vibration modes according to the variation of mode shapes along the r and z-directions is more difficult than that according to the variation in the θ-direction (i.e. Fourier order) because of the physical complexity of the structure. To assist the classification of vibration modes according to their similarity in the $r-z$ plane, the AutoMAC diagram of the cross-section for each of the tophat models is calculated, as shown in Figures 3.15 (b), 3.16 (b) and 3.17 (b). If the variation along the r and z-directions of any 2 vibration modes with different Fourier orders is similar, the value of the AutoMAC should be close to 100% and, hence, the two modes are deemed to belong to the same "family". For example, it is clear from the AutoMAC diagram for Step 1 that modes 1, 2, 3, 4, 5, 6, 7, 9, 12, 15, 21, 24, 27 and 31 all belong to the same family.

However, the AutoMAC can sometimes mislead the classification and so particular care must be taken when using it. For example, considering the vibration modes in

Step 2, it is clear from the AutoMAC diagram in Figure 3.16 (b) that, for modes with Fourier orders less than 4, modes 7, 10 and 13 should belong to the same family whereas modes 14, 15, 16 and 18 belong to another family. As for modes with Fourier orders higher than or equal to 4, modes 20, 24, 30, 34 and 37 belong to the same family whereas modes 23, 31, 35 and 39 belong to another family. The remaining difficulty is how to join the families with Fourier orders less than 4 to those with Fourier orders higher than or equal to 4. If only the correlations between the end points of each family are considered, one might mistakenly classify modes 7, 10, 13, 20, 24, 30, 34 and 37 into the same family and modes 14, 15, 16, 18, 23 31, 35 and 39 into another family. However, the AutoMAC diagram also indicates that modes 7 and 10 do not correlate at all with modes 30, 34 and 37 although they do show some correlation with modes 31, 35 and 39. As a result, a better classification is to group modes 7, 10, 13, 23, 31, 35 and 39 into the same family and modes 14, 15, 16, 18, 20, 24, 30, 34 and 37 into another family, as shown in Figure 3.16 (a).

As a final remark, vibration modes which belong to the same family may behave in a similar way if some certain modifications are made to the design of brake discs. For example, from the case studies conducted in this chapter, the change in the cylinder length has very little effect on all the natural frequencies of the modes which belong to the first family of each tophat model (as indicated by the blue lines on Figures 3.15 (a), 3.16 (a), 3.17 (a)). Thus, by understanding the vibration characteristics of the "tophat-like" structures, mode classification might become a useful tool to assist brake disc designers for necessary modifications to brake discs to avoid squeal.

3.4.6.3 The minimum number of nodal variables for mode identification

In general, to identify vibration modes of three-dimensional "tophat-like" structures, all of the 11 nodal variables are required. However, when considering relatively low-frequency modes - say, the first 40 - it is possible to reduce the number of essential nodal variables in the identification method. A detailed study on the mode shapes shows that the nodal variables can be categorised into 2 sets: (i) primary and (ii)

secondary. The primary set consists of the nodal variables which are essential for distinguishing the low-frequency modes from one another. As a result, if one of the nodal variables in the primary set is omitted, vibration modes cannot be distinguished uniquely. On the other hand, the nodal variables in the secondary set are not critical for distinguishing low-frequency modes and can be omitted without losing the uniqueness in the identification process.

The question of how many and which nodal variables should belong to the primary set depends entirely on the physical dimensions of the structures. For example, for a tophat disc with a short cylinder section, i.e. approaching a plain disc, the primary set would consist of nodal variables of the "nodal diameter" and "nodal circle" types. On the other hand, if the tophat disc has a long connecting cylinder, the primary set would consist of nodal variables of the "nodal diameter" and "nodal ring" types.

From the three tophat models described in Section 3.4.2, it has been found that the primary set consists of 6 nodal variables which are Fourier order, NC_θ, NC_z, NR_r, NCR_θ and NRR_θ. By specifying only these 6 nodal variables, the first 40 modes of the three tophat models in Section 3.4.2 can be distinguished uniquely.

3.5 Conclusions

In this chapter, a systematic method for mode identification of three-dimensional "tophat-like" structures using nodal variables has been introduced. There are, in total, 11 nodal variables - 9 associated with zero translation and 2 associated with zero rotation - required to distinguish vibration modes of "tophat-like" discs. The study shows, however, that it is possible to reduce the number of essential nodal variables in the identification process when considering low-frequency modes - the first 40 modes, say. For the three examples given in this chapter, it has been found that only 6 nodal variables are critical to the mode identification process and they are Fourier order, NC_θ, NC_z, NR_r, NCR_θ and NRR_θ. Moreover, the work also shows a systematic method for mode classification of three-dimensional "tophat-like" structures according to their similarity both in the $r-\theta$ and $r-z$ planes with the aid of the AutoMAC diagram.

Chapter 4

Dynamics of linear pin-on-disc systems

4.1 Overview

As described previously in Chapter 1, most of the past theoretical studies of brake squeal can be classified into 2 extreme categories: (i) qualitative models, and (ii) detailed models. The qualitative models usually come in the form of lumped-mass-parameter models with a small number of degrees-of-freedom (typically, between 2 to 8 DOFs) and are used to study the basic mechanisms involved in squeal generation. The detailed models, on the other hand, aim to predict squeal characteristics as accurately as possible. Thus, it becomes essential for the detailed models to capture the precise geometries and features of the actual brake assembly. As a result, most of the detailed models consist of a large number of degrees-of-freedom and are normally handled by commercial Finite Element packages.

Although a number of squeal phenomena, such as the lock-in characteristic, can be studied by the qualitative models, many others have been omitted in the past because the qualitative models are not realistic enough. In contrast, the detailed models, which have realistic components, may have too many parameters and, hence, might be too time-consuming to conduct useful parameter studies. Due to these drawbacks, it is

deemed necessary to bridge the gap between the two extremes of the theoretical studies so that the basic understanding gained from the qualitative models can be conveyed correctly and effectively to the large-scale models. Thus, it is appropriate to create an intermediate model which can exhibit the multi-natural frequency feature due to the flexibility of real components but is simple enough to be used for qualitative studies.

In general, a real brake assembly consists of many components, and this makes the theoretical modelling difficult and time-consuming. However, the precise geometry of the actual brake assembly is not critical for studying general squeal characteristics. Thus, a pin-on-disc system, which can produce similar squeal behaviour but has a relatively simple geometry, is chosen as an intermediate step between the simple qualitative models and the complex detailed models. The main advantage of the pin-on-disc system is that the dynamics of its components can be controlled more easily than those of the actual brake assembly. Hence, the validation between its theoretical model and the experimental measurements can be done easily.

From a theoretical perspective, there are two major areas involved in the pin-on-disc modelling: (i) the component modelling, and (ii) the interface modelling. The first part involves structural modelling of each individual component to obtain their modal properties - namely the natural frequencies and mode shapes. This step can be accomplished straightforwardly using the Finite Element (FE) method. The second part concerns the modelling of the friction and contact properties at the interface between the pin and the disc. Friction is a difficult subject and deserves a detailed study on its own right. In the past, many researchers have developed very sophisticated friction models (e.g. Allgaier *et al.* [64] or Pilipchuk *et al.* [17]). Most of these advanced friction models normally lead to non-linear systems, which are usually solved by time integration or the Harmonic Balance method. Both of these could be very time consuming and, hence, are not suitable for parameter studies. However, if only the onset of instability (i.e. eigensolutions) is of primary interest, previous studies have shown that, when the pin and the disc are in a sliding contact and the coefficient of friction is assumed to be constant, a linear model can be derived. Although squeal

is known to be a highly non-linear phenomenon, a linear model would provide some crucial information about the onset of squeal behaviour.

Thus, a linear pin-on-disc model is constructed and studied in this chapter. The pin and the disc are modelled using the Finite Element method. The pin is assumed to make a line contact with the disc along the radial direction. The friction between the two components is assumed to obey Amonton's friction law. In addition to friction forces, a number of contact elements, which consist of linear springs and dashpots, are used to couple the pin and the disc in both the normal and tangential directions. These contact elements would represent the stiffness and damping of the asperities at the contact points. The onset of instability can then be determined from the eigensolution of the combined system. Parameter studies are performed in order to find the ranges in which the instability is most likely to occur for each parameter. Finally, discussions of the validity of the linear pin-on-disc model and a possible explanation of squeal generation are given. Note: the work presented in this chapter is an extension of the study conducted by Tuchinda *et al.* [65, 66].

4.2 Modelling

To study the squeal phenomenon, a pin-on-disc rig has been constructed, as shown in Figure 4.1. The disc of a uniform thickness is attached to the front end of the shaft by mean of a taper fit provided on both components. They are locked together using a screw located on the axis of the shaft. The shaft itself is supported on the platform by two ball bearings. The disc and the shaft are driven by a motor through a pulley-belt system located at the back end of the shaft. A pin of a uniform cross-sectional area is held in position by a four-jaw chuck which is mounted onto a rail system. The pin is kept in contact with the disc by the aid of a dead weight and pulley system (refer to Figure 6.6 in Chapter 6). The pin and the disc are both made of mild steel.

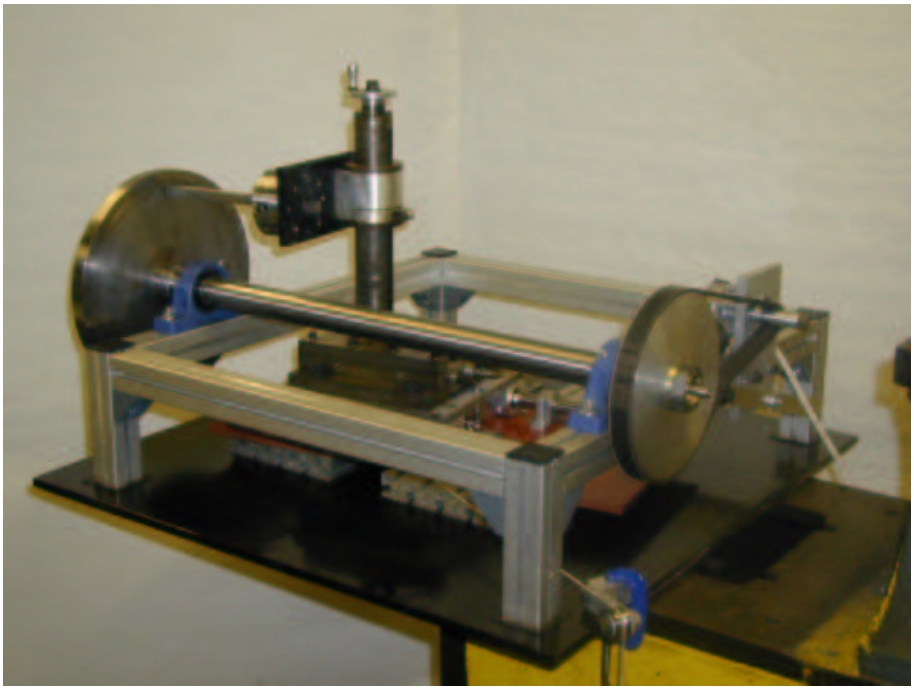

Figure 4.1: *The IC pin-on-disc rig.*

In the following modelling process, the pin and the disc will first be modelled separately using the Finite Element (FE) method to obtain their modal properties - namely, mode shapes and natural frequencies. By considering forces and displacements at the interface between the pin and the disc, the two components can then be coupled together. Finally, the stability and instability regimes can be determined from the eigensolutions of the combined pin-on-disc model.

4.2.1 Modelling of the disc

The FE model of the disc shown in Figure 4.2 assumes it to have a uniform thickness and to be perfectly tuned. For simplicity, the inner bore of the disc is assumed to be fully clamped and the outer rim to be free. The elements used in the FE model of the disc are 20-node brick elements - 16 elements along the radial direction, 120 elements along the circumferential direction and 4 elements through the thickness.

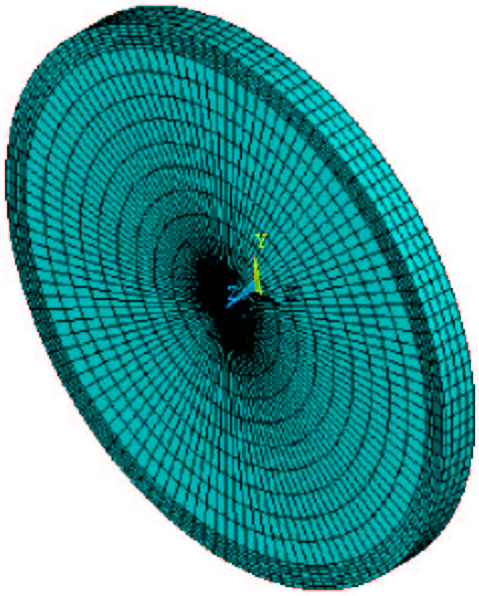

Figure 4.2: *The FE model of the disc.*

The general form of the governing equations of motion for the disc subjected to external forces in the physical coordinates can be written as follows:

$$[M_d]\,\{\ddot{x}_d\} + [K_d]\,\{x_d\} = \{F_d\}, \tag{4.1}$$

where $[M_d]$ is the mass matrix of the disc, $[K_d]$ the stiffness matrix of the disc, $\{F_d\}$ the vector of applied forces and $\{x_d\}$ the physical coordinates of the disc. Subscript d refers to "disc".

It is generally more convenient to work in generalised coordinates. So, by pre-multiplying equation (4.1) by the transpose of the mass-normalised mode shape matrix, $[\Phi_d]^T$, and substituting the physical coordinates, $\{x_d\}$, by the generalised coordinates, $\{q_d\}$, equation (4.1) can be rewritten as:

$$[\grave{}\, I \,\acute{}]\{\ddot{q}_d\} + [\grave{}\, \omega_d^2 \,\acute{}]\,\{q_d\} = [\Phi_d]^T\,\{F_d\}, \tag{4.2}$$

where

$$\{x_d\} = [\Phi_d]\{q_d\}. \tag{4.3}$$

4.2.2 Modelling of the pin

The pin is modelled as a uniform cross-section beam. The elements used in the FE model of the pin are also 20-node-brick elements - 38 elements in the lengthwise direction, 6 elements across the width and 6 elements through the thickness, as shown in Figure 4.3. According to the experimental setup described in Chapters 6 and 7, one end of the pin is clamped by a four-jaw chuck. A close-up of the clamped end in Figure 4.4 (a) shows that the chuck only makes four line-contacts with the pin. Hence, the boundary conditions of the pin in the FE model are set such that there is no motion in the direction normal to the surface of the pin at all nodes along the four contact lines, as shown in Figure 4.4 (b). However, the pin is free to move in the axial direction. It should also be noted that the mass of the chuck has been ignored in this model.

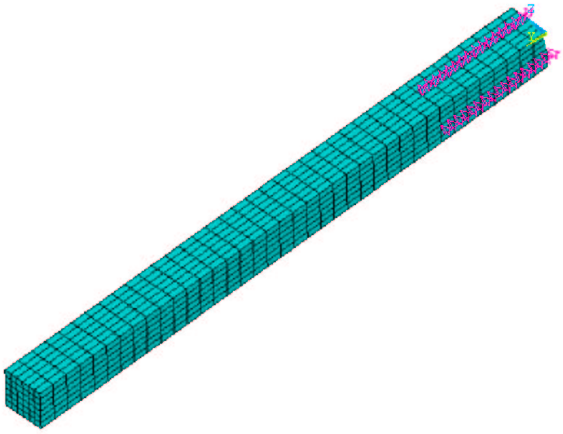

Figure 4.3: *The FE model of the pin.*

Similarly to the analysis of the disc, the equations of motion of the pin can be written as:

$$[M_p]\{\ddot{x}_p\} + [K_p]\{x_p\} = \{F_p\}, \tag{4.4}$$

where $[M_p]$ is the mass matrix for the pin, $[K_p]$ the stiffness matrix of the pin, $\{F_p\}$ the vector of applied forces and $\{x_p\}$ the physical coordinates of the pin. Subscript p refers to "pin". The corresponding equations of motion in the generalised coordinates

can be written as:

$$[\grave{} I \backprime]\{\ddot{q}_p\} + [\grave{} \omega_p^2 \backprime]\,\{q_p\} = [\Phi_p]^T\,\{F_p\}, \tag{4.5}$$

where

$$\{x_p\} = [\Phi_p]\{q_p\}. \tag{4.6}$$

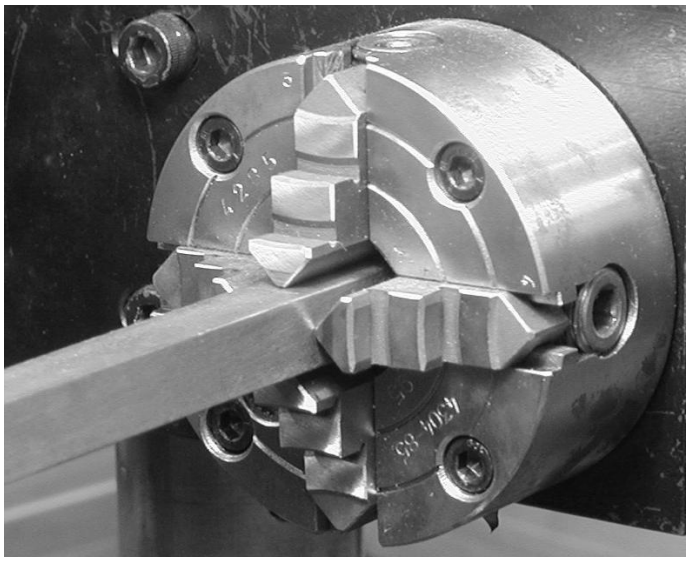

(a)

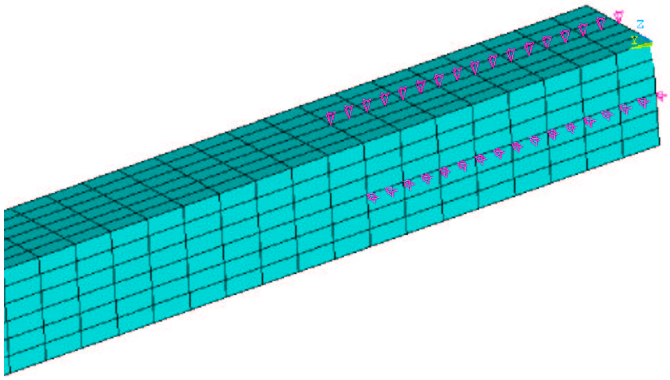

(b)

Figure 4.4: *Boundary conditions of the pin at the clamped end.*

4.2.3 Coupling between the pin and the disc

In this step, the pin and the disc are put together to form a pin-on-disc model, as shown in Figure 4.5. The model assumes that the pin makes a line contact with the disc along the radial direction. At this stage, the model also assumes that the friction force between the pin and the disc is proportional to the normal contact force and the coefficient of friction, μ, is constant and is not a function of the relative speed between the two surfaces. A more realistic friction model will be used in the next chapter when the limit-cycle characteristics are investigated. To keep the system linear, the model assumes further that the in-plane velocity of the pin does not exceed the disc rotational speed and, hence, there is no change in the direction of the friction force.

If the orientation of the pin is in the same sense as the rotation of the disc, the pin is said to be in the "leaning" position, as illustrated in Figure 4.5. On the other hand, if the the orientation of the pin opposes the rotation of the disc, the pin is said to be in the "digging" position. The angle of inclination, α, is defined as the angle between the pin and the disc axis and is positive when the pin is in the leaning position.

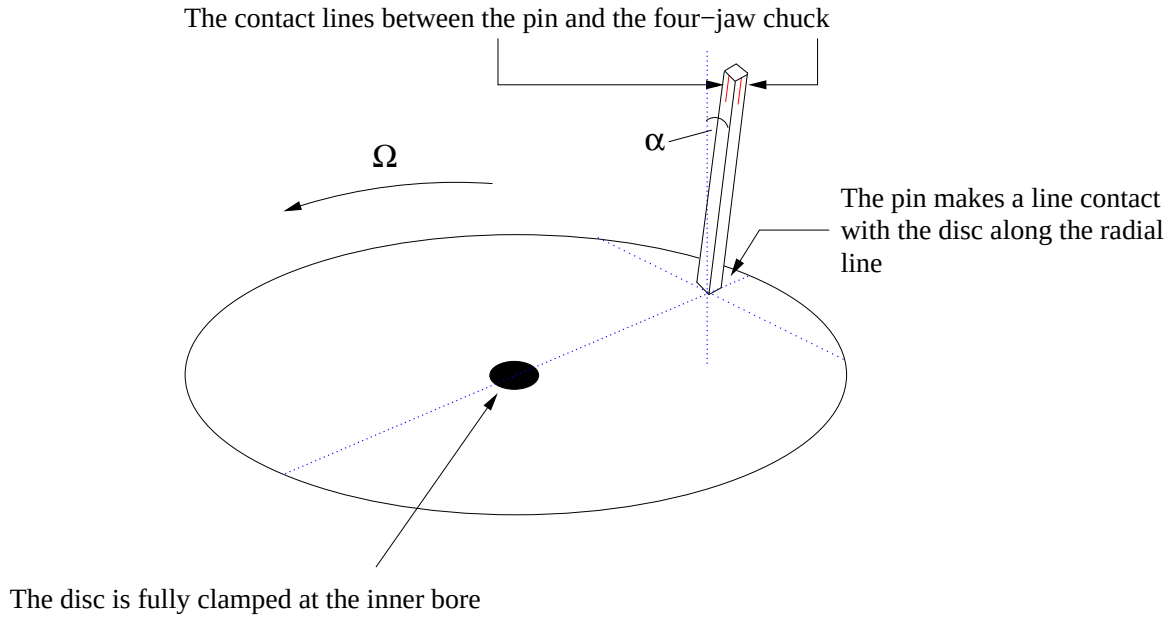

Figure 4.5: *The pin-on-disc model, showing the pin in the leaning position.*

Apart from friction forces, the pin and the disc are additionally coupled together by a number of linear spring-dashpot elements which are used to represent the contact stiffness and damping between the two surfaces. At each contact node, two spring-dashpot elements are used to connect the pin and the disc, as illustrated in Figure 4.6. The first spring-dashpot element couples the two components in the direction normal to the disc surface whereas the second spring-dashpot element couples the two components in the tangential direction. For simplicity, the model assumes that the pin and the disc are in contact with the spring-dashpot elements at all times.

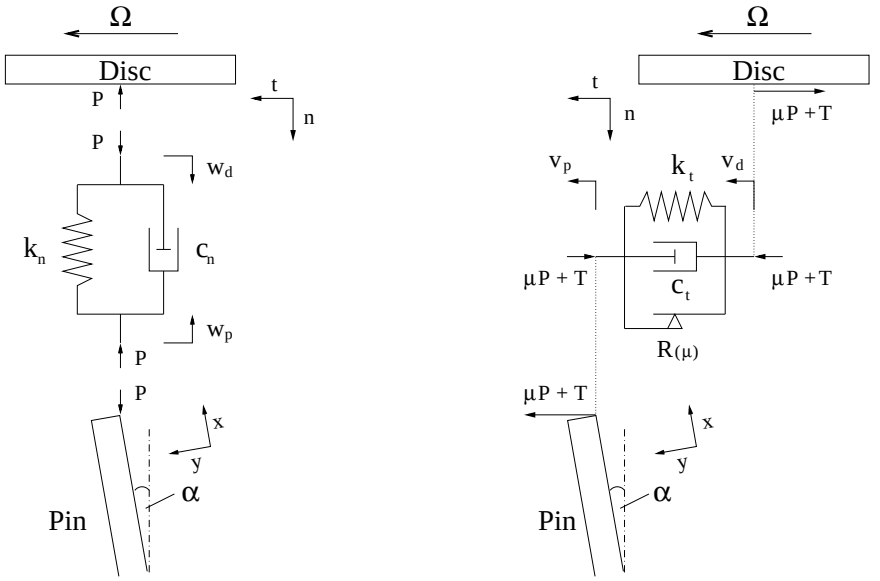

(a) Forces in the direction normal to the disc surface

(b) Forces in the direction tangential to the disc surface

Figure 4.6: *The force system at the interface between the pin and the disc in the: (a) normal direction, and (b) tangential direction.*

Figures 4.6 (a) and (b) illustrate the contact and friction forces in the directions normal and tangential to the disc surface, respectively. By considering the free body diagrams of the spring-dashpot elements, internal forces P and T in the normal and tangential directions, respectively, can be expressed in terms of disc and pin displacements as follows:

$$ {}_hP = {}_hk_n({}_hw_d + {}_hw_p) + {}_hc_n({}_h\dot{w}_d + {}_h\dot{w}_p), \tag{4.7} $$

$$ {}_hT = {}_hk_t({}_hv_d - {}_hv_p) + {}_hc_t({}_h\dot{v}_d - {}_h\dot{v}_p), \tag{4.8} $$

where k is the contact stiffness, c the contact damping, w the displacement in the direction normal to the disc surface, and v the displacement in the tangential direction to the disc surface. The left-hand subscript h indicates that the forces and displacements are considered at the h^{th} contact node. The right-hand subscripts d, p, n and t refer to "disc", "pin", "normal direction" and "tangential direction", respectively.

To define the disc and pin displacements at the points of contact in terms of generalised coordinates, it is easier if the relevant components of the mode shape vectors are re-arranged in the following form:

$$ {}_h\{\Phi_d^t\} = \begin{Bmatrix} {}_1\Phi_d^t \\ \vdots \\ {}_i\Phi_d^t \end{Bmatrix}_h, \qquad {}_h\{\Phi_d^n\} = \begin{Bmatrix} {}_1\Phi_d^n \\ \vdots \\ {}_i\Phi_d^n \end{Bmatrix}_h, $$

$$ {}_h\{\Phi_p^x\} = \begin{Bmatrix} {}_1\Phi_p^x \\ \vdots \\ {}_j\Phi_p^x \end{Bmatrix}_h, \qquad {}_h\{\Phi_p^y\} = \begin{Bmatrix} {}_1\Phi_p^y \\ \vdots \\ {}_j\Phi_p^y \end{Bmatrix}_h, \tag{4.9} $$

where subscripts i and j denote the numbers of the original disc and pin modes included in the pin-on-disc model, respectively. Thus, the displacements of the pin and the disc at the contact points can be expressed in terms of generalised coordinates as follows:

$$
\begin{aligned}
{}_h w_d &= {}_h\{\Phi_d^n\}^T\{q_d\},\\
{}_h w_p &= \left\{{}_h\{\Phi_p^x\}\cos\alpha - {}_h\{\Phi_p^y\}\sin\alpha\right\}^T\{q_p\},\\
{}_h v_d &= {}_h\{\Phi_d^t\}^T\{q_d\},\\
{}_h v_p &= \left\{{}_h\{\Phi_p^x\}\sin\alpha + {}_h\{\Phi_p^y\}\cos\alpha\right\}^T\{q_p\}.
\end{aligned} \tag{4.10}
$$

By considering the contact forces as well as the friction forces, the explicit forms of the applied forces, $\{F_d\}$ and $\{F_p\}$, in equations (4.2) and (4.5) can be expressed in terms of displacements at the contact points as follows:

$$
\{F_d\} = \begin{Bmatrix} 0\\ \vdots\\ 0\\ {}_1f_t\\ {}_1f_n\\ {}_2f_t\\ {}_2f_n\\ \vdots\\ {}_hf_t\\ {}_hf_n\\ 0\\ \vdots\\ 0 \end{Bmatrix}, \qquad \text{and} \qquad \{F_p\} = \begin{Bmatrix} 0\\ \vdots\\ 0\\ {}_1f_x\\ {}_1f_y\\ {}_2f_x\\ {}_2f_y\\ \vdots\\ {}_hf_x\\ {}_hf_y\\ 0\\ \vdots\\ 0 \end{Bmatrix}, \tag{4.11}
$$

where

$$
\begin{aligned}
{}_hf_n &= -{}_hk_n({}_hw_d + {}_hw_p) - {}_hc_n({}_h\dot{w}_d + {}_h\dot{w}_p), && (4.12)\\
{}_hf_t &= -\mu_h k_n({}_hw_d + {}_hw_p) - \mu_h c_n({}_h\dot{w}_d + {}_h\dot{w}_p)\\
&\quad -{}_hk_t({}_hv_d - {}_hv_p) - {}_hc_t({}_h\dot{v}_d - {}_h\dot{v}_p), && (4.13)\\
{}_hf_x &= c_1\{{}_hk_n({}_hw_d + {}_hw_p) + {}_hc_n({}_h\dot{w}_d + {}_h\dot{w}_p)\}\\
&\quad +{}_hk_t({}_hv_d - {}_hv_p)\sin\alpha + {}_hc_t({}_h\dot{v}_d - {}_h\dot{v}_p)\sin\alpha, && (4.14)\\
{}_hf_y &= c_2\{{}_hk_n({}_hw_d + {}_hw_p) + {}_hc_n({}_h\dot{w}_d + {}_h\dot{w}_p)\}\\
&\quad +{}_hk_t({}_hv_d - {}_hv_p)\cos\alpha + {}_hc_t({}_h\dot{v}_d - {}_h\dot{v}_p)\cos\alpha, && (4.15)\\
c_1 &= \mu\sin\alpha - \cos\alpha, && (4.16)\\
c_2 &= \mu\cos\alpha + \sin\alpha. && (4.17)
\end{aligned}
$$

Note: the present study is concerned only with the onset of instability of the combined system (i.e. the eigensolutions) and, hence, all the static forces can be neglected from the pin-on-disc model. Although the static forces do not appear explicitly in the equations of motion, their influence could still be present via other system parameters. For example, Thomas and Sayles [67] suggested that the contact stiffness in the normal direction is linearly proportional to the normal static load. Hence, by varying the contact stiffness, the effect of the static load on the stability of the system can be studied.

By defining a new set of generalised coordinates, $\{q_c\}$, and substituting equations (4.10) and (4.11) into equations (4.2) and (4.5), the governing equations of motion of the combined system can be written as:

$$[\,I\,]\,\{\ddot{q}_c\} + \begin{bmatrix} [\,\omega_d^2\,] & 0 \\ 0 & [\,\omega_p^2\,] \end{bmatrix} \{q_c\} = \sum_{h=1}^{\infty} \Big[{}_h k_n \; {}_h[G] + {}_h k_t \; {}_h[H] \Big] \{q_c\} + \sum_{h=1}^{\infty} \Big[{}_h c_n \; {}_h[G] + {}_h c_t \; {}_h[H] \Big] \{\dot{q}_c\}, \tag{4.18}$$

where

$$\{q_c\} = \begin{Bmatrix} \{q_d\} \\ \{q_p\} \end{Bmatrix}. \tag{4.19}$$

The explicit forms of matrices ${}_h[G]$ and ${}_h[H]$ can be written as follows:

$${}_h[G] = \begin{bmatrix} -\mu \;\; {}_h\{\Phi_d^t\} & - & {}_h\{\Phi_d^n\} \\ \\ c_1 \;\; {}_h\{\Phi_p^x\} & + \;\; c_2 & {}_h\{\Phi_p^y\} \end{bmatrix} \begin{bmatrix} {}_h\{\Phi_d^n\} \\ \\ {}_h\{\Phi_p^x\}\cos\alpha - {}_h\{\Phi_p^y\}\sin\alpha \end{bmatrix}^T, \tag{4.20}$$

and

$${}_h[H] = - \begin{bmatrix} -{}_h\{\Phi_d^t\} \\ \\ {}_h\{\Phi_p^x\}\sin\alpha + {}_h\{\Phi_p^y\}\cos\alpha \end{bmatrix} \begin{bmatrix} -{}_h\{\Phi_d^t\} \\ \\ {}_h\{\Phi_p^x\}\sin\alpha + {}_h\{\Phi_p^y\}\cos\alpha \end{bmatrix}^T. \tag{4.21}$$

Since all the matrices in equation (4.18) contain only constant coefficients, the standard state-space technique can be used to obtain the eigenvalues, λ, of the combined system. The combined system is considered to be unstable when the real part of at least one of the eigenvalues is positive.

4.3 Numerical simulations

Before embarking on intensive numerical simulations, the first stage is to find suitable material properties, e.g. density and Young's modulus, for the pin and disc. This can be done by comparing the predicted natural frequencies of the individual components from the FE calculations with the experimental data: refer to Chapters 6 and 7 for experimental setup and results. The comparisons suggested that the pin and disc should have the following material properties:

- Disc: $E = 212\ GPa$, $\rho = 8330\ kg/m^3$, and $\nu = 0.3$;
- Pin: $E = 241\ GPa$, $\rho = 7843\ kg/m^3$, and $\nu = 0.3$.

The numerical calculations in this section, unless stated otherwise, are conducted with the following conditions:

- the disc has the outer radius of 150 mm, the inner radius of 11.4 mm and the thickness of 20 mm;
- the pin has a square cross-sectional area of $13 \times 13\ mm^2$ and the length of 155 mm (measuring from the free end to the front end of the chuck);
- the vibration modes of the pin and the disc, which have their natural frequencies within the frequency range of 0 to 20 kHz, are included in the combined system (56 modes for the disc and 13 modes for the pin);
- the pin makes a line contact with the disc - 13 contact points equally spaced along the radial direction.

Apart from the modal properties of the pin and the disc - namely the natural frequencies and modal constants, equation (4.18) indicates that there are six other controlling parameters: (i) the coefficient of friction, μ, (ii) the angle of inclination, α, (iii) the contact stiffnesses, k_n and k_t and (iv) the contact damping coefficients, c_n and c_t. In the following parameter studies, the effects of these parameters on the instability of the combined system will be investigated systematically.

4.3.1 Case study A: The angle of inclination versus the normal contact stiffness

In this section, the angle of inclination, α, and the normal contact stiffness per unit length, $\hat{k}_n$, are the two main parameters that are varied. The angle of inclination is varied between -30 and +30 degrees and the normal contact stiffness per unit length is varied between 0 and 3 GN/m^2. The coefficient of friction, μ, and the tangential contact stiffness per unit length, $\hat{k}_t$, are kept constant at 0.15 and 40 MN/m^2, respectively. For simplicity, the contact damping in both the normal and tangential directions is assumed to be zero.

Figure 4.7 (a) shows the predicted squeal frequencies as functions of the angle of inclination and the normal contact stiffness per unit length. The corresponding positive real parts of the eigenvalues are shown in Figure 4.7 (b). From these calculations, the pin-on-disc model indicates two important features. First, it is shown that squeal can occur in both the leaning and digging positions. This result contradicts Earles' predictions [7], which stated that instability can only occur when the pin is in the digging-in positions (a necessary, but not sufficient, condition). The discrepancy between Earles' models and the current pin-on-disc model is due to the flexibility of the coupled components which will be discussed in Section 4.4.3. Second, squeal only occurs above a certain value of the normal contact stiffness. The precise value of this threshold depends also on the other system parameters. In the set of calculations shown on Figure 4.7, the critical normal contact stiffness per unit length is 1.25 GN/m^2.

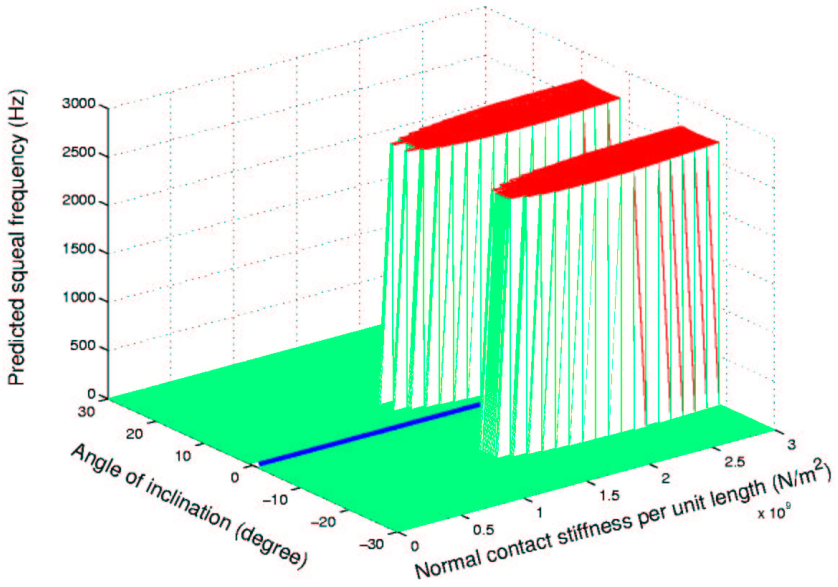

(a)

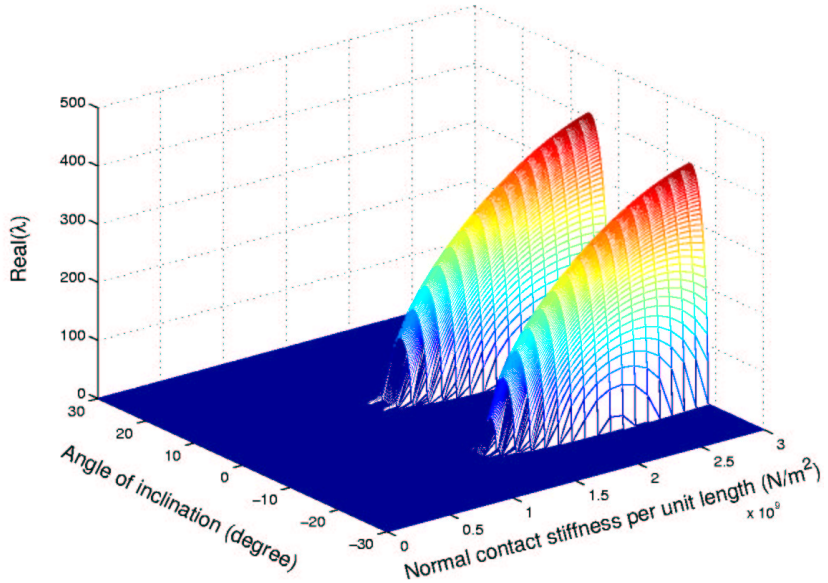

(b)

Figure 4.7: *Instability regimes as functions of the angle of inclination, α, and the normal contact stiffness per unit length, $\hat{k}_n$, (with $\mu = 0.15$ and $\hat{k}_t = 40\ MN/m^2$): (a) the predicted squeal frequencies, and (b) the real parts of the eigenvalues (positive values only).*

Having completed the parameter studies for the normal contact stiffness, it is now possible to compare the theoretical predictions against the experimental measurements. The objective here is to find a suitable normal contact stiffness for subsequent calculations. A slice cut through Figure 4.7 (a) at $\hat{k}_n = 2.4\ GN/m^2$ is compared with the experimental measurements, as shown in Figure 4.8. First, the experiments confirm that squeal can occur when the pin is in both the leaning and digging positions. Second, the majority of the predicted squeal frequencies are accurate to within 1 per cent of the measured frequencies. Hence, it may be concluded that the normal contact stiffness per unit length of the pin-on-disc system used in the experimental measurements has a value of 2.4 GN/m^2. The apparent disagreement between the prediction and the test data when the angle of inclination is at 4 degrees digging-in is discussed in Section 4.4.3.

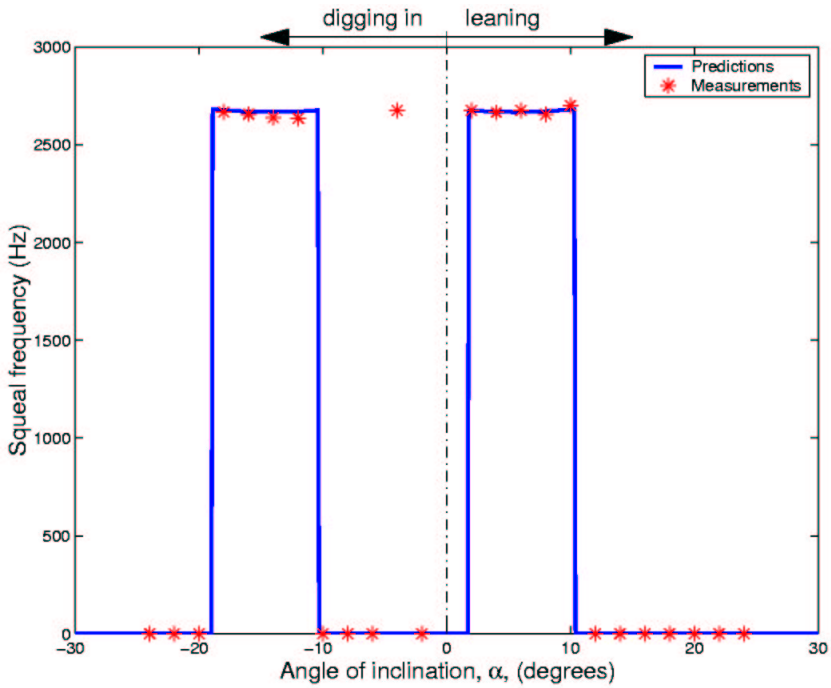

Figure 4.8: *Comparison of squeal frequencies between the theoretical predictions and the experimental measurements.*

4.3.2 Case study B: The normal contact stiffness versus the coefficient of friction

In this section, the normal contact stiffness per unit length, $\hat{k}_n$, and the coefficient of friction, μ, are the two main parameters that are varied. The normal contact stiffness per unit length is varied between 0 and 10 GN/m^2 and the coefficient of friction is varied between 0 and 0.5. The tangential contact stiffness per unit length, $\hat{k}_t$, and the angle of inclination, α, are kept constant at 40 MN/m^2 and 4 degrees in the leaning position, respectively. For simplicity, all of the damping coefficients are set to zero.

Figure 4.9 shows the eigenvalues of the combined system within the frequency range of 2500 to 3500 Hz as functions of the normal contact stiffness per unit length and the coefficient of friction. There are four vibration modes of the combined system lying within this frequency range and, for convenience, they will be referred to as modes 11, 12, 13 and 14 throughout this chapter. Mode 11 is dominated by the 3ND sine component of the original disc mode whereas mode 12 is dominated by the 3ND cosine component. Modes 13 and 14 are dominated by the second bending components of the original pin modes in the z- and y-directions, respectively.

In general, a vibration mode of the combined system will become unstable if the corresponding eigenvalue has a positive real part. Thus, Figure 4.9 (b), which shows only the positive real parts of the eigenvalues of the four modes described in Figure 4.9 (a), can be used to indicate the region of instability. The shape of Figure 4.9 (b) suggests that the region of instability will expand as the coefficient of friction and the normal contact stiffness increase.

A slice cut through Figure 4.9 (a) at $\hat{k}_n = 2.4$ GN/m^2 (indicated by the red dashed plane) reveals one of the squeal characteristics, the "lock-in", as shown in Figure 4.10 (a). In the case of initially-undamped systems, the onset of instability may occur when a pair of the eigenvalues of the combined system coincide. In this example, the vibration mode dominated by the second bending component of the original pin mode in the y-direction "locks into" the mode dominated by the 3ND cosine compo-

nent of the original disc mode. When there is no friction (i.e. $\mu = 0$), the two modes have two purely imaginary eigenvalues and, hence, are both asymptotically stable. As the coefficient of friction increases, the eigenvalues of the two modes move towards each other along the imaginary axis, as shown in Figure 4.10 (b). When the two eigenvalues coincide - referring to as the "lock-in" point, one of the two modes will become linearly unstable (i.e. the free-vibration response of this mode will grow linearly with time). However, if the coefficient of friction is increased beyond the lock-in point, the two eigenvalues will become complex: one of them will have a negative real part while the other has a positive real part. Modes corresponding to eigenvalues with positive real parts are considered to be exponentially unstable. On the other hand, modes corresponding to eigenvalues with negative real parts are damped, and thus stable.

If another slice cut through Figure 4.9 (a) is made at a constant coefficient of friction (indicated by the black dashed plane), a plot of natural frequencies as a function of the normal contact stiffness can be obtained, as illustrated in Figure 4.11 (a). In this case, the pin-on-disc model not only predicts "lock-in" behaviour but also a "lock-out" characteristic as well. The lock-out point occurs when the two eigenvalues of the damped mode and the unstable mode reunite on the imaginary axis, as shown in Figure 4.11 (b). If the normal contact stiffness is increased beyond the lock-out point, the two modes will become asymptotically stable again. The lock-in and lock-out characteristics together show that the combined system becomes unstable only for a specific range of the normal contact stiffness. The origin of the lock-in and lock-out characteristics will be discussed in Section 4.4.2.

As a final remark, although it cannot be proved analytically, a number of parameter studies suggest that the effect of the coefficient of friction on the squeal frequencies is different from that of the normal contact stiffness. Once the system reaches the lock-in point, increasing the coefficient of friction will usually reduce the squeal frequencies, as shown in Figure 4.10. On the other hand, increasing the normal contact stiffness will increase the squeal frequencies, as illustrated in Figure 4.11.

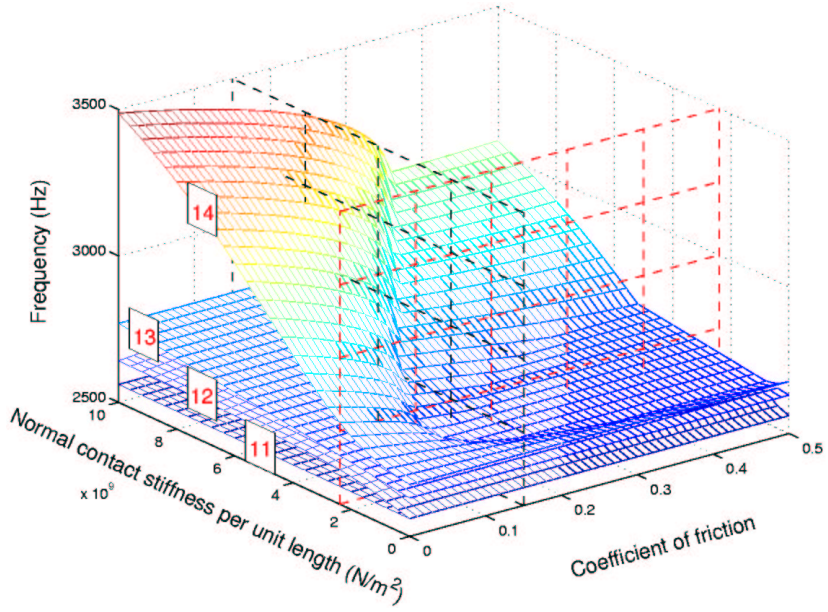

(a)

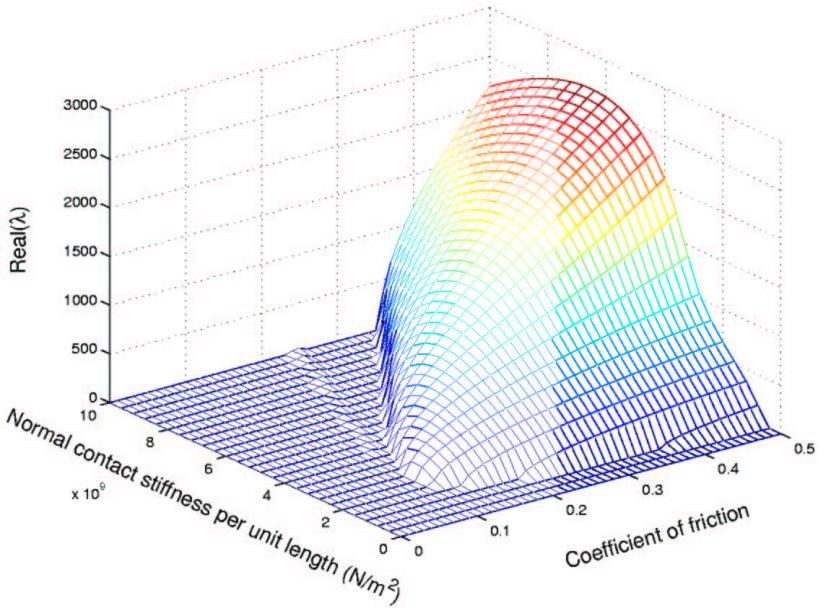

(b)

Figure 4.9: *Eigenvalues of the combined system as functions of the normal contact stiffness per unit length, $\hat{k}_n$, and the coefficient of friction, μ, (with $\alpha = 4°$ and $\hat{k}_t = 40\ MN/m^2$): (a) the natural frequencies, and (b) the real parts of the eigenvalues (positive values only).*

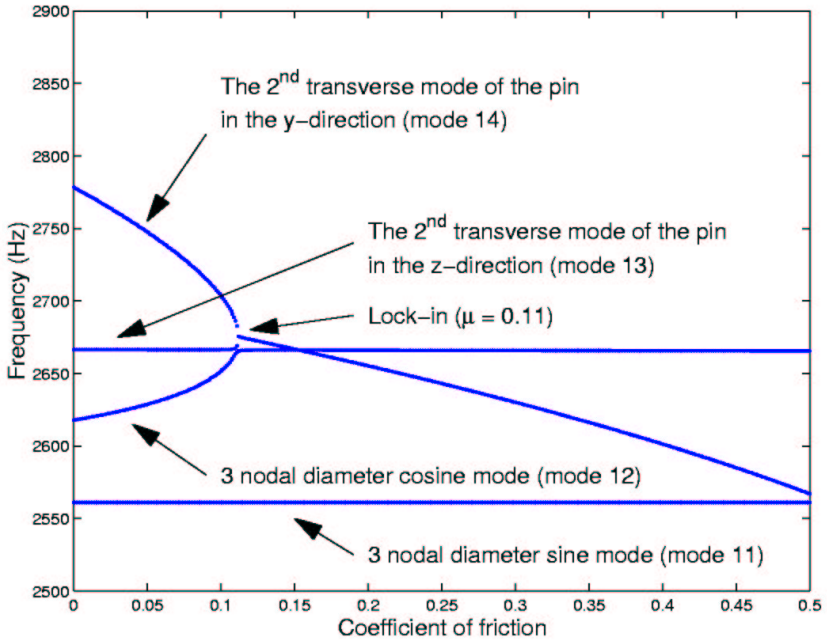

(a) Natural frequencies as a function of the coefficient of friction.

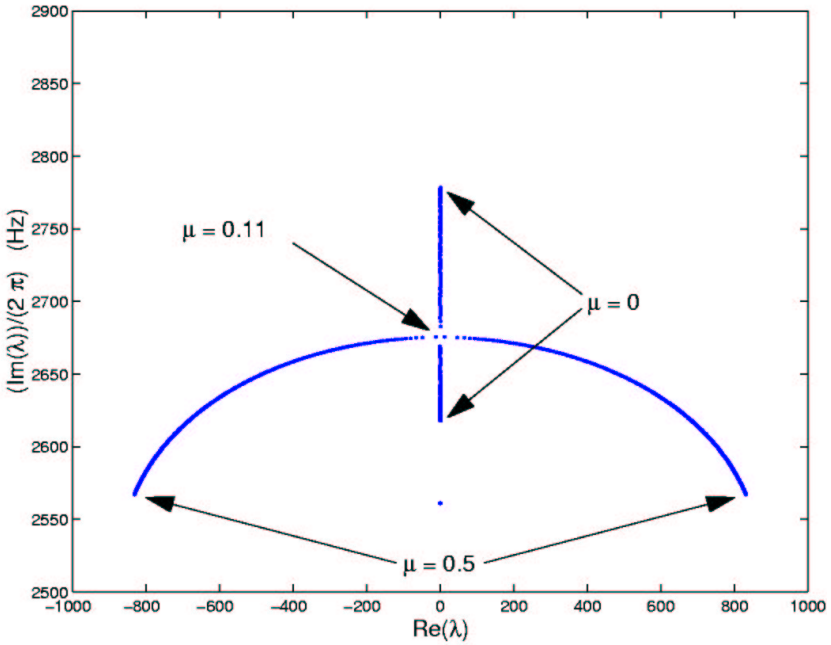

(b) Eigenvalues on the complex plane

Figure 4.10: *Eigenvalues of the combined system as a function of the coefficient of friction ($\hat{k}_n = 2.4\ GN/m^2$, $\alpha = 4°$, and $\hat{k}_t = 0.04\ GN/m^2$).*

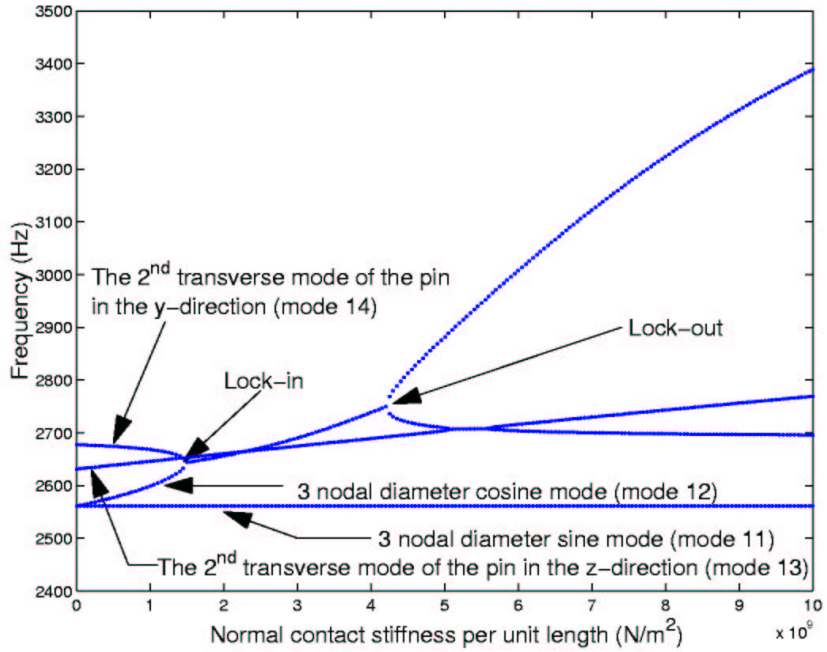

(a) "Lock-in" and "Lock-out" characteristics.

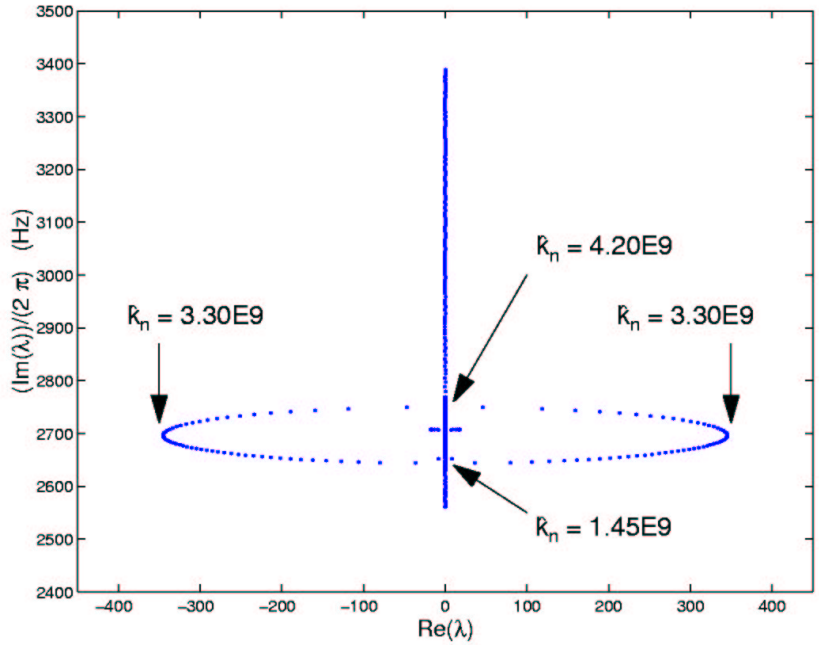

(b) Eigenvalues on the complex plane

Figure 4.11: *Eigenvalues of the combined system as a function of the normal contact stiffness per unit length ($\mu = 0.15$, $\alpha = 4°$, and $\hat{k}_t = 0.04\ GN/m^2$).*

4.3.3 Case study C: The normal contact stiffness versus the tangential contact stiffness

In this section, the normal and tangential contact stiffnesses per unit length are the two main parameters that are varied. The numerical simulations are performed into 2 stages. The first stage is conducted without the presence of friction, and the aim here is to create a theoretical map of the natural frequencies of the combined system which will later be compared with test data to estimate the values of the normal and tangential contact stiffnesses per unit length of the pin-on-disc rig. The second stage is conducted with the presence of friction. The aim here is to determine the instability region of the combined system as functions of these two contact stiffnesses. In both stages, the normal contact stiffness per unit length is varied between 0 and 10 GN/m^2 whereas the tangential contact stiffness per unit length is varied between 0 and 0.8 GN/m^2.

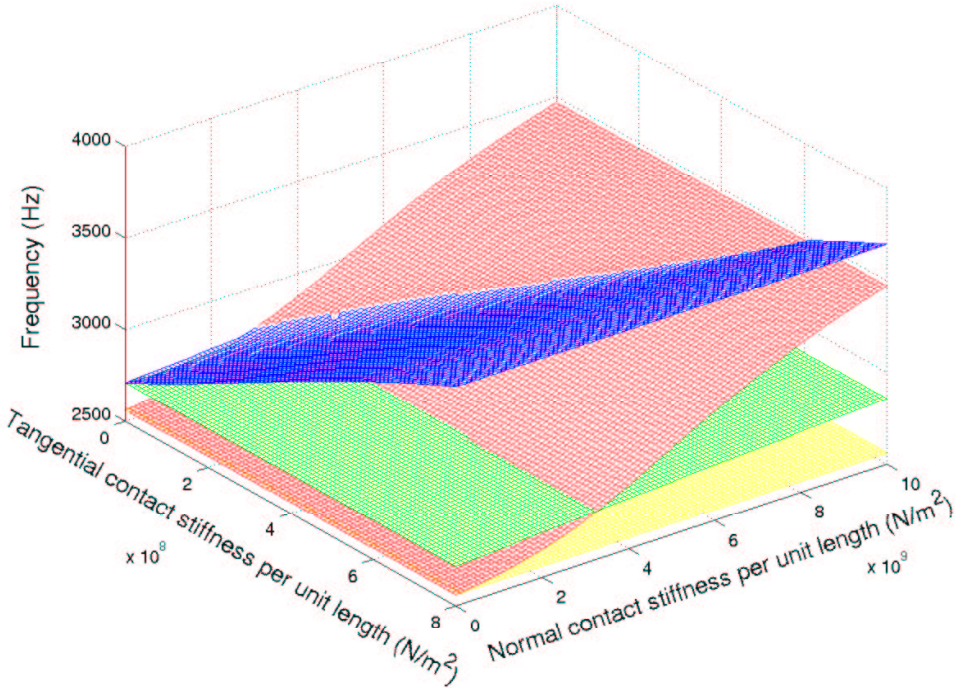

Figure 4.12: *A theoretical map of the natural frequencies of the combined system as functions of the normal and tangential contact stiffnesses per unit length within the frequency range of 2500 to 4000 Hz (with $\mu = 0$ and $\alpha = 8°$).*

It can clearly be seen from Figure 4.12 that, with any combination of the two contact stiffnesses, there exist four different modes within the frequency range of 2500 to 4000 Hz. The four planes in Figure 4.12, which are highlighted by different colours, indicate different families of modes. The yellow and red planes correspond to vibration modes which are dominated by the 3ND sine and cosine components of the original disc modes, respectively. The difference in the natural frequencies between the yellow and red planes can be interpreted as the split of the disc double mode due to the present of the pin. It is evident that the normal contact stiffness causes a greater change in the natural frequency of the mode dominated by the 3ND cosine component of the original disc mode (the red plane) than does the tangential contact stiffness. This is because the mode shape of the 3ND cosine mode of the disc has a much bigger amplitude in the out-of-plane direction than in the tangential direction.

The blue and green planes in Figure 4.12 correspond to vibration modes which are dominated by the second bending components of the original pin modes in the y- and z-directions, respectively. The effect of the tangential contact stiffness on the natural frequencies of the modes dominated by the second bending component of the original pin mode in the y-direction (the blue plane) is more pronounced than that of the normal contact stiffness. This is clearly because the second bending mode of the pin has a much bigger amplitude in the tangential direction than in the normal direction.

Now consider the case when friction is present. Figure 4.13 shows the eigenvalues of the combined system within the frequency range of 2500 to 4000 Hz as functions of the normal and tangential contact stiffnesses per unit length. First, it can be seen that the system becomes unstable only for some specific combinations of the two contact stiffnesses. If the values of the normal and tangential contact stiffnesses exceed 8.5 and 0.55 GN/m^2, respectively, squeal involved the 3ND cosine component of the original disc mode will not occur. Second, the result in Figure 4.13 (b) shows that instability can occur even when the tangential contact stiffness is equal to 0.

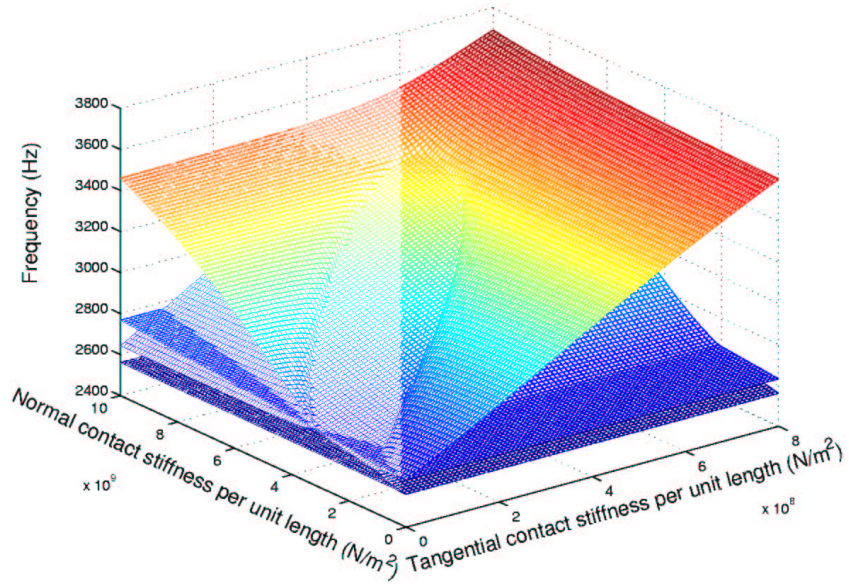

(a)

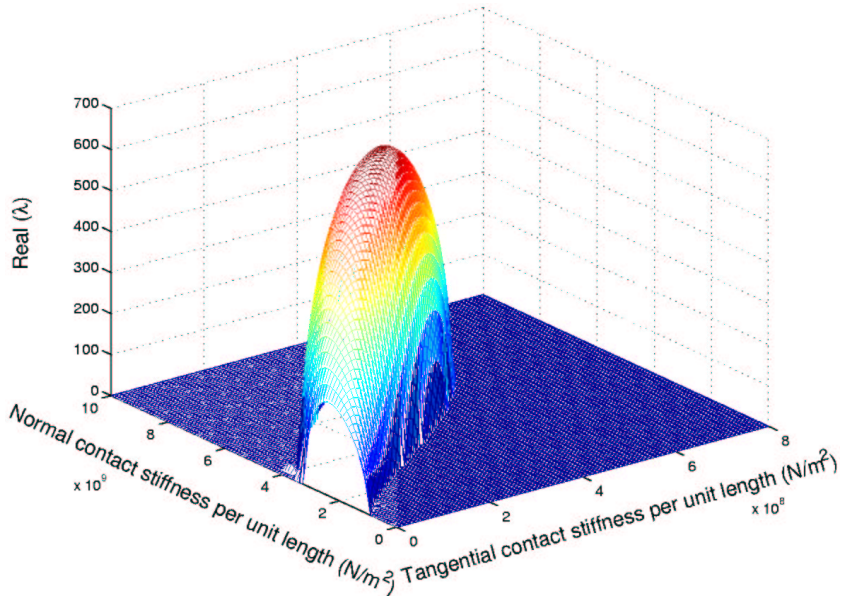

(b)

Figure 4.13: *Instability regimes as functions of the normal contact stiffness per unit length, $\hat{k}_n$, and the tangential contact stiffness per unit length, $\hat{k}_t$, (with $\mu = 0.15$ and $\alpha = 8°$): (a) the predicted squeal frequencies, and (b) the real parts of the eigenvalues (positive values only).*

As a final remark, there is an open question as to whether the tangential contact stiffness should be included in the theoretical model during a sliding contact in which the relative velocity between the two surfaces never changes sign. Nevertheless, the simulation in Figure 4.13 demonstrates that the tangential contact stiffness can influence the onset of instability of the coupled system and, thus, could become an important parameter in determining the precise condition for brake squeal.

4.3.4 Case study D: The effect of the contact damping

In this section, calculations are conducted with the presence of the contact damping terms. The main objective is to study the effect of contact damping on the onset of instability. In the present calculations, the normal contact damping per unit length, $\hat{c}_n$, is assumed to be 10 kNs/m^2 (about 0.1 % of the critical damping of mode 12 when there is no friction) and, for simplicity, the tangential contact damping per unit length, $\hat{c}_t$, is assumed to be zero.

In the absence of friction, vibration modes of the combined system are damped by the normal contact damping - except for modes with a nodal line passing along the contact line between the pin and the disc. In general, damped modes will have their eigenvalues on the left-hand side of the imaginary axis in the complex plane. However, when the friction is present, some eigenvalues may move towards the right-hand side of the imaginary axis. Once, they cross the imaginary axis (i.e. have positive real parts), vibration modes corresponding to these eigenvalues are said to be unstable. In the simulation shown in Figures 4.14, mode 14 starts off as a damped mode but, as the coefficient of friction increases, it becomes less heavily damped and eventually becomes unstable, as shown by the black curve in Figures 4.14 (a) and (b). It must be noted that mode 14 becomes unstable without passing through the lock-in point (i.e. the coincidence of the eigenvalues). The discussion of this behaviour is given in Section 4.4.2.

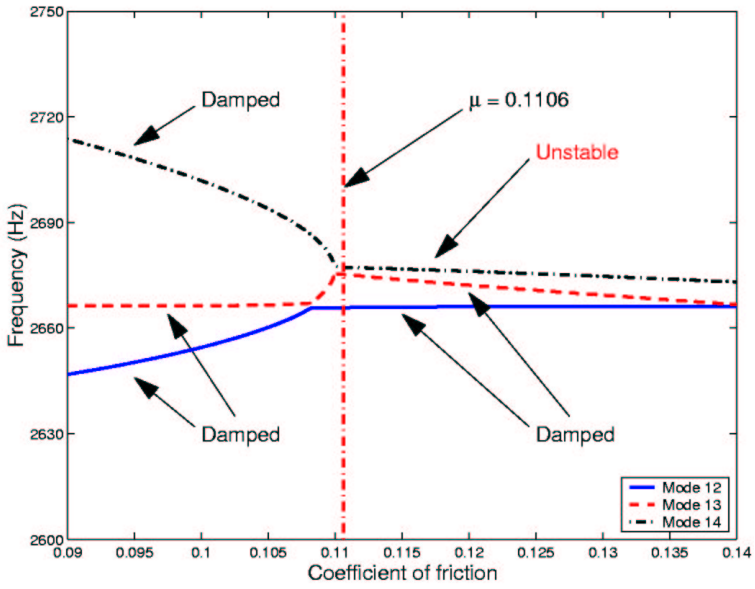

(a) Natural frequencies as a function of the coefficient of friction.

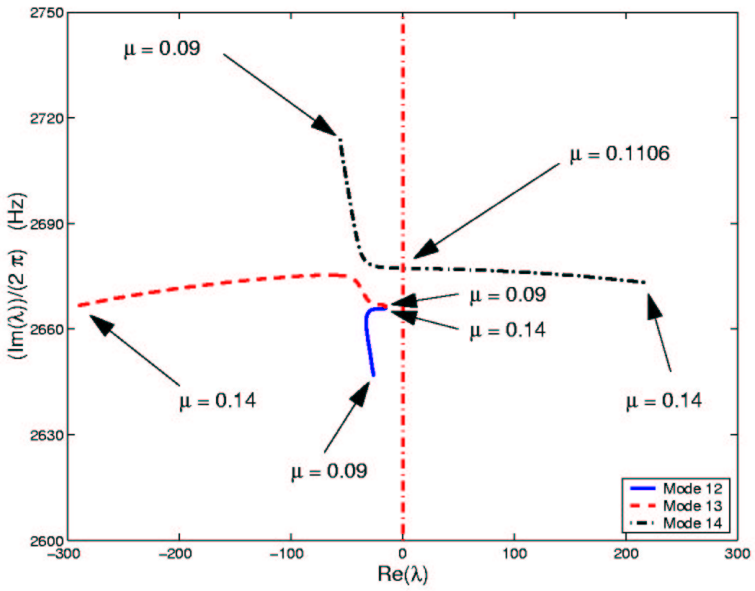

(b) Eigenvalues on the complex plane

Figure 4.14: *Eigenvalues of the combined system with the presence of the normal contact damping as a function of the coefficient of friction* ($\hat{c}_n = 10\ kNs/m^2$, $\hat{c}_t = 0\ kNs/m^2$, $\hat{k}_n = 2.4\ GN/m^2$, $\hat{k}_t = 0.04\ GN/m^2$, *and* $\alpha = 4°$).

4.4 Discussion

4.4.1 The validity of the linear pin-on-disc model

In the theoretical modelling process, two important assumptions have been made. First, the rotation of the disc is assumed to be slow enough that the change in the disc amplitude due to the disc rotation can be neglected. This first assumption will be valid only if the responses are being considered for a short length of time. The second assumption states that the velocity of the pin in the direction parallel to the disc surface does not exceed the disc velocity at the points of contact. However, in reality, it is possible that the velocity of the pin could exceed the velocity of the disc, especially when instability occurs. This second assumption is made to avoid the calculations of the non-linear behaviour, known as the "stick-slip" phenomenon, at this stage. From these two assumptions, the linear pin-on-disc is only valid at the onset of instability where the in-plane velocity of the pin is small in comparison with the disc velocity. In the next chapter, these two limitations will be removed when a non-linear friction model and the rotation of the disc are included in the theoretical model.

4.4.2 The mechanism for instability generation

Before discussing the mechanism for instability generation, it is worth considering the way in which the friction force is included in the model. According to equation (4.7), the magnitude of the normal contact force, P, (and, also, the magnitude of the friction force) depends on the relative motions of the pin and the disc at the point of contact in the direction normal to the disc surface. However, the direction of the friction force itself is parallel to the disc surface, as shown in Figure 4.15. Hence, the direction of flow of energy caused by the friction force (i.e. feeding net energy into or taking net energy away from the system in one complete vibration cycle) will depend on the phase relationship between the motions of the pin and disc in the normal and tangential directions.

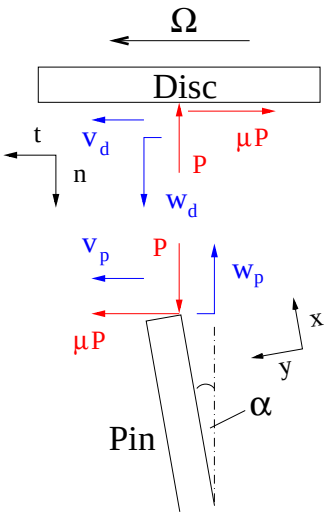

Figure 4.15: *The directions of the normal contact force, P, and the friction force, μP, and their corresponding displacements (Note: the red and blue arrows represent the forces and displacements, respectively).*

In general, the direction of flow of energy caused by a force in one complete cycle can be determined straightforwardly from the phase difference between that force and its corresponding displacement. For example, consider the friction force acting on the pin as shown in Figure 4.15. By defining the friction force, μP, and the displacement, v_p, in the same direction, the work done on the system by the force in one complete cycle will be positive if the phase of the force leads that of the displacement (Figure 4.16 (a)). Conversely, the force will dissipate net energy in one complete cycle if the phase of the force lags behind that of the displacement (Figure 4.16 (b)). On the other hand, if the phase difference between the force and the displacement is either 0 or 180 degrees, then there will be no net energy transfer due to this force in one complete cycle. For convenience, throughout this chapter, the term "relative phase shift" will be referred to as the phase of the force with respect to that of the displacement in the direction of the force. It is now appropriate to consider the onset of instability of the pin-on-disc system. The discussion is divided into 2 parts: (i) initially-undamped systems, and (ii) initially-damped systems.

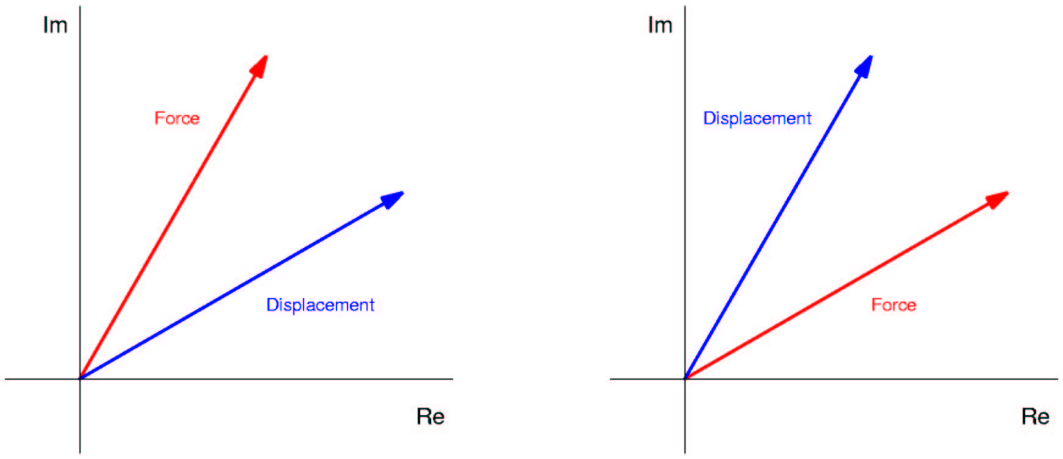

(a) Positive relative phase shift

(b) Negative relative phase shift

Figure 4.16: *The relative phase shift between the force and its corresponding displacement: (a) positive or "leading", and (b) negative or "lagging".*

4.4.2.1 Initially-undamped systems

In the case of initially-undamped systems, when there is no friction (i.e. $\mu = 0$), all the eigenvalues of the combined system are purely imaginary and, thus, all the vibration modes are real. In effect, real modes imply that every part of the structure will reach the maximum amplitude at the same instant. If friction is then introduced with a friction coefficient which is less than the "lock-in" value, the relative phase shift of the friction force will either be 0 or 180 degrees. According to the above discussion, the friction will not create or dissipate net energy in one complete cycle. Thus, the vibration modes will remain real and, hence, asymptotically stable.

Although the presence of the friction force does not immediately lead to instability, it will act as an extra "restoring" force which may reinforce or oppose the system stiffness forces. As a result, the natural frequencies of the combined system may change as the coefficient of friction or the normal contact stiffness varies. In the example given in Figure 4.10, the friction force acts against the stiffness forces generated by the motion mode 14 but reinforces those generated by the motion of mode 12. Thus, as

the coefficient of friction increases, the natural frequency of mode 14 will decrease while that of mode 12 will increase. Due to the opposite effect of the friction force on the natural frequencies of modes 12 and 14, it is possible that the eigenvalues of the two modes may coincide at a particular value of coefficient of friction - the "lock-in" point.

When the eigenvalues of the two modes are identical, the resulting system may become defective (i.e. independent eigenvectors cannot be found for all repeated eigenvalues). According to Newland [68], if the system is defective, one of the two modes will be asymptotically stable while the other may be linearly unstable. Furthermore, Newland has also shown that not all the points on the structure of the unstable mode will have the same time dependence. In other words, there is a phase difference between points on the structure (although it is not a phase difference in the conventional sense). The phase difference between the motions in the directions normal and tangential to the disc surface would cause the friction force to start feeding net energy into the system for each complete vibration cycle which would result in the mode becomes unstable.

If the coefficient of friction is increased beyond the lock-in point, the eigenvalues of the two modes will be complex with non-zero real parts and the corresponding eigenvectors will also be complex. In effect, there will be a phase difference between the motions in the directions normal and tangential to the disc surface. Thus, the friction force will have a different phase to the displacement in the direction of the friction force. According to the previous discussion, the friction force will either feed energy into or take energy away from the system. Because the system has no initial damping, if the motion of a mode causes the friction force to feed net energy into the system for every complete vibration cycle, that particular mode will become unstable. In contrast, if the motion of a mode causes the friction force to take net energy away from the system for every complete vibration cycle, that particular mode will become damped.

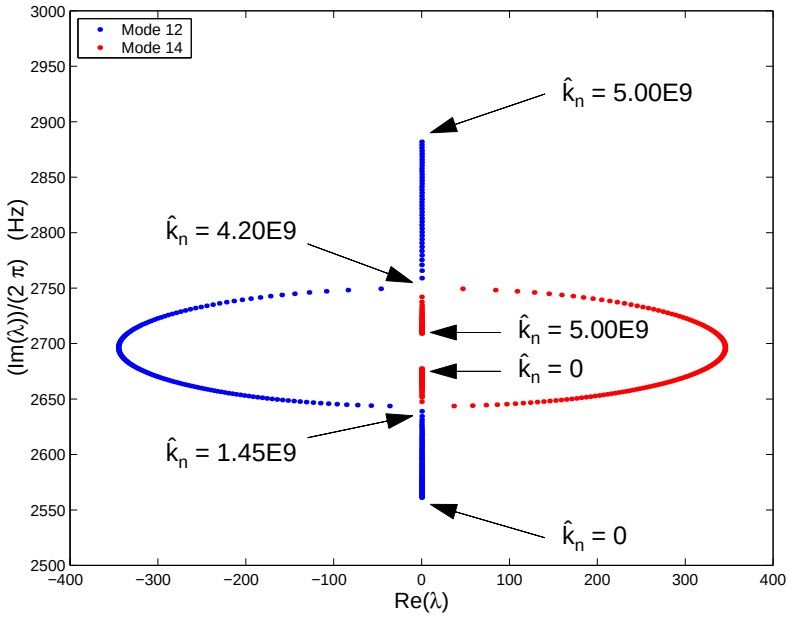

Figure 4.17: *The eigenvalues of the initially-undamped system; showing modes 12 and 14.*

For clarity, the results from Figure 4.11 (b) are redisplayed in Figure 4.17 but showing the eigenvalues of modes 12 and 14 only. To demonstrate the relationship between the relative phase shift of the friction force and the instability of the system, Figure 4.18 shows the relative phase shift of the friction force generated by each of the two modes at one of the contact points. It should also be noted that the friction force acts on both the pin and the disc simultaneously. Thus, to determine whether the friction force will feed net energy to or take net energy away from the system, the relative phase shift of the friction force acting on the two components must be taken into consideration. In Figure 4.18, it can be seen clearly that, between the lock-in and lock-out points, the relative phase shift of the friction force due to the motion of mode 14 is positive for both the pin and the disc. As a result, the friction force will feed net energy into mode 14 for each complete vibration cycle and, hence, mode 14 will become unstable. Conversely, the the friction force due to the motion of mode 12 dissipates net energy in one complete cycle and would result in mode 12 becomes

damped.

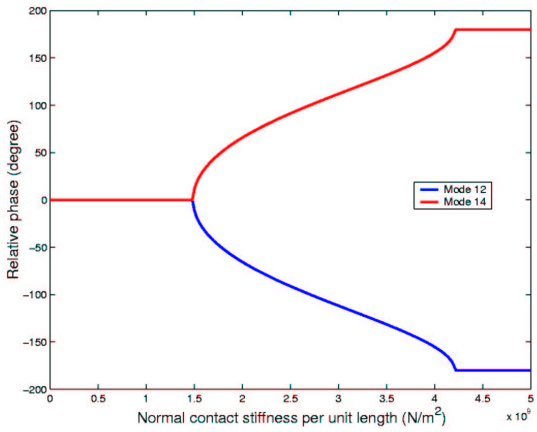

(a) friction force acting on the pin

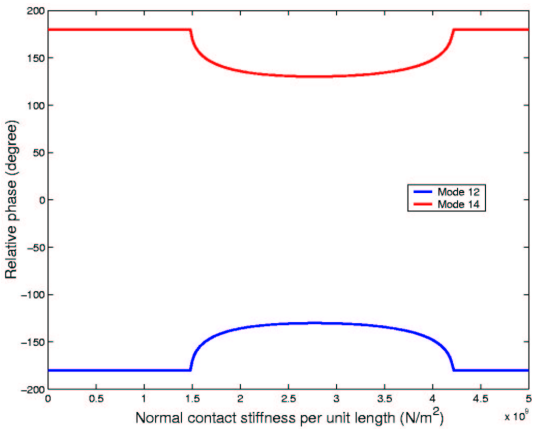

(b) friction force acting on the disc

Figure 4.18: *The relative phase shifts of the friction forces acting on (a) the pin, and (b) the disc.*

4.4.2.2 Initially-damped systems

In this section, the discussion focuses on the mechanism which causes some vibration modes of the combined system with initial damping to become unstable. To demonstrate the principle, the examples used throughout the following discussion are calculated with the same system parameters as those described in Section 4.3.4 and it should also be noted that the normal contact damping is the only source of damping in that model. Thus, the model contains two sources of non-conservative forces: (i) the damping forces generated by the contact elements, and (ii) the friction forces. For clarity, Figure 4.19 illustrates the directions of these two non-conservative forces and their corresponding displacements.

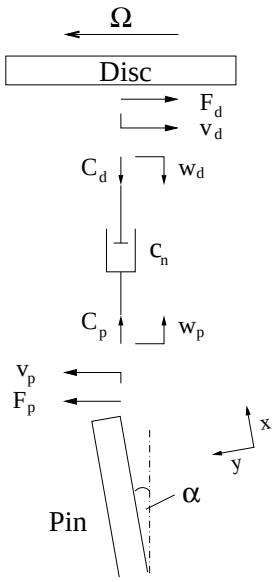

Figure 4.19: *The directions of the non-conservative forces and their corresponding displacements.*

In the absence of friction, it is clear that vibration modes of the combined system will be damped - except those modes with a nodal line coinciding with the contact line between the pin and the disc. The eigenvectors of damped modes are generally complex, which can imply that there may be a phase difference between the motions in the directions normal and tangential to the disc surface. Unlike the initially-undamped systems, if the friction force is then introduced, it will immediately start feeding net energy into or taking energy away from the system for each complete vibration cycle due to this initial phase difference.

To explain how a mode of the combined system with initial damping could become unstable, the work done by the friction force and the energy dissipated by the dampers must be considered. For each force and displacement pair shown in Figure 4.19, a relative phase diagram could be constructed. Figure 4.20 illustrates the relative phase shifts for modes 12, 13 and 14 of the combined system at one of the contact points as a function of the coefficient of friction.

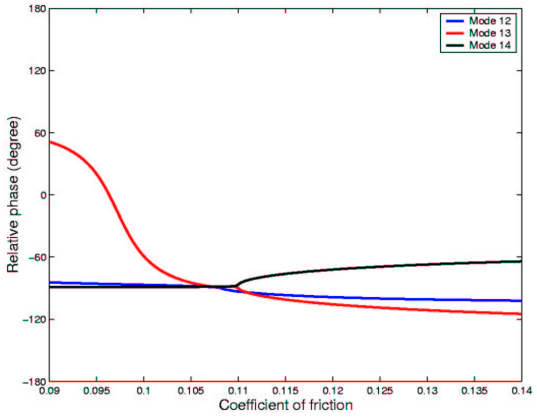

(a) damping force acting on the pin

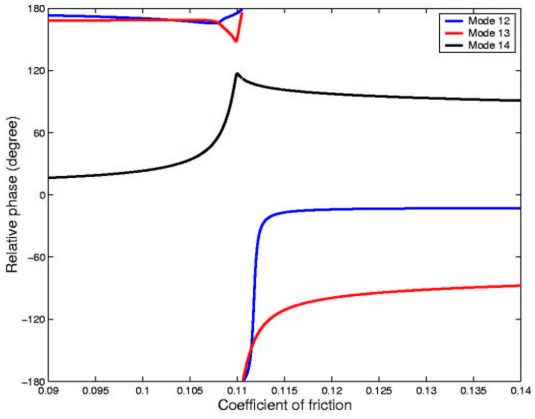

(b) friction force acting on the pin

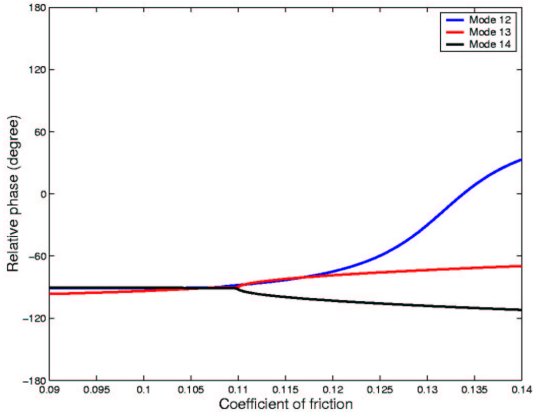

(c) damping force acting on the disc

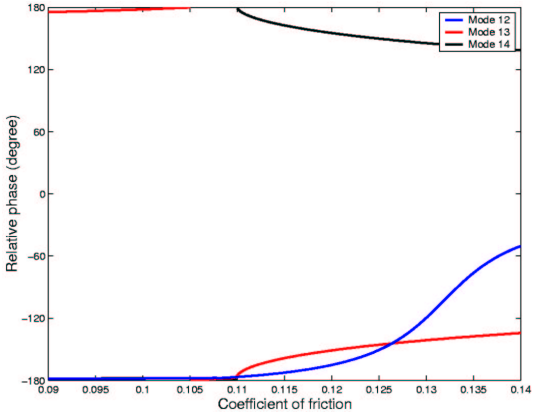

(d) friction force acting on the disc

Figure 4.20: *Relative phase diagrams of the non-conservative forces for modes 12, 13 and 14 of the combined system.*

The relative phase diagrams immediately reveal the direction of energy flow caused by that particular force (i.e. feeding net energy into or taking net energy away from the system in one complete cycle). For example, the friction force which is generated by the motion of mode 14 and is acting on the tip of the pin (as indicated by the black line in Figure 4.20 (b)), always has a positive relative phase shift within this specified range of the coefficient of friction. Thus, this friction force will feed net energy into the system for every complete vibration cycle. However, the reaction of this friction force which acts on the disc (Figure 4.20 (d)) does not always feed energy into the system as its counterpart. In fact, the friction force acting on the disc will start feeding net

energy into the system if the coefficient of friction exceeds 0.11, as shown by the black line in Figure 4.20 (d). When the friction forces acting on the pin and the disc both feed energy to the system, the instability of the system increases rapidly (as can be seen by the change of the real part of the eigenvalues of mode 14 shown in Figure 4.21 (a)).

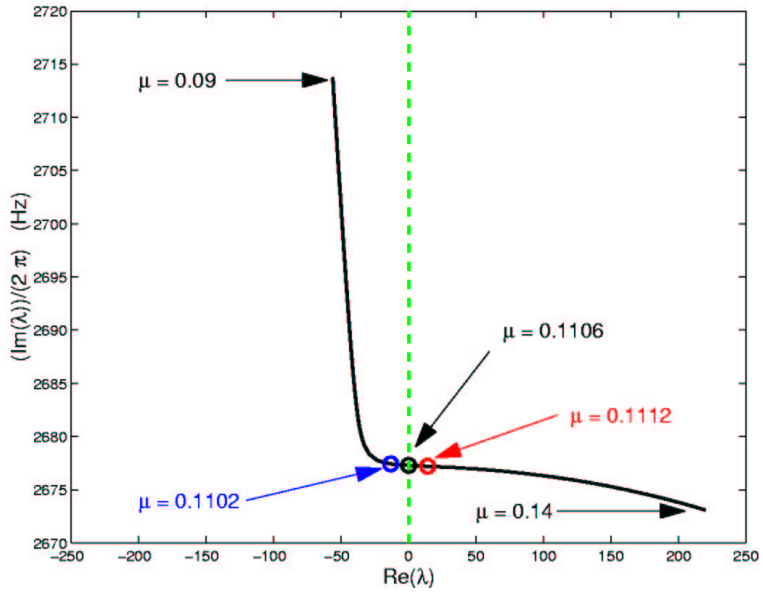

(a) Eigenvalues of mode 14

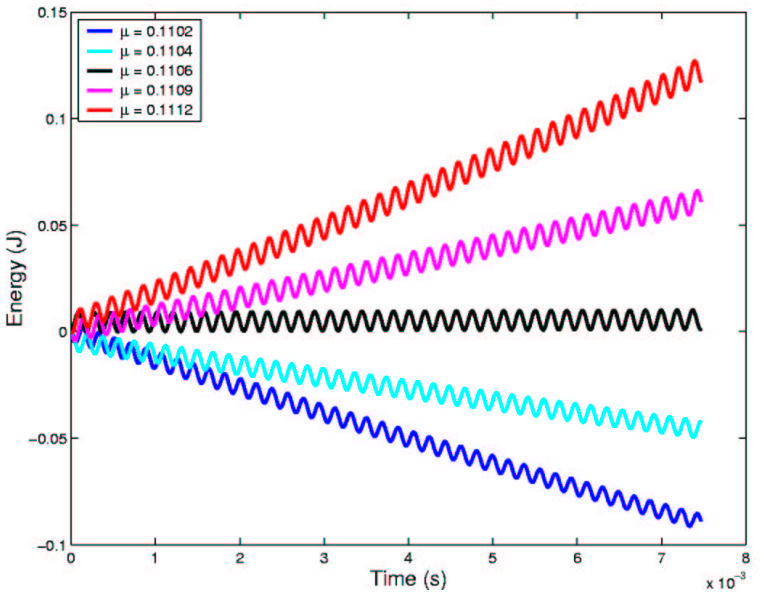

(b) The total work done by the non-conservative forces

Figure 4.21: *Instability of mode 14 of the linear pin-on-disc system.*

Although the relative phase diagram can indicate the direction of flow of energy, it does not show the total amount of energy transfered in one complete cycle. Thus, to demonstrate the relationship between the overall energy transferred by the non-conservative forces and the instability of a particular mode, it is necessary to calculate the total work done by the non-conservative forces at all the contact points. For clarity, the eigenvalues of mode 14 taken from Figure 4.14 (b) are plotted in Figure 4.21 (a). The total energy generated by the non-conservative forces due to the motion of mode 14 at different values of friction coefficient is given in Figure 4.21 (b). When the coefficient of friction is less than 0.1106, the total work done is negative (i.e. the energy is continuously extracted from the system) and, hence, the mode is damped. However, if the coefficient of friction exceeds 0.1106, the energy fed into the system by the friction force will be greater than the total energy dissipated by the dampers. As a result, mode 14 will become unstable when the coefficient of friction exceeds 0.1106.

In summary, the phase difference between the motions in the directions normal and tangential to disc surface plays a critical role in determining the direction of flow of energy caused by the friction force. In the case of initially-damped systems, a vibration mode of the combined system will become unstable if the friction force generated by the motion of that particular mode feeds more net energy into the system in one complete cycle than the energy which is dissipated by the dampers.

4.4.3 The effect of the pin finite width on the instability of the pin-on-disc system

In the theoretical modelling, when the angle of inclination is non-zero, the contact line is assumed to take place at the corner of the pin, as illustrated in Figure 4.22 (a). However, when the surface of the pin used in the experiments is examined, it has been found that the surface is not perfectly flat. The surface appears slightly curved due to wear. Hence, with a small angle of inclination, it may be possible that the contact line is not at the corner of the pin but moves closer to the neutral axis. Thus, in the case

of small angles e.g. less than 5 degrees, the model with the contact line being on the neutral axis (Figure 4.22 (b)) may give better predictions for squeal characteristics than the one with the contact line being at the corner of the pin, as shown in Figure 4.23.

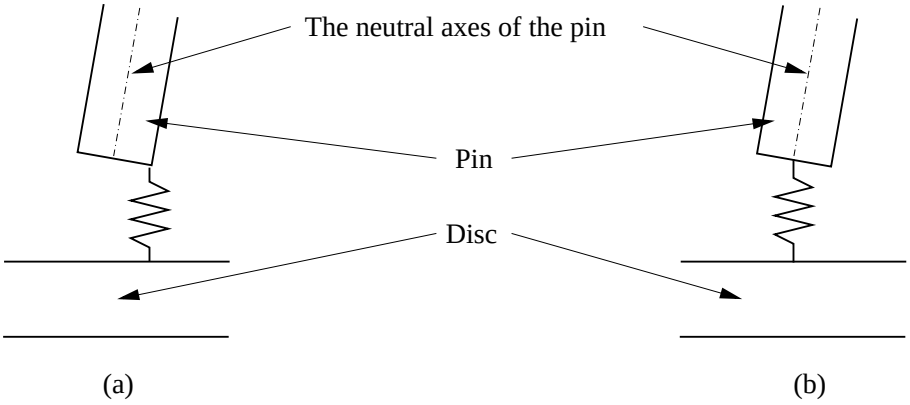

Figure 4.22: *The spring is placed at one of two different locations: (a) at the corner of the pin and, (b) on the neutral axis of the pin.*

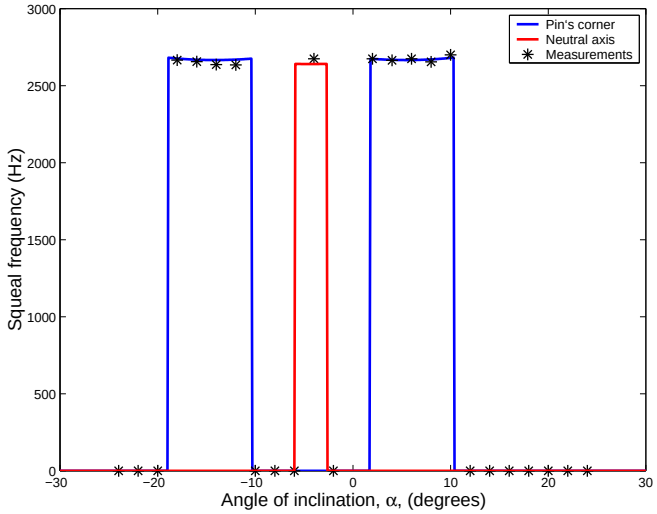

Figure 4.23: *The squeal frequency against the angle of inclination of the pin: (i) predictions with the contact point at the corner of the pin, (ii) predictions with the contact point on the neutral axis of the pin and (iii) experimental measurements.*

As can be seen from Figure 4.23, the predictions of squeal angles with the contact being on the neutral axis of the pin are completely different from those obtained with

the contact line being at the corner of the pin. When the contact line is on the neutral axis of the pin, squeal is predicted only if the pin is in a digging-in position. A closer look at the tip of the pin could provide an explanation for the differences in the predictions: refer to Figure 4.24. When the pin vibrates, for example in the second bending mode, the displacement of the pin on the neutral axis may not always have the same amplitude and phase as the displacement at the corner of the pin, as illustrated in Figure 4.24 (b). In this example, the displacements on the neutral axis and at the corner of the pin have the same phase in the direction parallel to the disc surface (direction t in Figure 4.24) but are out-of-phase in the direction normal to the disc surface (direction n in Figure 4.24). The phase difference between the two contact points would result in different predictions of squeal characteristics.

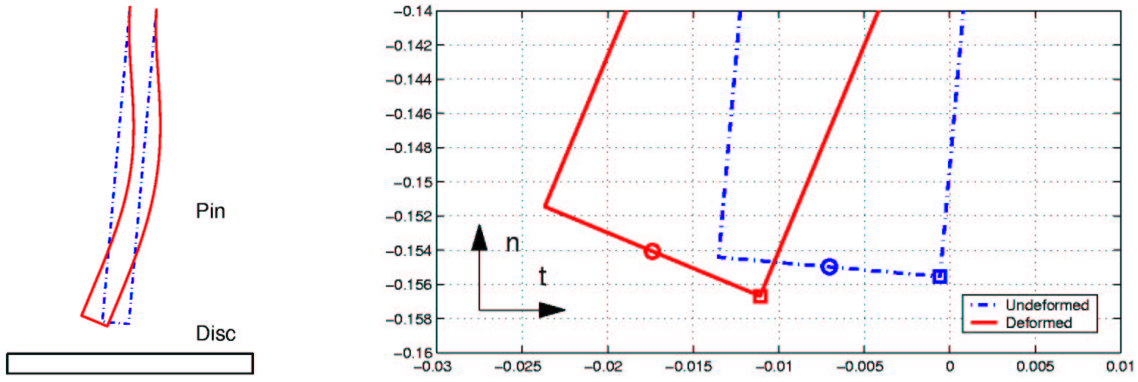

(a) (b)

Figure 4.24: *The pin has the angle of inclination of 5 degrees in the leaning direction: (a) the second bending mode of the pin and (b) the close up at the pin's tip.*

4.5 Conclusions

In this chapter, a linear pin-on-disc model has been constructed to study the basic mechanisms involved in squeal generation. Parameter studies have been conducted on the following features: (i) the coefficient of friction, (ii) the angle of inclination, (iii) the normal contact stiffness, (iv) the tangential contact stiffness and, (v) the normal contact damping. The key results found in this chapter are as follows:

- theoretical predictions from the linear pin-on-disc model show that squeal can occur when the pin is in both the leaning and digging positions. These results have been validated by experimental measurements which indicate that the predicted squeal frequencies are accurate to within 1 per cent of the measured values. Thus, it can be concluded that the theoretical model of the pin-on-disc system can represent the dynamics of the real structure;

- the linear pin-on-disc model presented in this chapter shows the "lock-out" characteristic as well as the "lock-in" characteristic;

- relative phase diagrams can be used to determine the direction of flow of energy of the non-conservative forces and thus to explain the incidence of squeal.

Chapter 5

Non-linear dynamics of pin-on-disc systems

5.1 Overview

As already discussed in the previous chapter, the linear pin-on-disc model will be valid only when the pin and the disc are in a sliding contact in which the relative velocity between the two surfaces never changes sign and the coefficient of friction is assumed to be constant. However, in reality, the in-plane velocity of the pin could exceed that of the disc and, as a result, the friction force may change its direction. Thus, to make the pin-on-disc model more realistic, a model of friction coefficient which is a function of relative velocity and which can take into account the change in friction direction will be included in the following pin-on-disc model.

Many past studies on disc brake squeal, such as those by Ouyang *et al.* [41], usually used Amonton's (or Couloumb) type of friction model in which the value of the coefficient of friction depends on the state of motion (i.e. stick or slip phases), as described in Chapter 1. However, with this description of friction, the theoretical model yields a set of differential equations with discontinuity on the right-hand side (also known as the differential inclusion problem [69]), which could be difficult and time-consuming to solve. To avoid this discontinuity, a friction model in which the friction coefficient

is a function of the relative velocity, and has a smooth variation around the zero relative velocity region, will be used in the current pin-on-disc model. Furthermore, as the coefficient of friction can now vary as a function of relative velocity, it becomes necessary to include the rotation of the disc in the theoretical model of the system. However, the rotational speed of the disc is assumed to be slow enough that gyroscopic and centrifugal stiffening effects can be neglected.

According to experiments conducted by Stanbridge *et al.* [70], the effect of mistuning on the squeal characteristics is also worth investigating. They have shown experimentally that when the disc is perfectly tuned, the operating deflection shape (ODS) of the disc during squeal is in the form of a stationary wave fixed in the stationary frame of reference. However, when the disc is mistuned with a small mass, the ODS response during squeal is no longer a pure stationary wave but appears to be a combination of stationary and travelling waves. From a theoretical perspective, most past studies of disc brake squeal have usually assumed that the disc component is perfectly tuned. However, real brake discs do possess some degree of mistuning due to the presence of the mounting holes, as demonstrated experimentally by Di Maio [71]. Thus, one of the objectives of the current study is to investigate the effect of mistuning on the squeal characteristics.

In this chapter, the equations of motion are derived for a pin-on-disc system which has a small mistuning mass attached to the disc. An improved friction model in which the friction coefficient is a function of the relative velocity and has a smooth variation around the zero relative velocity region is presented. To calculate the response of the theoretical model, the time integration method based on Runge-Kutta formulae is utilised. The main objective of this work is to investigate the non-linear dynamics of the pin-on-disc system with a particular interest concentrated on the limit-cycle characteristics.

5.2 Modelling

In this section, a model is presented to describe the dynamics of a pin-on-disc system which has a small mistuning mass attached to the disc, as shown in Figure 5.1. The disc is modelled using classical plate theory which only involves the out-of-plane motion. The primary reason for choosing classical plate theory instead of the full FE model is to limit the size of the problem when the rotation of the disc is to be included. However, the accuracy of the theoretical model can be improved by updating the modal properties of the disc using values calculated from the validated FE model in Chapter 4. As for the pin, its modelling is exactly the same as that described in Section 4.2.2.

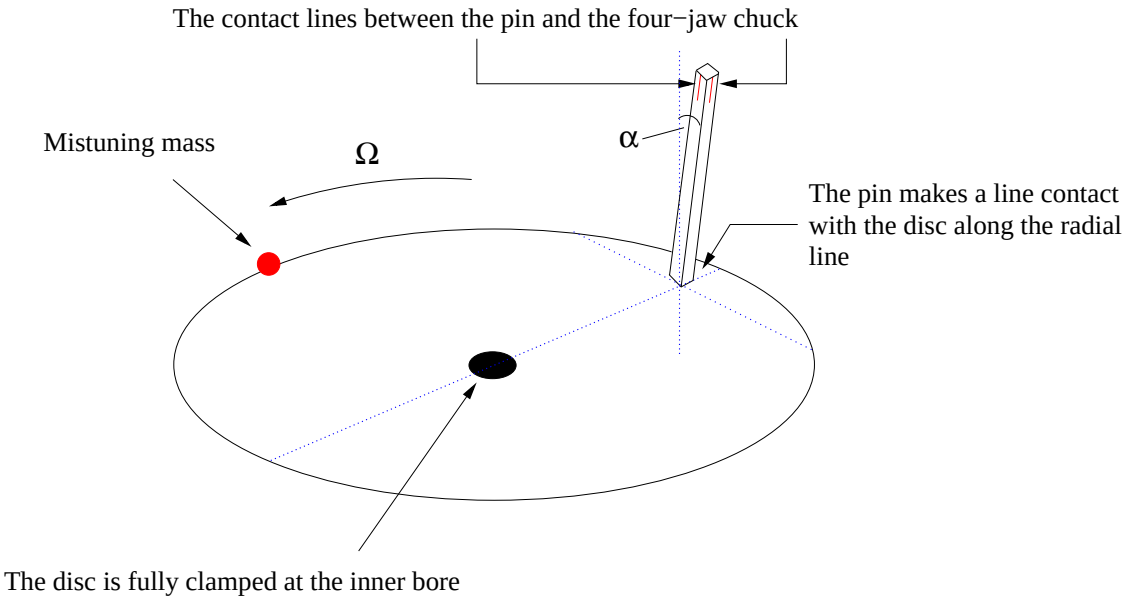

Figure 5.1: *The pin-on-disc model with a mistuning mass attached to the disc.*

In summary, the current pin-on-disc model has the following features:

- the disc can be mistuned by a small mass (or masses);
- the rotation of the disc is taken into consideration;

- the coefficient of friction is a function of the relative velocity between the pin and the disc and has a smooth variation around the zero relative velocity region.

The formulation of the equations of motion of the pin-on-disc model with the above features will be described in the following section.

5.2.1 Equations of motion

In the case of a rotating disc with a mistuning mass attached to the disc, the derivation of the equations of motion is similar to that described in Section 2.2.2. For convenience, only the governing equation of motion in the stationary frame of reference is shown here:

$$D\nabla^4 w + \left\{\rho h + \frac{m_0}{r}\delta(r-\hat{r}_0)\delta(\theta-\Omega t-\hat{\theta}_0)\right\} \times \left[\frac{\partial^2 w}{\partial t^2} + 2\Omega\frac{\partial^2 w}{\partial\theta\partial t} + \Omega^2\frac{\partial^2 w}{\partial\theta^2}\right] = f(t) \quad (5.1)$$

where

- w is the out-of-plane displacement of the disc in the stationary frame of reference,
- m_0 is the mistuning mass,
- r and θ define a set of coordinates in the stationary frame of reference,
- $\hat{r}_0$ and $\hat{\theta}_0$ are the initial location of the mistuning mass at $t = 0$, and
- $f(t)$ is the external forces applied on the disc.

As for the pin, its governing equation of motion in the generalised coordinates, q_p, can be written as:

$$[\grave{}\, I \,\acute{}]\{\ddot{q}_p\} + [\grave{}\, \omega_p^2 \,\acute{}]\,\{q_p\} = [\Phi_p]^T\,\{F_p\}, \quad (5.2)$$

where $[\Phi_p]$ is the mode shape matrix of the pin, and $\{F_p\}$ is the vector of applied forces. Note: the moment generated due to the fact that the friction force is not acting on the neutral axis of the disc has been neglected in the current model.

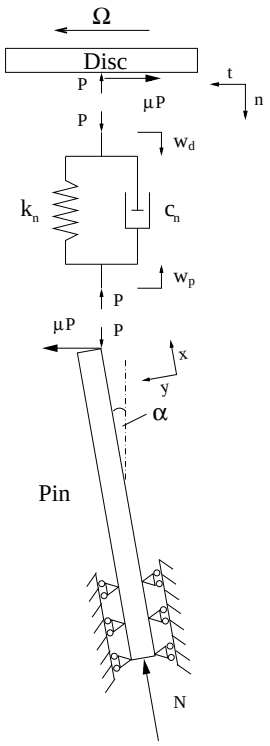

Figure 5.2: *The force system at the interface.*

To represent the static load, a constant force, N, is applied at the back end of the pin in the lengthwise direction, as illustrated in Figure 5.2. By considering the forces and displacements at the contact points, as shown in Figure 5.2, the governing equation of motion of the combined pin-on-disc system can be written as:

$$\begin{bmatrix} [I]+[L(t)] & 0 \\ 0 & [I] \end{bmatrix}\begin{Bmatrix} \ddot{q}_d \\ \ddot{q}_p \end{Bmatrix}+\begin{bmatrix} [E]+[P(t)] & 0 \\ 0 & 0 \end{bmatrix}\begin{Bmatrix} \dot{q}_d \\ \dot{q}_p \end{Bmatrix}+\begin{bmatrix} [F]+[J]+[S(t)] & 0 \\ 0 & [\,\dot{}\,_p\omega_n^2\,\dot{}\,] \end{bmatrix}\begin{Bmatrix} q_d \\ q_p \end{Bmatrix}$$
$$=\sum_{h=1}^{\infty} {}_hk_n \begin{bmatrix} -{}_h\{\phi_d^n\} \\ {}_hc_1\ {}_h\{\phi_p^x\}+{}_hc_2\ {}_h\{\phi_p^y\} \end{bmatrix}\begin{bmatrix} {}_h\{\phi_d^n\} \\ {}_h\{\phi_p^x\}\cos\alpha-{}_h\{\phi_p^y\}\sin\alpha \end{bmatrix}^T\begin{Bmatrix} q_d \\ q_p \end{Bmatrix}+\begin{Bmatrix} 0 \\ \{\phi_p^x\}_b\ N \end{Bmatrix}$$
$$+\sum_{h=1}^{\infty} {}_hc_n \begin{bmatrix} -{}_h\{\phi_d^n\} \\ {}_hc_1\ {}_h\{\phi_p^x\}+{}_hc_2\ {}_h\{\phi_p^y\} \end{bmatrix}\begin{bmatrix} {}_h\{\phi_d^n\} \\ {}_h\{\phi_p^x\}\cos\alpha-{}_h\{\phi_p^y\}\sin\alpha \end{bmatrix}^T\begin{Bmatrix} \dot{q}_d \\ \dot{q}_p \end{Bmatrix}, \qquad (5.3)$$

where matrices $[E]$, $[F]$, and $[J]$ are defined by equations (2.6), (2.7) and (2.8), respec-

tively, and

$$\begin{aligned} {}_hc_1 &= {}_h\mu \sin\alpha - \cos\alpha, \\ {}_hc_2 &= {}_h\mu \cos\alpha + \sin\alpha, \end{aligned} \tag{5.4}$$

and the left-hand subscript h indicates that the forces and displacements are considered at the h^{th} contact node. The terms in $[L(t)]$, $[P(t)]$ and $[S(t)]$ matrices are periodic and their explicit expressions can be found in Appendix C. The vectors, ${}_h\{\phi_d^n\}$, ${}_h\{\phi_p^x\}$, and ${}_h\{\phi_p^y\}$ are the same as those defined by equation (4.9). Finally, the vector $\{\phi_p^x\}_b^T$ is the row of the pin's mode shape matrix, $[\Phi_p]$, corresponding to the degree-of-freedom at which the static force, N, is applied.

As a final remark, if the friction coefficient is assumed to be constant as in Chapter 4, the system matrices in equation (5.3) will be periodic and the eigensolutions can be found using Floquet's theory. However, this technique will not be covered in this thesis because the friction coefficient will be assumed to vary as a function of the relative velocity of the two contact surfaces, as described in the next section. Practical examples of Floquet's theory can be found in Von Groll [72].

5.2.2 Friction model

In this section, an improved version of Amonton's (Coulomb) type of friction model is presented. The friction coefficient of the new model is a continuous function of the relative velocity and has a smooth variation around the zero relative velocity region. By defining the normalised relative velocity as $V = V_{relative}/V_0$, the friction coefficient of the new friction model can be expressed as follows:

$$\mu(V) = \frac{a_1 V}{V^4 + \alpha V^2 + \beta} + \frac{2\mu_d}{\pi} \arctan(\eta V) \tag{5.5}$$

where a_1, α, β and η are constant coefficients, V_0 is the velocity of the disc at the point of contact, and μ_d is the dynamic coefficient of friction. The first term of equation (5.5) is an analogous function to that of the real part of a receptance FRF of a damped single-degree-of-freedom system. This function possesses two interesting features which make

it suitable for modelling the transition between the dynamic and static coefficients of friction around the zero relative velocity region. First, it has one maximum peak on the positive side of the relative velocity and also has a minimum peak on the negative side, as shown in Figure 5.3 (a). Second, its contribution dies away as the relative velocity approaches $+\infty$ or $-\infty$. The second term in equation (5.5) is used to model the coefficient of friction away from the zero relative velocity region where the coefficient of friction is constant and equal to the dynamic coefficient of friction, as illustrated in Figure 5.3 (b).

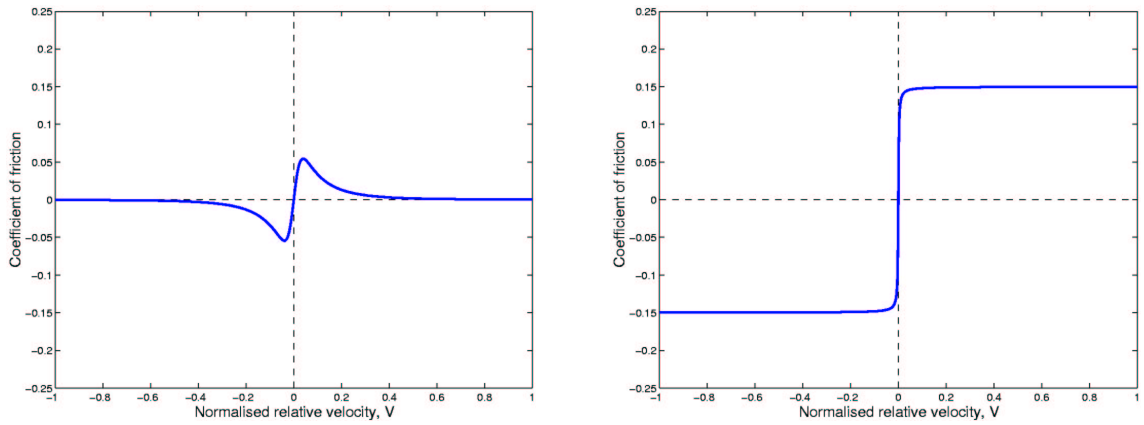

(a) $\frac{a_1 V}{V^4+\alpha V^2+\beta}$ (b) $\frac{2\mu_d}{\pi}\arctan(\eta V)$

Figure 5.3: *The contribution of the terms in equation (5.5) as a function of the normalised relative velocity ($a_1 = 0.023$, $\alpha = 100$, $\beta = 10^{-4}$, $\mu_d = 0.15$ and $\eta = 1000$).*

Figure 5.4 shows the friction coefficient defined in equation (5.5) as a function of the normalised relative velocity. By selecting appropriate values for the constant coefficients in equation (5.5), the maximum value of the friction coefficient can be assigned to the value of the static friction coefficient, μ_s. At high relative velocities, the contribution of the first term in equation (5.5) would rapidly disappear and, thus, the value of the friction coefficient will asymptotically converge to the dynamic coefficient of friction, μ_d.

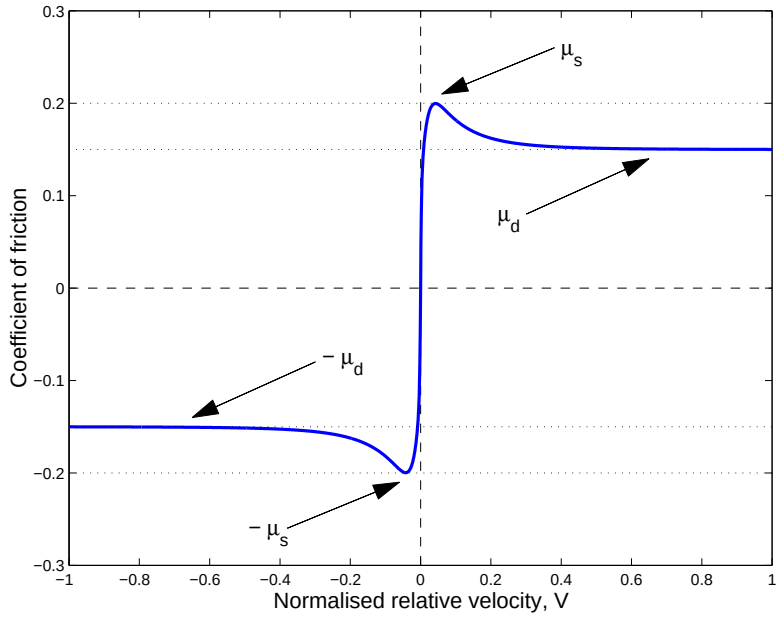

Figure 5.4: *The coefficient of friction as a function of the normalised relative velocity with a smooth variation around the zero relative velocity region ($\mu_s = 0.2$ and $\mu_d = 0.15$).*

5.3 Method of solution

Due to the new friction model and the mistuning of the disc, the equations of motion of the pin-on-disc system derived in the previous sections become more complex, and non-linear. To find the responses of the new pin-on-disc model, the time-integration method is used. All the numerical results presented in the next section have been produced entirely with MATLAB, which provides a number of standard time integration solvers for ordinary differential equations (ODEs). The ODE solver used in the current calculations is of *ode45* type (MATLAB terminology) which is a one-step solver based on an explicit Runge-Kutta formula.

As applied to any type of time-integration solver, the most critical parameter, which determines the accuracy of the solutions, is the integration step size. For the *ode45* solver, the step size is not controlled directly but depends on two tolerance parameters:

(i) the relative accuracy tolerance, and (ii) the absolute error tolerance. The first parameter controls the error relative to the size of each solution component and its default value is 0.1 % accuracy. The second parameter sets a threshold below which the values of the corresponding solution components are unimportant and its default value is 10^{-6}. However, to cope with the rapid change in the coefficient of friction around the zero relative velocity region, both the relative and absolute tolerance parameters have been reduced to 0.001 % and 10^{-8}, respectively.

5.4 Numerical simulations

In this section, systematic parameter studies are conducted on the non-linear pin-on-disc model presented in Section 5.2. The calculations are performed with two initial disc configurations: (i) a perfectly-tuned disc (i.e. without the mistuning mass), and (ii) a mistuned disc (i.e. with the mistuning mass). Apart from the mistuning of the disc, the other controlling parameters can be listed as follows:

- the physical dimensions of the pin and the disc;
- the angle of inclination, α;
- the normal contact stiffness and damping per unit length, $\hat{k}_n$ and $\hat{c}_n$;
- the normal static load, N;
- the rotational speed of the disc, Ω; and
- the dynamic and static coefficients of friction, μ_d and μ_s.

For simplicity, the physical dimensions of the pin and the disc are fixed in all the following calculations and are the same as those described in Section 4.3. Unless stated otherwise, the angle of inclination is also fixed at 8 degrees in the leaning position for all of the following calculations. With the static load varying between 9.8 and 98 N, the experimental measurements conducted in Chapter 7 suggest that the numerical

values of the normal contact stiffness per unit length vary between 2.3 and 2.9 GN/m^2 and those of the normal contact damping per unit length vary between 15 and 19 kNs/m^2. The damping factors for each mode of the pin are the same as those found experimentally in Chapter 7. However, the damping of the disc is assumed to be small enough that it can be neglected.

5.4.1 Case A: Pin-on-disc systems with a perfectly-tuned disc

The numerical simulations conducted in this section are calculated without the presence of the mistuning mass. For simplicity, the initial conditions of the system are calculated when the the disc is not rotating and, thus, the initial velocities are assumed to be zero for all components. The continuous function of the friction coefficient is assumed to be the same as that described by Figure 5.4.

Figure 5.5 shows various responses of the non-linear pin-on-disc model when $\hat{k}_n = 2.9\ GN/m^2$, $\hat{c}_n = 19\ kNs/m^2$, $\Omega = 4$ rev/min and $N = 98$ N. The in-plane vibration of the pin at its tip is plotted in Figure 5.5 (a) while the out-of-plane vibration of the disc at the same contact point is shown in Figure 5.5 (b). The red horizontal lines in Figure 5.5 indicate the velocity of the disc at the corresponding contact point. As can clearly be seen from Figures 5.5 (a) and (b), the pin-on-disc system becomes unstable initially (the first 0.1 seconds) but starts to converge to limit-cycle oscillations as the in-plane vibration of the pin approaches the disc velocity. The exponential build-up of squeal vibration (Figure 5.5 (c)) is approximately the same as the exponential envelope predicted by the linear model, as indicated by the red dashed line. This agreement arises because the pin is in a full sliding contact with the disc and the vibration takes place away from the zero relative velocity region. According to Figure 5.4, the coefficient of friction is approximately constant during the build-up period and this is precisely the requirement for the linear pin-on-disc model in Chapter 4 to be valid. Thus, it is no surprise that the linear model can give accurate predictions of squeal responses during the build-up period.

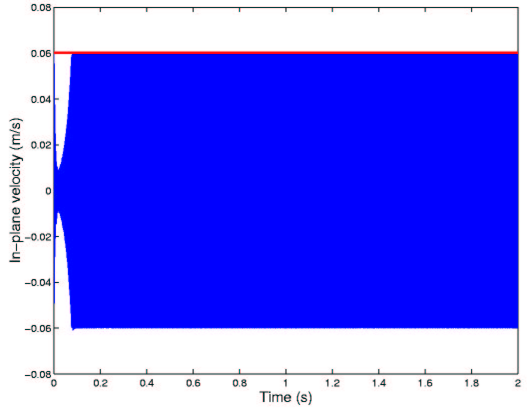

(a) In-plane vibration of the pin

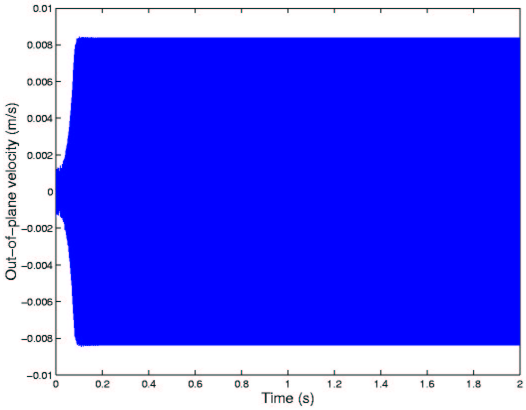

(b) Out-of-plane vibration of the disc

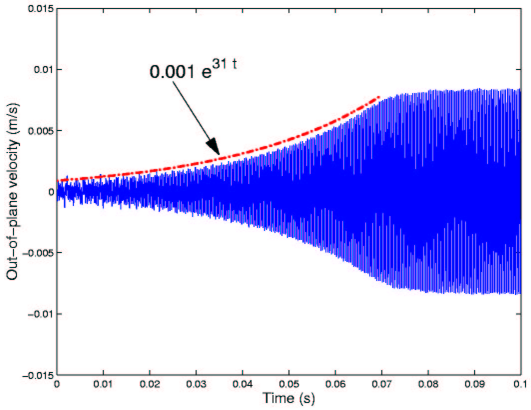

(c) Build-up of squeal vibration

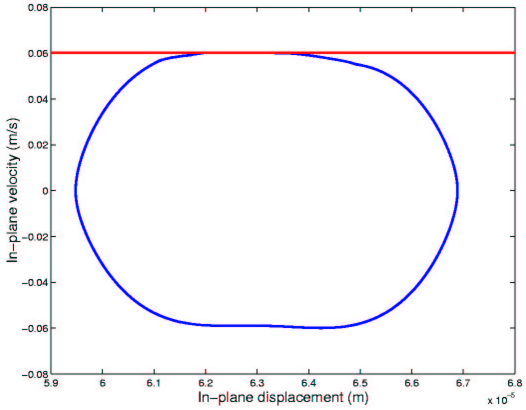

(d) Displacement-velocity diagram of the pin

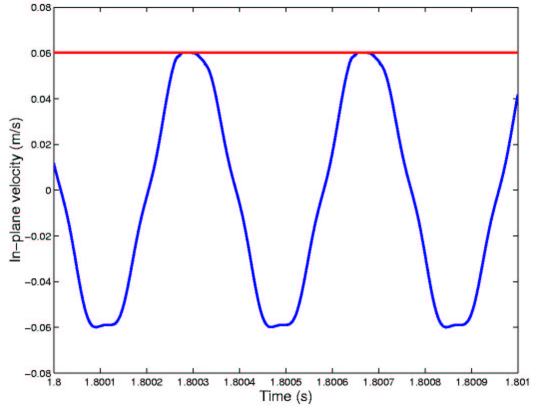

(e) Close-up of Figure 5.5 (a)

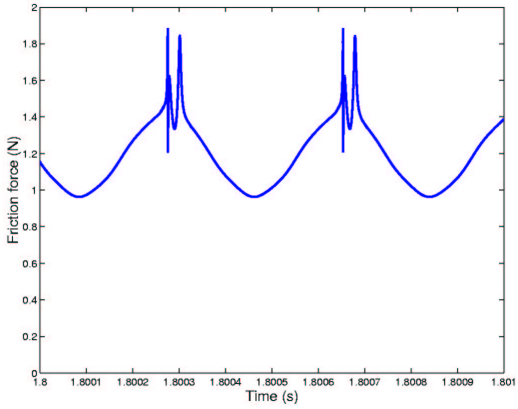

(f) the friction force

Figure 5.5: *Squeal characteristics of the pin-on-disc system predicted by the non-linear model.*

The limit-cycle characteristics of the pin can be seen in Figure 5.5 (d) where the in-plane velocity at the tip of the pin is plotted against its displacement. This velocity-displacement diagram shows the responses of the pin only after the limit-cycle oscillations have been fully reached. It is clear from Figures 5.5 (e) and (f) that the in-plane vibration of the pin is limited by the velocity of the disc and velocity reversal does not occur in this case. As a result, the friction force always stays positive (i.e. no change in its direction). The sudden fluctuations of the friction force observed in Figure 5.5 (f) arise due to the change in the coefficient of friction near the zero relative velocity region in the friction-velocity curve (refer to Figure 5.4).

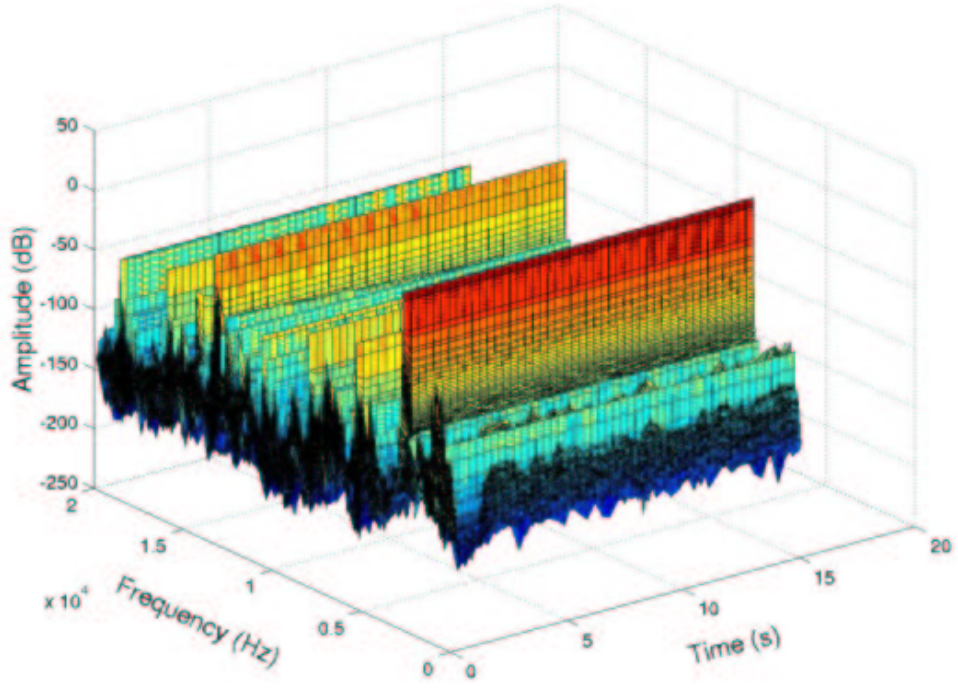

Figure 5.6: *A spectrogram plot of the out-of-plane vibration of the disc (showing one complete revolution).*

To determine the frequency content as well as the time variation, the spectrogram technique is used to analyse squeal responses predicted by the non-linear pin-on-disc model. For example, a spectrogram plot of the out-of-plane vibration of the disc, which has been calculated for an interval of one complete revolution of the disc, is shown in

Figure 5.6. The squeal frequency is found at 2648 Hz and is constant throughout the whole revolution of the disc. A number of peaks other than at the squeal frequency can also be observed. A slice cut through Figure 5.6 at a constant time shows that these peaks are, in fact, mostly higher harmonics of the squeal frequency, as illustrated in Figure 5.7. The high harmonic components arise from the non-linear characteristic of the friction-velocity curve used in the non-linear pin-on-disc model.

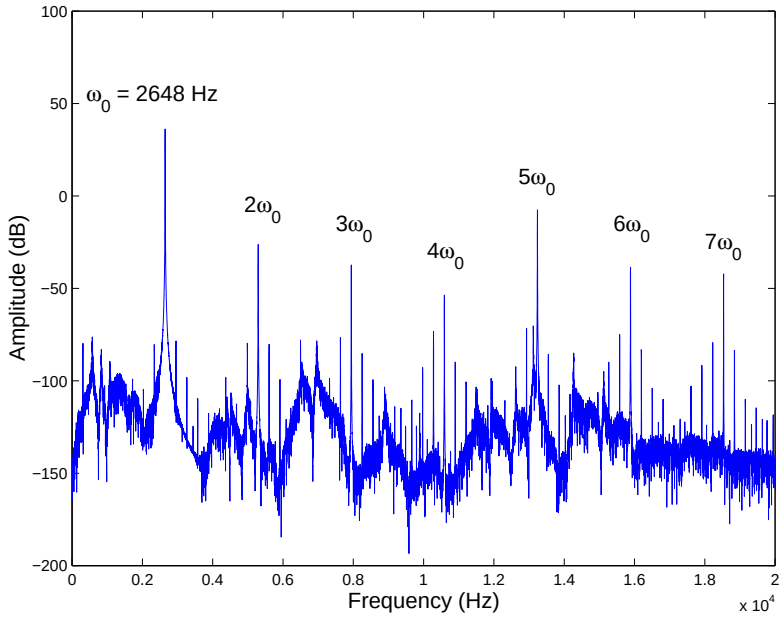

Figure 5.7: *A slice cut through Figure 5.6 at $t = 14$ s.*

Although the theoretical model can easily provide the ODS of the disc by plotting the responses at different instants of time, it might be appropriate at this stage to demonstrate the use of the observer frame of reference described in Chapter 2 to obtain the ODS of the disc along its circumferential line. The results obtained here will be compared with the measurements in Chapter 7. In the following calculation, the observer is assumed to be rotating with a constant angular speed of 10 Hz in the same direction as the disc rotation. The spectrum of the out-of-plane vibration of the disc as seen by the observer is plotted in Figure 5.8. Two major sidebands are observed with a frequency separation of 60 Hz. This immediately indicates that the ODS of the

disc along a circumferential line during squeal consists mainly of the 3 ND component. Furthermore, the amplitudes of the two sidebands are identical which implies that the 3ND component is in the form of a stationary wave fixed in the stationary frame of reference.

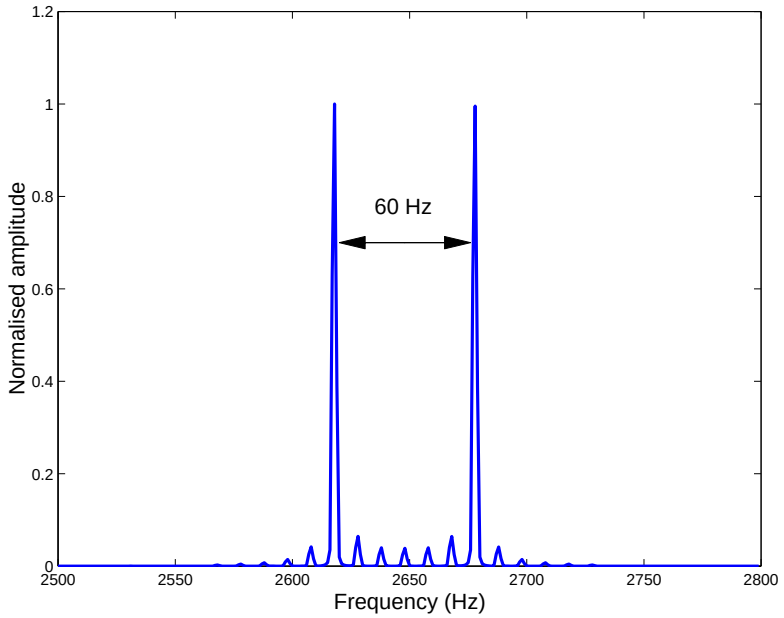

Figure 5.8: *Frequency spectrum of the out-of-plane vibration of the disc as observed by a rotating observer (Ω_b = 10 Hz).*

In the next set of simulations, the responses of the non-linear pin-on-disc model are calculated at different rotational speeds of the disc. Figure 5.9 shows the out-of-plane vibration of the disc and the normal contact force between the pin and the disc when the angular speeds of the disc are at 1, 2, 4 and 24 rev/min. In general, the amplitude of the out-of-plane vibration of the disc, which is directly related to the level of squeal noise, increases as the angular speed of the disc increases. However, if the disc spins too fast, the amplitude of the out-of-plane vibration of the disc could be high enough that the normal contact force becomes negative, as shown in Figure 5.9 when $\Omega = 24$ rev/min. In this case, the pin will lose contact with the disc and the theoretical model becomes invalid.

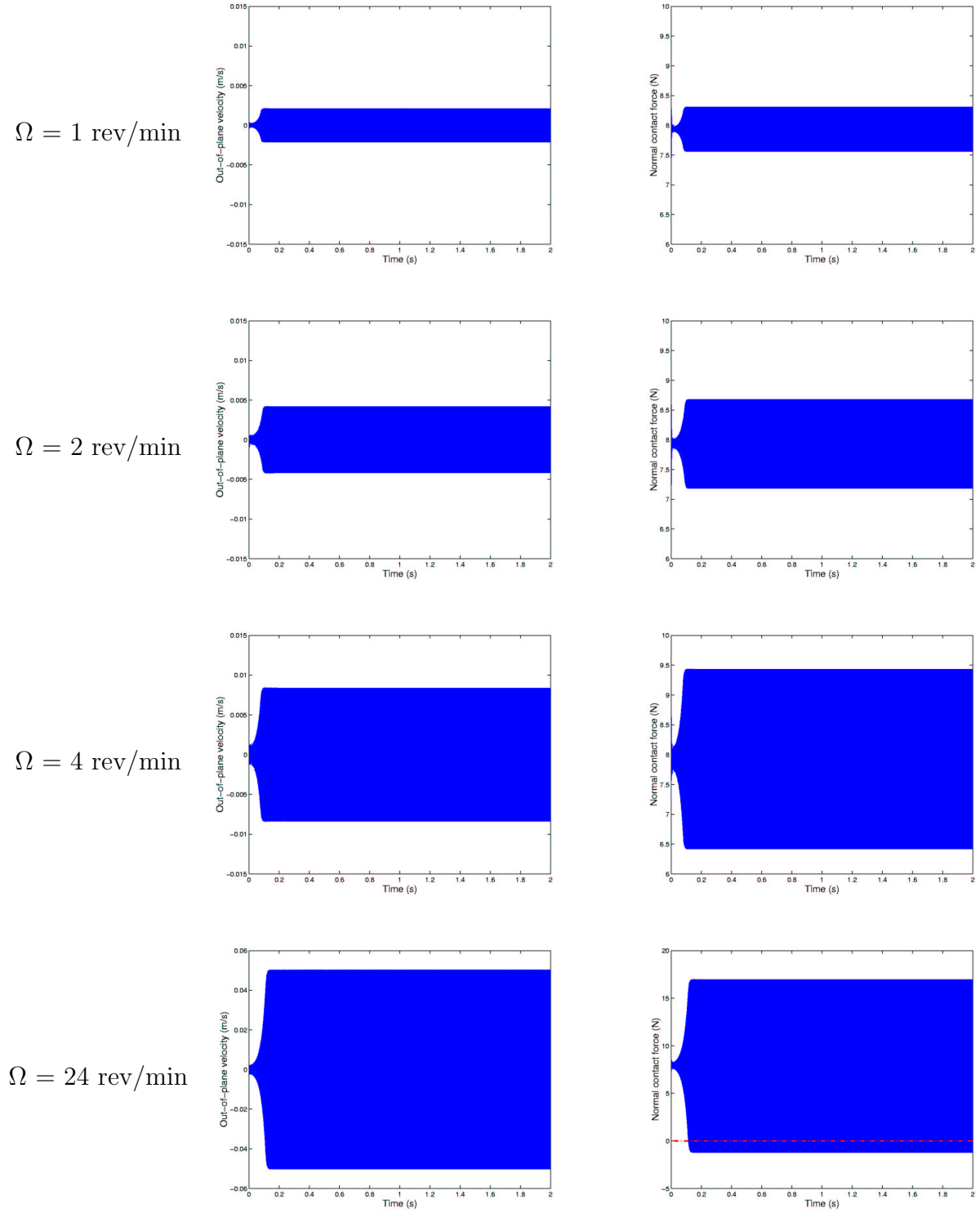

Figure 5.9: *Out-of-plane vibration of the disc and the normal contact force between the pin and disc at different angular speeds.*

5.4.2 Case B: Pin-on-disc systems with a mass-mistuned disc

The numerical simulations conducted in this section are calculated when the disc is mass-mistuned. As mentioned earlier, real brake discs do possess some degree of mistuning due to the presence of the mounting holes and ventilated fins. The primary reason for using masses as a way of mistuning the disc in the following simulations is that it can be reproduced more easily in experiments than any other type of mistuning. Although the actual brake disc is unlikely to be mass-mistuned, the generic results found in this section are still valid in general: for example, the nodal lines of mistuned discs are fixed with the discs and how the vibration modes are excited.

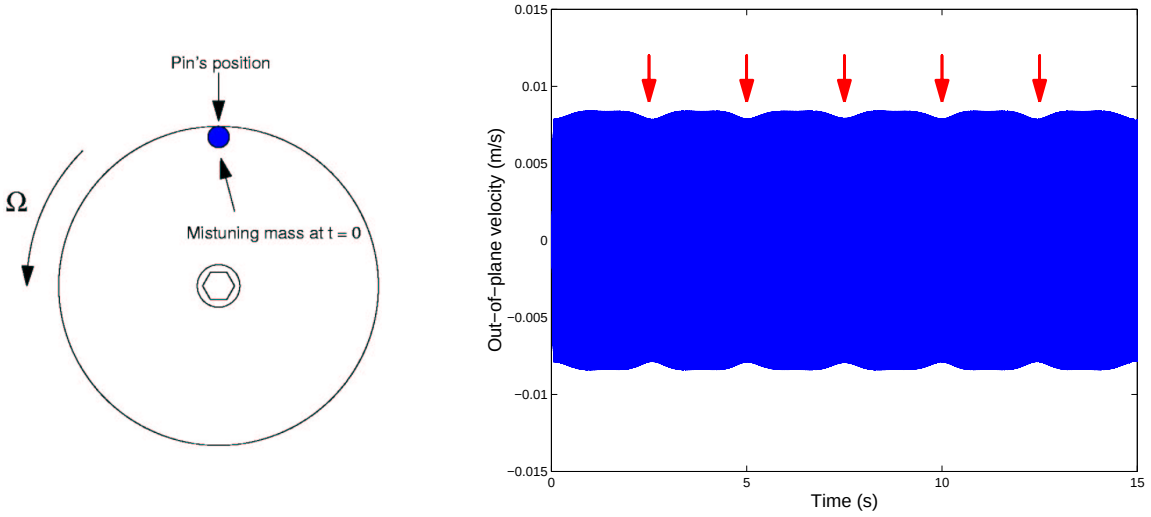

Figure 5.10: *The out-of-plane vibration of the disc which has been mistuned by a mass of 40 g at its outer edge.*

Figure 5.10 shows a time response of the out-of-plane vibration of the disc which has been mistuned by a mass of 40 g at its outer edge. The disc is rotating at an angular speed of 4 rev/min. At $t = 0$, the mistuning mass is located at the same position as the pin but on the opposite side of the disc. Unlike in the case of a perfectly-tuned disc where the amplitude of limit-cycle oscillations is constant, a number of small "dips" in the disc response can be observed when the disc is mistuned, as indicated by the red arrows in Figure 5.10. The occurrence of these dips depends on the position of the

mistuning mass with respect to the contact point between the pin and the disc, and will be discussed later.

If the out-of-plane response of the disc shown in Figure 5.10 is analysed using the spectrogram, the time-dependent frequency content of squeal response can be studied, as illustrated in Figure 5.11. It is found that the squeal frequency varies sinusoidally between 2634 and 2648 Hz. Similarly to previous analyses, the ODS of the disc can be determined using the observer frame of reference technique. The spectra of the out-of-plane vibration of the disc as seen by the observer at different instants of time are plotted in Figure 5.12 and the corresponding positions of the mistuning mass with respect to the pin's position are illustrated in Figure 5.13. The ODS of the disc during squeal is still dominated by the 3ND components of the original disc modes as in the case of the perfectly-tuned disc. However, at some instants (e.g. the red spectrum), the amplitudes of the two major sidebands are not identical which implies that there is a small component of a travelling wave in the ODS response.

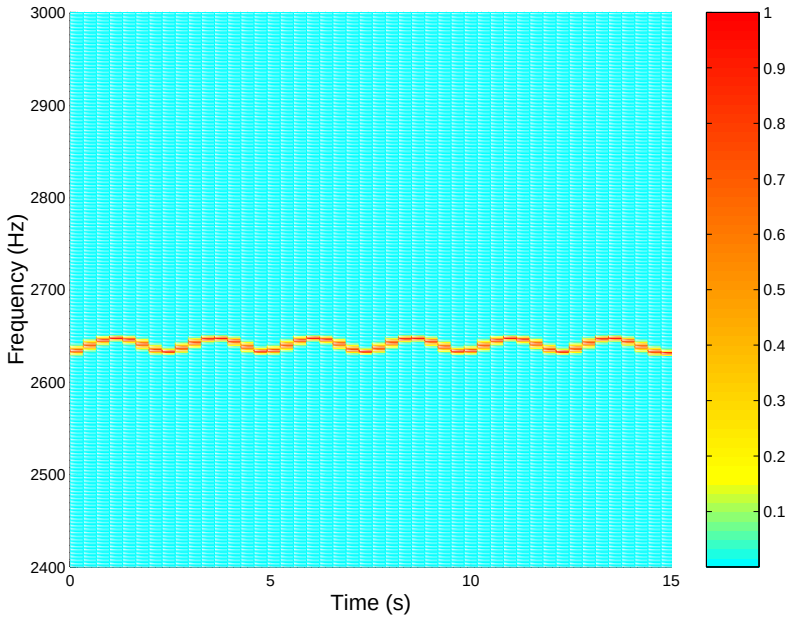

Figure 5.11: *Spectrogram plot of the out-of-plane vibration of a rotating mistuned disc (mistuning mass of 40 g).*

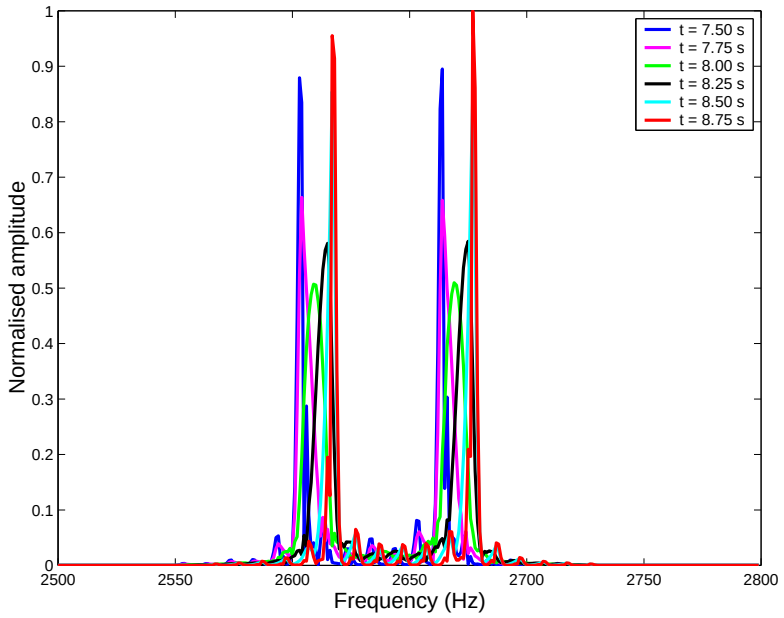

Figure 5.12: *Frequency content of squeal responses at different instants.*

Before discussing the reason for the variation in squeal frequency, the effect of a mistuning mass on the vibration characteristics of the disc must be described. First, the mistuning mass will split each of the pairs of double modes of the the disc into two distinct modes each with its own different natural frequency. Second, the nodal lines of each split mode pair are fixed in the disc with respect to the mistuning mass. For example, the 3ND mode pair splits, say, into "sine" and "cosine" modes. If the sine mode has one of its nodal lines passing through the mistuning mass, the cosine mode will have one of its anti-nodal lines passing through the mistuning mass. Third, the mode shapes of the sine and cosine modes are orthogonal to each other. Fourth, the natural frequencies of the sine modes are the same as those of the perfectly-tuned disc while the natural frequencies of the cosine modes are lower.

Now, we are in a position to discuss the variation of squeal frequency when the disc is mistuned with a single point mass. Figure 5.13 shows the positions of the mistuning mass and the nodal lines of the 3ND sine and cosine modes at different instants corresponding to the spectra shown in Figure 5.12. When the mass passes the

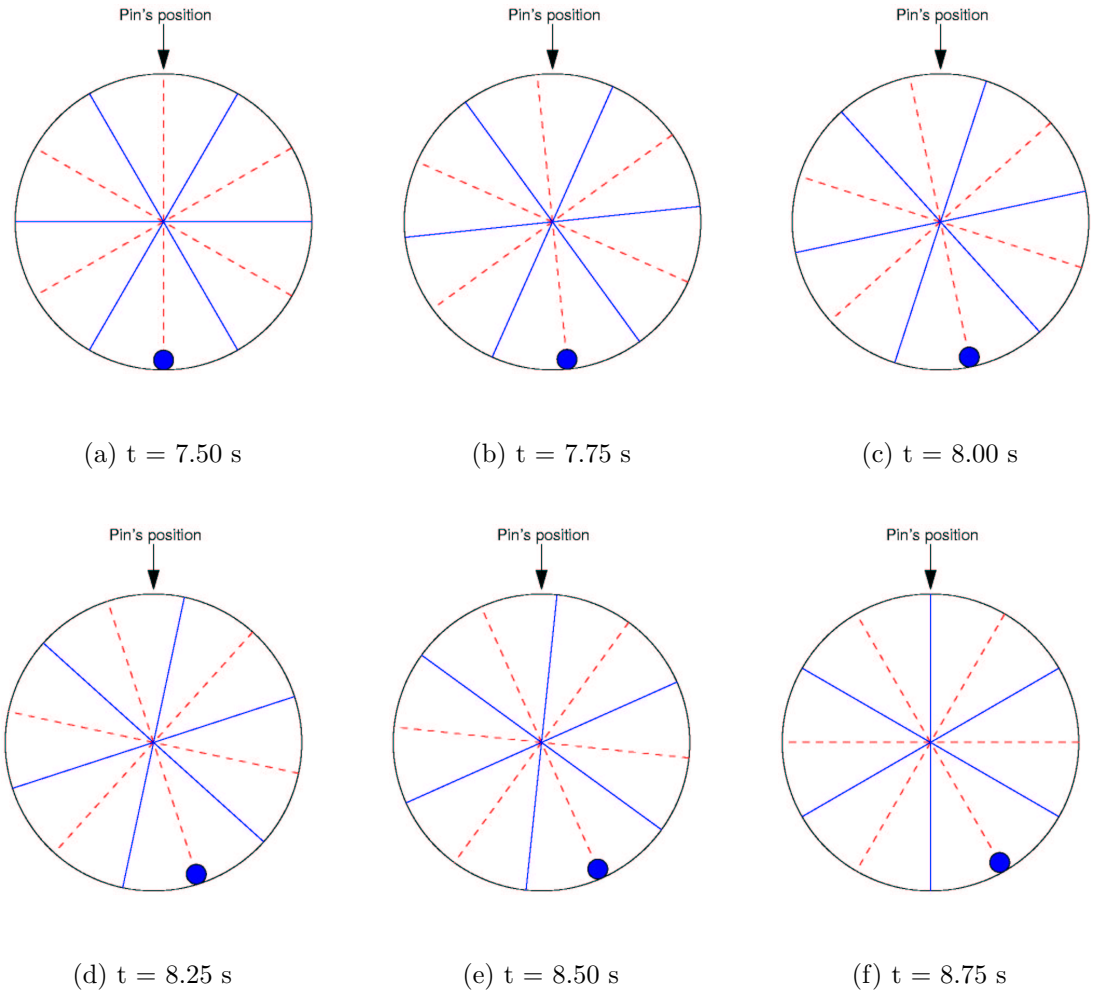

(a) t = 7.50 s (b) t = 7.75 s (c) t = 8.00 s

(d) t = 8.25 s (e) t = 8.50 s (f) t = 8.75 s

Figure 5.13: *The positions of the mistuning mass and the nodal lines of the 3ND sine (red dashed lines) and cosine (blue lines) modes with respect to the pin.*

lowest point of the disc at $t = 7.5$ s, as shown in Figure 5.13 (a), one of the nodal lines of the 3ND sine mode (the red dashed line) will pass by the pin. Thus, the 3ND sine mode of the mistuned disc will not be excited by the friction force. At the same instant, the 3ND cosine mode has an anti-nodal line at the contact point between the pin and the disc and, thus, it will be excited. Since it is the 3ND cosine mode that is excited, the natural (squeal) frequency of the combined system at this particular instant will reach its minimum value, as indicated by the blue spectrum in Figure 5.12. At $t = 8.75$ s, the situation is reversed. This time the 3ND sine mode is excited because it

has an anti-nodal line at the contact point between the pin and the disc. As a result, the squeal frequency will reach its maximum value, as indicated by the red spectrum in Figure 5.12. Between these two extremes, the natural (squeal) frequency of the combined system oscillates continuously and sinusoidally depending on the positions of the nodal lines of the 3ND sine and cosine modes with respect to the pin's position, as illustrated in Figures 5.13 (b) to (e). Since the nodal lines of the 3ND sine and cosine modes pass by the the pin 6 times in one complete revolution of the disc, there will be six cycles of rise and fall of the squeal frequency, as shown in Figure 5.11.

In the next simulation, the disc is mistuned by six masses equally spaced around its circumference and each mass weights 25 g. The out-of-plane vibration of the disc in one complete revolution of the disc is plotted in Figure 5.14. In this case, the dips in the response are more significant than the single mistuning mass because of the increase in the overall mistuning mass. However, the maximum amplitude of the out-of-plane vibration of the disc remains the same as in the case of a single mistuning mass. This is because the pattern of the mistuning masses does not affect the vibration characteristics of the 3ND sine mode of the disc. Hence, the locking between the second bending mode of the pin and the 3ND sine mode of the disc can still produce squeal. Figure 5.15 shows the variation of the squeal frequency calculated from the out-of-plane vibration of the disc plotted in Figure 5.14 as a function of time. It can be seen that the squeal frequency pattern is similar to the case of a single mistuning mass shown in Figure 5.11 - except the squeal frequency varies in a wider range due to the increase in the overall mistuning mass.

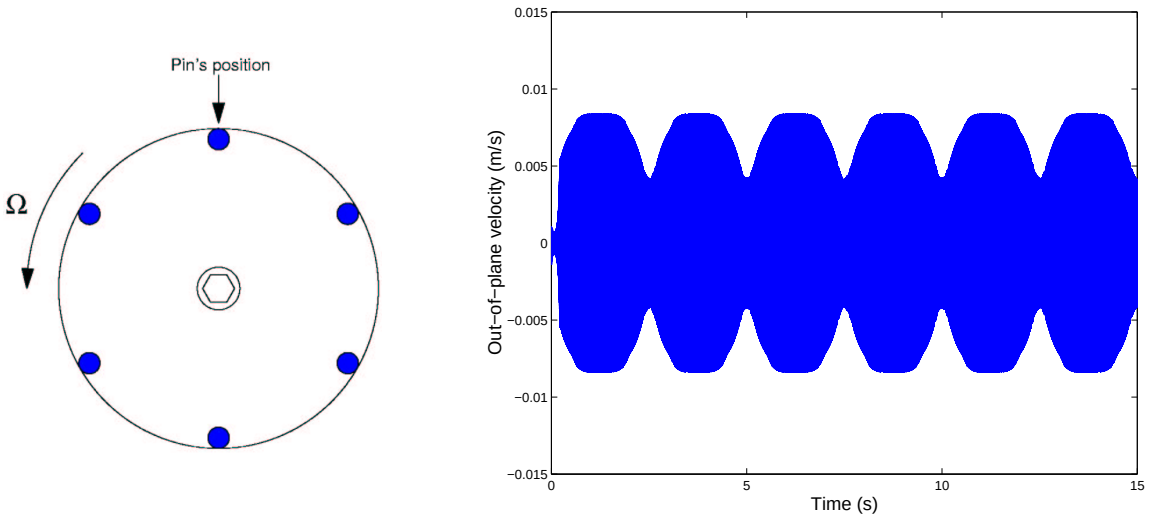

Figure 5.14: *The out-of-plane vibration of the disc which has been mistuned by six 25g masses equally spaced around its outer edge.*

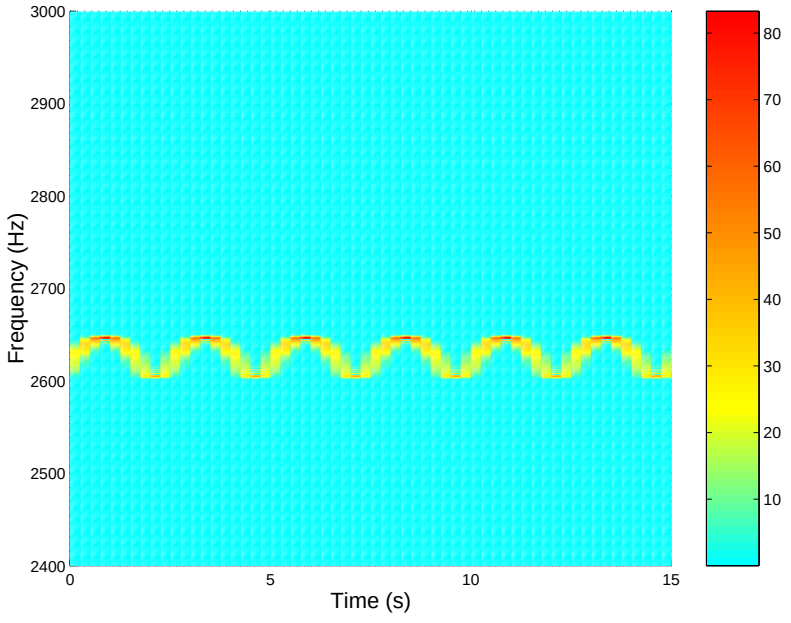

Figure 5.15: *Spectrogram plot of the out-of-plane vibration of the disc shown in Figure 5.14.*

As a final example, the next simulation aims to demonstrate that it may be possible to suppress squeal completely if the disc is modified by the additional of an appropriate pattern of masses (sometimes referred to as "mistuning" the disc). As can be seen from the previous simulations in this chapter, squeal interacts strongly with the 3ND modes of the disc and, thus, adjusting the natural frequencies of both the 3ND sine and cosine modes of the disc (by adding masses) might have the effect of altering the locking between the pin and the disc. Accordingly, the disc is now mistuned by 12 masses equally spaced around its circumference (alternating between the 25g masses and the 26g masses as shown in Figure 5.16) while the other system parameters are kept the same as those described in the previous simulation (Figure 5.14). These masses have the dual effect of shifting the 3ND mode frequencies (due to the 25.5 average mass) and splitting them (because of the $\pm 0.5g$ variation). The first effect may put the onset of instability out of the operating range, while the second effect may inhibit instability because the disc no longer has equal-frequency modes and, as such, cannot sustain a travelling wave motion (in the disc coordinates). Any initial perturbation will be damped by the damping of the system, as shown by the out-of-plane vibration of the disc plotted in Figure 5.16.

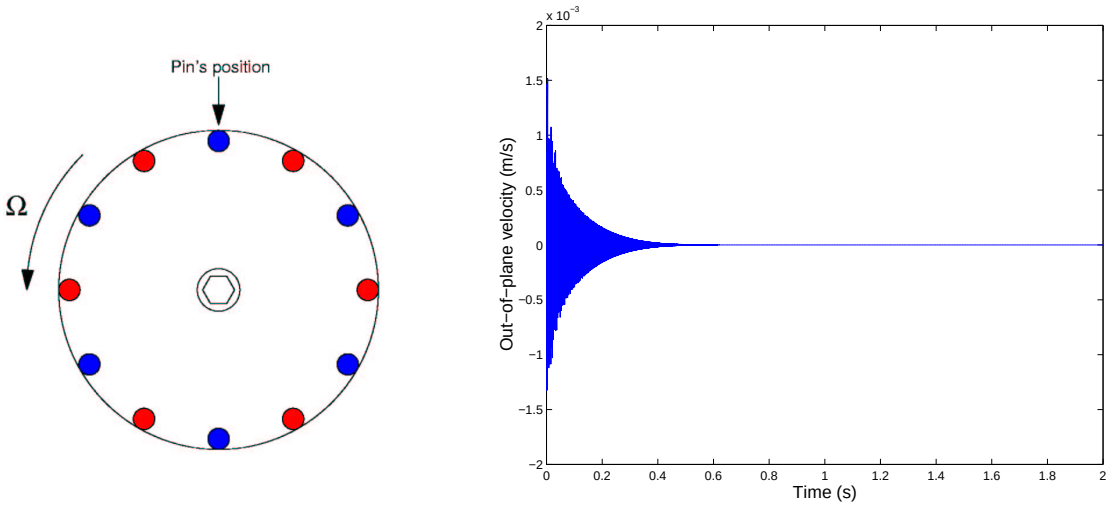

Figure 5.16: *The out-of-plane vibration of the disc when 12 mistuning masses are used (Note: the blue masses are 25g each and the red masses are 26g each).*

5.5 Conclusions

In this chapter, the linear pin-on-disc model has been extended to include the non-linear friction behaviour in order to study the limit-cycle characteristics of squeal responses. To avoid discontinuity in the equations of motion and to improve calculation time, a friction model in which the friction coefficient is a continuous function of the relative velocity and has a smooth variation around the zero relative velocity region, has been proposed. The non-linear pin-on-disc model also includes the effect of the rotational speed of the disc and the presence of mistuning masses. The responses of the combined system are calculated using the time integration method based on Runge-Kutta formulae.

In the numerical simulations conducted in this chapter, it has been found that the in-plane vibration of the pin is limited by the velocity of the disc at the contact point. Although velocity reversal can occur in theory, it has not been observed in any theoretical simulations presented here. If the disc is perfectly tuned, the squeal frequency is found to be constant throughout the whole revolution of the disc. The observer frame of reference technique has been applied in order to determine the ODS of the disc during squeal vibration. It has been shown that the ODS of the disc along a circumferential line during squeal consists mainly of the 3ND component and is a purely stationary wave. If the pin remains in contact with the disc during squeal, the amplitude of the out-of-plane vibration of the disc is found to increase as the disc angular velocity increases.

In the case of mistuned discs, the squeal frequency varies continuously and sinusoidally and its instantaneous value depends on the the positions of the nodal lines of the sine and cosine modes with respect to the position of the pin. The simulation presented in this chapter shows that it may be possible to suppress squeal completely if the disc is modified by the additional of an appropriate pattern of masses.

Chapter 6

Design and development of the test rig

6.1 Overview

Over the past few decades, pin-on-disc rigs have been widely used to study basic squeal characteristics. The first pin-on-disc rig was designed by Jarvis and Mills [6] in 1963. Since then, many other researchers have made a number of improvements to the design of the basic pin-on-disc rig. The most recent developments have been carried out by Akay *et al.* [73] in 1998 and by Duffour [74] in 2001. However, the designs of these rigs usually have the pin mounting system on the opposite side of the disc to the drive shaft and thus leave only a small area of the disc surface for measurement.

In this chapter, the design of the IC (Imperial College) pin-on-disc rig used in the experimental studies described in Chapter 7 is presented. One of the major requirements in the design of the IC pin-on-disc rig is to have one of the disc surfaces completely free for viewing. This feature would be very useful when the circular-scanning technique using a laser Doppler vibrometer (LDV) is conducted. Apart from this requirement, the IC pin-on-disc rig must also have the ability to vary the system parameters used in the numerical simulations conducted in the previous chapters. The main system parameters taken into consideration during the design of the IC pin-on-disc rig are as

follows:

- the angle of inclination of the pin;
- the contact location between the pin and the disc;
- the physical dimensions of the pin and the disc;
- the rotational speed of the disc;
- the static normal contact load.

In the final part of this chapter, the data acquisition system used in the circular scanning technique will be described.

6.2 Rig design

To fulfil the first major requirement, the IC pin-on-disc rig has been designed such that the pin mounting system and the shaft driving system are on the same side of the disc. This would leave the disc surface on the other side completely free for measurements, as shown in Figure 6.1. The schematic sketches of the IC pin-on-disc rig are presented in Figures 6.2 and 6.3. The other key design features of the IC pin-on-disc rig can be grouped into 4 parts: (i) the mounting of the disc and the drive shaft, (ii) the mounting of the pin, (iii) the rail system, and (iv) the motor-belt system.

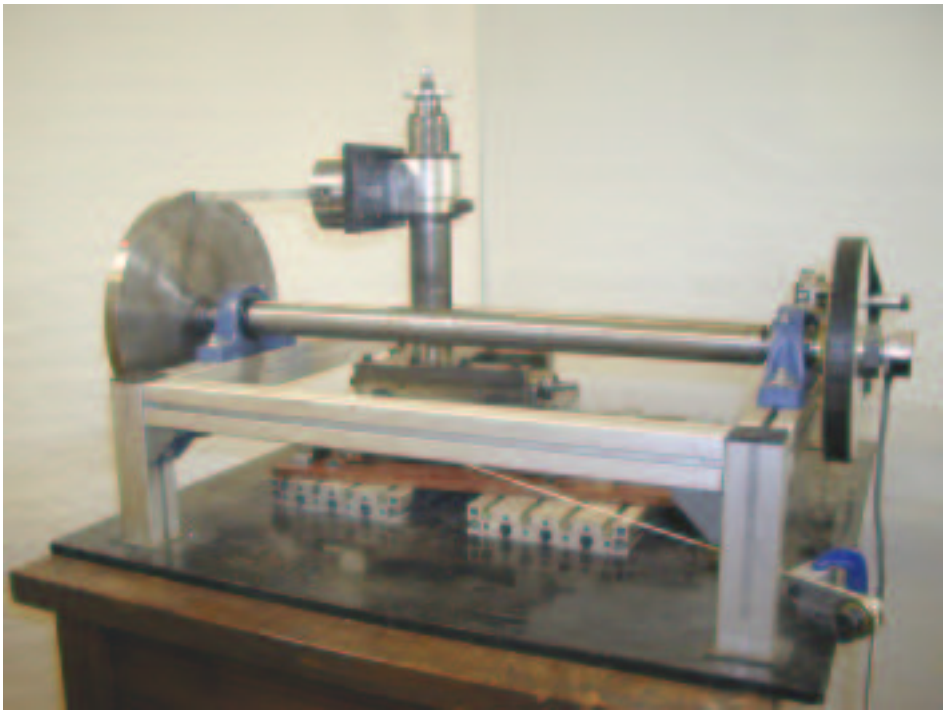

Figure 6.1: *The IC pin-on-disc rig.*

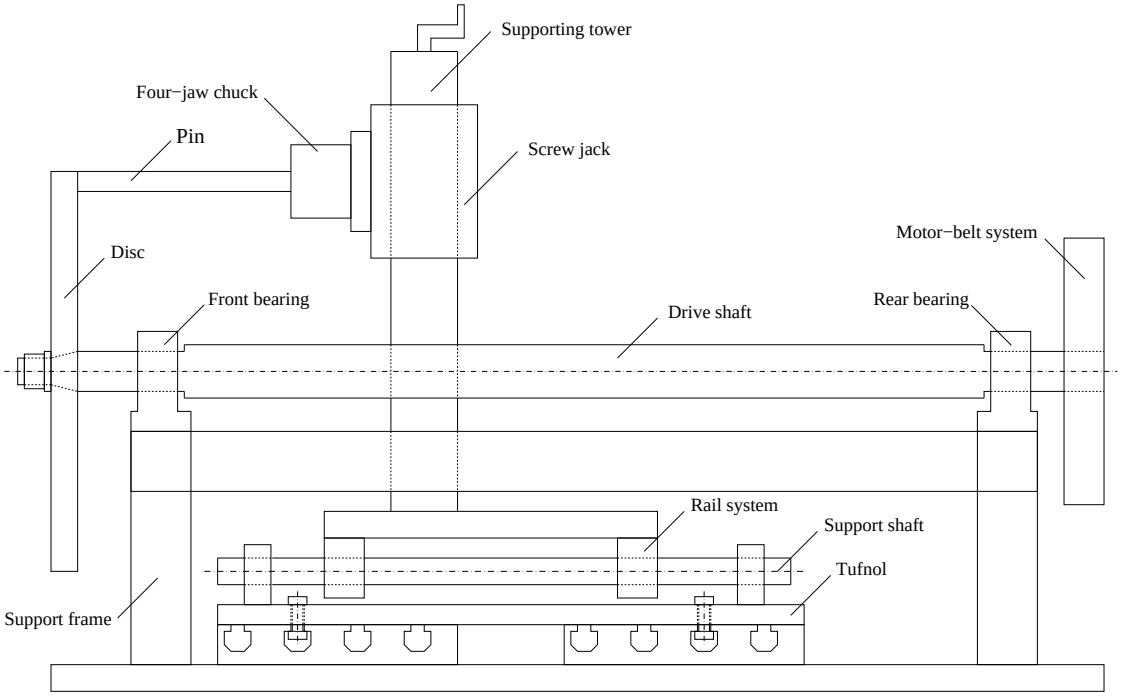

Figure 6.2: *Schematic sketch of the IC pin-on-disc rig (side view).*

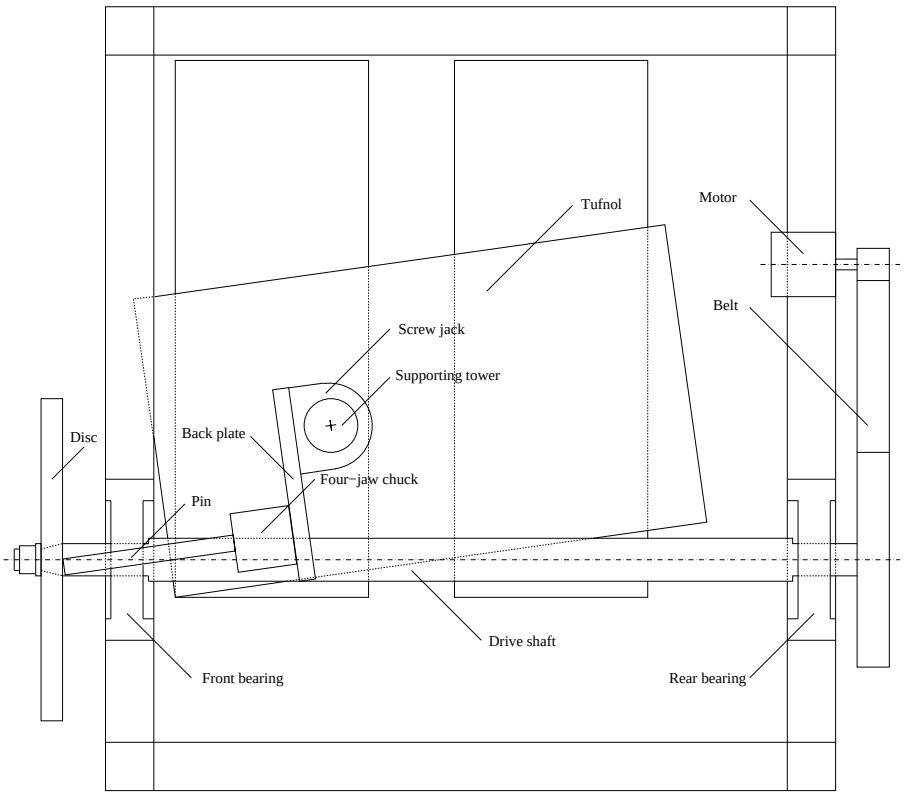

Figure 6.3: *Schematic sketch of the IC pin-on-disc rig (top view).*

6.2.1 Mounting of the disc and drive shaft

The disc is attached to the front end of the shaft by mean of a taper fit provided on both components. They are locked together using a screw located on the axis of the drive shaft. The shaft itself is supported on the platform by two ball bearings, as illustrated in Figure 6.4. The disc and the shaft are driven by a motor-belt system located at the back end of the drive shaft. Note: the bearings used in this rig have not been pre-loaded.

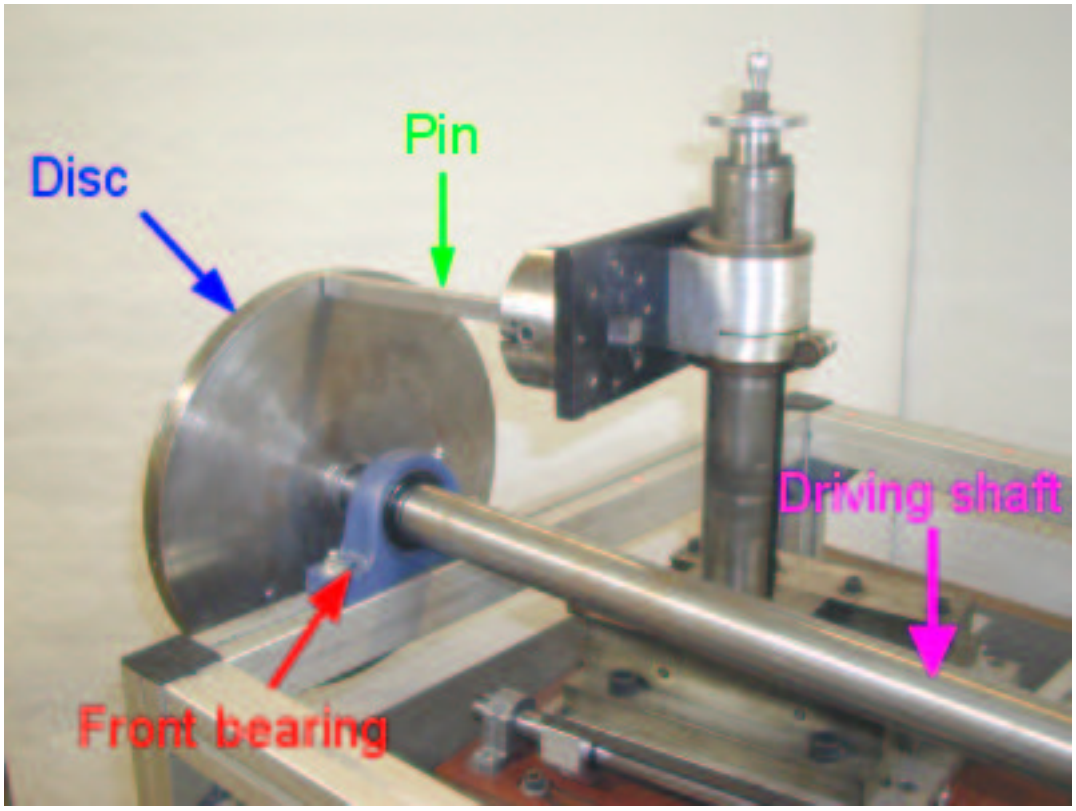

Figure 6.4: *The mounting of the disc and the drive shaft.*

6.2.2 Mounting of the pin

The pin is held in position by a four-jaw chuck, which is mounted onto one end of the back plate, as shown in Figures 6.4 and 6.5. The other end of the back plate is fixed onto a simplified version of a screw jack. The purpose of the back plate is to provide a necessary offset between the supporting tower and the drive shaft. The vertical contact location between the pin and the disc can be adjusted by moving the screw jack up and down the supporting tower. The whole pin support is fixed onto the rail system, as illustrated in Figures 6.5 and 6.6.

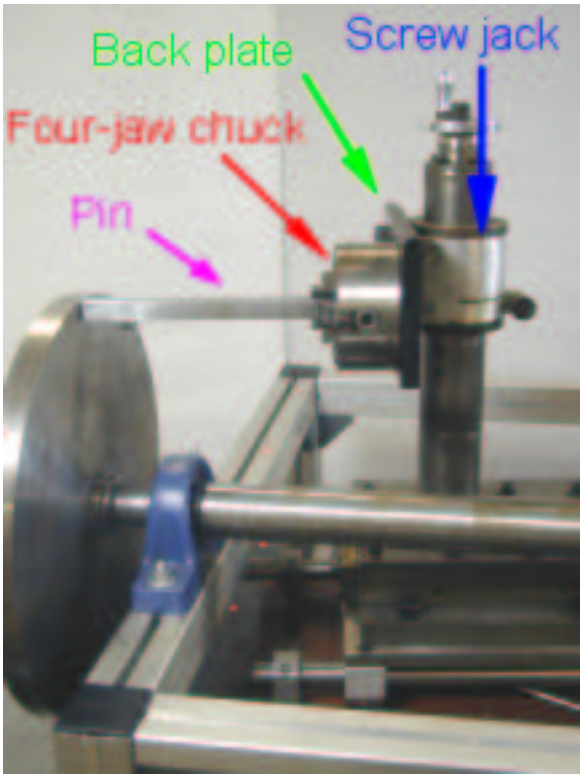

Figure 6.5: *The mounting of the pin.*

6.2.3 The rail system

To provide a constant contact pressure even when the running of the disc is not entirely true, a rail system (guide rails) is used, as shown in Figure 6.6. The base of the rail system comprises of two support shafts and four shaft supports rigidly fixed onto a tufnol plate. The top part of the rail system consists of four linear ball bearings fixed onto a steel platform. The four linear bearings slide on the two support shafts and sit between the four shaft supports, as illustrated in Figure 6.6. With this arrangement, the whole pin support, which is mounted on top of the rail system, can move freely along the two supporting shafts. The pin is then kept in contact with the disc by a static load via a cord passing around a pulley underneath the rail platform. The angle of inclination of the pin can be set by orientating the tufnol plate.

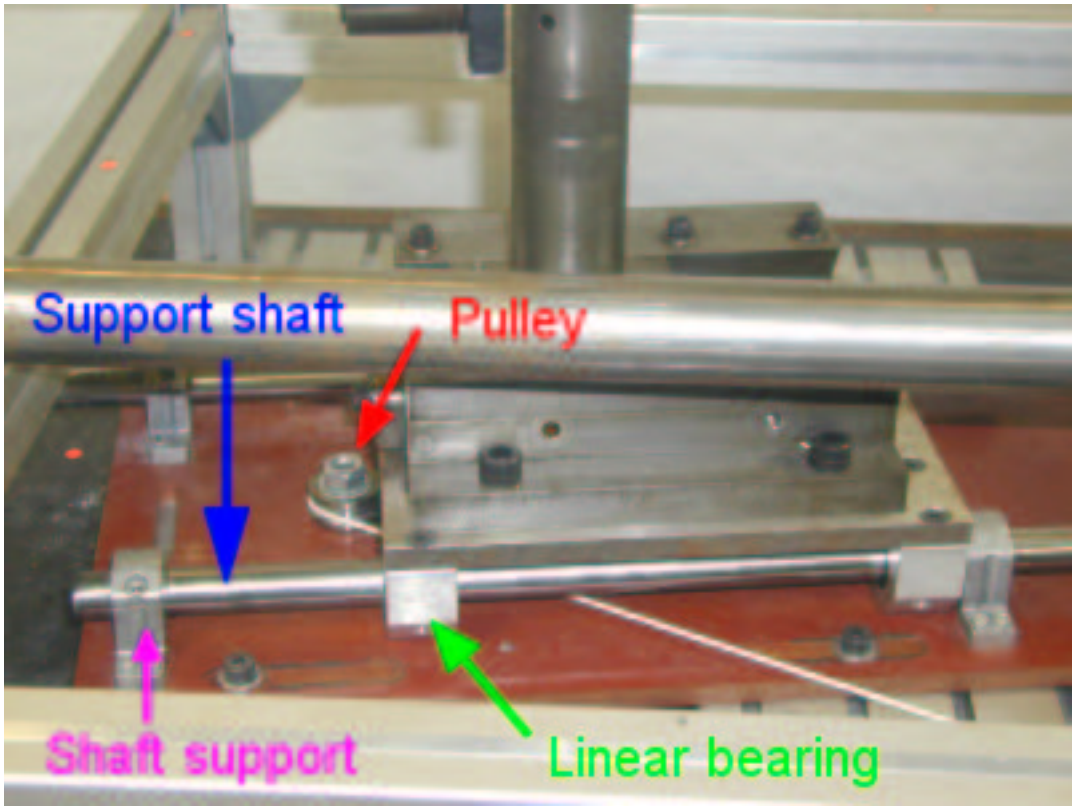

Figure 6.6: *The rail system.*

6.2.4 The motor-belt system

The disc and the shaft are driven by a motor-belt system located at the back end of the drive shaft, as shown in Figure 6.7. The belt is kept in tension by the aid of a jockey wheel. The motor is capable of driving the shaft up to 60 rev/min and can drive the shaft in both the clockwise and anti-clockwise directions. The latter feature provides a convenient way to perform experiments when the tests must be conducted for both the leaning and digging positions with the same angle of inclination. An encoder, which is used to record the angular speed of the disc, is attached to the back end of the drive shaft next to the motor-belt system.

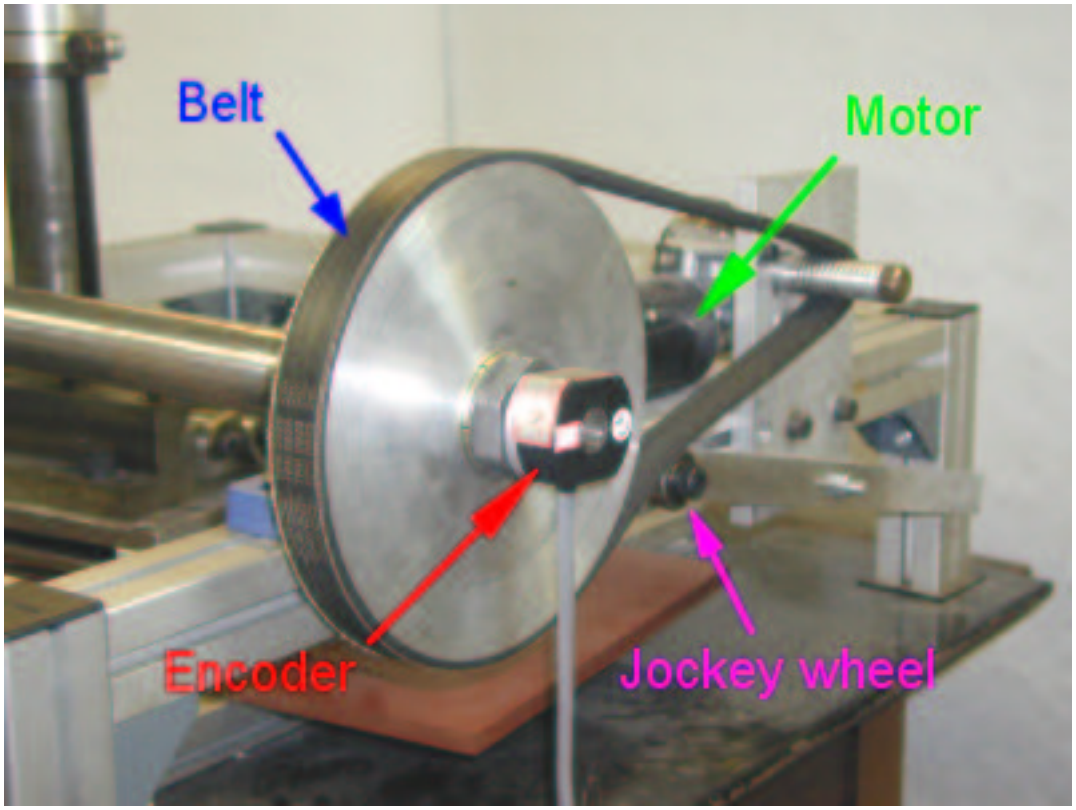

Figure 6.7: *The motor-belt system used to drive the main shaft and the disc (for clarity the mounting of the encoder has been removed during the photograph).*

6.3 Data acquisition system

In most experiments conducted in the next chapter, the responses are measured using a laser Doppler vibrometer (LDV). The data acquisition system for the LDV can be described in 2 parts: (i) the control of the mirrors, and (ii) the acquisition of the laser signals. The diagram of the data acquisition system is given in Figure 6.8. When the circular-scanning technique is employed, the computer generates sine and cosine signals with the same frequency and scan length. The two signals are then passed to the LDV controller via the output channels of a data acquisition card (NI 4451) to control the movement of the two mirrors inside the laser head. The computer programs used to controls the mirrors come by courtesy of Dr. Martarelli [32] and are written in Labview. The laser signal coming from the laser head is acquired by a 4-input data

acquisition card (NI 4452: maximum sampling rate of 204.8 kS/s). The shaft angular speed measured from the encoder is also recorded. Finally, all the input signals are saved onto the hard disc using a Labview routine for further analysis.

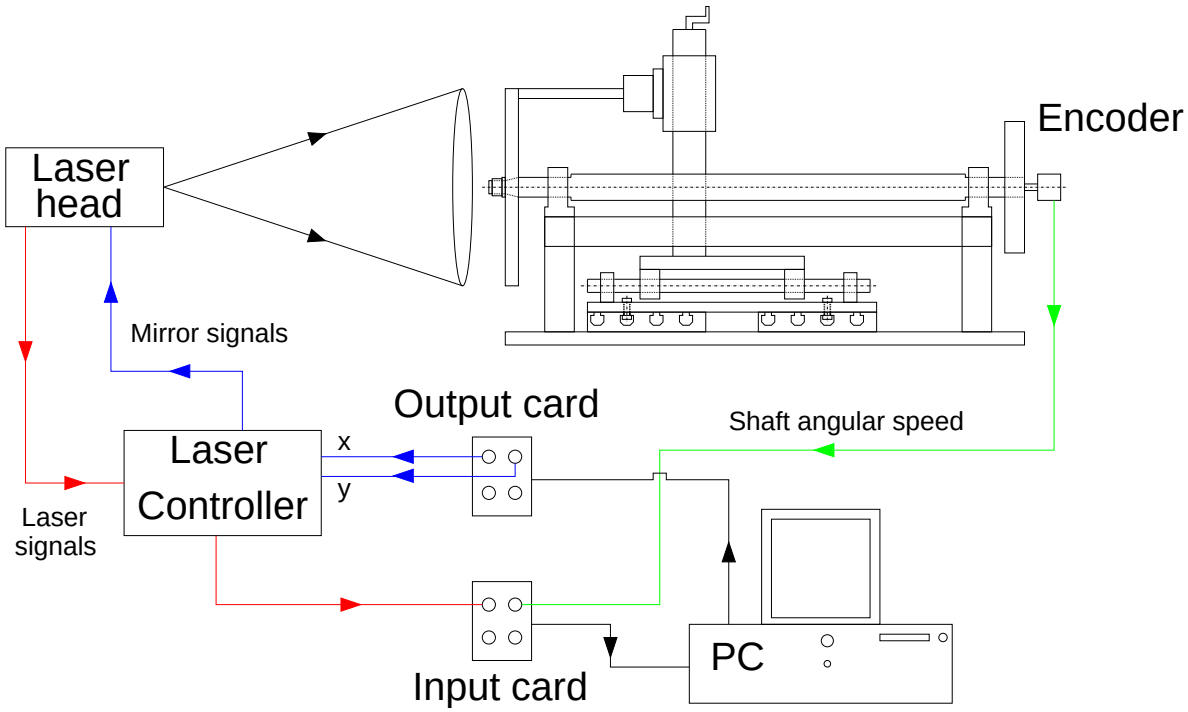

Figure 6.8: *The data acquisition system for the LDV.*

6.4 Conclusions

In this chapter, the design and development of the IC pin-on-disc rig has been described. The main advantage of the IC pin-on-disc rig over the other types of pin-on-disc rigs is that it provides a completely free surface for measurements. The data acquisition system for a circular scanning LDV has also been set up.

Chapter 7

Experimental studies

7.1 Overview

In this chapter, the results of experimental studies on the IC pin-on-disc rig are presented. The roles of the experiments can be divided into 2 parts: (i) to provide the numerical values for some of the system parameters, and (ii) to validate the theoretical models created in previous chapters. For some of the system parameters, for example the contact stiffnesses, numerical values cannot easily be predicted by theoretical models but could be estimated by deduction from experimental measurements. A procedure in which the numerical values of the contact stiffnesses and damping can be obtained is presented in this chapter. The second role of the experimental measurements is to validate the theoretical predictions and to make certain that the theoretical models are capable of representing the dynamic behaviour of the actual structure. The key experimental measurements which are conducted in this chapter can be listed as follows:

- modal tests of each individual component;
- modal tests of the pin-on-disc system when the pin is in contact with the disc;
- squeal measurements.

7.2 Modal tests of individual component

In this section, modal tests were conducted on the pin and the disc individually. The main objective was to obtain the modal properties - namely, the natural frequencies and mode shapes - of each component for comparison with predictions from the FE models. The experimental technique employed in this section for obtaining the modal properties was the stepped-sine test method in which the shaker was supplied by a discrete sinusoidal signal with a fixed amplitude and frequency. In order to encompass a frequency range of interest, the excitation frequency was stepped from one discrete value to another. After steady-state conditions were attained for each discrete frequency, the excitation force and responses were acquired in order to obtain the FRFs. The modal properties of the structures were then extracted from these FRFs using ICATS [1]. Once the modal properties were known, the FE models of the disc and pin were then manually updated by adjusting the material properties - mainly the Young's modulus.

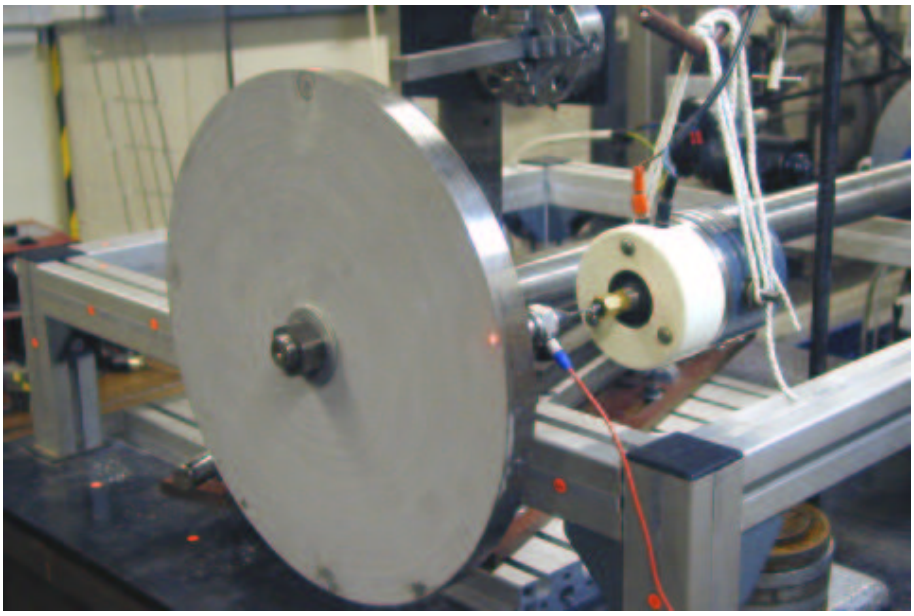

Figure 7.1: *Arrangement for stepped-sine tests of the disc (Note: the pin is not in contact with the disc).*

[1] Modal analysis software - property of Imperial College, London

Figure 7.1 depicts the experimental setup for the stepped-sine test of the disc. Excitation was provided by a shaker attached to one side of the disc and the response was measured by a LDV on the other side. The tests were conducted within the frequency range of 10 Hz to 7 kHz with a frequency increment of 1 Hz. The measured and predicted mobility FRFs of the disc are shown in Figure 7.2. During the updating process of the disc FE model, the (3,0) mode was chosen as the primary target because squeal generated by the pin-on-disc rig in the subsequent measurements appeared to interact strongly with this particular mode. It should also be noted that, after the updating, the predicted natural frequencies of the (2,0), (4,0) and (5,0) modes also agreed well with the measured data, to within 1 % accuracy. However, the measured natural frequencies of modes with zero or one nodal diameter did not agree well with the theoretical predictions. This was to be expected since the FE model of the disc did not include the presence of the drive shaft and the mounting of the disc.

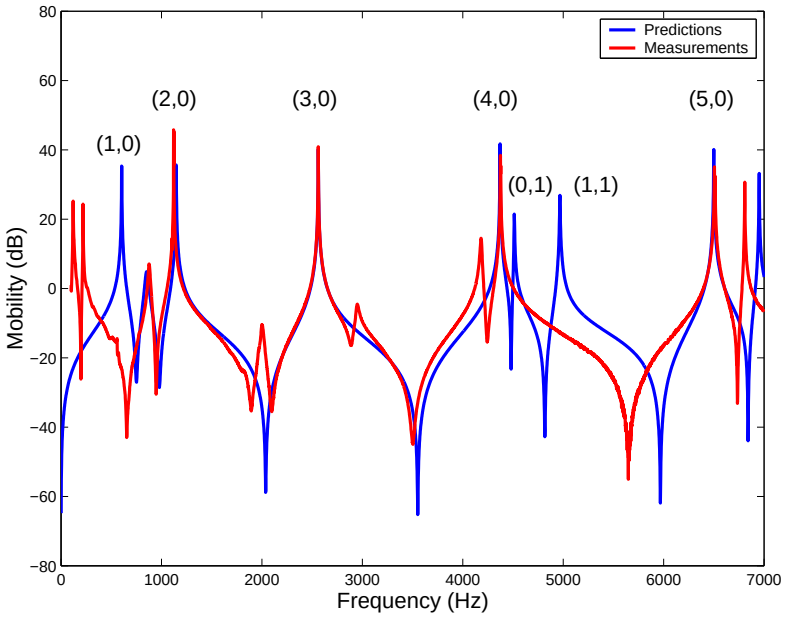

Figure 7.2: *Mobility FRFs of the disc: FE predictions after updating (blue) and measurements (red).*

As for the pin, the shaker was attached at the tip of the pin and the response was measured on the other side, as illustrated in Figure 7.3. The tests were conducted within the frequency range of 10 Hz to 6 kHz with a frequency increment of 1 Hz. Within this frequency range, four distinct modes associated with the bending of the pin were found at 256, 390, 2050 and 2645 Hz (with the structural damping factors of 4 %, 2 %, 4 % and 1 % of the critical damping, respectively), as shown in Figure 7.4. Although the pin itself had a square cross-section, its mounting was not perfectly symmetric and, as a result, each double mode pair of the pin split into two distinct modes. In this case, the first and second modes corresponded to the split of the "first bending mode of a clamped beam" and had their principal vibration in the z- and y-directions, respectively. The third and fourth modes corresponded to the split of the "second bending mode of a clamped beam" and had their principal vibration in the z- and y-directions, respectively.

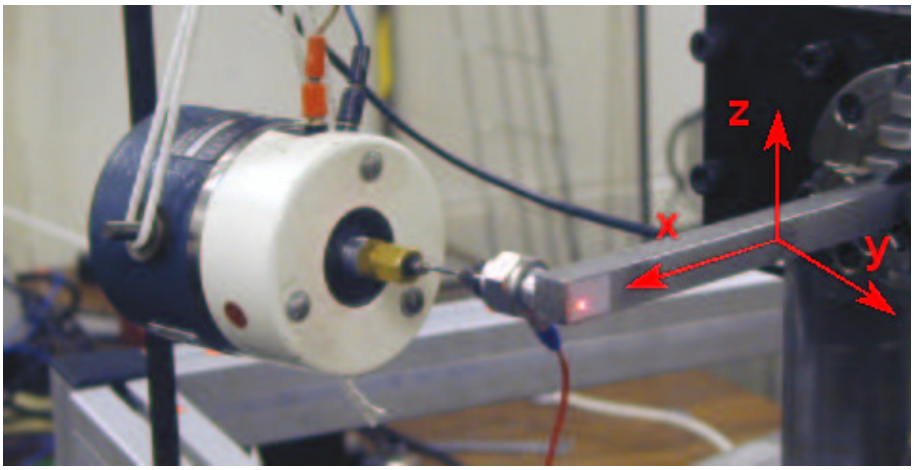

Figure 7.3: *Arrangement for stepped-sine tests of the pin.*

The comparison between the measured and predicted FRFs is shown in Figure 7.4. It can be seen that the FE model of the pin produced only two peaks on the FRF curve but, in fact, there were 4 modes (i.e. 2 double mode pairs) within this frequency range. Since the FE model of the pin was assumed to have a perfectly symmetric clamping in

both the y- and z-directions, the split of the double modes did not occur. The model updating of the pin focused on the fourth mode because squeal tended to interact with this mode of vibration.

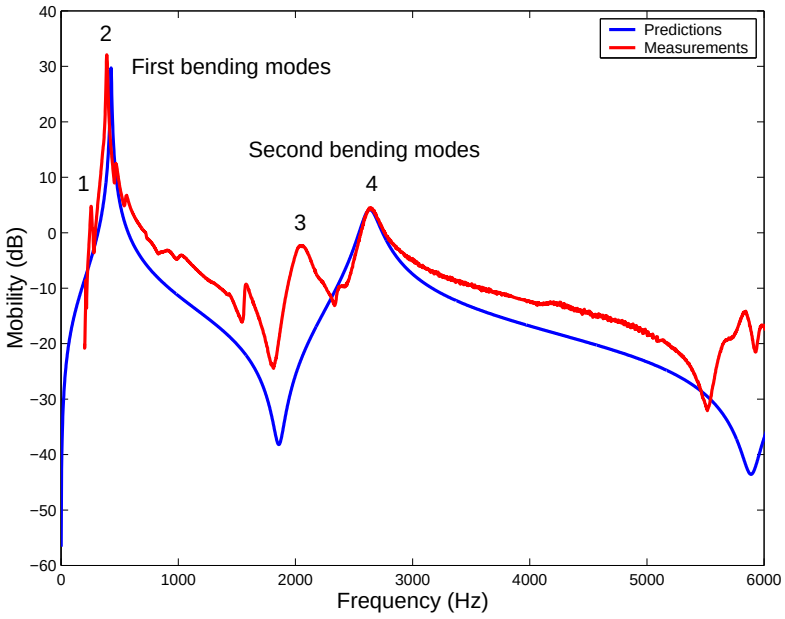

Figure 7.4: *Mobility FRFs of the pin: FE predictions (blue) and measurements (red).*

7.3 Modal tests on the combined pin-on-disc system

In this section, we repeat the modal tests which were conducted when the pin was in contact with the disc. It must be emphasised that the experiments were performed in the stationary configuration (i.e. with the disc not rotating). The primary objective of these experiments was to estimate the contact stiffnesses and damping between the pin and the disc using a combination of test data and the theoretical models presented in Chapter 4. The method of obtaining the contact stiffnesses and damping can be outlined as follows:

- measure the natural frequencies and damping of the combined pin-on-disc system

as a function of the static load;

- obtain the predicted natural frequencies of the theoretical pin-on-disc model as functions of the normal and tangential contact stiffnesses;
- compare the measured natural frequencies with the predictions in order to find a combination of the contact stiffnesses which gives the predicted natural frequencies the same values as the measured ones for each level of static load;
- use the contact stiffnesses found in the previous step to recalculate the eigenvalues of the pin-on-disc model but this time as functions of the normal and tangential contact damping coefficients;
- find a combination of the normal and tangential contact damping coefficients which gives the damping of the pin-on-disc model the same values as the measured ones for each level of static load.

The rationale behind the above procedure is based on the surmise that the contact stiffnesses between the pin and the disc increase as the static contact load increases: refer to Thomas and Sayles [67]. The increase in the contact stiffnesses would also lead to an increase in the natural frequencies of the combined system. Thus, by measuring the change in the natural frequencies and comparing them to the theoretical predictions, the contact stiffnesses could then be estimated.

To obtain the natural frequencies of the combined system experimentally, the stepped-sine excitation technique was used. Excitation was provided by a shaker attached to one side of the disc and the response was measured at the same location but on the opposite side of the disc, as shown in Figure 7.5. The measurements were conducted with a frequency increment of 1 Hz. During the sweep, the excitation force was controlled to a constant level (to within 2 % error). The angle of inclination of the pin was set to 8 degrees.

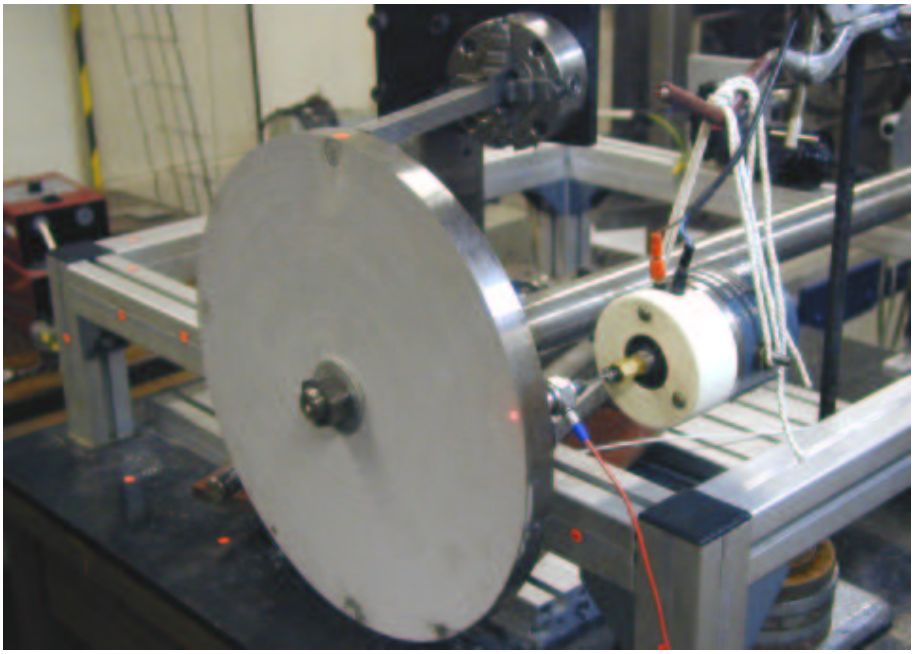

Figure 7.5: *The experimental setup of the combined system (the angle of inclination is set to 8 degrees).*

Since there are two types of contact stiffness parameter (i.e. normal and tangential), the procedure requires at least two modes of the combined system for comparison. In the following measurements, modes dominated by the (2,0) and (3,0) components of the original disc modes were chosen for comparison because the updated FE model of the disc can predict the natural frequencies of these two modes closer to the measured values than any other modes. Figure 7.6 shows mobility FRFs in the vicinity of the (2,0) modes of the disc at different values of static load. It is clear that there were two peaks on each FRF curve. The first peak corresponded to a mode dominated by the (2,0) sine component of the original disc mode. The natural frequency of this mode was not affected by the change in the static contact load because one of the nodal lines of the disc mode passed through the contact line between the pin and the disc. The second peak corresponded to a mode dominated by the (2,0) cosine component of the original disc mode. This mode, in contrast, had an anti-nodal line passing through the contact line and, thus, its natural frequency will be affected if the contact stiffnesses change. Figure 7.7 shows a similar characteristic for the (3,0) modes of the disc.

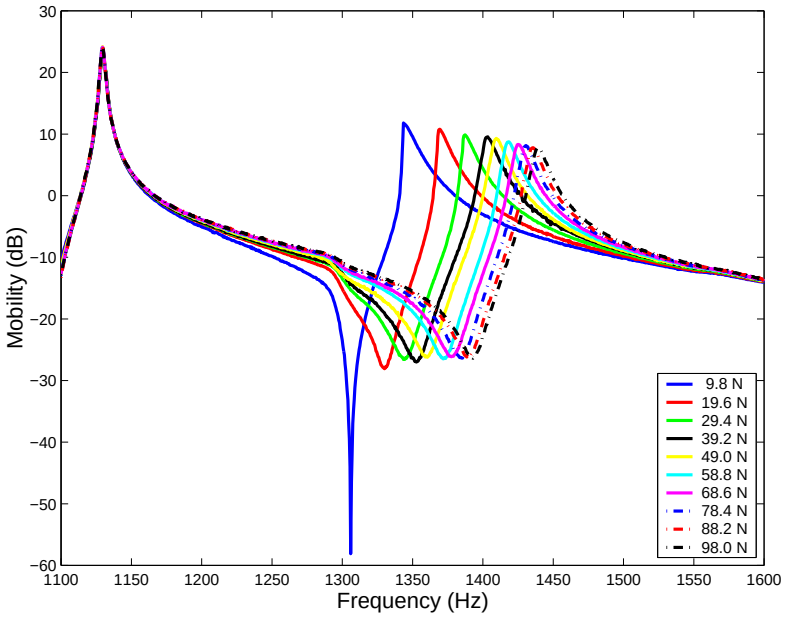

Figure 7.6: *Mobility FRFs in the vicinity of the (2,0) modes of the combined system at different values of static load.*

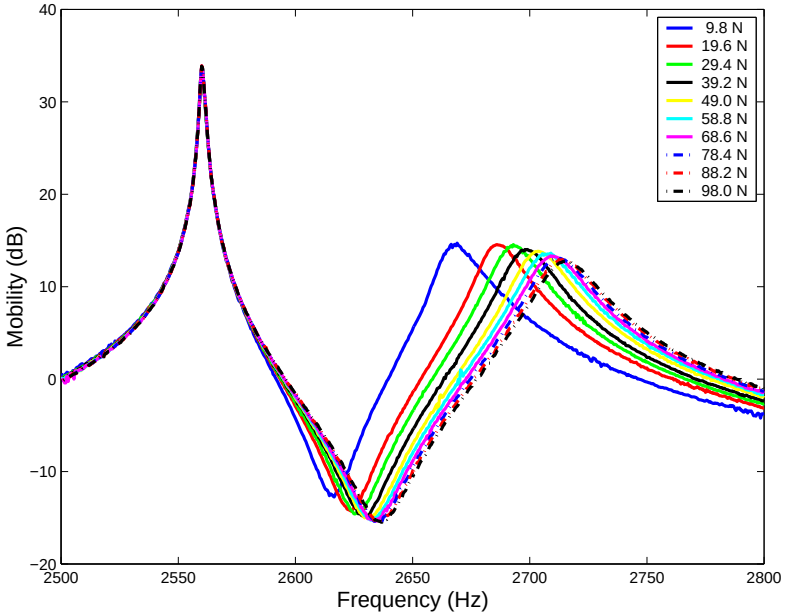

Figure 7.7: *Mobility FRFs in the vicinity of the (3,0) modes of the combined system at different values of static load.*

The natural frequencies and damping factors of the second peak for each of the FRF curves in Figures 7.6 and 7.7 were obtained using ICATS and are listed in Table 7.1.

Static load (N)	(2,0) cosine mode		(3,0) cosine mode	
	Natural frequency (Hz)	Structural damping (% critical damping)	Natural frequency (Hz)	Structural damping (% critical damping)
9.8	1343.5	0.353	2669.0	0.650
19.6	1369.5	0.404	2686.5	0.761
29.4	1387.5	0.454	2693.0	0.807
39.2	1403.5	0.683	2699.0	0.853
49.0	1409.5	0.680	2703.5	0.850
58.8	1418.5	0.691	2709.0	0.925
68.6	1425.0	0.674	2709.0	0.914
78.4	1430.5	0.728	2712.0	0.921
88.2	1435.5	0.709	2714.0	0.900
98.0	1439.0	0.682	2716.0	0.939

Table 7.1: *The natural frequencies and damping factors of the combined system at different values of static load.*

For clarity, the theoretical maps of the natural frequencies predicted by the linear pin-on-disc model are shown in Figures 7.8 and 7.9. By comparing the measured natural frequencies of each mode with the theoretical maps, the combinations of the two contact stiffnesses which gave the predicted natural frequencies the same values as the measured ones can be obtained for each value of static load. For example, considering the case when the static load was equal to 49 N, the measured natural frequency of the (2,0) cosine mode was found at 1409.5 Hz. The combinations of the two contact stiffnesses which gave the natural frequency of the theoretical model equal to this value are shown by the red curves in Figure 7.10. The same procedure can be applied to the (3,0) cosine mode and the combinations of the two contact stiffnesses are described by the blue curve in Figure 7.10. The point where the two curves intersect indicates the combination of the normal and tangential contact stiffnesses which will

match the predicted natural frequencies to the measured values for both the (2,0) and (3,0) modes simultaneously. For each value of static load, a plot similar to Figure 7.10 could be constructed. Thus, the values of the normal and tangential stiffnesses as a function of the static load can be obtained, as shown in Figures 7.11 (a) and (b).

The next step was to find the values of the contact damping (which was assumed to be a viscous type). By using the values of the normal and tangential contact stiffnesses from Figures 7.11 (a) and (b), the complex eigenvalues of the linear pin-on-disc model can be calculated as functions of the normal and tangential contact damping coefficients. Comparing the damping values between the predictions and the measured data, combinations of normal and tangential contact damping coefficients which will match the predicted damping to the measured values can be obtained, as shown in Figures 7.12 (a) and (b).

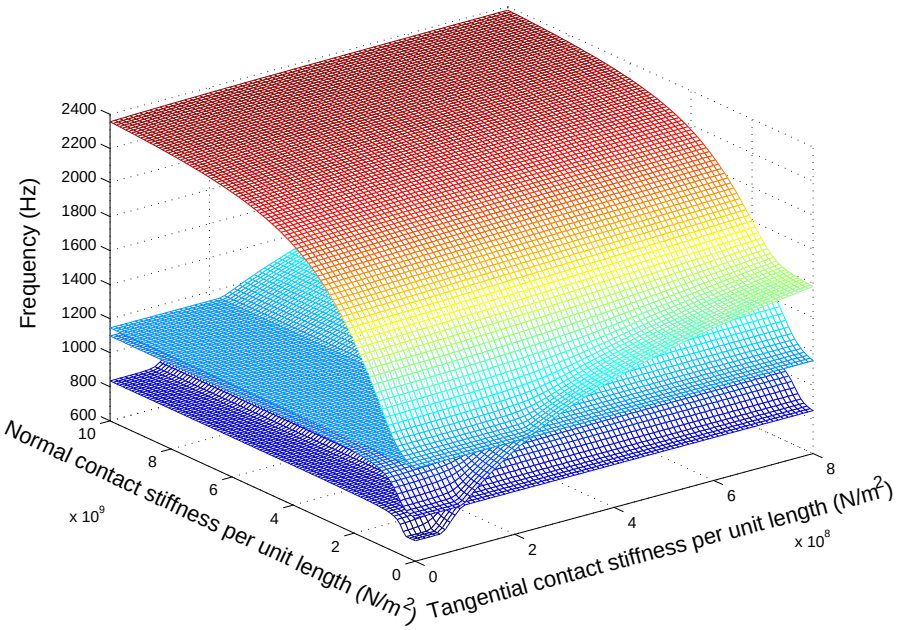

Figure 7.8: *Predicted natural frequencies of modes within the frequency range of 600 to 2400 Hz.*

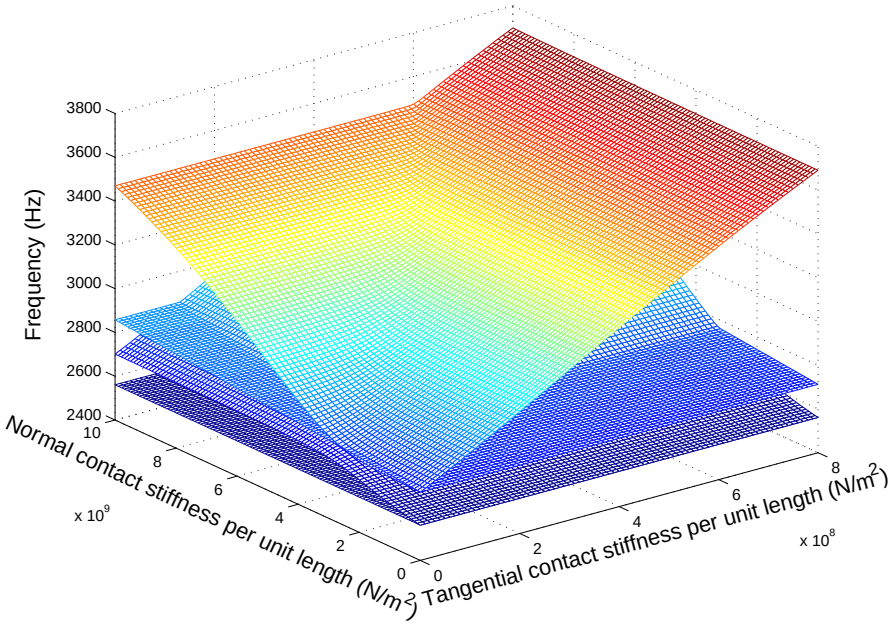

Figure 7.9: *Predicted natural frequencies of modes within the frequency range of 2400 to 3800 Hz.*

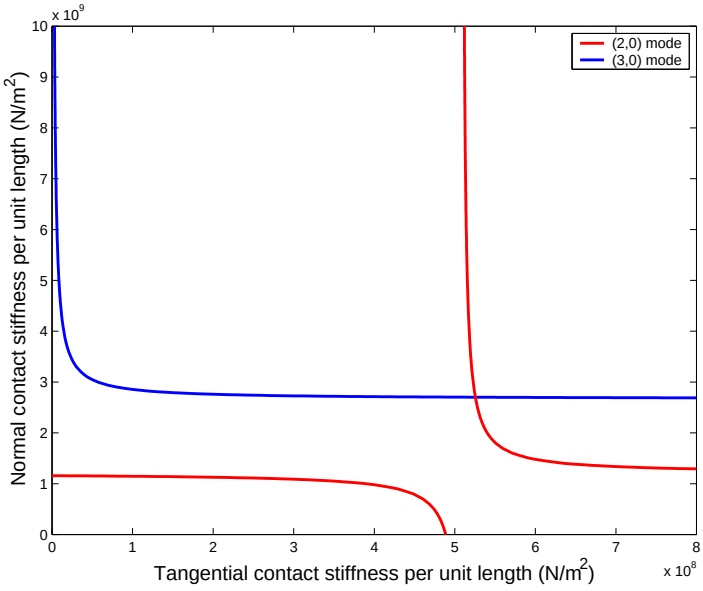

Figure 7.10: *Possible combinations of the normal and tangential contact stiffnesses, which will match the predicted natural frequencies to the measured values.*

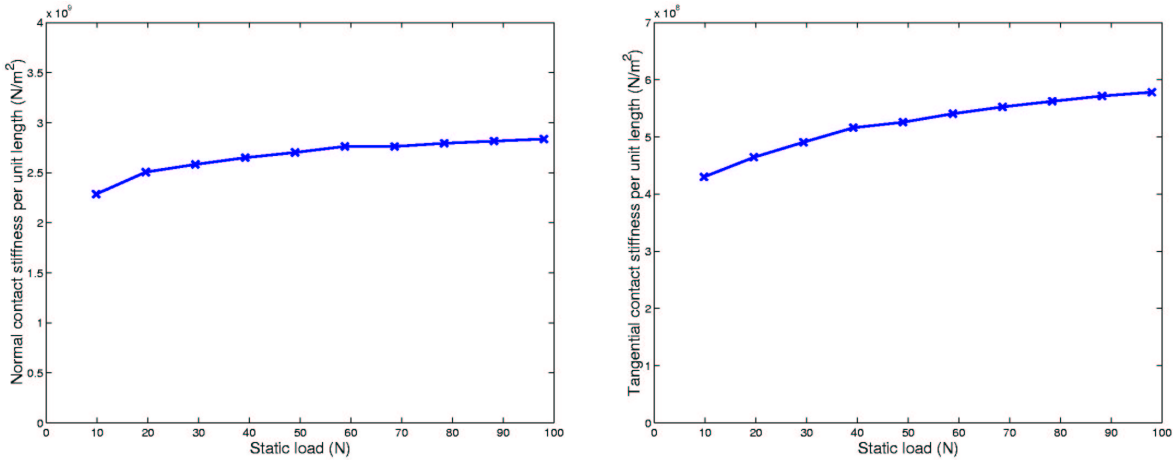

(a) Normal contact stiffness (b) Tangential contact stiffness

Figure 7.11: *The normal and tangential contact stiffnesses as a function of static load.*

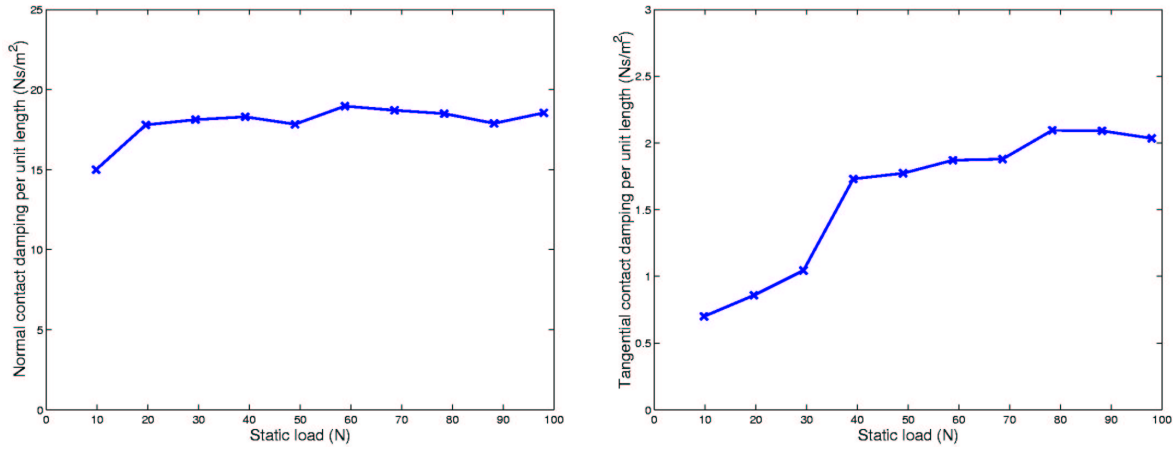

(a) Normal contact damping (b) Tangential contact damping

Figure 7.12: *The normal and tangential contact damping as a function of static load.*

In the region above a static load of 30 N, both the normal and tangential contact stiffnesses appear to vary linearly with the static load, as shown in Figures 7.11 (a) and (b). However, as the static load decreases below 30 N, the two contact stiffnesses veer off non-linearly. The variation of the contact stiffnesses with respect to the change in the static load may be explained in the following discussion. First, when the static

load is low, contact between the pin and the disc has not been fully established. As a result, some asperities may lose contact during the vibration, especially near resonance where the the amplitude of vibration is high. The loss of contact of some asperities could lead to non-linear behaviour within the contact zone and may result in a non-linear variation of the contact stiffnesses with respect to the static load. As the static load increases above 30 N, a full contact would have been established and the loss of contact of some asperities no longer affects the overall behaviour of the system. Hence, the sign of the non-linearity disappears at high regions of static load. Furthermore, increasing the static load would generally lead to the increase in the real contact area or, in other words, the increase in the number of contact asperities. Since asperities can also be thought of as "small" springs connected in parallel, increasing the number of contact asperities would, in effect, raise the overall contact stiffnesses.

In summary, a combination of test data and the theoretical models can be used to estimate the values of the contact stiffnesses and damping. With the static load varying between 9.8 and 98 N, it has been found that the normal contact stiffness per unit length of the pin-on-disc system varies between 2.3 and 2.9 GN/m^2 and the tangential contact stiffness per unit length varies between 0.43 and 0.58 GN/m^2. As for the damping, the normal contact damping per unit length varies between 15 and 19 kNs/m^2 and the tangential contact damping per unit length varies between 0.7 and 2.1 kNs/m^2.

7.4 Experimental measurements during squeal

The results presented in this section are used mainly to validate the theoretical models created in Chapters 4 and 5. First, a set of experimental measurements were conducted to determine the operating deflection shapes (ODS) of the disc and the pin during squeal. Second, the transient build-up of squeal response predicted by the non-linear pin-on-disc model was verified. Comparisons of the limit-cycle amplitudes between predictions and measurements were then made at different values of disc rotational

speeds. Finally, squeal tests were performed with a mass-mistuned disc.

7.4.1 ODS of the disc during squeal

To determine the variation of the ODS of the disc along a circumferential line during squeal, a circular scanning LDV has been used to measure the out-of-plane vibration of the disc. Figure 7.13 shows the LDV output spectrum (red line) in which two sidebands were found at 2626 and 2686 Hz. This suggests that the squeal frequency was at 2656 Hz if measured in the stationary frame of reference. In the same figure, the predicted spectrum (blue line), which has been calculated by the non-linear model presented in Figure 5.8, is also shown for comparison. The predicted squeal frequency was found at 2648 Hz and was within 0.3 % of the measured value. Both spectra show the frequency separation of 60 Hz between the two sidebands. Since the scan rate is at 10 Hz, the separation of the sidebands immediately indicates that the ODS of the disc consisted mainly of the 3ND component during squeal. Furthermore, the two sidebands had identical magnitudes which implies that the corresponding ODS was a pure stationary wave.

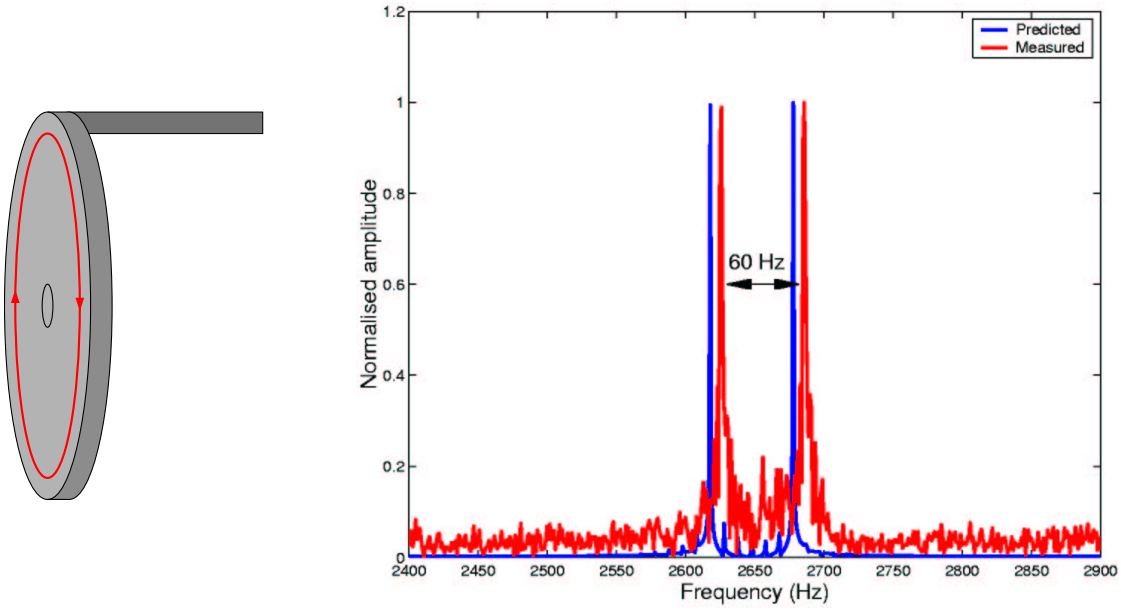

Figure 7.13: *Comparison between the circular scanning LDV spectrum and the prediction from the non-linear model.*

It is also possible to determine the ODS of the disc along a radial line by using straight-line sinusoidal scans. In this case, only one of the LDV mirrors was supplied with a sinusoidal signal which caused the laser beam to scan continuously and sinusoidally along a straight line. The analysis of the straight-line scan can be described by the following procedure. First, it is assumed that the complex ODS of the disc, V_z, can be expressed as:

$$V_z(x,t) = V_R(x)\cos\omega t + V_I(x)\sin\omega t, \tag{7.1}$$

where x is the normalised position vector representing all the points along the scan line, ω is the squeal frequency, and V_R and V_I are the real and imaginary components of the vibration, respectively. It is further assumed that the complex ODS of the disc has a smooth deflection pattern and can be described by the following polynomials:

$$\begin{aligned} V_R(x) &= \sum_{j=0}^{p} V_{R_j}\, x^j, \\ V_I(x) &= \sum_{j=0}^{p} V_{I_j}\, x^j. \end{aligned} \tag{7.2}$$

If the measurement points are sinusoidally scanned at frequency Ω along the radial line of the disc, the instantaneous position of the laser spot can be represented by

$$x(t) = \cos \Omega t. \tag{7.3}$$

By substituting equations (7.2) and (7.3) into equation (7.1), the vibration of the disc can now be expressed solely as a function of time as:

$$V_z(t) = \sum_{j=0}^{p} V_{R_j} \cos^j \Omega t \cos \omega t + \sum_{j=0}^{p} V_{I_j} \cos^j \Omega t \sin \omega t. \tag{7.4}$$

By expanding the trigonometric terms in the above equation and re-arranging them according to the terms $(\omega \pm j\Omega)$, the vibration of the disc can also be rewritten as:

$$V_z(t) = \sum_{j=0}^{p} A_{R_j} \cos(\omega \pm j\Omega)t + \sum_{j=0}^{p} A_{I_j} \sin(\omega \pm j\Omega)t, \tag{7.5}$$

where A_{R_j} and A_{I_j} are the amplitudes of the real and imaginary components of the LDV output spectrum at $(\omega \pm j\Omega)$. By comparing equation (7.4) with equation (7.5), it is possible to derive the relationships between the sideband coefficients, A_R and A_I, and the polynomial coefficients, V_R and V_I, by a simple matrix transformation, $[T]$, as follows:

$$\begin{aligned} \{V_R\} &= [T]\,\{A_R\}, \\ \{V_I\} &= [T]\,\{A_I\}. \end{aligned} \tag{7.6}$$

As an example, matrix $[T]$ for a polynomial up to the third order (i.e. $p = 3$) is given

in the following equation.

$$[T] = \begin{bmatrix} 1 & 0 & -2 & 0 \\ 0 & 2 & 0 & -6 \\ 0 & 0 & 4 & 0 \\ 0 & 0 & 0 & 8 \end{bmatrix}. \tag{7.7}$$

Note: the form of matrix $[T]$ up to the fifteenth order can be found in Martarelli [32]. Once the polynomial coefficients, V_R and V_I, are found, the ODS can be reconstructed using equation 7.1. It should also be noted that the spatial resolution of the ODS can be chosen arbitrarily, depending on the desired display.

Figure 7.14 shows the real and imaginary components of the ODS of the disc along a radial line during squeal. It can be seen clearly that the out-of-plane vibration of the disc along this radial line was dominated by the zero nodal circle component. With the fact that the imaginary component was not zero, the ODS of the disc was slightly complex (i.e. each point along the radial line reached its own maximum deflection at a different instant in the vibration cycle to that of its neighbours). The measured ODS of the disc at different time instants is plotted in Figure 7.15 (a) and the corresponding ODS obtained from the non-linear model is plotted in Figure 7.15 (b) for comparison. The results shown in Figures 7.13 and 7.15 confirm that the disc component has been adequately represented by the theoretical model.

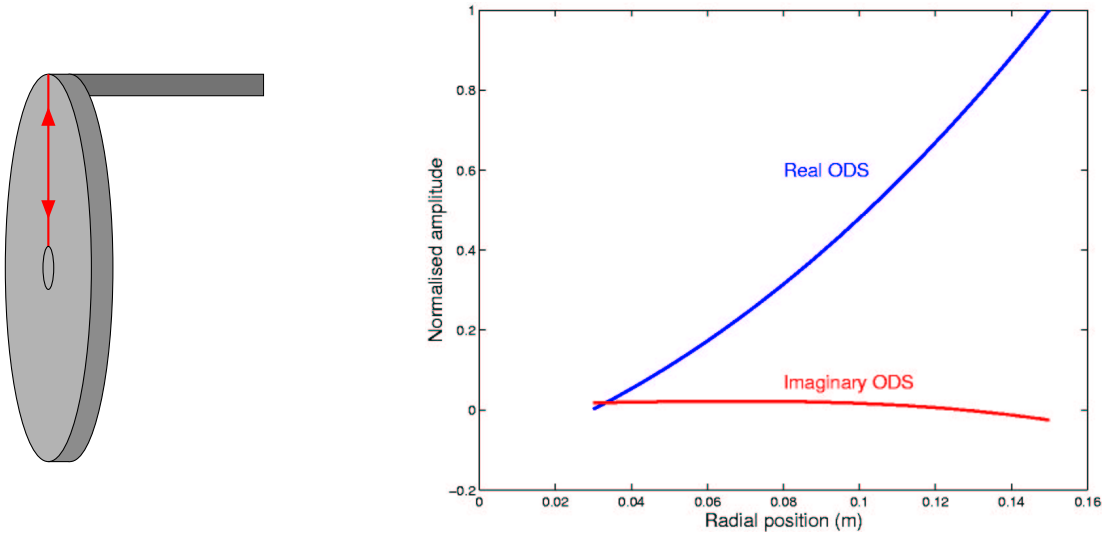

Figure 7.14: *Polynomial description of the real and imaginary components of the ODS of the disc along a radial line during squeal.*

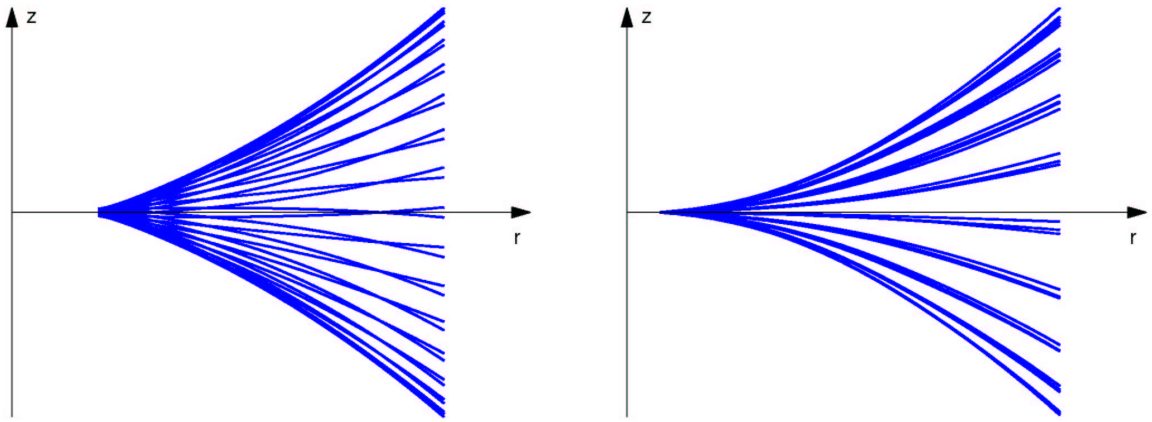

(a) (b)

Figure 7.15: *Vibration pattern of the disc during squeal at different time instants obtained from: (a) measurements (b) predictions.*

7.4.2 ODS of the pin during squeal

Turning now to consider the pin, the straight-line scan was conducted along the lengthwise direction of the pin. The real and imaginary components of the pin during squeal are plotted in Figure 7.16. In this case, the amplitudes of the real and imaginary components are comparable which indicates a strongly complex ODS, as illustrated in Figure 7.17 (a). The ODS of the pin during squeal is clearly associated with the second bending mode of a clamped beam which is similar to the prediction given by the non-linear model, as illustrated in Figure 7.17 (b).

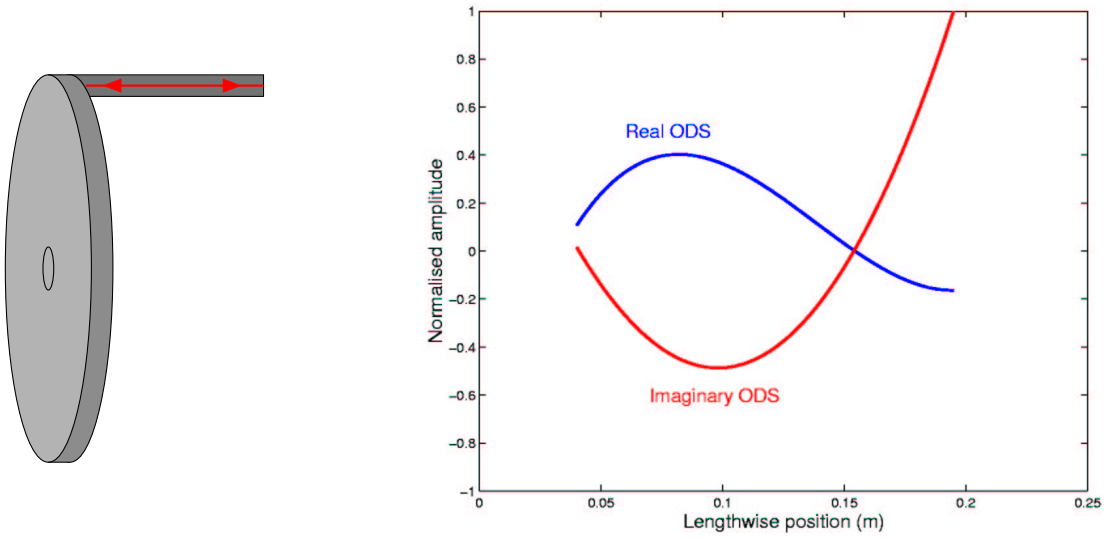

Figure 7.16: *Polynomial description of the real and imaginary components of the ODS of the pin during squeal.*

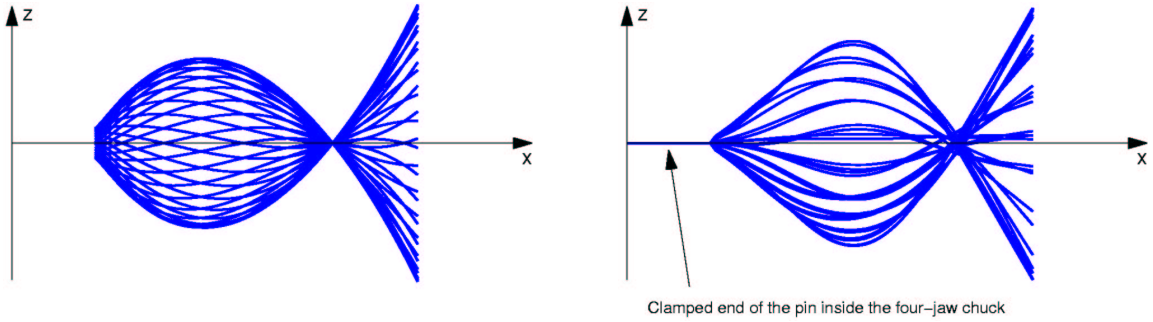

(a) (b)

Figure 7.17: *Vibration pattern of the pin during squeal at different time instants obtained from: (a) measurements (b) predictions.*

7.4.3 Transient build-up of squeal vibration

In the case of squeal, the transient build-up refers to the vibration which grows from an initial perturbation into a limit-cycle oscillation. Although the question of how quickly squeal reaches its limit-cycle condition is not the main concern for the brake squeal problem, it does provide another indication as to whether the theoretical model can represent the dynamics of the real structure accurately.

Figure 7.18 shows a comparison of the transient build-up between the measured data and the theoretical prediction (taken from Figure 5.5 (c)). As can be seen, the two responses have approximately the same exponential envelope which demonstrates that the non-linear pin-on-disc model is capable of representing the dynamics of the real system well during the transient build-up period. Furthermore, the exponential envelope which is obtained from the real part of the eigenvalue predicted by the linear pin-on-disc model in Chapter 4, is also shown by the red lines for comparison. The agreement indicates that the linear pin-on-disc model is also capable of predicting the onset of instability.

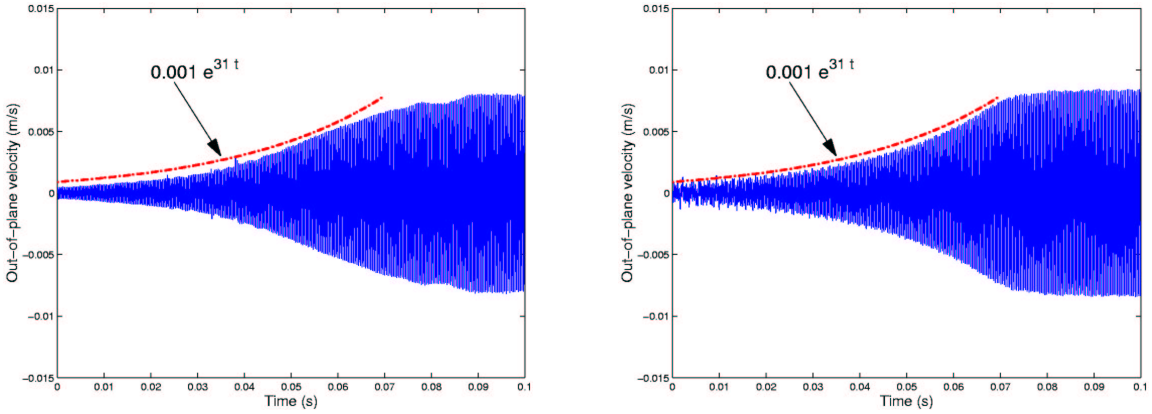

(a) (b)

Figure 7.18: *Transient build-up of squeal vibration: (a) the measured data and (b) the theoretical prediction.*

7.4.4 Effect of the rotational speed of the disc on squeal characteristics

As discussed previously in Chapter 5, the limit-cycle oscillation of squeal may be reached when the magnitude of the in-plane vibration of the pin approaches the disc velocity. Thus, it is important to verify the in-plane vibration of the pin first before considering other limit-cycle characteristics of squeal vibration.

In the following measurement, the velocity of the pin was measured at its tip in the direction parallel to the disc surface. The laser beam was directed as close as possible to the point of contact. The in-plane velocity of the pin was then compared with the velocity of the disc (Figure 7.19 (a)) which was recorded via an encoder located at the back end of the drive shaft. In general, the in-plane vibration of the pin was limited by the disc velocity but, at some instants, velocity reversal occurred. However, it should also be borne in mind that the disc velocity derived from the encoder signal may not be the actual disc velocity at the point of contact. The velocity of the disc indicated by the red line in Figure 7.19 (a) has been calculated simply from the product

between the angular velocity of the drive shaft and the distant of the contact point from the centre of the shaft. Thus, it did not take into account the contribution of the in-plane movement of the disc, nor did it consider any slip between the shaft and the disc. As a result, it cannot be concluded for certain that velocity reversal occurred. A theoretical prediction of the pin's in-plane velocity is also plotted in Figure 7.19 (b) for comparison. Although the prediction does not predict velocity reversal, it can still be used to estimate the average magnitude of the in-plane vibration of the pin.

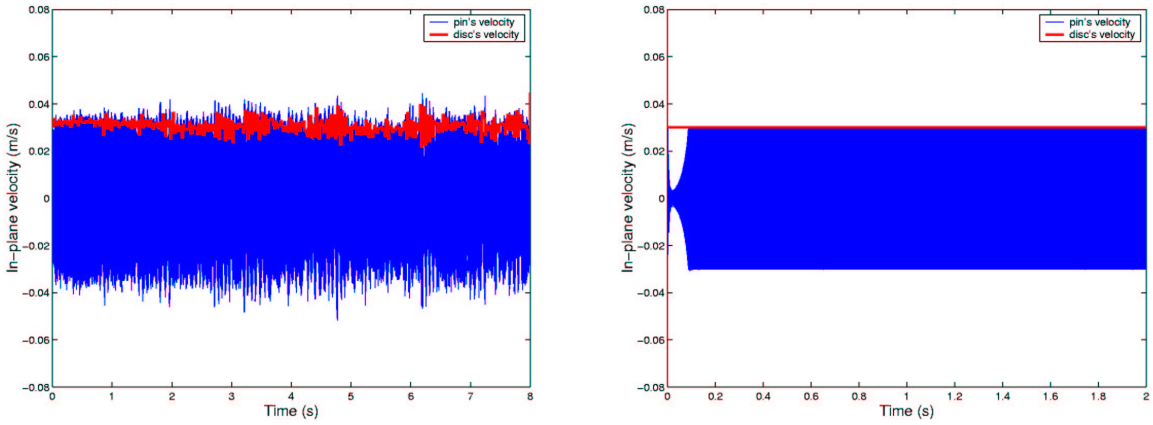

(a) (b)

Figure 7.19: *In-plane velocity of the pin: (a) measurement, and (b) prediction.*

In the next set of measurements, the effect of the rotational speed on the out-of-plane vibration of the disc was investigated. The responses were measured at the same location as the contact point between the pin and the disc but on the opposite side of the disc. The measurements were conducted at three different rotational speeds: 1, 2 and 4 rev/min. The measured out-of-plane velocities of the disc are plotted on the left-hand column of Figure 7.20 and the corresponding velocities calculated by the non-linear model are shown on the right-hand column for comparison. In general, the amplitudes of the out-of-plane velocities of the disc predicted by the theoretical model agree well with those obtained experimentally. It should also be noted that the out-of-plane vibration of the disc became less "smooth" at $\Omega = 4$ rev/min than at 1 rev/min

because it was more difficult to keep a smooth contact between the pin and the disc when the magnitude of vibration was high and the change in the surface topography was more sudden.

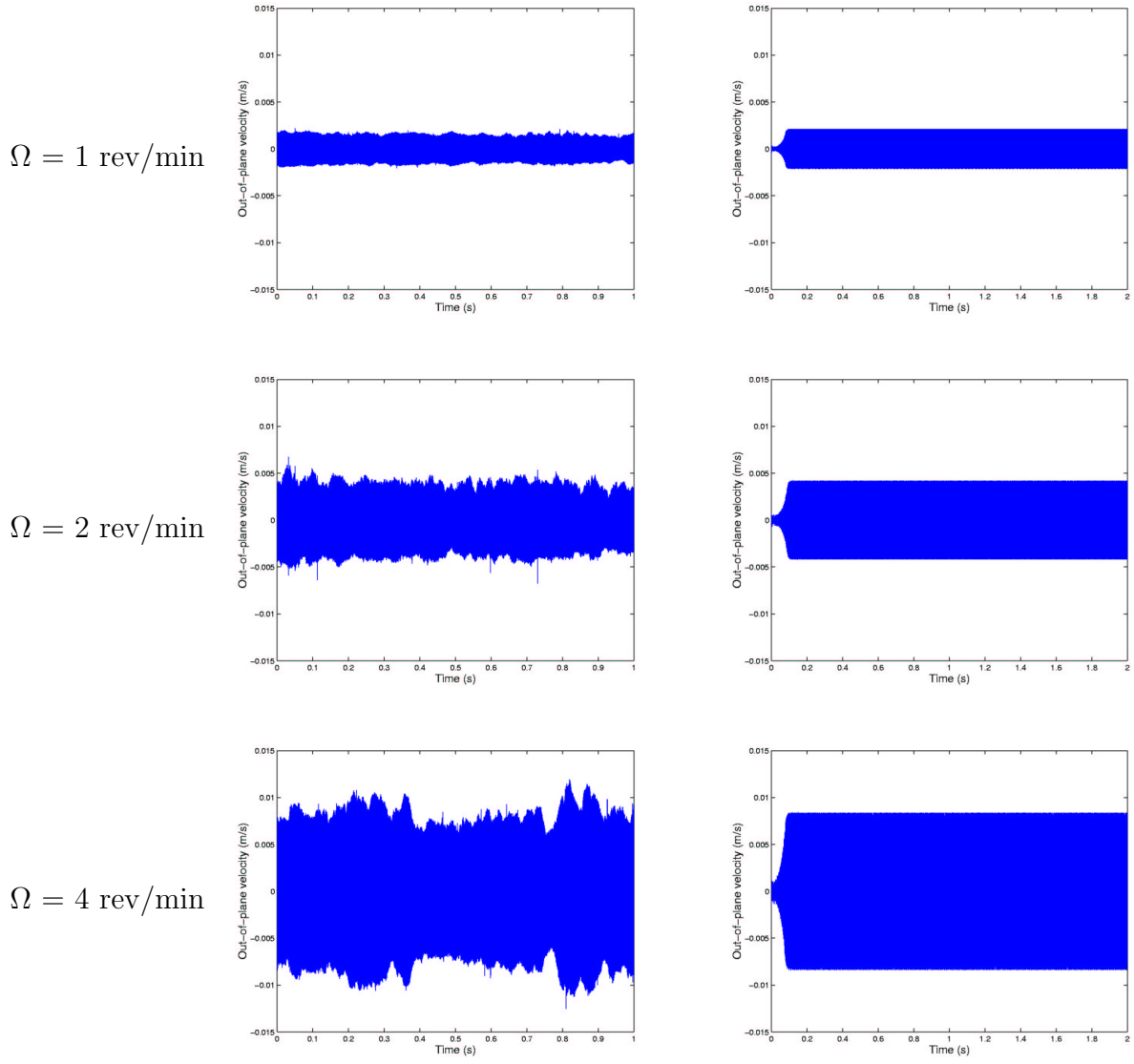

(a) measurements (b) predictions

Figure 7.20: *Comparisons of the out-of-plane vibration of the disc between measurements and predictions at different disc rotational speeds.*

7.4.5 Effect of mistuning on squeal characteristics

In this section, squeal tests were conducted with two disc configurations: (i) a perfectly-tuned disc and (ii) a mistuned disc. In the case of a mistuned disc, a small mass was glued at the outer edge of the disc. The out-of-plane vibration of the disc, which was measured at at the same location as the contact point between the pin and the disc but on the opposite side of the disc, was analysed using a spectrogram. The aim of this investigation was to verify the variation of squeal frequency with respect to the position of mistuning mass predicted by the non-linear pin-on-disc model in Chapter 5.

Before considering the effect of mistuning, it is worth examining squeal characteristics generated from a perfectly-tuned disc as a reference case. Figure 7.21 (a) shows a spectrogram plot of the out-of-plane vibration of the disc measured during squeal and the corresponding prediction calculated by the non-linear model is also plotted in Figure 7.21 (b) for comparison. It can be seen that the measured squeal frequency remained almost constant throughout the whole revolution of the disc as that predicted by the theoretical model. However, at some instants, squeal frequency may vary slightly. This behaviour may arise from the fact that the surface conditions of the disc were not uniform throughout the whole surface of the disc.

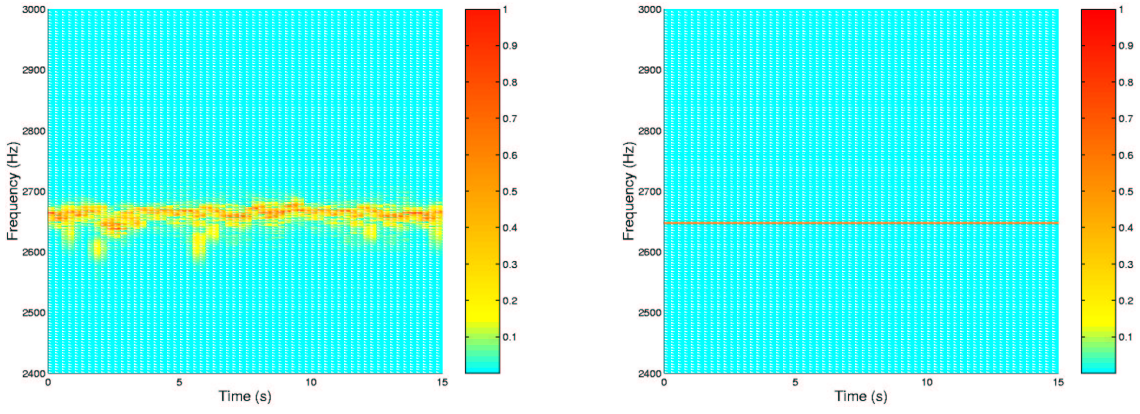

(a) (b)

Figure 7.21: *Spectrogram plots of the out-of-plane vibration for a perfectly tuned disc: (a) measurement and (b) prediction.*

In the next measurement, the disc was mistuned with a mass of 40 g. The spectrogram plot of the out-of-plane vibration of the disc is shown in Figure 7.22 (a) and the corresponding spectrogram plot obtained from the non-linear model is also shown in Figure 7.22 (b) for comparison. It can be seen that the squeal frequency changed with respect to the position of the mistuning mass as discussed in Chapter 5. The variation of the squeal frequency obtained from the measurement may appear more vigorous than the theoretical prediction. That is because it was very difficult to maintain constant squeal. Nevertheless, the theoretical prediction is in line with the observation.

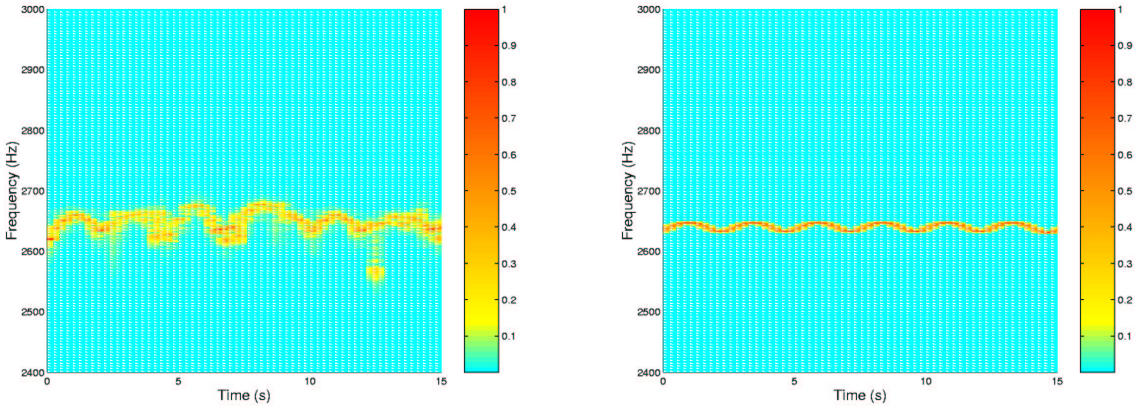

(a) (b)

Figure 7.22: *Spectrogram plots of the out-of-plane vibration for the disc with a mistuning mass of 40 g: (a) measurement and (b) prediction.*

7.5 Conclusions

Modal tests were conducted on the disc and the pin individually. The measured modal properties were used to update the FE model of each component. In the second part of this chapter, a combination of test data and the theoretical models was used to estimate the numerical values of the contact stiffnesses and damping. With the static load varying between 9.8 and 98 N, it was found that the normal contact stiffness per unit length of the pin-on-disc system varied between 2.3 and 2.9 GN/m^2 and the tangential contact stiffness per unit length varied between 0.43 and 0.58 GN/m^2. As

for the damping, the normal contact damping per unit length varied between 15 and 19 kNs/m^2 and the tangential contact damping per unit length varied between 0.7 and 2.1 kNs/m^2.

The experimental measurements conducted in the last part of this chapter were used mainly to validate the non-linear model created in Chapter 5. The key results can be listed as follows:

- continuous LDV scans along the circumferential and radial lines confirmed that the ODS of the disc during squeal consisted mainly of the (3,0) component;
- the ODS of the pin during squeal corresponded to the second bending mode of a clamped beam;
- the build-up of the squeal vibration predicted by the non-linear model agreed well with the experimental observations;
- the magnitude of the out-of-plane vibration increased as the rotational speed of the disc increased;
- the effects of mistuning on the squeal frequency predicted by the non-linear model were in line with the experimental observations.

Chapter 8

Conclusions

8.1 Summary of the work done

In this section, a summary of the work conducted during the course of this project is given. The main conclusions and contributions to the subject will be described in the next section. The overall objective of this project, as stated in the introduction, was to gain some new and better insight into the contributing mechanisms involved in brake squeal generation and the dynamic characteristics of squeal vibration. This objective has been successfully accomplished by completing a number of steps which can be summarised below.

In Chapter 1, the problem of disc brake squeal was introduced and a comprehensive literature review of previous work was given. Chapter 2 investigated the free vibration characteristics of a simple rotor/stator system. The use of the observer frame of reference for determining the ODS of the disc along the circumferential direction was also demonstrated. In chapter 3, the research focused on identifying and understanding the free vibration characteristics of the three-dimensional "tophat-like" structures which are widely used in disc brake design. From this study, a systematic method for identifying and classifying vibration modes of tophat-type disc structures was developed.

In Chapters 4 and 5, a pin-on-disc system which was used as a representative model to include the essential features of the actual brake assembly was studied in detail. The first pin-on-disc model which was introduced in Chapter 4 assumed that the friction coefficient was always constant and the friction force never changed its direction. As a result, a set of linear equations of motion could be derived. Instability regions of the linear pin-on-disc model behaviour were obtained via a complex eigenvalue analysis. In Chapter 5, the linear pin-on-disc model was extended to a more realistic (non-linear) model by incorporating a new friction model in which the friction coefficient was assumed to be a continuous function of the relative velocity between the two contact surfaces and which could take into account the change in the friction direction. The solutions for the dynamic behaviour of the non-linear pin-on-disc model were calculated using a time-integration method. The non-linear pin-on-disc model was used primarily to study the limit-cycle characteristics of squeal vibration. Furthermore, the study in Chapter 5 also considered the mistuning of the disc as a possible way of suppressing squeal vibration.

In Chapter 6, the design and development of the IC pin-on-disc rig were presented. The experimental investigations on the IC pin-on-disc rig were conducted in Chapter 7. The first part of the experimental investigations aimed at obtaining the contact stiffnesses and damping using a combination of test data and the theoretical models. The experimental measurements carried out in the second part of Chapter 7 were used to validate the theoretical models created in Chapters 4 and 5.

8.2 Main conclusions and contributions to the subject

The main conclusions drawn from the current research and the contributions to the subject can be listed below.

- The linear pin-on-disc model presented in this thesis shows the "lock-out" characteristic as well as the "lock-in" characteristic.

- A relative phase diagram can be used to determine the direction of flow of energy of the non-conservative forces (i.e. friction and damping forces) and thus to explain the incidence of squeal. In general, the work done on the system by a force in one complete cycle will be positive if the phase of the force leads that of the displacement. Conversely, a force will dissipate net energy in one complete cycle if the phase of the force lags behind that of the displacement. On the other hand, if the phase difference between the force and the displacement is either 0 or 180 degrees, then there will be no net energy transfer due to this force in one complete cycle.

- Theoretical predictions from the linear pin-on-disc model have shown that squeal can occur when the pin is in both the leaning and digging positions. This result has also been validated by experimental measurements. Thus, it can be concluded that the theoretical model can represent the dynamic behaviour of the real structure.

- For rotor/stator interaction systems, such as disc brake applications, an observer frame of reference which rotates at an independent speed can be used to determine: (i) the amount of each of the original disc modes which is present in the mode shapes of the combined system, and (ii) the patterns of the mode shapes of the combined system, i.e. forward or backward travelling waves. This technique can be applied directly to brake applications in order to instantly determine the

vibration pattern of the brake disc during squeal.

- A systematic method for mode identification of three-dimensional "tophat-like" structures using nodal variables has been developed. In general, 11 nodal variables are required to distinguish the vibration modes of these structures uniquely. However, if only the low-frequency modes are of primary interest, the current study has shown further that only a subset of these 11 parameters are needed for unambiguous mode identification. The question of how many and which nodal variables are important depends on the physical dimensions of the structures. From the case studies conducted in this research, 6 nodal parameters are found to be important and they are Fourier order, NC_θ, NC_z, NR_r, NCR_θ and NRR_θ.

- The current study has also demonstrated a systematic method for classifying vibration modes of "tophat-like" structures into appropriate families according to their similarity both in the $r-\theta$ and $r-z$ planes with the aid of the AutoMAC diagram. By understanding the vibration characteristics of the "tophat-like" structures, mode classification might become a useful tool to assist brake disc designers for necessary modifications to brake discs to avoid squeal.

- According to the numerical simulations predicted using the non-linear pin-on-disc model, the in-plane vibration of the pin is limited by the velocity of the disc at the contact point. Although velocity reversal can occur in theory, it has not been observed in the numerical simulations conducted in this research.

- The results obtained in this research have shown both theoretically and experimentally that the amplitudes of out-of-plane vibration of the disc increase as the disc angular velocity increases. The implication of this result is that squeal will become louder as the disc angular velocity increases.

- The simulation presented in this thesis shows that it may be possible to suppress squeal completely if the disc is modified by the additional of an appropriate pattern of masses.

- A simple friction model in which the friction coefficient is a continuous function of the relative velocity and has a smooth variation around the zero relative velocity region, has been developed. This friction-velocity curve can be used to predict the limit-cycle characteristics of the pin-on-disc system.

- A combination of test data and the theoretical models can be used to estimate the numerical values of the contact stiffnesses and damping which are required to perform the numerical studies.

- As a final conclusion, the numerical simulations conducted in the current research have shown that the friction coefficient, contact stiffnesses and damping, the rotational speed of the disc, and the mistuning of the disc can all influence the squeal characteristics. Thus, they must be included in the theoretical models of the actual brake assembly in order to be able to predict squeal accurately.

8.3 Suggestions for future work

The work carried out during the course of this project has provided the basic understanding of the mechanism for instability generation. However, the numerical simulations were performed using the pin-on-disc system which has significant geometry differences to the actual brake assembly. Thus, it would be interesting to apply the modelling technique described in the thesis to real brake components. When modelling real brake components, a number of important issues which must be taken into consideration can be listed below.

1. **Number of brake components.** A natural question arises as to how many and which components of a practical brake assembly must be included in the modelling process in order to be able to predict squeal accurately. Although there is no definite answer to this question, it is possible to draw some broad guidelines. If only the high-frequency squeal where vibration occurs locally is of the primary interest, squeal may be predicted using only a few brake components,

such as the brake rotor, the two brake pads and the calliper. However, if the objective is to predict low-frequency squeal, it might be important to include part or all of the mounting of the brake assembly (e.g. the knuckle and the drive shaft).

2. **Boundary conditions.** The boundary conditions of each brake component could also become one of the major difficulties in brake squeal modelling because, in some cases, they cannot be clearly defined. Inappropriate boundary conditions may lead to inadequate models which cannot accurately predict the dynamics of brake components. As can be seen from the pin-on-disc simulations, the accuracy of squeal predictions depends largely on the accuracy of each individual component model. Thus, the boundary conditions which influence the dynamics of each brake component might play a critical role in order to obtain the precise conditions for instability.

3. **Resulting couple due to unbalanced friction forces.** In actual braking conditions, it is possible that the magnitudes of the normal contact forces on either side of the brake disc may not be identical, thereby, resulting in two unbalanced friction forces. As a result, a friction couple might be generated about the mid-plane of the brake disc. This friction couple could become another source of instability generation and would need to be included in the model.

Apart from the squeal modelling using the real brake components, discussed above, future research could also consider alternative methods for obtaining numerical values for the contact properties, i.e. contact stiffnesses and damping. The current method presented in this thesis uses a combination of test data and the theoretical models and, thus, relies heavily on the accuracy of the updated model of each individual component. An alternative and possibly better method might be to obtain these contact properties solely through an experimental approach. However, a number of attempts made during the course of this project have encountered two major difficulties. The first and foremost difficulty is the measurement of the contact force at the contact point. The

second difficulty is the measurement of the displacements of the two contact surfaces at (or as near as possible to) the contact point. If these two quantities (i.e. the contact forces and displacements) can be accurately acquired, then the contact stiffnesses and damping can be estimated. As a final suggestion, it might be an idea to re-design future pin-on-disc rigs such that these two quantities can be accessed more easily.

8.4 Closure

The overall objective of the current project was to gain some new and better insight into the contributing mechanisms involved in brake squeal generation and the dynamic characteristics of squeal vibration. This has been accomplished via the use of pin-on-disc models. Due to the time and computational power constrains, a number of simplifications have been made. Nevertheless, it is believed that the research presented in this thesis makes significant steps towards a better understanding of brake squeal phenomenon and, hence, a better prediction capability.

Appendix A

An example of a simple rotor/stator system.

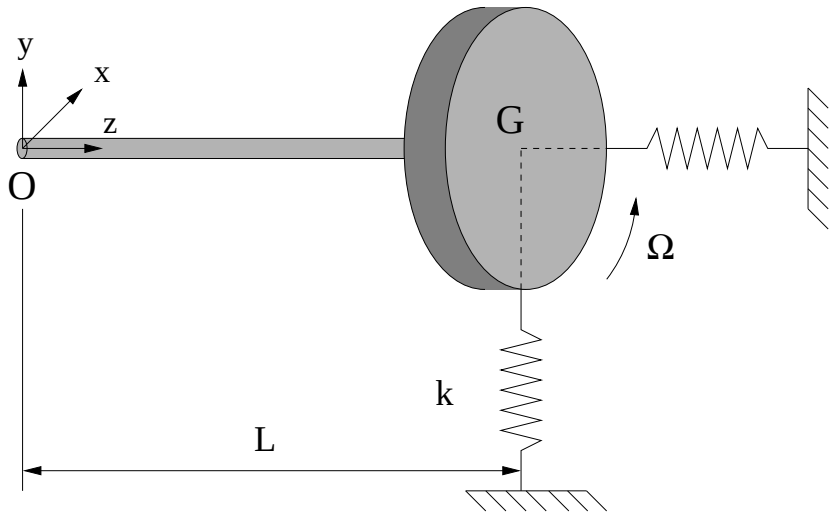

Figure A.1: *Simple 2DOF rotor-stator system.*

The notations used in equation (2.19) can be listed as follows:

- J is the polar moment of the disc and shaft, and
- I_0 its moment of inertia about a lateral axis through O,

- Ω is the angular velocity of the disc in the anticlockwise viewed from the free end of the shaft,
- L is the length of the shaft
- k is the stiffness of the support bearings,
- x_R and y_R define the physical coordinates in the rotating frame of reference.

Appendix B

Cross-sectional view of the mode shapes of the tophat models.

B.1 Tophat model in Step 1

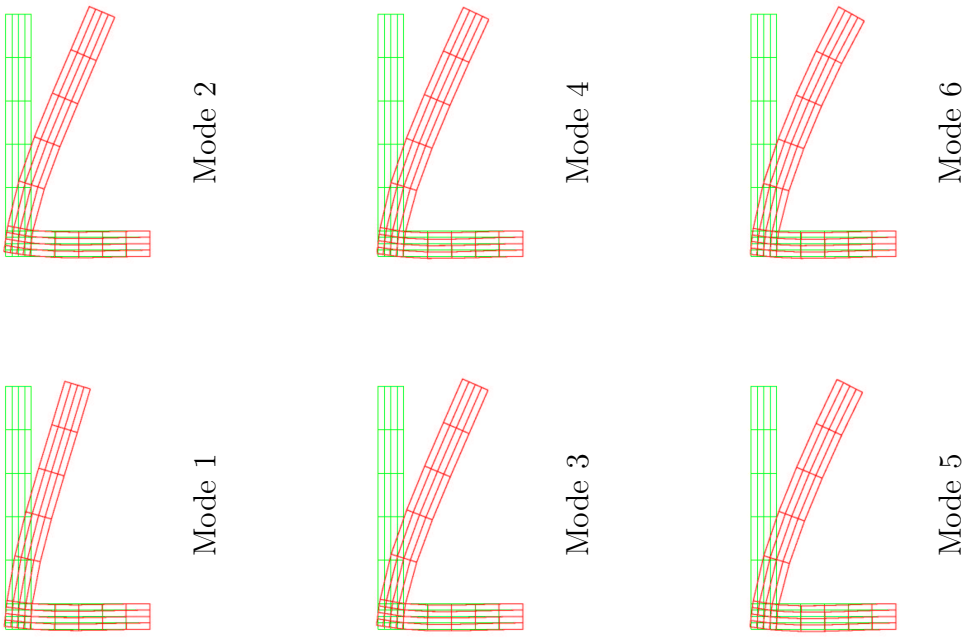


Mode 10
Mode 14
Mode 18
Mode 9
Mode 13
Mode 17
Mode 8
Mode 12
Mode 16
Mode 7
Mode 11
Mode 15


Mode 22
Mode 26
Mode 30
Mode 21
Mode 25
Mode 29
Mode 20
Mode 24
Mode 28
Mode 19
Mode 23
Mode 27

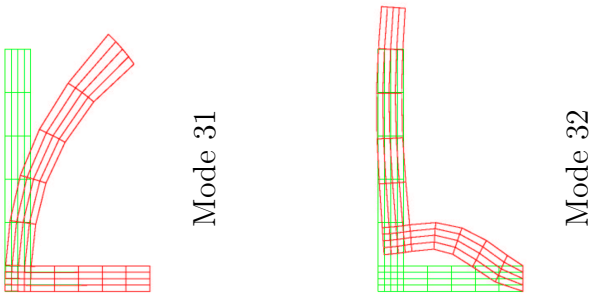

Table B.1: *Cross-sectional view of mode shapes of the tophat model in Step 1*

B.2 Tophat model in Step 2

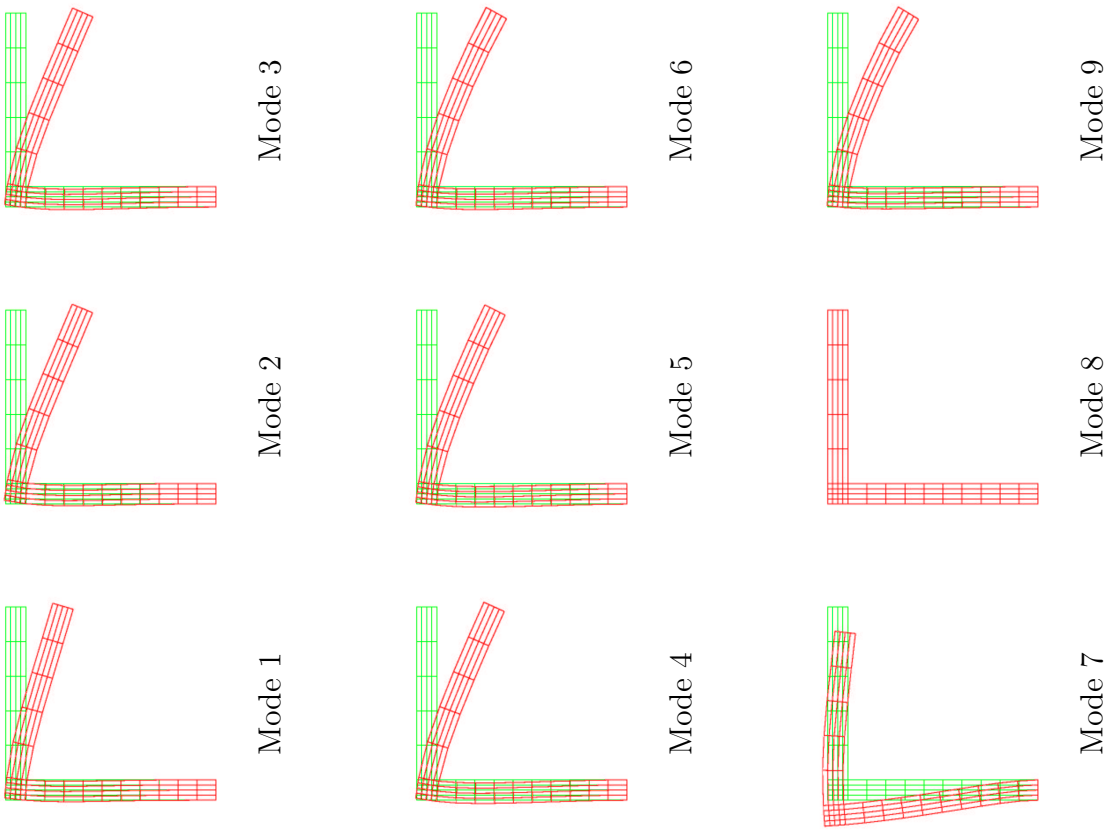

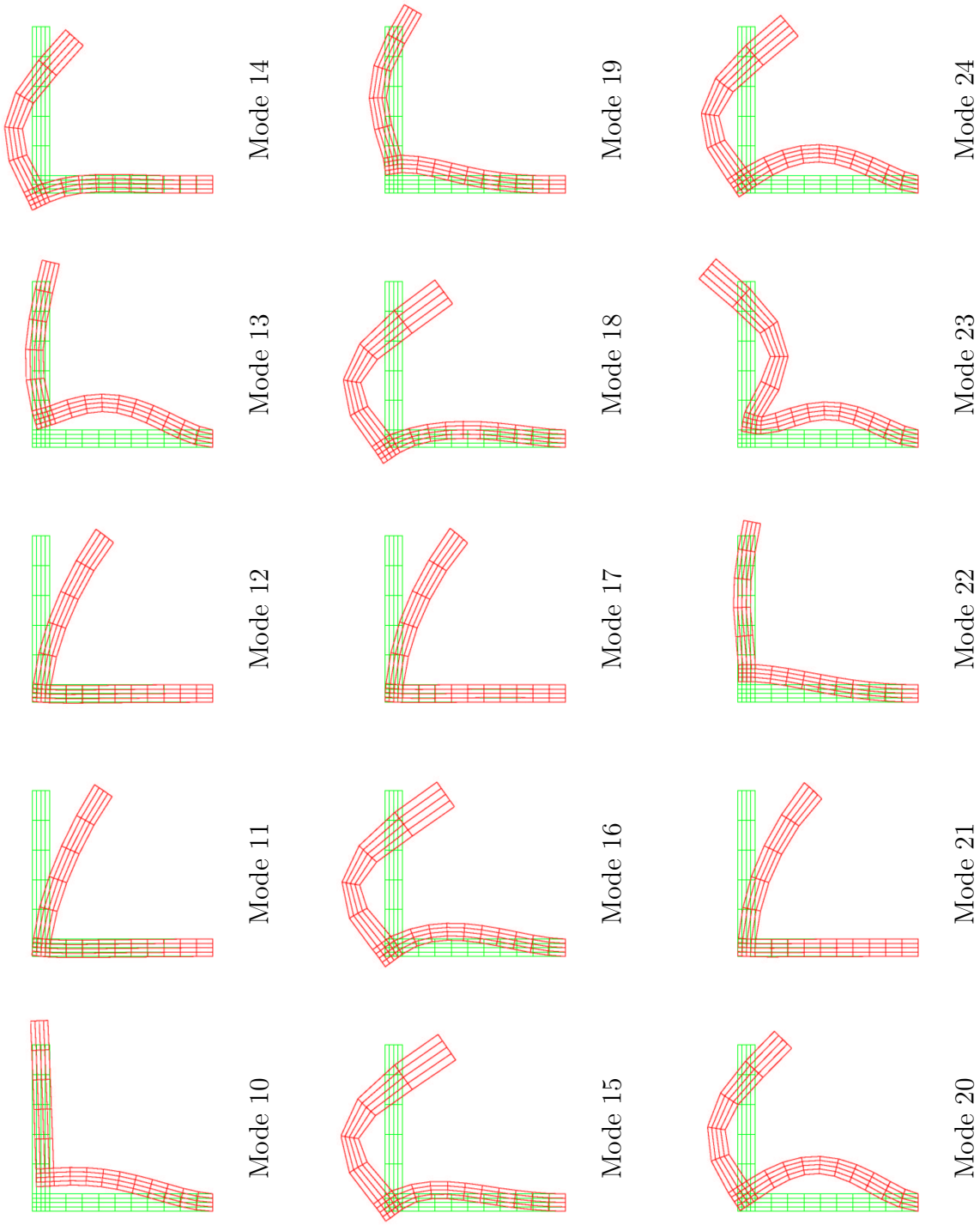
Mode 14
Mode 19
Mode 24
Mode 13
Mode 18
Mode 23
Mode 12
Mode 17
Mode 22
Mode 11
Mode 16
Mode 21
Mode 10
Mode 15
Mode 20

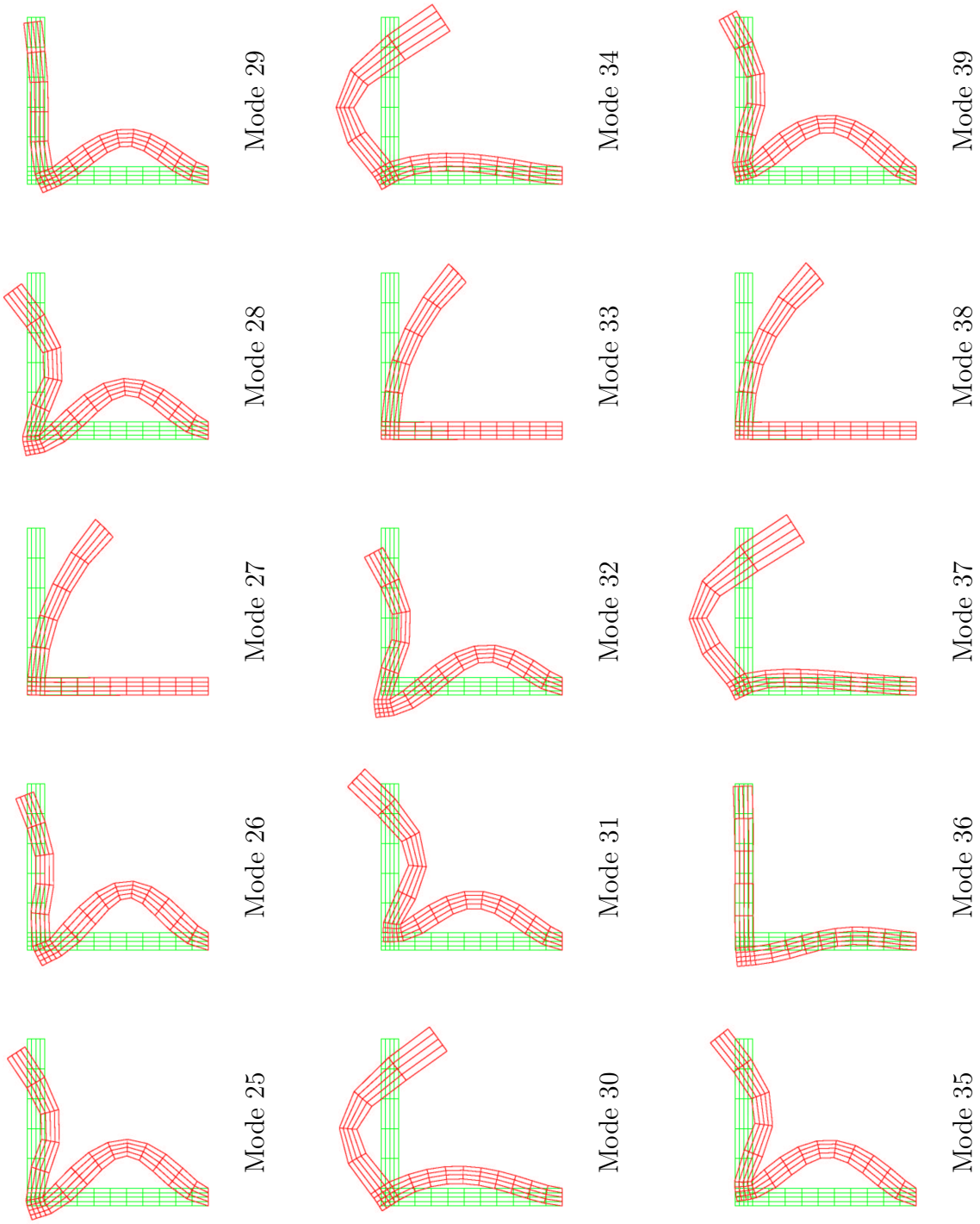

Table B.2: *Cross-sectional view of mode shapes of the tophat model in Step 2*

B.3 Tophat model in Step 3

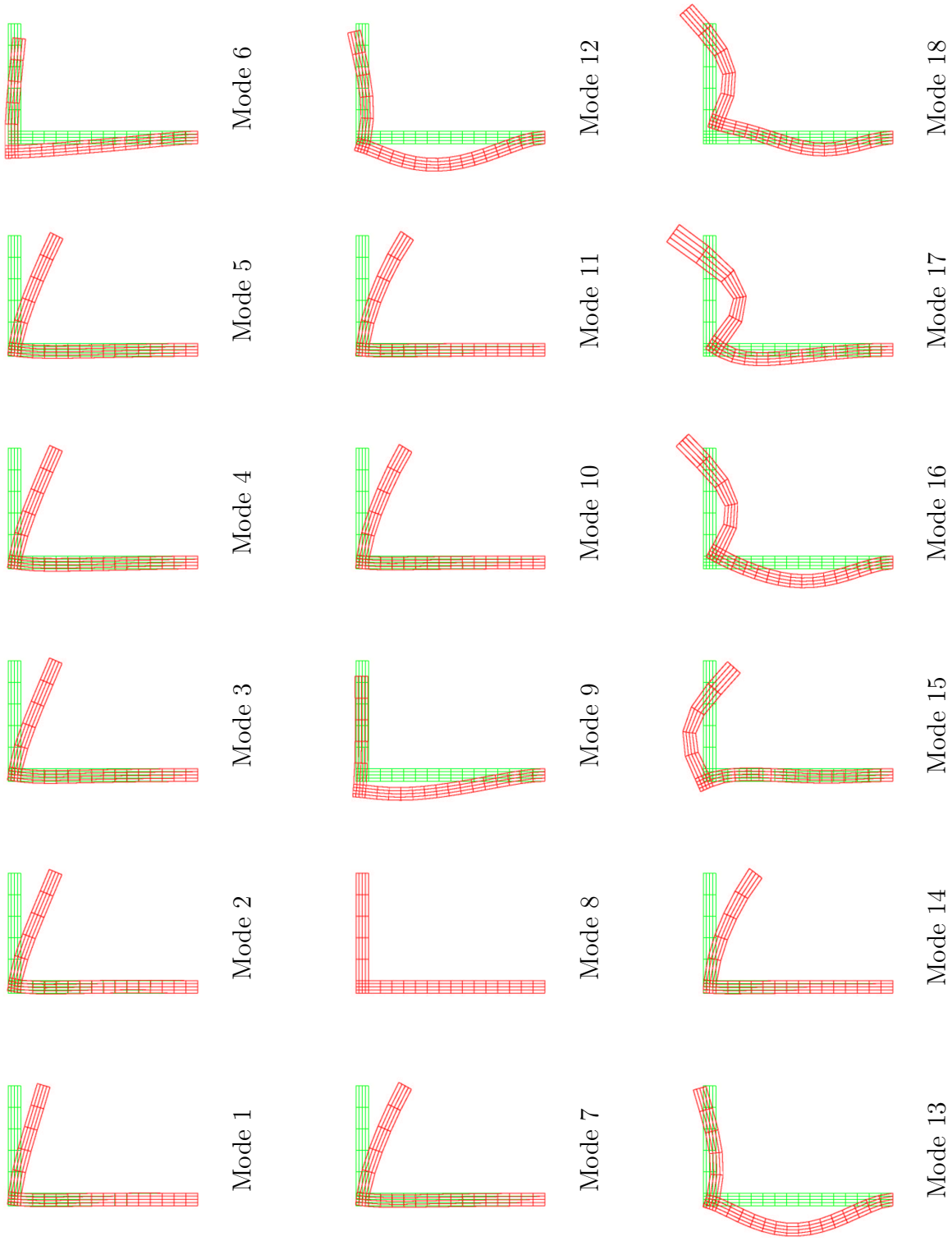

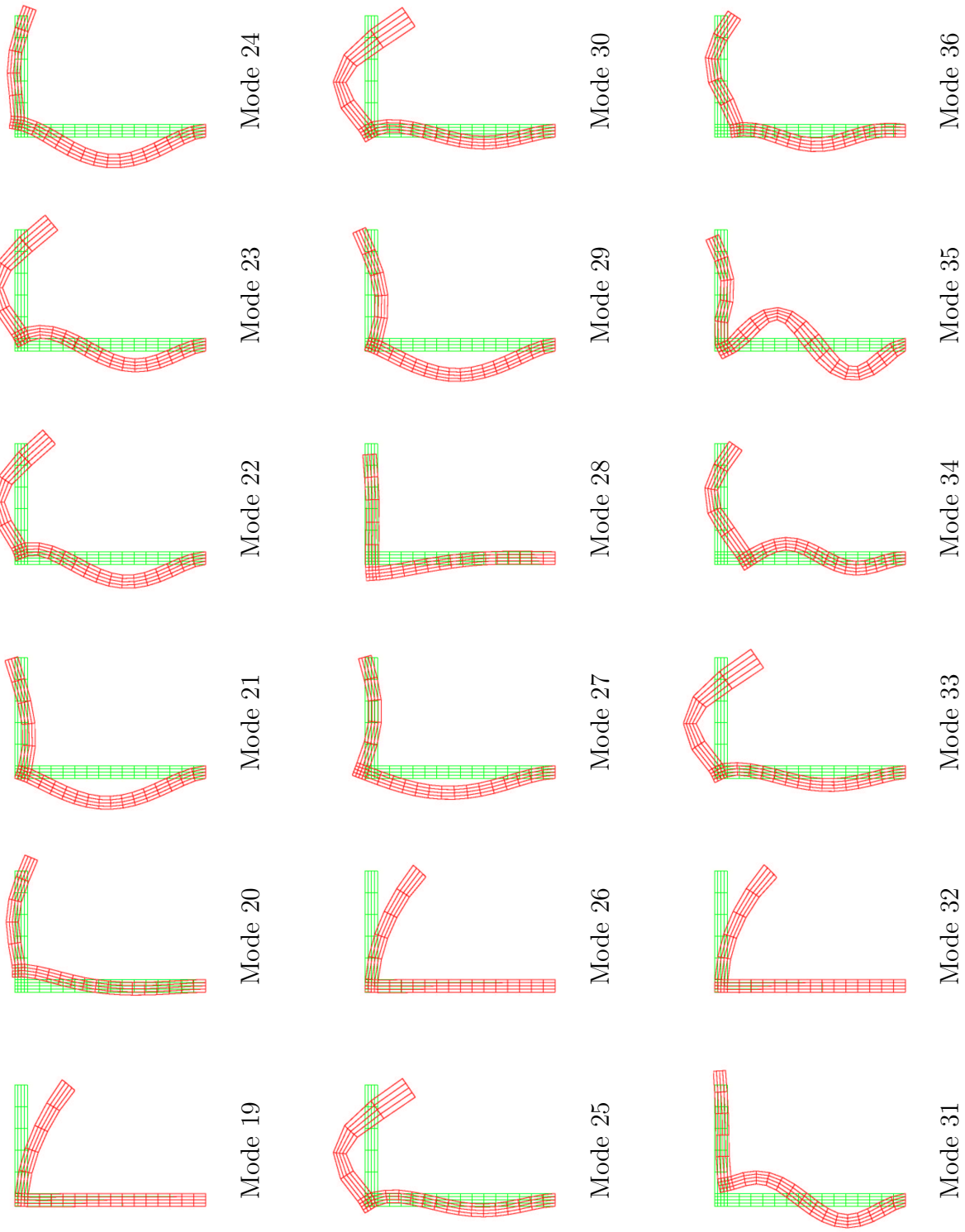
Mode 24
Mode 30
Mode 36
Mode 23
Mode 29
Mode 35
Mode 22
Mode 28
Mode 34
Mode 21
Mode 27
Mode 33
Mode 20
Mode 26
Mode 32
Mode 19
Mode 25
Mode 31

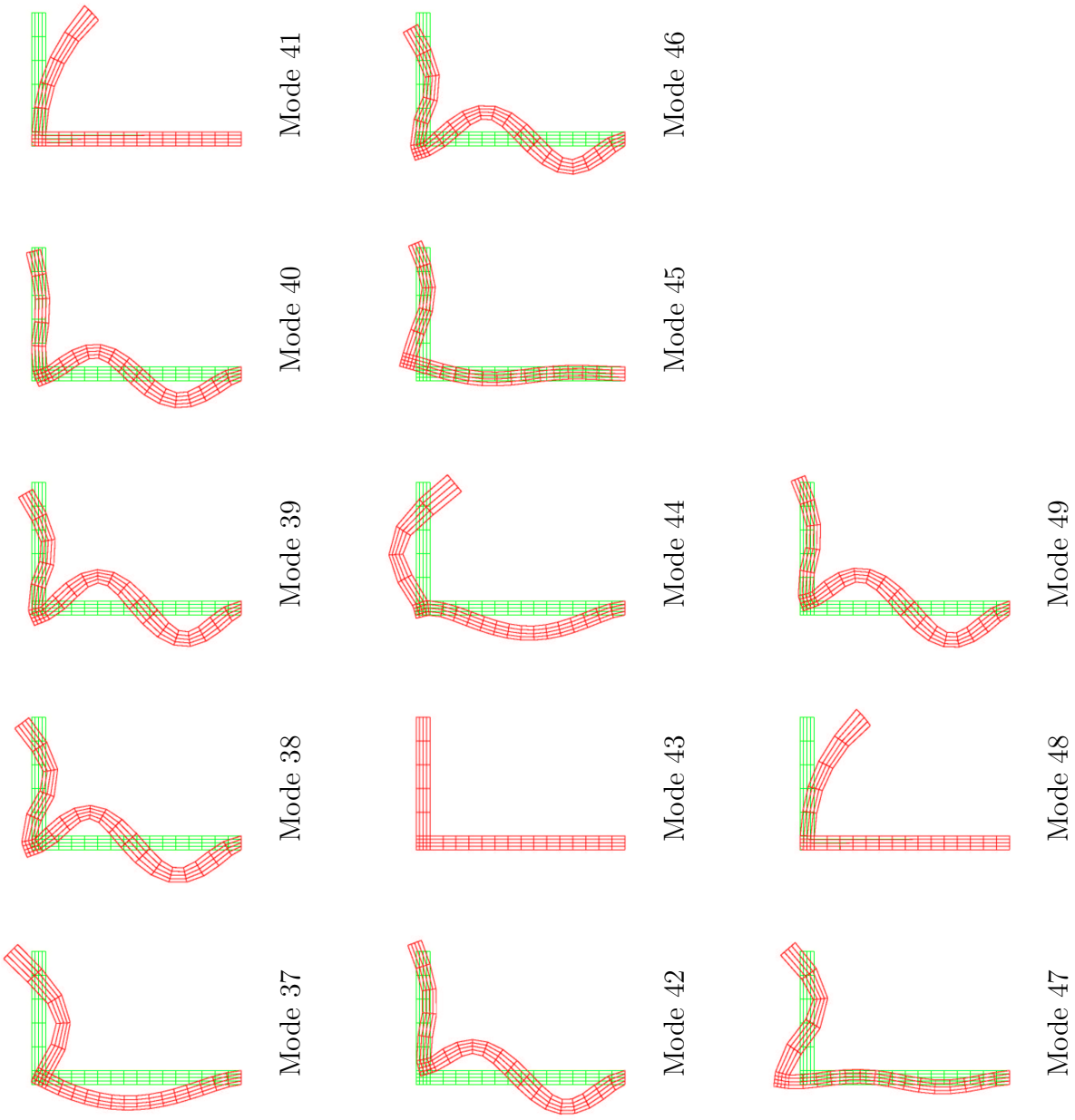

Table B.3: *Cross-sectional view of mode shapes of the tophat model in Step 3*

Appendix C

Derivation of the equations of motion of mistuned-rotating discs

The governing equation of motion for free vibration of a mistuned-rotating disc in the stationary frame of reference, (r, θ), can be written as:

$$D\nabla^4 w + \left\{\rho h + \frac{m_0}{r}\delta(r - \hat{r}_0)\delta(\theta - \Omega t - \hat{\theta}_0)\right\} \times \left[\frac{\partial^2 w}{\partial t^2} + 2\Omega\frac{\partial^2 w}{\partial\theta\partial t} + \Omega^2\frac{\partial^2 w}{\partial\theta^2}\right] = 0 \quad \text{(C.1)}$$

where m_0 is the mistuning mass and the out-of-plane displacement, w, can be expressed in terms of the generalised coordinates, q as

$$\begin{aligned} w(r,\theta,t) = & \sum_{m=0}^{\infty} {}_c\phi_{0m}(r)\ {}_cq_{0m}(t) \\ & + \sum_{m=0}^{\infty}\sum_{n=1}^{\infty} {}_c\phi_{nm}(r)\ \cos n\theta\ {}_cq_{nm}(t) + \sum_{m=0}^{\infty}\sum_{n=1}^{\infty} {}_s\phi_{nm}(r)\ \sin n\theta\ {}_sq_{nm}(t) \end{aligned} \quad \text{(C.2)}$$

By substituting equation (C.2) into equation (C.1) and multiplying by $r\,{}_c\phi_{nm}$ or $r\,{}_s\phi_{nm}$, integrating from 0 to 2π in θ and from b to a in r, and making use of the orthogonality of the eigenfunctions of the free disc problem, the equation of motion can be expressed as:

$$\Big[[I] + [L(t)]\Big]\ddot{q} + \Big[[E] + [P(t)]\Big]\dot{q} + \Big[[F] + [J] + [S(t)]\Big]q = 0 \quad \text{(C.3)}$$

where a is the outer radius, b is the inner radius, n is the number of nodal diameters, and m is the number of nodal circles. Matrices $[E]$, $[F]$, and $[J]$ are defined by equations (2.6), (2.7) and (2.8), respectively. To define matrices $[L(t)]$, $[P(t)]$ and $[S(t)]$, it is easier if the modal constants of the disc are re-arranged in the following form:

$$\{\Phi_1\} = \begin{Bmatrix} {}_c\phi_{00}(\hat{r}_0) \\ \vdots \\ {}_c\phi_{0m}(\hat{r}_0) \\ {}_c\phi_{10}(\hat{r}_0)\cos(\Omega t + \hat{\theta}_0) \\ {}_s\phi_{10}(\hat{r}_0)\sin(\Omega t + \hat{\theta}_0) \\ \vdots \\ {}_c\phi_{nm}(\hat{r}_0)\cos n(\Omega t + \hat{\theta}_0) \\ {}_s\phi_{nm}(\hat{r}_0)\sin n(\Omega t + \hat{\theta}_0) \end{Bmatrix}, \qquad \{\Phi_2\} = \begin{Bmatrix} 0 \\ \vdots \\ 0 \\ -2\Omega_c\phi_{10}(\hat{r}_0)\sin(\Omega t + \hat{\theta}_0) \\ 2\Omega_s\phi_{10}(\hat{r}_0)\cos(\Omega t + \hat{\theta}_0) \\ \vdots \\ -2n\Omega_c\phi_{nm}(\hat{r}_0)\sin n(\Omega t + \hat{\theta}_0) \\ 2n\Omega_s\phi_{nm}(\hat{r}_0)\cos n(\Omega t + \hat{\theta}_0) \end{Bmatrix},$$

$$\{\Phi_3\} = \begin{Bmatrix} 0 \\ \vdots \\ 0 \\ \Omega^2{}_c\phi_{10}(\hat{r}_0)\cos(\Omega t + \hat{\theta}_0) \\ \Omega^2{}_s\phi_{10}(\hat{r}_0)\sin(\Omega t + \hat{\theta}_0) \\ \vdots \\ n^2\Omega^2{}_c\phi_{nm}(\hat{r}_0)\cos n(\Omega t + \hat{\theta}_0) \\ n^2\Omega^2{}_s\phi_{nm}(\hat{r}_0)\sin n(\Omega t + \hat{\theta}_0) \end{Bmatrix}. \tag{C.4}$$

Thus, matrices $[L(t)]$, $[P(t)]$ and $[S(t)]$ can simply be written as:

$$[L(t)] = m_0\{\Phi_1\}\{\Phi_1\}^T \tag{C.5}$$

$$[P(t)] = m_0\{\Phi_1\}\{\Phi_2\}^T \tag{C.6}$$

$$[S(t)] = -m_0\{\Phi_1\}\{\Phi_3\}^T \tag{C.7}$$

Bibliography

[1] A. Papinniemi, J.C.S. Lai, J. Zhao, and L. Loader. Brake squeal: a literature review. *Applied Acoustics*, 63(4):391–400, 2002.

[2] N.M. Kinkaid, O.M. O'Reilly, and P. Papadopoulos. Automotive disc brake squeal. *Journal of Sound and Vibration*, 2003.

[3] L. Gaul and R. Nitsche. The role of friction in mechanical joints. *Applied Mechanics Reviews*, 54(2):93–106, 2001.

[4] M.R. North. A survey of published work on vibration in braking systems. *The Motor Industry Research Association (M.I.R.A.) Report*, Bulletin Number 4, 1969.

[5] R.T. Spurr. A theory of brake squeal. In *The Institution of Mechanical Engineers (A.D.)*, number 1, pages 33–40, 1961-1962.

[6] R.P. Jarvis and B. Mills. Vibrations induced by dry friction. In *The Institution of Mechanical Engineers*, volume 178, pages 847–866, 1963-64.

[7] S.W.E. Earles and C.K. Lee. Instabilities arising from the frictional interaction of a pin-disk system resulting in noise generation. *Transactions of the ASME, Journal of Engineering for Industry*, 98(1):81–86, 1976.

[8] S.W.E. Earles. A mechanism of disc-brake squeal. *Society of Automotive Engineers*, 770181:800–805, 1978.

[9] S.W.E. Earles and M.N.M. Badi. Oscillatory instabilities generated in a double-pin and disc undamped system: a mechanism of disc-brake squeal. *The Institution of Mechanical Engineers*, 198(4):43–50, 1984.

[10] S.W.E. Earles and P.W. Chambers. Disc brake squeal noise generation: Predicting its dependency on system parameters including damping. *International Journal of Vehicle Design*, 8(4-6):538–552, 1987.

[11] A.M. Lang and T.P. Newcomb. An experimental investigation into drum brake squeal. *EAEC Conference on New Developments in Powertrain and Chassis Engineering*, (C382/051):431–444, 1989.

[12] A.M. Lang and T.P. Newcomb. The vibration characteristics of squealing brakes. *FISITA Congress (Turin, Italy), Society of Automotive Engineers*, (90 51 70), 1990.

[13] A.M. Lang. *An Investigation into Heavy Vehicle Drum Brake Squeal*. PhD thesis, Loughborough University of Technology, 1994.

[14] M.R. North. Disc brake squeal - a theoretical model. In *The Motor Industry Research Association (M.I.R.A.) Report*, number 1972/5, 1972.

[15] R. Stribeck. Die wesentlichen eigenschaften der gleit- und rollenlager. *Zeitschrift des Vereins deutscher Ingenieure*, 46(36,38):1341–1348,1432–1438, 1902.

[16] R.I. Leine, D.H. Van Campen, A. de Kraker, and L. Van Den Steen. Stick-slip vibrations induced by alternate friction models. *Nonlinear Dynamics*, 16(1):41–51, 1998.

[17] V.N. Pilipchuk, R.A. Ibrahim, and P.G. Blaschke. Disc brake ring-element modelling involving friction-induced vibration. In *Proceedings of the International Modal Analysis Conference – IMAC XX*, pages 535–541, 2002.

[18] J.P. Den-Hartog. Forced vibrations with combined coulomb and viscous damping. *Transactions of the ASME, Journal of Applied Mechanics (APM)*, 53(9):107–115, 1931.

[19] P. Chambrette. *Stabilité de systèmes dynamiques avec frottement sec: Application au crissement de freins à disques*. PhD thesis, Ecole Centrale de Lyon, 1991.

[20] H. Lamb and R.V. Southwell. The vibrations of a spinning disk. In *Proceedings of the Royal Society of London*, volume 99 of *A*, pages 272–280, 1921.

[21] R.V. Southwell. On the free transverse vibrations of a uniform circular disc clamped at its centre; and on the effects of rotation. In *Proceedings of the Royal Society of London*, volume 101 of *A*, pages 133–153, 1921.

[22] S.A. Tobias and R.N. Arnold. The influence of dynamic imperfections on the vibrations of rotating disks. In *Proceedings of The Institute of Mechanical Engineers*, volume 171, pages 669–690, 1957.

[23] H. Mehdigholi. *Forced Vibration of Rotating Discs and Interaction with Non-rotating Structures*. PhD thesis, Imperial College London, 1991.

[24] W.D. Iwan and K.J. Stahl. The response of an elastic disc with a moving mass system. *Transactions of the ASME, Journal of Applied Mechanics*, pages 445–451, 1973.

[25] W.D. Iwan and T.L. Moeller. The stability of spinning elastic disk with a transverse load system. *Transactions of the ASME, Journal of Applied Mechanics*, pages 485–490, 1976.

[26] K. Ono, J.S. Chen, and D.B. Bogy. Stability analysis for the head-disk interface in a flexible disk drive. *Transactions of the ASME, Journal of Applied Mechanics*, 58:1005–1014, 1991.

[27] S.G. Hutton, S. Chonan, and B.F. Lehmann. Dynamic response of a guided circular saw. *Journal of Sound and Vibration*, 112(3):527–539, 1987.

[28] B.F. Lehmann and S.G. Hutton. Self-excitation in guided circular saws. *Transactions of the ASME, Journal of Vibration Acoustics Stress and Reliability in Design*, 110(3):338–344, 1988.

[29] L. Yang and S.G. Hutton. Interactions between an idealized rotating string and stationary constraints. *Journal of Sound and Vibration*, 185(1):139–154, 1995.

[30] A.B. Stanbridge and D.J. Ewins. Modal testing of rotating discs using a scanning LDV. In *ASME Conference on Noise and Vibration 15*, 1995.

[31] A.B. Stanbridge and D.J. Ewins. Modal testing using a scanning laser doppler vibrometer. In *Mechanical Systems and Signal Processing*, pages 255–270, 1999.

[32] M. Martarelli. *Exploiting the Laser Scanning Facility for Vibration Measurements.* PhD thesis, Imperial College of Science, Technology & Medicine, University of London, 2001.

[33] A.B. Stanbridge, M. Martarelli, and D.J. Ewins. Continuous-scan vibration measurements on moving components. In *Proceedings of the International Modal Analysis Conference – IMAC XX*, 2002.

[34] A. Felske, G. Hoppe, and H. Matthäi. Oscillations in squealing disk brakes - analysis of vibration modes by holographic interferometry. *Society of Automotive Engineers*, 780333:1576–1595, 1979.

[35] C.A. Beveridge and J.D. Fieldhouse. Noise investigations of a commercial disc brake using holographic interferometry. In *The International Conference on Brakes 2000*, pages 85–99, 2000.

[36] J.D. Fieldhouse and C.J. Talbot. Visualising brake noise - from holographic investigations to 3d animated images of real brakes generating noise. In *Proceedings of the International Modal Analysis Conference – IMAC XXI*, 2003.

[37] R. Krupka and A. Ettemeyer. Brake vibration analysis with threedimensional pulsed espi. In *Proceedings of the International Modal Analysis Conference – IMAC XIX*, volume 1, pages 78–82, 2001.

[38] S.N. Chan, J.E. Mottershead, and M.P. Cartmell. Parametric resonances at subcritical speeds in discs with rotating frictional loads. In *Proceedings of the Institution of Mechanical Engineers, Part C*, volume 208, pages 417–425, 1994.

[39] A.H. Nayfeh and D.T. Mook. *Nonlinear Oscillations*. Wiley-Interscience, New York, 1979.

[40] H. Ouyang, J.E. Mottershead, M.P. Cartmell, and M.I. Friswell. Friction-induced parametric resonances in discs: Effect of a negative friction-velocity relationship. *Journal of Sound and Vibration*, 209:251–264, 1998.

[41] H. Ouyang, J.E. Mottershead, M.P. Cartmell, and D.J. Brookfield. Friction-induced vibration of an elastic slider on a vibrating disc. *International Journal of Mechanical Sciences*, 41:325–336, 1999.

[42] H. Ouyang and J.E. Mottershead. Optimal suppression of parametric vibration in discs under rotating friction loads. In *Proceedings of the Institution of Mechanical Engineers, Part C*, volume 215, pages 65–75, 2001.

[43] H. Ouyang and J.E. Mottershead. Unstable travelling waves in the friction-induced vibration of discs. *Journal of Sound and Vibration*, 248(4):768–779, 2001.

[44] S. Mahajan, Y.K. Hu, and K. Zhang. Vehicle disc brake squeal simulations and experiences. *Society of Automotive Engineers*, 1999-01-1738, 1999.

[45] W.V. Nack. Brake squeal analysis by finite elements. *Society of Automotive Engineers*, 1999-01-1736, 1999.

[46] S.W. Kung, K. Brent Dunlap, and R.S. Ballinger. Complex eigenvalue analysis for reducing low frequency brake squeal. *Society of Automotive Engineers*, 2000-01-0444, 2000.

[47] T. Hamabe, I. Yamazaki, K. Yamada, H. Matsui, S. Nakagawa, and M. Kawamura. Study of a method for reducing drum brake squeal. *Society of Automotive Engineers*, 1999-01-0144:53–60, 1999.

[48] P. Blaschke, M. Tan, and A. Wang. On the analysis of brake squeal propensity using finite element method. *Society of Automotive Engineers*, 2000-01-2765, 2000.

[49] Y.K. Hu, S. Mahajan, and K. Zhang. Brake squeal DOE using nonlinear transient analysis. *Society of Automotive Engineers*, 1999-01-1737, 1999.

[50] D.J. Ewins. *Modal Testing: Theory, Practice and Application*. Research Studies Press Ltd, second edition, 2000.

[51] G. Kirchhoff. Über das Gleichgewicht und die Bewegung einer elastischen Scheibe. *J. Reine Angew. Math.*, 40:51–58, 1850.

[52] Lord Rayleigh (J.W. Strutt). *The Theory of Sound*. Dover Publications Inc, originally published in 1877 edition, 1945.

[53] A.W. Leissa. *Vibration of Plates*. NASA, 1975.

[54] J. Prescott. *Applied Elasticity*. Dover Publications, inc, 1924.

[55] W. Soedel. *Vibrations of Shells and Plates*. Marcel Dekker, inc, 1981.

[56] S.P. Timoshenko and S. Woinowsky-Krieger. *Theory of Plates and Shells*. McGraw-Hill International Book Company, second edition, 1959.

[57] R.D. Mindlin. Influence of rotary inertia and shear on flexural motions of isotropic, elastic plates. *Transactions of the ASME, Journal of Applied Mechanics*, 18:31–38, 1951.

[58] H. Deresiewicz and R.D. Mindlin. Axially symmetric flexural vibrations of a circular disk. *Transactions of the ASME, Journal of Applied Mechanics*, 22:86–88, 1955.

[59] J.R. Hutchinson. Vibrations of thick free circular plates, exact versus approximate solutions. *Transactions of the ASME, Journal of Applied Mechanics*, 51:581–585, 1984.

[60] K.I. Tzou, J.A. Wickert, and A. Akay. In-plane vibration modes of arbitrarily thick disks. *Transactions of the ASME, Journal of Vibration and Acoustics*, 120:384–391, 1998.

[61] J. So and A.W. Leissa. Three-dimensional vibrations of thick circular and annular plates. *Journal of Sound and Vibration*, 209(1):15–41, 1998.

[62] G.M.L. Gladwell and D.K. Vijay. Natural frequencies of free finite-length circular cylinders. *Journal of Sound and Vibration*, 42(3):387–397, 1975.

[63] J.C. Bae and J.A. Wickert. Free vibration of coupled disk-hat structures. *Journal of Sound and Vibration*, 235(1):117–132, 2000.

[64] R. Allgaier, L. Gaul, W. Keiper, and K. Willner. Mode lock-in and friction modelling. In *Computational Methods in Contact Mechanics IV*, pages 35–47, 1999.

[65] A. Tuchinda, N.P. Hoffmann, D.J. Ewins, and W. Keiper. Mode lock-in characteristics and instability study of the pin-on-disc system. In *Proceedings of the International Modal Analysis Conference – IMAC XIX*, volume 1, pages 71–77, 2001.

[66] A. Tuchinda, N.P. Hoffmann, and D.J. Ewins. Effect of pin finite width on instability of pin-on-disc systems. In *Proceedings of the International Modal Analysis Conference – IMAC XX*, volume 1, pages 71–77, 2002.

[67] T.R. Thomas and R.S. Sayles. Stiffness of machine tool joints: A random-process approach. *Transactions of the ASME, Journal of Engineering for Industry*, pages 250–256, 1977.

[68] D.E. Newland. *Mechanical Vibration Analysis and Computation.* Longman Scientific and Technical, 1989.

[69] A. Filippov. Differential equations with discontinuous right-hand sides. *American Mathematical Society Translations*, 42:199–231, 1964.

[70] A.B. Stanbridge, M. Martarelli, and D.J. Ewins. Rotating disc vibration analysis with a circular scanning ldv. In *Proceedings of the International Modal Analysis Conference – IMAC XIX*, 2001.

[71] D. Di Maio. Analisi teorica e sperimentale di un sistema frenante a disco: Applicazione ai problemi di rumorosità (squeal) derivanti da fenomeni vibratori. Master's thesis, Università degli studi di Ancona, 2001.

[72] G. Von Groll. Dynamic properties of rotating structures: Modelling and visualisation and experimental results. Master's thesis, Imperial College of Science, Technology and Medicine, 1995.

[73] A. Akay, J. Wickert, and Z. Xu. Investigating criteria for the onset of mode lock-in. Technical report, Carnegie Mellon University, 1998.

[74] P. Duffour. Brake noise test rig with an instrumented pin. Technical report, Cambridge University Engineering Department, 2001.